Homogeneous high-temperature gas-phase processes for energy storage and carbon dioxide utilization

Von der Fakultät für Ingenieurwissenschaften, Abteilung Maschinenbau und Verfahrenstechnik

der

Universität Duisburg-Essen

zur Erlangung des akademischen Grades

einer

Doktorin der Ingenieurwissenschaften

Dr.-Ing.

genehmigte Dissertation

von

Charlotte Rudolph
aus
Hamburg

Gutachter: Univ.-Prof. Dr. Burak Atakan
Prof. Dr. Eric L. Petersen
Tag der mündlichen Prüfung: 17.02.2023

Acknowledgments

At this point, I would like to thank all those who have supported me over the past four years and during the preparation of my thesis. Not only would this thesis have never been written without this amazing support, but I was also allowed to gain important and beautiful experiences and make wonderful friends.

First, I would like to dedicate special thanks to *Professor Burak Atakan*, who gave me the opportunity to do a Ph.D. in the field of thermodynamics. Already in the first semesters of my bachelor studies, your thermodynamics lectures guided me. Thanks to you, the initial fear about the complexity of thermodynamics quickly turned into a special interest in thermodynamic processes. You not only supported me with many helpful discussions and talks but also enabled me to expand my knowledge and interests by spending several months abroad. Thank you very much!

Also, special thanks go to *Professor Eric Petersen* for giving me the opportunity to conduct research at the Turbolab at Texas A&M. It allowed me to discover a new field of work for myself and gain a lot of valuable experience and knowledge. It was a wonderful time, which I often think back to with joy. Thank you very much!

I would also like to thank *Henning Rudolph, Dennis Kaczmarek* and *Sean Cooper* for proofreading my thesis and supporting me over the past four years with helpful discussions and appreciated advice. Thank you very much for taking the time and effort!

Furthermore, many thanks go to the members of the research unit FOR1993, especially *Dominik Freund*, *Kai Banke*, *Sebastian Kaiser*, *Jürgen Herzler*, *Simon Drost*, and *Tina Kasper*, for the successful collaborations, stimulating discussions, as well as the pleasant company during the excursions of the research unit meetings.

For the amazing time in Texas and the successful collaboration, I would like to thank *Claire Grégoire*, *Sean Cooper*, *Olivier Mathieu*, and *Mattias Turner*. The events we visited, like the Football Game or Santas Wonderland, and the time we spent together will always stay in my mind!

Special thanks are also dedicated to *Ulf Bergmann*, who always helped me with words and deeds and with whose company I was allowed to spend many coffee rounds! Many thanks for your constant support and your open ear! I would also like to thank *Stephan Steinbrink* and *Andreas Görnt*, who helped me with many computer and lab problems,

no matter how obvious or obscure the solution was. Also, thank you, *Dennis Kaczmarek*, *Sascha Lau*, *Dominik Freund*, *Lisa Meiers*, *Christoph Horn*, *Michael Aps*, *Julian Quenel*, *Sebastian Grimm*, *Alexandra Welp*, and *Yasin Karakaya*, for your mental support and the many day and night hours we spent in our microscopy lab with hot or cold liquid fluids. Thank you all for letting me be a part of the Thermodynamics Family!
Finally, I would like to thank my *family*, who always had an open ear for me and supported me with good advice. Thank you very much!

Kurzfassung

Zu den bedeutendsten Klimazielen dieses Jahrzehnts gehört, dass die Treibhausgasemissionen bis 2030 weltweit halbiert werden müssen, um die verheerenden Auswirkungen des Klimawandels zu minimieren. Dafür werden Technologien benötigt, die einerseits nachhaltig und sofort einsetzbar, andererseits aber auch kosteneffizient und sicher sein müssen um politisch und sozial akzeptiert zu werden. Eine vielversprechende Lösung bietet die Anwendung etablierter Technologien in Verbindung mit alternativen Betriebsstrategien. Insbesondere sind an dieser Stelle Verbrennungsmotoren zu nennen, deren Einsatz es ermöglicht verschiedenste Energieformen in allen Sektoren nach Bedarf. Anstelle des üblicherweise brennstoffarmen Motorbetriebs und der damit verbundenen Bereitstellung von mechanischer oder elektrischer Energie führt der Einsatz brennstoffreicher Gemische im Verbrennungsmotor zu der simultanen Bereitstellung von Wärme, mechanischer oder elektrischer Energie und wertvollen Grundchemikalien. Auch im Bereich „Power-to-Gas" kann der Motor eine wertvolle Ergänzung für das zukünftige Energiesystem sein, da die dem Motor zugeführte elektrische oder mechanische Energie zur Erzeugung wertvoller und energiereicher Chemikalien dienen kann. Der Motor würde dann vielmehr als Hubkolbenverdichter betrachtet werden, dessen Zylinderinnenraum einem Reaktor im chemischen Sinn entspräche. Durch die zugeführte Arbeit während der Verdichtung und dem damit verbundenen Temperaturanstieg können die Pyrolyse oder die Trockenreformierung von Methan oder Erdgas auch ohne den Einsatz eines Katalysators ablaufen. Dabei entstehen Chemikalien (u.a. Wasserstoff, Olefine oder Aromaten), deren chemische Exergie bedeutend größer ist als die der Ausgangsstoffe. Im thermodynamischen Sinn kann dies als *Exergiespeicherung* benannt werden, da die zugeführte Arbeit in chemische Exergie umgewandelt und somit gespeichert werden kann. Befindet sich darüber hinaus CO_2 in dem Ausgangsgemisch, welches zusammen mit Methan oder Erdgas Verwendung in der Erzeugung von Synthesegas findet, so kann dieser Prozess im Sinne der *CO_2-Abscheidung und Verwendung* (engl. *carbon capture and utilization*) auch CO_2 neutral sein.
Ausgehend von den ersten methodischen Überlegungen ist das Ziel dieser Arbeit die Realisierbarkeit und Effizienz solcher motorischen Exergiespeicher- und Trockenreformierungsprozesse zu untersuchen und mögliche Betriebsvoraussetzungen und -bedingungen zu ermitteln. Dafür werden systematische Untersuchungen mittels Motorsimulationen und Validierungsexperimenten durchgeführt. Die Motorsimulationen

ermöglichen die kinetische und exergetische Untersuchung und Bewertung der Pyrolyse- und Trockenreformierungsprozesse im Motor, ohne dass kostspielige oder riskante Experimente durchgeführt werden müssen. Das Ergebnis dieser Motorensimulationen wird jedoch durch die dabei verwendeten Modelle, wie bspw. von thermodynamisch-kinetischen Modellen zur Beschreibung der zustandsabhängigen Stoffdaten und der Reaktionsraten von chemischen Reaktionen beeinflusst. Aus diesem Grund werden die Simulationen um Validierungsexperimente in einem Stoßwellenrohr ergänzt, um zu prüfen, ob die gewünschten chemischen Reaktionen unter den Bedingungen stattfinden und inwiefern thermodynamisch-kinetische Modelle den Reaktionsfortschritt und die entstehenden Produkte vorhersagen können. Die Stoßwellenrohrexperimente fanden bei 1800–2700 K und 1 atm statt und untersuchten die CO-Bildung bei der Trockenreformierung von Alkanen bei einer Reaktionszeit von bis zu 3 ms. Die experimentellen Daten werden außerdem umfassend mithilfe von Reaktionsfluss- und Sensitivitätsanalysen analysiert.

Die Ergebnisse der Simulationen zeigen, dass Temperaturen von 1400–1800 K im Motor notwendig sind, um die Edukte, wie Methan, Erdgas oder CO_2, umzusetzen. Diese Temperaturen können auf Grund der hohen Wärmekapazität der Edukte jedoch nur erreicht werden, wenn die Edukte mit bis zu 97% Argon verdünnt werden. Die Hauptprodukte sind Wasserstoff, Acetylen, Ethen und Benzol, sowie zusätzlich CO, sofern sich CO_2 im Ausgangsgemisch befindet. Durch Variation der Anfangsbedingungen und der Anfangsgemischzusammensetzung können bestimmte Chemikalien bedarfsgerecht erzeugt werden: Bei niedrigen bis mittleren Temperaturen (1300–1600 K) im Motor bilden sich verstärkt Ethen und Benzol, bei hohen Temperaturen (>2000 K) verstärkt Acetylen und Wasserstoff. Ein unerwünschtes Nebenprodukt stellt dabei Ruß dar. Die Zugabe von Wasserstoff zu der Ausgangsmischung bewirkt eine Verschiebung des Produktspektrums zu den C_2-Spezies wie Acetylen und Ethen und hemmt dabei die Rußbildung. Eine ähnliche Wirkung hat die Zugabe von CO_2, da durch die O-Atome im CO_2 Oxidationsreaktionen stattfinden können, die das Produktspektrum leicht zu den C_2-Spezies und zu dem Gleichgewichtsprodukt CO verschieben. Die exergetische Analyse ergibt, dass Exergieverluste infolge der Entropieproduktion bei chemischen Reaktionen sehr gering sind und dementsprechend exergetische Wirkungsgrade von bis zu 75% erzielt werden können.

Die simulativ erzielten Ergebnisse werden durch die Ergebnisse der experimentellen Untersuchung gestützt, da diese zeigen, dass die Temperaturen und Zeitrahmen des Motors ausreichend für die chemischen Prozesse sind. Die Experimente zeigen außerdem, dass die treibende Kraft für die CO-Bildung bei der Trockenreformierung von Kohlenwasserstoffen die Bildung und der Verbrauch von Wasserstoffradikalen ist. Diese werden insbesondere von C_2 Kohlenwasserstoffen abgespalten oder an diese

angelagert. Die experimentellen Ergebnisse stimmen grundsätzlich gut mit denen der kinetischen Stoßwellenrohrsimulationen überein. Mögliches Verbesserungspotential für präzisere Vorhersagen wird im Rahmen dieser Arbeit ermittelt.

Abstract

One of the key goals of this decade is halving greenhouse-gas emissions by 2030 to minimize the devastating effects of climate change. Therefore, incorporated technologies must be sustainable and immediately applicable while remaining cheap and safe to be socially and politically acceptable. A promising solution is the application of established and technically matured technologies with alternative operating strategies. Combustion engines are established techniques that make it possible to provide various forms of energy in all sectors according to demand and to guarantee energy supply based on renewable energies. However, instead of the usually fuel-lean engine operation and the associated provision of mechanical or electrical energy, the use of fuel-rich mixtures in the combustion engine leads to the simultaneous provision of heat, mechanical or electrical energy, and valuable base chemicals. The engine can also complement the future energy system in the context of "power-to-gas", as the electrical or mechanical energy supplied can lead to the formation of valuable, high-energy chemicals. Then, the engine would be a reciprocating compressor whose cylinder is essentially a chemical reactor, not for producing work, but for chemical production. Due to the work supplied during the compression stroke and the corresponding temperature increase, the pyrolysis or the dry reforming of methane or natural gas can occur without the use of a catalyst. These processes produce chemicals (*e.g.*, hydrogen, olefins, or aromatics) with significantly higher chemical exergy than their reactants. Thermodynamically, this con be called *exergy storage* since the work supplied is converted into chemical exergy, which can be stored. The CO_2 neutral equivalent in the context of *carbon capture and utilization* occurs when CO_2 and methane or natural gas is converted to synthesis gas.

Based on the first considerations, this work aims to investigate the feasibility and efficiency of such engine-based exergy storage and dry reforming processes and to identify possible operating conditions and principles. For this purpose, systematic investigations were conducted by performing engine simulations and validation experiments. The engine simulations allow the kinetic and exergetic investigation and assessment of engine-based pyrolysis and dry reforming without having to perform expensive or hazardous experiments. However, the outcome of these engine simulations is affected by the thermodynamic-kinetic models describing the state-dependent fluid properties and reaction rates of chemical reactions. Consequently, the simulations are

complemented by validation experiments in a shock tube to identify what chemical reactions occur under the conditions and to validate thermodynamic-kinetic models. The shock tube experiments were performed at 1800–2700 K and 1 atm, investigating the CO formation during the dry reforming of alkanes at a reaction time of 3 ms. The experimental data will also be analyzed extensively using reaction pathway and sensitivity analyses.

The results of the simulations show that maximum temperatures in the engine of 1400–1800 K are required to convert ~70-80% of the reactants, methane, natural gas, or CO_2. However, due to the high heat capacity of the reactants, an argon dilution of up to 97% is required to achieve the needed maximum temperatures. The main products are hydrogen, acetylene, ethylene, and benzene, as well as CO if CO_2 is present in the initial mixture. The variation of the initial conditions and the mixture composition allows for the production of certain chemicals on demand: Ethylene and benzene are favored when the maximum temperatures are small or intermediate (1300–1600 K). In contrast, acetylene and hydrogen are favored when the maximum temperatures are high enough (>2000 K). An undesirable by-product is soot, but, by adding hydrogen to the initial mixture, the product distribution is shifted toward C_2-species, such as acetylene and ethylene, inhibiting soot formation. The addition of CO_2 has a similar effect since the O-atoms in CO_2 cause oxidation reactions, shifting the product distribution slightly toward C_2-species and the equilibrium product CO. The exergetic analysis showed that exergy losses due to entropy production in chemical reactions are minimal; accordingly, exergetic efficiencies achieve values of up to 75%.

The results obtained by the engine simulations are supported by the results of the experimental investigation, as they show that the temperatures and time frames of the engine are sufficient for the chemical processes. The analysis of the experimental data showed that the driving force for CO formation during the dry reforming of hydrocarbons is the formation and consumption of hydrogen radicals. Specifically, this occurs from abstraction or addition by or from C_2 hydrocarbons. The experimental results generally agree with those of the kinetic shock tube simulations. Sensitivity analyses performed as part of this work revealed potential improvements for more accurate predictions.

Table of contents

List of figures

List of tables

Nomenclature

Abbreviations

Abbreviation	Description
AMR	Autothermal methane reforming
ATDC	After top dead center
BDC	Bottom dead center
BTDC	Before top dead center
CAES	Compressed air energy storage
CHP	Combined heat and power plant
DME	Dimethyl ether
DMR	Dry methane reforming
EES	Electrical energy storage
HCCI	Homogeneous charge compression ignition
IC, ICE	Internal combustion engine
IVO	Inlet valve opening
NDC	Nationally Determined Contributions
ODE	Ordinary differential equation
PAH	Polycyclic aromatic hydrocarbons
PEM	Polymer electrolyte membrane
PHES	Pumped hydro energy storage
PHS	Pumped hydro storage
PtG	Power-to-Gas
PtL	Power-to-Liquid
SMES	Superconducting electrical energy storage
SMR	Steam methane reforming
SOE	Solid oxide electrolysis
TDC	Top dead center

Symbols

Symbol	Unit	Description
A	m^2	Surface area

C		Constant
C_1		Constant
C_2	m/s/K	Constant
d	m	Bore, Diameter
e_{chem}	J/kg	Specific chemical exergy
e_{in}	J/kg	Specific exergy (inflow)
$e_{mixture}$	J/kg	Specific exergy of a mixture
e_{out}	J/kg	Specific exergy (outflow)
e_{phys}	J/kg	Specific physical exergy
E_{loss} , E_{Loss}	J, kJ	Exergy loss
E_Q	J, kJ	Exergy of heat
ΔE	J, kJ	Exergy increase of a mixture
$\dot{E}_{loss}$	W, kW	Exergy loss rate
f		Factor 10^6
f_k		Uncertainty factor for reaction rates
Δg^0	kJ/mol	Change in specific gibbs energy for 298 K
h	J/kg	Specific enthalpy
h_{air}	J/kg	Specific enthalpy for air
h_{eq}	J/kg	Specific enthalpy for chemically equilibrated mixture
h_{in}	J/kg	Specific enthalpy (inflow)
h_{out}	J/kg	Specific enthalpy (outflow)
h_{sur}	J/kg	Specific enthalpy at surrounding conditions
I_0	(arb. unit)	Incident intensity
I_t	(arb. unit)	Transient intensity
k_1, k_2, k_3, k_r	cm^3/mol/s	Reaction rate k for reaction 1, 2, 3 or r
k_ν	1/cm/atm	Absorption coefficient
L	m	Path length for laser diagnostic
m	kg	Mass
$\dot{m}$	kg/s	Mass flow rate
$\dot{m}_{in}$	kg/s	Mass flow rate (inflow)
$\dot{m}_{out}$	kg/s	Mass flow rate (outflow)
M_k	kg/kmol	Molecular weight of species k
n_E	mol	Molar amount of an educt species
$n_{E,0}$	mol	Initial molar amount of an educt species
n_P	mol	Molar amount of a product species
$n_{P,0}$	mol	Initial molar amount of a product species
N	1/min, 1/s	Rotation speed
p	Pa, atm, bar	Pressure
p_0	Pa, bar	Initial, inlet pressure
p_m	Pa	Motored pressure
p_r	Pa	Reference pressure

P_5	atm	Pressure behind reflected shockwave
P	atm	Pressure
P	W, kW	Mechanical power, storage power
P_{mech}	W, kW	Mechanical power
$P_{storage}$	W, kW	Storage power
q_i	mol/m³/s	rate of progress of species i
Q	J, kJ	Heat
$\dot{Q}$	W, kW	Heat flow rate
R		Connecting rod length to crank radius
R		Coefficient of determination
ROP	mol/cm³/s	Rate of production
s	J/kg/K	Specific entropy
s_{air}	J/kg/K	Specific entropy for air
s_E, s_{Educt}	J/kg/K	Specific entropy of educt mixture
s_{eq}	J/kg/K	Specific entropy for chemically equilibrated mixture
s_P, $s_{Product}$	J/kg/K	Specific entropy of product mixture
s_{sur}	J/kg/K	Specific entropy at surrounding conditions
s	m, mm	Stroke
s_p	m/s	Piston velocity
$\bar{s}_p$	m/s	Mean piston velocity
S_{irr}	J/K, kJ/K	Irreversible entropy
S		Sensitivity
t	s, ms, µs	Time
T	K	Temperature
T_0	K	Initial, inlet temperature
T_C	K	Coolant temperature
T_{CW}	K	Cooling water temperature
T_r	K	Reference temperature
T_{sur}	K	Surrounding temperature (298 K)
T_5	K	Temperature behind reflected shockwave
U	J, kJ	Internal Energy
V	m³	Volume
V_D	m³	Displacement volume
V_r	m³	Reference volume
W	J, kJ	Work
x		Mole fraction
x_{Ar}		Argon mole fraction
X_{CH4}		CH_4 mole fraction
X_{CO2}		CO_2 mole fraction
x_{CO}		CO mole fraction
x_k, x_i		Mole fraction of species k or species i

$x_{CO,max}$		Maximum CO mole fraction
$x_{CO,rel}$		Relative CO mole fraction
X	(%)	Conversion
y_k		Mass fraction of species k
$y_{k,in}$		Mass fraction of species k (inflow)
y_i		Mole fraction at timestep i of experiments
$\hat{y}_i$		Mole fraction at timestep i of simulations
$\bar{y}$		Average experimental mole fraction
Y	(%)	Yield

Greek symbols

Symbol	Unit	Description
α	$W/m^2/K$	Convection coefficient
Δ		Difference
ε		Compression ratio
η		Exergetic efficiency
Θ	°, °CA, °CAD	Crank angle
ν_E		Number of atoms in educt species
ν_P		Number of atoms in product species
$\nu''_{i,r}$		Stoichiometric coeff. of forward (') reaction r for species i
$\nu'_{i,r}$		Stoichiometric coeff. of reverse ('') reaction r for species i
P		Coefficient of determination
τ_{20}	µs	CO formation time, CO delay time
Φ		Equivalence ratio
$\dot{\omega}_k$	$mol/m^3/s$	molar production rate of species k

1 Introduction

Anthropogenic climate change and the mitigation of its devastating consequences is a central hallmark of the 21st century [1]. To limit global warming to 1.5°C (compared to 1850), the Paris Climate Agreement provides an international framework by encouraging each country to comply with the intended Nationally Determined Contributions (NDCs) [2]. However, according to the 2021 Emissions Gap Report [3], achieving the Paris Climate Agreement's 1.5°C-goal is not possible if only the NDCs are realized. Emissions would continue to rise by 14% [4], and global warming up to 2.7°C is predicted [3]. The additional adopted net-zero emissions commitments are an essential step toward keeping global warming within the 1.5°C-target of the Paris climate agreement. In a 100-year time frame, it is expected that reaching net-zero CO_2 emissions by 2050 would stabilize the emissions-induced global temperature increase at 1.6°C [3]. Reaching net-zero greenhouse gas emissions in 2067 or even net-negative CO_2 and greenhouse gas emissions would even lead to an overall global temperature decrease [3]. However, the net-zero emission pathways and targets are individual for each country, for example, China by 2060 [5], the United States by 2050 [6], the European Union by 2050 [7], and India by 2070 [8]. Also, each contribution has unique relevance as each country accounts for a particular share of global greenhouse-gas emissions [3]. Either way, the global carbon budget toward the 1.5°C-target is expected to be depleted by 2045 [3]. In this context, Inger Andersen proclaimed 2021:

„*We have a duty of care – to the planet and to every person upon it. We must fulfill it by making our energy system clean, efficient and affordable*." (Inger Andersen, 2021) [9].

During her speech at the United Nations "High-level Dialogue on Energy" in New York, this wake-up call addresses global energy access and energy transition by 2030, aiming to halve greenhouse gas emissions within eight years to meet the 1.5°C-target [9]. Developing and integrating complex and interconnected climate technologies, such as carbon capture and utilization technologies, into our existing energy system can hardly be accomplished within eight years. Likewise, using renewable energies as a fixed factor in the energy-efficient and climate-neutral future energy system requires using fluctuation-balancing technologies to ensure a stable and reliable energy supply for all sectors [10].

In terms of technological change, we are facing the challenge of balancing the integration of climate technologies across all sectors within eight years and keeping acceptance from society. One possible solution for the transition period regarding efficient and sector-wide energy supply could be polygeneration processes, such as conventional combined heat and power plants (CHP), gas-fired power plants (as Brayton cycles) [11], or integrated fuel-cell processes [12]. Generally, polygeneration processes allow the provision of two or, most likely, three types of energy simultaneously, such as cooling, heating, and power [13], or heating, power, and hydrogen [12], and therefore have promising high energetic efficiencies [12]. Also, the alternative operation mode of technically matured and frequently integrated technologies, such as gas turbines or internal combustion engines (ICE), could be promising to meet the 8-year target. As knowledge and techniques from the commercial use and research of the last decades are available, these technologies are immediately applicable.

Engine-based polygeneration and energy storage by natural gas conversion

The use of piston engine-based polygeneration and energy storage via conversion of natural gas could overcome these challenges. In particular, the application of piston engines allows for a high degree of flexibility as the cylinder charge can be adapted according to the demand by varying the equivalence ratio. Thus, the engine could be an inherent part of the energy supply because mechanical/electrical energy, heat, and interesting chemicals such as synthesis gas (*i.e.*, H_2 and CO) could be provided simultaneously when the engine is operated under fuel-rich conditions. If the electricity demand is significantly greater than the supply due to fluctuations in renewable energies, the engine can be operated under stoichiometric or lean conditions, favoring mechanical/electrical energy generation. Engine-based power-to-gas processes in the context of chemical energy storage are possible if the engine is motored using excess energy from renewable sources. Then, mechanical energy is converted to chemical energy or, more precisely, exergy, as the chemical exergy of the cylinder charge is increased due to work input during the compression stroke. A temperature-activated endothermic, endergonic thermal decomposition (*i.e.*, pyrolysis or dry reforming) occurs at the end of the compression stroke. These processes lead to the formation of high-energy chemicals. It should be noted that such chemicals are not usually formed during oxidation in fuel-lean or fuel-rich engines. The expansion stroke allows for rapid quenching and the avoidance of unwanted chemicals due to well-defined time frames of the chemical process.

The development of fuel-rich operated ICE engines can rely on well-known concepts, such as the use of homogeneous charge compression ignition (HCCI) engines. Their performance is not affected by, for example, low flame speeds [14] or the use of

reactive additives (e.g., dimethyl ether, ethanol, or nitromethane) to improve the cetane number and to control the combustion phasing as is the case in conventional diesel engines [15]. However, engine-based exergy storage entails a new area with unknown problems. The question of whether the process is efficient and effective beyond the first glance requires a holistic examination of the thermodynamic, exergetic, and kinetic aspects. But, before an industrial-scale engine can be used for this process, a fundamental understanding of the process is required. This can be obtained through kinetic-thermodynamic simulations, which help to identify the general behavior of the process, optimal operating conditions and are not limited by technical or financial constraints. In addition, unforeseen behaviors or extremely hazardous products can be predicted to be prepared for future experiments. As the simulation of these unusual processes is limited to the accuracy of the kinetics and thermodynamics of the model, the performance of validation experiments is key to understanding the chemical kinetics and improving the predictive ability of kinetic models. This work bridges the gap between theoretical considerations and experimental findings.

Task and objective

The present thesis aims to understand the underlying thermodynamic and chemical processes of engine-based exergy storage by performing engine simulations and validation experiments. Combining theory and experiment is crucial, as the questions left unanswered by one method might be addressed by the other. Together, these two methods provide a solid basis for analyzing such novel concepts as the one presented here.

The engine simulations were performed using a single-zone model based on the kinematics of an engine, thermodynamics and homogeneous gas-phase reactions as well as chemical kinetics provided by reaction mechanisms. The simulations of engine-based pyrolysis and dry reforming intend to reveal the exergetic performance of these processes, as well as their potential and the viability of producing the desired chemicals. Pyrolysis or dry reforming is typically conducted catalytically [16]. The question must be clarified whether the pyrolysis or dry reforming as homogeneous gas-phase processes can proceed within the time frame, temperature, and pressure limitations of the piston engine. Modeling the piston engine under pyrolysis or dry reforming conditions allows the assessment of the process by considering the thermodynamic, exergetic, and kinetic aspects to identify operating principles and limits of the optimum operating conditions. For instance, the operating conditions that lead to the production of a certain target chemical (*e.g.*, benzene, or the highest exergetic efficiency) can be precisely predicted for future engine experiments. To achieve these goals, reaction

mechanisms with accurate prediction capabilities under these unusual conditions are required. This implies the need for fundamental validation experiments.
These fundamental experiments were performed in a shock-tube/CO Laser absorption set-up, to enable the investigation of dry reforming of natural gas components (*i.e.*, methane, ethane, and propane). So, the experiments aim to understand the chemical processes, validate the literature reaction mechanisms, and find the most appropriate reaction mechanism for these unusual conditions. Shock tube investigations are particularly suitable for this purpose since the reaction times and achievable temperatures correspond to the reaction times and maximum temperatures occurring in piston engines. Beyond the fact that CO is an essential component of synthesis gas, the reaction progress of the initial binary hydrocarbon/CO_2 system can be easily monitored by measuring the time-resolved CO formation. This information can be used to reveal knowledge gaps, emphasize the need for updated thermochemistry and chemical kinetics, and improve reaction mechanisms.
The objectives of this thesis, as written above, are summarized below.

Engine simulations

a) Verification of the general feasibility
b) Understanding the thermodynamic processes
c) Assessment of the exergetic performance
d) Identification of optimal operating conditions

Shock-tube experiments

a) Validation of literature reaction mechanisms
b) Understanding of the chemical processes
c) Suggestion of improvements

This work is embedded in the framework of the DFG research group FOR1993: "Multifunctional Material Conversion and Energy Conversion" and therefore benefits from the knowledge gained with respect to polygeneration processes. Among others, kinetic models have been developed within the research unit [17], which have been used frequently in this work. In addition, the first piston-engine experiments have been successfully conducted in rapid compression machines (RCM) [18]. In conjunction with the fundamental thermodynamic-kinetic piston engine simulations and the fundamental validation experiments presented in this thesis, the exergy storage and dry reforming can be analyzed comprehensively. The investigations carried out for this purpose are briefly introduced below.

Chapter three provides a comprehensive theoretical study on the pyrolysis of methane and ethane in the context of exergy storage to verify the general feasibility of the process and to reveal the underlying thermodynamic relations. Chapter four presents the influence of hydrogen as an additive for the pyrolysis of natural gas on product distribution and exergetic performance in terms of exergy storage. In this context, hydrogen addition seems promising as it leads to increased reactivity of the mixture and a reduced soot formation.

In chapter five, the exergy storage concept is extended to carbon dioxide utilization by performing dry reforming of a methane/CO_2 mixture in a piston engine. The CO_2 addition poses new challenges for the process because CO_2 is even more stable than methane, so more extreme conditions such as higher temperatures are required for its conversion.

Finally, chapters six and seven cover the experimental studies of methane, ethane, and propane / CO_2 mixtures, focusing on the predictive capabilities of literature reaction mechanisms and the analysis of the chemical kinetics using the most appropriate reaction mechanism.

2 From theoretical ideas to experimental validation

The principle of exergy storage in piston engines by pyrolysis or dry reforming is the conversion of mechanical energy into chemical energy. Thermodynamically speaking, it is the conversion of the work input during the compression stroke into chemical exergy due to the formation of higher-exergy products from simple hydrocarbons or hydrocarbon mixtures, such as methane or natural gas. The products formed in that process can be further used as a substitute fuel, energy carrier, or base chemical for subsequent processes (*e.g.*, Fischer-Tropsch synthesis).

The exergy balance accounts for the work and the chemical exergy of the reactants on the input side and the exergy of heat, exergy losses, and the chemical exergy of the products on the output side. Consequently, the increase of the chemical exergy per work input is maximized when a) the reactants are completely converted and b) exergy losses are minimized (ideally, a reversible, adiabatic process). Also, considering the net reaction equation of the pyrolysis ($CH_4 \rightleftharpoons 1.5\ H_2 + 0.5\ C_2H_2$, $\Delta g^0 = 155$ kJ/mol) or dry reforming ($CH_4 + CO_2 \rightleftharpoons 2\ H_2 + 2\ CO$, $\Delta g^0 = 172$ kJ/mol) and the corresponding Gibbs energies, two conclusions can be drawn. Firstly, the change of Gibbs energies of both processes is strongly positive at a reference condition of 298 K, so the process is endergonic. To overcome the high activation energies, temperatures around 1200–1500 K are needed. Secondly, the change of Gibbs energy indicates the chemical exergy that can, in principle, be stored when the corresponding reaction products are formed as the change of Gibbs energy at 298 K represents reversible work on the environment. However, assuming a reversible, adiabatic process, the temperature and pressure increase due to the compression of the cylinder charge can be easily estimated by the isentropic relation for perfect gases ($T_{compression} = T_0 \cdot \varepsilon^{c_p/c_v-1}$). This estimation reveals that high initial temperatures T_0, high compression ratios ε, or small heat capacities are required. Due to technical constraints of the engine, the initial temperature and the compression ratio are also limited. Therefore, the reactants are diluted within a monatomic inert gas, namely argon, which has a low heat capacity. The subsequent step was to investigate which conditions (*i.e.*, initial temperatures or pressures, argon dilution, and geometric and kinematic engine parameters) are suitable in terms of the exergy balance and the product spectra.

First, the pyrolysis of methane and ethane in a piston engine are modeled to verify the general feasibility of the process. To model the entire concept, a single-zone model is used, solving energy and species balances at each time step, assuming homogeneous conditions in the cylinder. However, to represent the heat transfer and the chemical kinetics, further models are required (*i.e.*, heat transfer correlations and reaction mechanisms). Since literature heat transfer models were developed for fuel-lean combustion, including for example flame propagation, the influence of these heat transfer models on important parameters, such as temperature, pressure, or mole fraction during pyrolysis in piston engines, was investigated. Also, the use of different reaction mechanisms leads to different temperature, pressure, or mole fraction predictions. This work already indicates the need to validate models, such as reaction mechanisms, for unusual conditions. Beyond that, this work demonstrates that the concept is feasible, as small exergy losses and high exergetic efficiencies can be achieved while still allowing for production of certain chemicals, such as acetylene or benzene. Two undesirable facts become apparent: the argon dilution required to reduce the heat capacity is very high, and large amounts of soot precursors and soot are predicted. This leads to the investigation of hydrogen addition during pyrolysis of natural gas in terms of engine-based exergy storage.

While the pioneering study of methane and ethane pyrolysis in the context of exergy storage addresses both the thermodynamics and the chemical kinetics of the process, the investigation of the hydrogen-assisted exergy storage process focuses on the chemical effect of hydrogen addition. The aim is to increase reactivity to reduce argon dilution and shift the main reaction patterns from soot to the main species, like acetylene. Another motivation for investigating the natural gas/hydrogen mixture is the increasing amount of hydrogen in natural gas pipelines, up to 20% [19] caused by the energy and technology transition.

To connect the flexibility of engine-based exergy storage with the CO_2 neutrality of carbon capture and utilization technologies, dry reforming of methane in piston engines is the subject of the subsequent investigation. This process allows the utilization of CO_2, captured from the surrounding air, in an exergetically feasible process by producing synthesis gas. The feedstock is a mixture of methane and CO_2 with various blends comparable to biogas. The addition of CO_2 has a significant impact on operating conditions as well as on exergetic performance and product distribution. Biogas is widely used as a substitute fuel in, for example, combined heat and power plants or in the transport sector [20,21]. Therefore, a comparison is made between engine-based exergy storage and polygeneration.

Additionally, the engine simulation predicts that methane and CO_2 are almost completely converted at maximum temperatures above 1800 K in the time periods ranging

from microseconds to milliseconds, forming large amounts of synthesis gas. To validate the conversion and product formation under these conditions and to verify the viability of storing exergy using piston engines, fundamental validation experiments are performed using a shock-tube/CO laser absorption set-up. The studied mixtures were hydrocarbon/CO_2 mixtures similar to those used in the simulations. CO laser absorption measurements allowed monitoring of time-resolved CO formation, which is directly linked to the reaction progress of dry reforming. The data obtained from the experiments were compared with simulations to assess the predictive ability of different reaction mechanisms. The chemical kinetics were analyzed by performing rate-of-production and sensitivity analyses. The insights gained from the analysis of the experiments were then used to make recommendations for improvements.

3 Engine-based exergy storage: Pyrolysis of methane and ethane

The content of this chapter was published in Energy Technology:
C. Rudolph, B. Atakan, Pyrolysis of methane and ethane in a compression–expansion process as a new concept for chemical energy storage: A kinetic and exergetic investigation, Energy Technology 9, pp. 2000948 (2021), DOI: 10.1002/ente.202000948.

Author contribution

My contribution embraced developing the concept, designing the computer code, conducting the simulations, analyzing and graphing the results, and writing the manuscript. Burak Atakan developed the concept and reviewed the manuscript. He also coordinated the project and acquired funding.

Abstract

The production of chemical energy carriers utilizing electrical energy from renewable sources is essential for the future energy system. A motored piston engine may be used as a reactor to convert mechanical to chemical energy by the pyrolysis of methane and ethane; this is analyzed here. The piston engine is modeled as a compression-expansion cycle with detailed chemical kinetics. The main products are hydrogen and high-energy hydrocarbons such as acetylene, ethylene, and benzene. To reach the required high temperatures for conversion after compression, the educt is diluted with argon. The influence of the operating conditions (temperature, pressure, dilution) on the product gas composition, the stored exergy, and the ratio of exergy gain to work input (efficiency) is investigated. A conversion of >80% is predicted for an argon dilution of 93 mol% at inlet temperatures of 573 K (methane) and 473 K (ethane), respectively. A storage power of 7.5 kW (methane) and 6 kW (ethane) for a 400 ccm four-stroke single-cylinder is predicted with an efficiency of 75% (methane) and 70% (ethane), respectively. Conditions are identified, where high yields of the target species are achieved, and soot formation can be avoided.

3.1 Introduction

The future energy demand will be covered by renewable energies. Their weather dependence results in a fluctuating electrical energy production: Energy surpluses or deficits arise. To provide a stable and flexible energy supply, the topic of energy storage is becoming increasingly important. To store energy for later usage, several methods of energy storage exist, which differ in storage capacity and storage duration and in the type of stored energy [22–24]. The most direct way to store electrical energy is electrical energy storage (EES) in applications such as (super-) capacitors or superconducting magnetic energy storage (SMES). These types of energy storage provide high efficiencies up to 95%, a fast response within milliseconds, and a long cycle life (106 cycles). Their main problem is a short storage period (seconds or hours) and a low energy density (<5 Wh kg^{-1}) and capacity [25,26]. Also battery energy storage is well-known for medium power capacities and short response times and a short lifetime but high efficiencies of up to 85%, depending on the type of battery [27]. Therefore, these short-term energy storage methods are a good option for short-term energy compensation [28]. A choice for medium-term energy storage is the compressed air energy storage (CAES), which uses excess energy to compress air and stores it in caverns afterward. CAES has a storage duration of hours to days at medium energy densities (<60 Wh kg^{-1}) and capacity [24]; they have a fast response time and, depending on their design, efficiencies of 60–90% [24]. Their major disadvantage is that certain geological requirements limit their general usage [29,30]. Another medium-term energy storage technology is the pumped hydro energy storage (PHES). PHES uses the potential energy of water, which increases, when water is pumped from a lower level to a higher level. In contrast to CAES, PHES is developed to commercial maturity with efficiencies of up to 85% with high capacities and a storage duration of up to months [31,32], but is also limited by geological restrictions. Power-to-Gas (PtG) or Power-to-Liquid (PtL) do not only offer a long-term energy storage but also a cross-sector energy compensation. These concepts use excess energy to produce hydrogen first and synthetic methane or ammonia afterward, which can be stored with a high energy density in caverns, tanks, pipelines, or in chemical compounds [23,24]. If needed, the stored gas can be converted back to electricity using fuel cells, gas turbines or engines [33], or converted to liquid fuels such as higher alkanes via the Fischer–Tropsch synthesis [34].

Hydrogen can be produced in different ways. A distinction is made between methods, which need fossil fuels and those that are based on renewable energies [35], as *e.g.*, electrolysis of water. Hydrogen is mainly produced by steam methane reforming (SMR) because the cost for natural gas is low and the technologies are already developed for

large scale. SMR is the catalytic reaction of methane and water to hydrogen and carbon dioxide at relatively high temperatures (>900 K) and pressures (3–25 bar) according to Equation (R3.1)) [36–38].

$$CH_4 + 2\ H_2O \rightleftharpoons CO_2 + 4\ H_2 \qquad \Delta g^0 = 114\ \text{kJ/mol} \qquad \text{(R3.1)}$$

After the carbon dioxide removal, hydrogen is obtained with a purity of 99.99%. Overall, the process can achieve a thermal efficiency (based on the higher heating values) of 85% and the hydrogen production costs for the complete process are comparably low [35,36,39].

The electrolysis of water is a method that uses water and renewable energy sources. One benefit of this method is, that no carbon dioxide is produced and therefore no post-treatment is necessary. Although the efficiencies are similar to SMR, they are not competitive as the large-scale plants are technically not matured [40,41]. A carbon-dioxide-free method to produce hydrogen with very low costs is the decomposition of methane, according to (Equation (R3.2)).

$$CH_4 \rightleftharpoons C_s + 2\ H_2 \qquad \Delta g^0 = 50.8\ \text{kJ/mol} \qquad \text{(R3.2)}$$

In this process, methane is converted to hydrogen and solid carbon by pyrolysis. The needed catalysts for this reaction as well as the temperature range has been studied many times [42–45]. In early studies, Muradov [42,46] found out, that metal or metal oxide catalysts are very advantageous, yielding hydrogen purities in hydrogen–methane mixtures of >80% at temperatures above 1100 K, which is very close to the chemical equilibrium. The additionally produced solid carbon is used industrially or can be buried in the ground. The disadvantage of this method is the comparably low thermal efficiency (based on the higher heating values) of 35–50% [35], if only hydrogen is sought as product. The overall efficiency of the process can be increased, if not only hydrogen and carbon but also larger amounts of higher hydrocarbons are produced in the methane pyrolysis [47–51].

Bartholomé [47] developed a method in 1954 for acetylene production from methane in which the thermal decomposition of methane is initiated by oxidation and, after a very short reaction time (10−2 s), stopped by cooling and therefore quenching the mixture. The methane pyrolysis toward higher hydrocarbon and hydrogen formation was investigated several times [48–51], and it is known that the endothermal reactions starts at temperatures of 1300 K, producing mainly benzene at these temperature. At higher temperatures (>1500 K), mainly acetylene and ethylene are formed according to the net reactions (Equation (R3.3)–(R3.5)).

$CH_4 \rightleftharpoons 0.5\ C_2H_2 + 1.5\ H_2$	$\Delta g^0 = 155$ kJ/mol	(R3.3)
$CH_4 \rightleftharpoons 0.5\ C_2H_4 + H_2$	$\Delta g^0 = 85$ kJ/mol	(R3.4)
$CH_4 \rightleftharpoons 0.167\ C_6H_6 + 1.5\ H_2$	$\Delta g^0 = 72$ kJ/mol	(R3.5)

Depending on reaction time and temperature, the main species are acetylene, ethylene, and benzene always together with a high amount of hydrogen but also species such as propene, propane, 1,3-butadiene but polycyclic aromatic hydrocarbons (PAHs) and soot are formed as well. Experimental investigations of methane pyrolysis by Nativel et al. [52] in a single-pulse shock tube and by Keramiotis et al. [53] in a flow reactor showed the same trends. In the shock tube study, in which the decomposition of methane was examined at different temperatures and very short residence times, a methane conversion of up to 80% at a temperature of 2400 K was observed. In the flow reactor study with comparably long residence times, a methane conversion of up to 85% could already be reached at temperatures of 1500 K. In both studies, the major products are acetylene, ethylene, and benzene but also soot is formed. Especially, long residence times lead to a high amount of soot as it is expected in equilibrium. As not only methane but also natural gas is used for such processes, the pyrolysis of ethane is also considered. The ethane conversion starts at temperatures of 1100 K. The main products are ethylene at lower temperatures of 1300 K and acetylene and methane at higher temperatures >1500 K, following the net reactions (Equation (R3.6)–(R3.8)) below [54,55].

$C_2H_6 \rightleftharpoons C_2H_4 + H_2$	$\Delta g^0 = 100$ kJ/mol	(R3.6)
$C_2H_6 \rightleftharpoons C_2H_2 + 2\ H_2$	$\Delta g^0 = 241$ kJ/mol	(R3.7)
$C_2H_6 + H_2 \rightleftharpoons 2\ CH_4$	$\Delta g^0 = -69$ kJ/mol	(R3.8)

Internal combustion (IC) engines, running in homogeneous charge compression ignition (HCCI) mode, can also be used as chemical reactors for partial oxidation with respect to flexible and versatile energy conversion in polygeneration processes, which was investigated theoretically [56] and experimentally [57,58]. Engines can also be considered for pyrolysis processes, where the endothermal reactions are initiated by the high temperatures at the top dead center (TDC) after compression. In addition, the mixture is diluted with an atomic inert gas to further increase the temperatures and to improve the conversion. The enthalpy of the cylinder charge increases due to work input during the compression stroke. Therefore, the product gas contains species with a higher enthalpy and exergy than the educt gas. It results that the input energy, possibly from excess renewable energy, is stored in the higher-energy product gas.

Possible applications for the product gas are: 1) utilization as a raw material for chemical synthesis, 2) feed into the natural gas grid to increase its heating value, 3) combustion to generate electricity, or 4) storage and later use. The basic principle is shown in Figure 3.1.

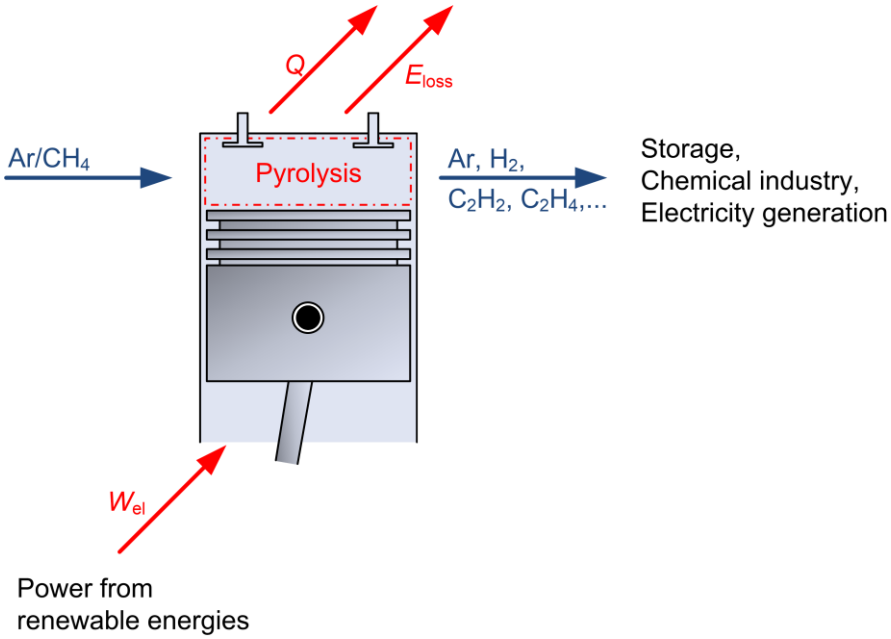

Figure 3.1. Basic principle of the process.

Atakan [59] optimized a compression-chemical equilibrium-expansion process for pyrolysis of methane, ethane, and hydrogen to defined expected species within initial temperature and pressure, compression ratio, and argon dilution. The target variable of the optimization was, *e.g.*, a maximum stored exergy. He only used thermodynamic equilibration, without regarding the chemical kinetics. The optimization predicts a maximum stored exergy at the upper bounds of inlet temperature, compression ratio and argon dilution, and the lower bounds of inlet pressure. Thus, the pyrolysis process appeared to be a feasible approach. An increase in exergy of more than 11% with exergetic efficiencies of up to 92% were predicted producing chemicals, such as acetylene, ethylene, and benzene. However, ethane in the equilibrium study seemed not to be very promising as in equilibrium it reacts exothermically to methane. A recent review contains experimental results for methane pyrolysis in a rapid compression machine [60]. Methane was diluted with 90% argon and 5% helium, so the mixture contains also only 5% methane. For a compression pressure of 18 bar and compression temperatures of 1450–1750 K, the conversion of methane was between 2.5% and 20%. The measured species were H_2, C_2H_2, and C_2H_4 with yields of up to 12% (H_2), 5% (C_2H_2), and 2% (C_2H_4), respectively.

The kinetics of the conversion of methane and ethane to higher energy fluids through pyrolysis in a piston engine is investigated theoretically in the present work with respect to energy storage, as they are the main components of natural gas. The endothermal reactions are initiated at high temperatures at the TDC due to compression stroke and argon dilution. A simplified time-dependent piston engine is modeled, only regarding the compression and expansion strokes. A detailed chemical reaction mechanism is used, as described in the following section. A comprehensive parameter study is performed to find feasible operating points within a reasonable amount of storable exergy and efficiency. In addition to exergy, the kinetics are also investigated, analyzing the educt conversion, the product gas composition, and the crank-angle dependent reaction path. The main aim is to analyze, whether the in-cylinder process is thermodynamically controlled or if the kinetics can lead to different conclusions with respect to the product formation and the thermodynamics, than those made by Atakan [59].

3.2 Modeling

The piston engine is simulated as a time-dependent single-zone model with detailed chemical kinetics in Cantera within Python [61]. The engine is modeled as a closed system, because only the compression and expansion strokes are considered. The complete engine cycle consists of one rotation of the crank, 360°, starting with the piston movement from bottom dead center (BDC) to TDC (compression stroke) and back from TDC to BDC (expansion stroke). A resolution of a tenth of a degree is selected. The cylinder volume V is determined from the crank-angle (θ) dependent position of the piston. The change in the cylinder volume is therefore dependent on the piston velocity s_p which is calculated from Equation (3.1)

$$\frac{s_p}{\bar{s}_p} = \frac{\pi}{2} \cdot \sin(\Theta) \cdot \left(1 + \frac{\cos(\Theta)}{\sqrt{R^2 - \sin^2(\Theta)}}\right) \tag{3.1}$$

where $\bar{s}_p$ is the mean piston velocity and R is the connecting rod length to crank radius ratio. The rotation speed converts the crank angle dependency into a time dependency. While piston speed and volume change, pressure and temperature also increase as a function of time. Ideal gas behavior is assumed for all changes of state. For every time step, the balances for species and energy conservation are solved. The time integration for the species and energy balances is solved using a stiff ordinary differential equation (ODE) solver, namely SUNDIALS [62]. The used absolute and relative tolerances are 10^{-21}. The equation for the conservation of species k (Equation (3.2)) is

$$m \cdot \frac{\mathrm{d}y_\mathrm{k}}{\mathrm{d}t} = V \cdot \dot{\omega}_\mathrm{k} \cdot M_\mathrm{k} \tag{3.2}$$

for a constant total mass m and without surface reactions, where y_k is the mass fraction, $\dot{\omega}$ is the molar production rate, and M_k is the molecular weight of each species k.
The energy conservation (3.3) calculates the change in internal energy due to transfer of work and heat for a closed system.

$$\frac{\mathrm{d}U}{\mathrm{d}t} = -p\frac{\mathrm{d}V}{\mathrm{d}t} + \dot{Q} \tag{3.3}$$

p is the pressure and $\dot{Q}$ the heat (loss) rate. The heat transfer through the cylinder walls is calculated from Newton's law of cooling (Equation (3.6)), using the Woschni correlation (Equation (3.4)) [63], to estimate the convective heat transfer coefficient α

$$\alpha = C \cdot d^{-0.2} \cdot p^{0.8} \cdot T^{-0.53} \cdot \left[C_1 \cdot \bar{s}_\mathrm{p} + C_2 \cdot \frac{V_\mathrm{D} \cdot T_\mathrm{r}}{V_\mathrm{r} \cdot p_\mathrm{r}} \cdot (p - p_\mathrm{m})\right]^{0.8} \tag{3.4}$$

where V_D is the displacement volume, T_r, p_r, and V_r are temperature, pressure, and volume at a reference state, and C and C_1 are constants according to Woschni. C_2 is set to zero as no combustion occurs and thus the actual pressure p and the motored pressure pm are similar to each other. The resistances for heat conduction through the cylinder walls and the convective heat transfer on the cooling water side were neglected, as their heat-transfer resistances are significantly smaller than the one for convection to the inner cylinder wall.
The chemical reactions are simulated with the complete Polimi elementary reaction mechanism [64–67], including 484 species and 19 341 reactions including species up to C_{20}, lumped species and chemistry of PAHs, because the formation of soot or soot precursors were expected. The mechanism is validated for pyrolysis, partial oxidation and combustion of hydrocarbons at low and high temperatures, and soot formation in (laminar) flames and in jet-stirred and flow reactors. Other reaction mechanisms for this purpose could be the Aramco 3.0 [68] or the PolyMech [17] but were not chosen here, because the Polimi is more detailed with respect to the PAH-submechanism. The PolyMech, in particular, contains only species up to C_6 and does not contain C_6 decomposition reactions. Although the choice of mechanism is important for this investigation, the main outcome is not influenced as tested for some conditions. With different mechanism, the mole fractions and the product distribution change to some extent, but the main tendencies remain unchanged, also the thermodynamic aspects and, thus, the study's outcome.

Table 3.1. Engine parameters used for the simulation.

Parameter	Specification	Unit
Displacement V_D	$4 \cdot 10^{-4}$	m^3
Bore d	$79.5 \cdot 10^{-3}$	m
Stroke s	$80.5 \cdot 10^{-3}$	m
Compression ratio ε	22	-
Connection rod / crank radius R	3.5	-
Rotation speed N	3000	RPM
Coolant temperature T_C	373	K

The chosen engine parameters are listed in Table 3.1 and correspond to typical stationary engine parameters, but with larger rotation speed and compression ratio, because this is more favorable for the storage process. A high compression ratio leads to a higher temperature increase and thus a higher temperature at TDC. In addition, the compression ratio is a low-cost method to increase TDC temperatures and pressures, compared to increased inlet conditions that required an additional energy input. Thus, a realistically high compression ratio of 22:1 was chosen, similar to recent HCCI engine investigations [69,70], and was not varied. In the present work, an effective compression ratio is assumed as the single-zone model does not consider uncertainties due to crevices, blow-by, or cold cylinder walls. A high rotation speed leads to shorter reaction times, which reduces the production of carbon due to quenching effects during the expansion stroke. This effect is explained in detail in the Section 3.3.1. The coolant of the cylinder walls is water. As no combustion takes place in this process, a reduction in the cooling power using air as a coolant would also be conceivable. This could lead to a more homogeneous temperature distribution and an increased reactant conversion. In addition to the geometric parameters, the varied process parameter ranges for initial temperature T_0, initial pressure p_0, and Ar mole fraction are listed in Table 3.2. The inlet temperature was chosen in a range of 323–573 K and it is assumed that the temperature between inlet valve opening (IVO) and BDC remains almost constant as it is not a fired operation. Especially, the upper boundary of the inlet temperature seems practicable according to Lim et al. [14], where spark-ignition engine experiments were performed with inlet temperatures up to 750 K. The inlet pressure was chosen in a range of 1–10 bar. Although an inlet pressure of up to 10 bar is unusual for IC engines, it is already used in multi-stage piston compressors. Thus, in principle, such a high inlet

pressure can be realized, even if the design of such a piston engine has to be adapted. In this study, it is shown to what extent these unusual conditions prove to be favorable in terms of thermodynamics and kinetics.

Table 3.2. Process parameters used for the simulation.

Parameter	Range	Unit
Initial temperature T_0	323 – 573	K
Initial pressure p_0	1 – 10	bar
Argon dilution	85 – 99	mol%

Methane and ethane are used as fuels, or better as educts as they are the main components of natural gas. The educts are diluted with an atomic inert gas to reduce the heat capacity of the mixture, which leads to a higher temperature at the end of compression stroke, and thus, to a higher educt conversion.
To describe and evaluate the process, a thermodynamic and a kinetic analysis is carried out. The thermodynamic analysis includes the calculation of the supplied work W and the heat loss Q according to Equation (3.5) and (3.6)

$$W = -\int p\mathrm{d}V \tag{3.5}$$

$$\dot{Q} = \alpha \cdot A \cdot (T_\mathrm{c} - T) \tag{3.6}$$

and the calculation of the irreversible entropy production S_irr and the exergy loss E_loss according to Equation (3.7) and (3.8). The European sign convention is used for the work, added work has a positive value.

$$S_\mathrm{irr} = m \cdot (s_\mathrm{Product} - s_\mathrm{Educt}) - \frac{Q}{T_\mathrm{c}} \tag{3.7}$$

$$E_\mathrm{loss} = T_\mathrm{sur} \cdot S_\mathrm{irr} \tag{3.8}$$

As a result of the endothermal reaction, the product gas composition changes, which leads to a change in the internal energy. The chemical and physical exergies of the mixture are chosen to describe the energetic value of the product gas mixture and to determine the storable exergy. The chemical exergy is calculated according to Atakan [59]. As described there, the gas mixture, whose exergy is to be determined, is chemically equilibrated with surrounding air in the ratio $1/f$ with $f = 10^6$. Assuming, the surrounding air is at standard conditions (298.15 K and 1.01325 bar) and has a relative

humidity of 70%, according to ref. [71], the chemical specific exergy e_{chem} is calculated using

$$e_{\mathrm{chem}} = \left(h_{\mathrm{sur}} + f \cdot h_{\mathrm{air}} - (f+1) \cdot h_{\mathrm{eq}}\right) - T_{\mathrm{sur}} \cdot \left(s_{\mathrm{sur}} + f \cdot s_{\mathrm{air}} - (f+1) \cdot s_{\mathrm{eq}}\right) \tag{3.9}$$

where h is the enthalpy and s is the entropy, the subscript sur is used for the mixture at surrounding (standard) conditions; the subscript air is used for air, which is described earlier and the subscript eq is used for the chemically equilibrated mixture. The physical specific exergy for an open system is calculated using

$$e_{\mathrm{phys}} = (h - h_{\mathrm{sur}}) - T_{\mathrm{sur}} \cdot (s - s_{\mathrm{sur}}) \tag{3.10}$$

Thus, the sum of the specific chemical and the physical exergy describes the total specific exergy of the mixture.

$$e_{\mathrm{mixture}} = e_{\mathrm{chem}} + e_{\mathrm{phys}} \tag{3.11}$$

The total increase in the exergy ΔE, and consequently, the total amount of energy which can be stored is the difference of product and educt-specific exergies multiplied with the mass.

$$\Delta E = m \cdot (e_{\mathrm{Product}} - e_{\mathrm{Educt}}) \tag{3.12}$$

The storage power for a four-stroke engine is then calculated using

$$P = \Delta E \cdot \frac{N}{2 \cdot 60\ {}^{\mathrm{s}}/_{\mathrm{min}}} \tag{3.13}$$

To describe the efficiency of the process, the storage efficiency η is calculated from the increase of exergy to supplied work ratio.

$$\eta = \frac{\Delta E}{W} \tag{3.14}$$

The kinetic analysis is done by analyzing the product gas composition and the reaction path. Furthermore, the conversion of the educt is calculated using Equation (3.15) and yields of species of interest are calculated using Equation (3.16)

$$X_{\mathrm{E}} = \frac{n_{\mathrm{E},0} - n_{\mathrm{E}}}{n_{\mathrm{E},0}} \tag{3.15}$$

$$Y_{\mathrm{P}} = \frac{n_{\mathrm{P}} - n_{\mathrm{p},0}}{n_{\mathrm{E},0}} \cdot \frac{\nu_{\mathrm{P}}}{\nu_{\mathrm{E}}} \tag{3.16}$$

where n is the molar amount of substance, the indices E and P describe the educt or the product and the index 0 describes the inlet state. The parameter ν is the number of C or H atoms of the species to be calculated. The yields of hydrocarbons are referred to the C-atoms and the yield of the hydrogen is referred to the H-atoms.
In addition, a reaction path analysis is performed using Cantera [61] for methane and ethane pyrolysis to identify the most important reactions responsible for the products and the differences in product gas composition. For each reaction and species involved, the net production rate, consisting of forward and reverse reaction rates, is calculated for a specified time during the engine cycle with the Cantera module. Based on the net production rates, the carbon fluxes between two or more species are then graphically displayed, with the largest carbon fluxes being the most important reactions for the selected time.

3.3 Results and discussion

First, the effect and the necessity of the argon dilution on the gas temperature and the methane conversion during compression and expansion stroke is shown in Figure 3.2. If only methane with a common inlet temperature of 323 K is compressed, the temperature at TDC reaches 650 K and no methane is converted (black dashed line). If the educt is now highly diluted with argon, the heat capacity of the mixture is strongly decreased and the temperature after compression increases. For the same inlet temperature of 323 K, the initial mixture consists of 95% argon and 5% methane (blue lines), a temperature of 1650 K is reached at the end of compression stroke and 37% of the methane is converted. An additional small increase in the inlet temperature to 423 K for the diluted mixture (red curves) leads then to a temperature of 1800 K at TDC and to a methane conversion of 77%.
The conversion of the educts mainly depends on the TDC temperature and the highest TDC temperatures result in the highest conversion. To achieve a reasonable conversion, *e.g.*, 80%, the needed TDC temperature can be reached by varying the inlet temperature or by varying the inlet argon mole fraction. The argon dilution affects directly the fuel content and the heat capacity of the mixture and therefore the temperature increases in the compression stroke and at the end of the compression stroke. The inlet temperature affects the complete charge in the cylinder and the supplied work, and as well as the inlet argon mole fraction, the TDC temperature.

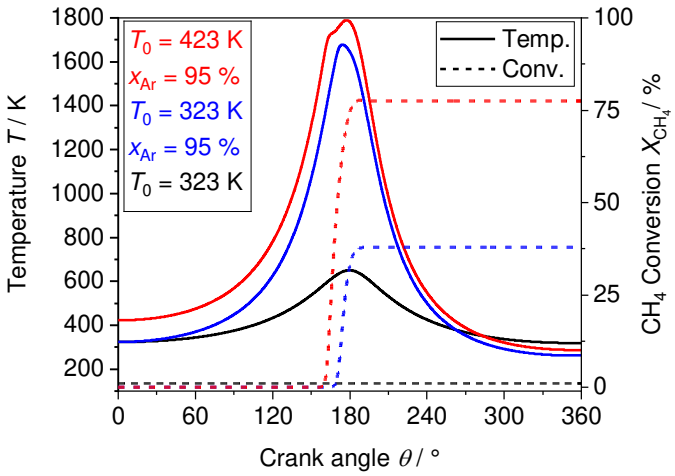

Figure 3.2. Temperature (left axis, solid lines) and methane conversion (right axis, dashed lines) as a function of crank angle for different inlet temperatures and argon dilution: 323 K inlet temperature and without argon (black lines), 373 K inlet temperature and 95% argon (blue lines), and 423 K and 95% argon (red lines).

The results of the variation of the inlet argon mole fraction and the inlet temperature on the conversion are shown in Figure 3.3 for methane (left) and ethane (right). The conversion of both, methane and ethane, increase with inlet temperature and inlet argon mole fraction. However, to keep the input temperatures within a realistic range, argon dilution is necessary. Thus, an increasing inlet argon mole fraction shifts the inlet temperature to lower values for a wanted conversion due to the achievable TDC temperature and even the lowest inlet temperature of 323 K leads to a range of the conversion between <10% and 100% depending on the inlet argon mole fraction. In addition, the TDC temperatures for different combinations of inlet argon mole fractions and inlet temperatures are shown as isothermal curves. The conversion of the educts increases with the TDC temperature. The comparison of methane and ethane shows that the needed TDC temperatures are ≈400 K lower for ethane than for methane at the same conversion. For a conversion of 12%, a TDC temperature of 1600 K (323 K<T_0<450 K) is necessary for methane, but only 1200 K (323 K<T_0<473 K) for ethane. A similar temperature difference is also observed for a conversion of, *e.g.*, 80%: for methane, a TDC temperature of at least 1800 K is needed, whereas for ethane 1400 K is sufficient. The reason for the lower TDC temperature is explained in a later section. In addition, the TDC temperatures and conversion rates at these operating conditions are shifted toward lower inlet argon mole fractions due to the higher density of ethane.

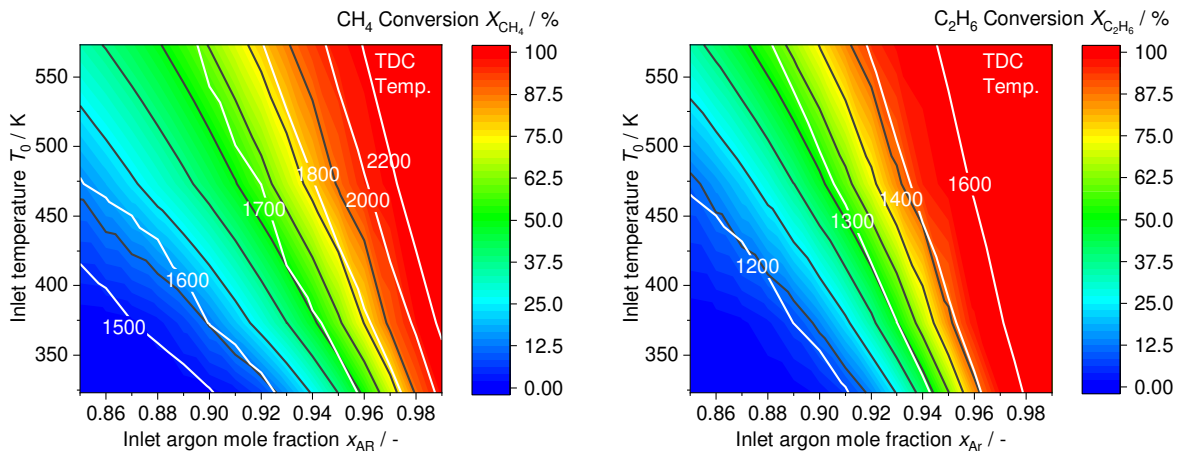

Figure 3.3. Left: CH_4 conversion (black lines, colored area) and TDC temperature (white lines) for methane pyrolysis as a function of inlet temperature and inlet argon mole fraction for an inlet pressure of 1 bar. Right: C_2H_6 conversion (black lines, colored area) and TDC temperature (white lines) for ethane pyrolysis as a function of inlet temperature and inlet argon mole fraction for an inlet pressure of 1 bar.

Although only the influence of inlet temperature and argon dilution on the educt conversion is shown here, there are also effects on the product gas composition and the stored exergy, as described in Section 3.3.4.

3.3.1 Process details

To get a deeper insight into the process, in the following section, both the course of energetic quantities related to the crank angle and the conversion of the educt to the target species are analyzed. As it is known from typical combustion engines, work is added during the compression stroke and removed in the expansion stroke and overall; the work removed is higher due to the combustion and the integral to calculate the total work is negative; work is transferred from the system. This process is now completely different. During the compression stroke, work is still added, but the amount of work that is added is higher than the work removed in the expansion stroke due to the endothermal reactions; this is shown in Figure 3.4. Both, heat losses and exergy losses are mainly high in the range of the TDC, and as soon as the mixture is cooled down through the expansion stroke, the heat-transfer rate drops and so do the exergy losses. It can also be seen in Figure 3.4, that physical-exergy losses (calculated from Equation (15)) are negligible in this process as they are less than 3% of the expended exergy (work and chemical exergy of the mixture). This is due to a seven times higher chemical exergy compared to physical exergy and supplied work in the system. Although the physical exergy decreases during the compression stroke due to entropy production, the chemical exergy in the mixture increases due to the endothermal reactions. The

physical exergetic efficiencies calculated from $\eta = 1 - {E_{\mathrm{loss,phys}}}/{W + E_{\mathrm{Educt}}}$ for every operating point are >97%, which once again illustrates how small the physical exergy losses are in this process. As the physical exergetic efficiency is not very revealing with respect to exergy storage, the efficiency in further sections is calculated according to Equation (3.14), which shows how much of the expended work is converted into chemical exergy of the mixture. The more of the educt is converted toward higher exergy chemicals per supplied amount of work, the higher is the efficiency. Compared to the physical exergetic efficiency, the efficiency according to Equation (3.14) is noticeably lower (here, 58%) because of chemical exergy losses due to the increased specific entropy after reaction. In comparison, the compression of methane requires, due to the needed higher temperatures, more work and results in larger heat losses than the compression of ethane, although there is a larger mass of ethane in the cylinder due to its higher density and higher molecular weight. The smaller amount of work addition in ethane pyrolysis is mainly caused by the lower isobaric and isochoric specific-heat capacities and their lower ratio for ethane, leading to a lower temperature and pressure increase. To give a numerical example of the operating point at T_0 = 573 K, p_0 = 1 bar, and x_{AR} = 0.93, the compression and expansion of methane requires 69 J of work and 33 J of heat is transferred; the compression of ethane requires only 59 J of work, whereas 25 J of heat is transferred.

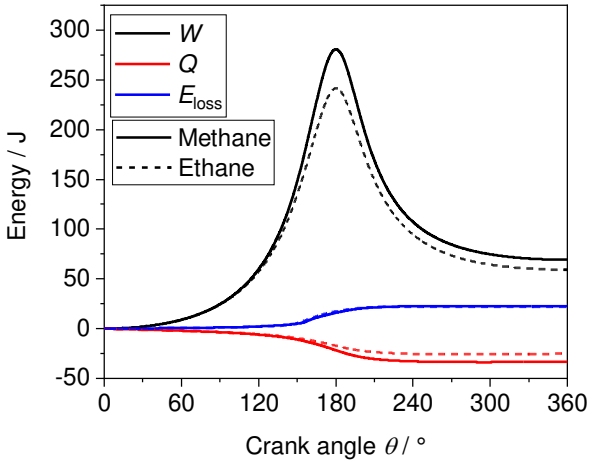

Figure 3.4. Work (black lines), heat loss (red lines) and physical exergy loss (blue lines) for methane (solid lines) and ethane (dashed lines) as a function of crank angle for an inlet temperature of 573 K, an inlet pressure of 1 bar and an inlet argon mole fraction of 0.93.

The conversion of methane and the formation of target species as well as the temperature trace are shown in Figure 3.5 (left) as a function of crank angle for the same exemplary operating point at T_0 = 573 K, p_0 = 1 bar, and x_{AR} = 0.93. The recognizable

consumption of methane starts 28° before TDC at 1620 K and 25 bar (1% CH_4 conversion). Thereafter, at 25° before TDC, at 1680 K, 29 bar, and 5% CH_4 conversion, a reduction in the temperature rise is observed due to the endothermal reactions, compared to a nonreacting mixture. This reduction in the temperature increase is also seen for the following crank angles. Up to this point, mainly ethylene together with a high amount of hydrogen is produced. At 10° before top dead center (BTDC), due to the increase in temperature to 1800 K, ethylene is first decomposed to acetylene, which is then further converted to benzene and light PAHs such as naphthalene and acenaphthylene. At TDC (75 bar), the temperature reaches 1850 K, with a maximum of 86% methane-consumption to acetylene and benzene. Immediately after the TDC, while temperature is still high, acetylene and benzene decompose and form heavy PAHs, e.g., $C_{20}H_{10}$ and $C_{20}H_{16}$ and soot particles. At 20° after TDC, the temperature and pressure decrease to 1350 K and 30 bar, respectively. Now all reactions are relatively slow, and the mixture is frozen and products such as acetylene survive. At the end of one cycle, at BDC, both, temperature and pressure are below (325 K, 0.6 bar) the initial values (573 K, 1 bar) due to the endothermal reactions and the conversion of physical exergy to chemical exergy. Overall, 85% of methane is converted. This is below the maximum conversion, due to backreactions to methane. The main products are hydrogen, acetylene, ethylene, and benzene with yields of 63%, 29%, 7%, and 5%, respectively, together with high amounts of light and heavy PAHs with yields of up to 32%. Yields of species that are represented in only very small quantities and unconverted educts as well were not calculated here. The total specific exergy of the mixture is increased by 118.7 kJ kg^{-1}, with the chemical exergy increased by 149.9 kJ kg^{-1} and the physical exergy decreased by 31.2 kJ kg^{-1}. Thus, the storage power for this process is 0.99 kW, and if one relates this to the work expended, the efficiency is 58%, meaning that 58% of the work is stored in the exergy of the mixture.

If ethane is used as educt, the process proceeds basically similar and is shown in Figure 3.5 (right) for the operating point at T_0 = 573 K, p_0 = 1 bar, and x_{AR} = 0.93. One percent conversion of ethane is found at 37° before TDC at 1180 K and 12 bar; this is at an earlier crank angle and at a lower temperature, due to the lower activation energy of the ethane pyrolysis. At 30° before TDC (1270 K and 18 bar), 12% of the ethane is consumed and a smaller temperature increase is observed, because of the fast formation of ethylene at this point. Nevertheless, the reduction in temperature increase, compared to a nonreacting mixture, is less pronounced in comparison to methane, because endothermal reactions are counterbalanced by exothermal methane formation. At higher temperatures, 20° BTDC to 20° ATDC, acetylene and benzene are formed: a part of the ethylene is consumed to form acetylene, which in turn to a small extent is further converted to benzene.

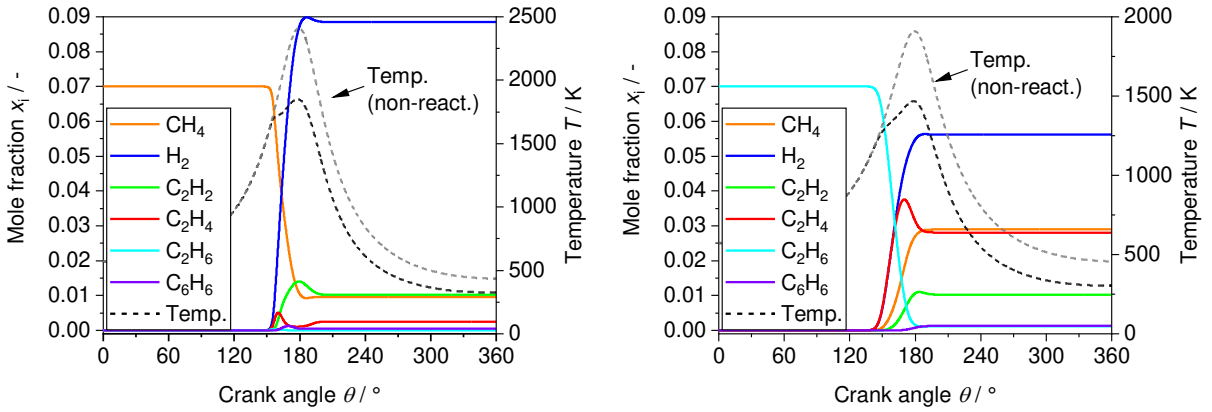

Figure 3.5. Left: Mole fractions (left axis, solid lines, colored), temperature (right axis, dashed lines, black) and temperature of the non-reacting mixture (right axis, dashed lines, grey) as a function of crank angle for an inlet temperature of 573 K, an inlet pressure of 1 bar and an inlet argon mole fraction of 0.93 for methane as reactant. Right: Mole fractions (left axis, solid lines, colored), temperature (right axis, dashed lines, black) and temperature of the non-reacting mixture (right axis, dashed lines, grey) as a function of crank angle for an inlet temperature of 573 K, an inlet pressure of 1 bar and an inlet argon mole fraction of 0.93 for ethane as reactant.

The maximum temperature and pressure at the TDC are 1465 K and 60 bar, which are comparably low and cause the absence of PAH and soot particle formation, although their precursors, acetylene and benzene, are present. At 20° after TDC, temperature and pressure drop to 1110 K and 25 bar and the mixture is frozen again. At the end of the expansion stroke, nearly all the ethane is consumed (97%) and temperature and pressure decrease to even lower values of 303 K and 0.56 bar due to the endothermal reactions and the large educt conversion. The main products are not only hydrogen and ethylene but also smaller amounts of acetylene and benzene are observed with yields of 27%, 40%, 14%, and 5%, respectively. Although there is no PAH and soot particle formation, 20% of the carbon of ethane remains in methane, which is energetically less valuable. Although the chemical exergy has increased by 128.5 kJ kg^{-1}, the physical exergy has decreased by 35.9 kJ kg^{-1}. In total, the storage power and the efficiency are 0.79 kW and 54%, which is lower than the storage power of methane in the same operating point and even the educt conversion is much higher. The lower storage power for ethane is caused by the lower work, that is supplied and by a different distribution of the main products: less hydrogen and acetylene but more ethylene. This will be discussed in more detail in Section 3.3.4.

3.3.2 Heat transfer models

The heat-transfer model has a significant influence on the dissipated heat, temperatures, and pressures in the cylinder. Thus, also the educt conversion and the

temperature/pressure dependent product formation is also affected. To show the influence on such parameters, the heat-transfer models from Woschni [63], Hohenberg [72], Annand [73], and Chang et al. [74] were compared. The heat-transfer model from Woschni, Hohenberg, and Annand are developed for spark ignition and diesel engines, whereas the one from Chang is applicable for HCCI engines. As none of these heat-transfer models has been validated for the present process, the results of such heat-transfer models are compared qualitatively. Although the correlations of Woschni, Hohenberg, and Chang are largely based on the temperature-/pressure and volume curves, the correlation of Annand also includes the dependence of the heat transfer on fluid properties such as the thermal conductivity and viscosity. The heat-transfer coefficients at BDC, *e.g.*, for Woschni and Annand, are 60 W $(m^2\ K)^{-1}$ and 230 W $(m^2\ K)^{-1}$, respectively at T_0 = 573 K, p_0 = 1 bar, and 93 mol% argon. At TDC, the heat-transfer coefficients increase to values of 800 W $(m^2\ K)^{-1}$ (Woschni) and 1500 W $(m^2\ K)^{-1}$ (Annand). Although these differences are considerable, it turns out that the influence on the process are not as large. Figure 3.6 (left) shows the pressure and temperature trace for an inlet temperature of 573 K; an inlet pressure of 1 bar and 93 mol% argon.

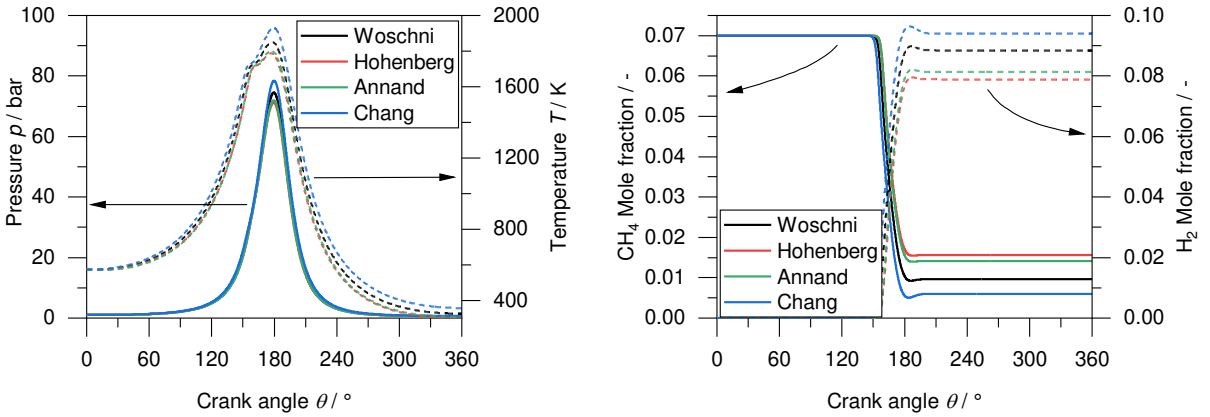

Figure 3.6. Left: Pressure (left axis, solid lines) and temperature (right axis, dashed lines. Right: CH_4 mole fraction (left axis, solid lines) and H_2 mole fraction (right axis, dashed lines). Both as a function of crank angle for an inlet temperature of 573 K, an inlet pressure of 1 bar and an inlet argon mole fraction of 0.93. The simulations were performed with the heat transfer model from Woschni [63] (black), Hohenberg [72] (red), Annand [73] (green) and Chang [74] (blue).

The pressure traces deviate by maximum 5% in the TDC from the average. The maximum pressure in TDC (78 bar) is obtained using the model from Chang and the minimum pressures in TDC (71 and 72 bar) are obtained using the models from Hohenberg and Annand, respectively. The deviation of the temperatures traces is more distinct. Similar to the pressure curves, the maximum TDC temperature is 1930 K, obtained by the model of Chang and the minimum TDC temperatures are 1790 and 1800 K, obtained by the models of Hohenberg and Annand, respectively. Although the relative

deviation from the average is also 5%, the absolute deviation is up to 80 K. Such temperature differences affect the endothermal reactions and the temperature traces during the expansion stroke. The CH_4 and H_2 mole fractions are shown in Figure 3.6 (right) and are representative for educt conversion and product generation. According to the maximum temperature and pressure, the CH_4 conversion and H_2 production, obtained using the model from Chang, are highest, whereas lower values are predicted using the models from Hohenberg and Annand.

The storage power as well as the storage efficiency (Table 3.3) are higher relative to the reference prediction from the Woschni model in accordance with the product yields for the model of Chang and lower for the models of Hohenberg and Annand. The deviation from the average is up to 15% for the storage power and up to 30% for the efficiency because of a changed product spectrum. Although the CH_4 conversion using Hohenberg and Annand is significantly lower, benzene yields have more than doubled due to the lower temperatures. Overall, the heat-transfer models affect not only the temperatures and the educt conversion but also the product distribution. The results obtained with the different heat-transfer models are summarized in Table 3.3. As the results obtained by the heat-transfer model from Woschni deviate least from the average regarding temperature, pressure, CH_4 conversion and storage power and efficiency, we chose the Woschni correlation in the present investigation.

Table 3.3. TDC temperature, TDC pressure, heat flux, CH_4 conversion, yields of H_2, C_2H_2 and C_6H_6, storage power and storage efficiency for different heat transfer models.

	TDC temperature [K]	TDC pressure [bar]	Heat flux [kW]	CH_4 conversion [%]	H_2 yield [%]	C_2H_2 yield [%]	C_6H_6 yield [%]	Storage power [kW]	Storage efficiency [%]
Woschni	1850	75	0.83	85	63	29	5	0.99	58
Hohenberg	1790	71	1.25	77	59	26	10	0.84	45
Annand	1800	72	1.11	79	61	27	9	0.88	49
Chang	1930	78	0.43	91	71	34	3	1.12	72

3.3.3 Reaction path analysis

The pyrolysis of methane and ethane leads to different main products. In this section, the formation paths of the different carbon-containing products are discussed. Carbon reaction path analysis is shown in Figure 3.7, for methane and ethane pyrolysis, performed at 50% conversion, respectively. This point was chosen for the reaction path

analysis because all relevant reactions to interesting products take place there. For CH_4, the conditions are 165°CA, 1750 K, and 47 bar, and for C_2H_6 they are 160°CA, 1350 K, and 29 bar. Both, methane and ethane, mainly produce hydrogen, whereas methane produces considerably more hydrogen due to the larger H/C ratio. For methane pyrolysis, the mainly produced hydrocarbons are acetylene, ethylene, benzene and soot precursors, whereas for ethane, it is methane. The differences in the main product distributions are mainly due to different intermediates. The first main product formed is ethylene. In case of ethane pyrolysis, up to 55% of the carbon remains in the product ethylene; for methane pyrolysis, it is significantly less. Ethylene is formed from ethyl radical (C_2H_5) decomposition (Equation (R3.9))

$$C_2H_5 (+M) \rightleftharpoons C_2H_4 + H (+M) \quad \text{(R3.9)}$$

For ethane pyrolysis, ethyl is directly formed after H-abstraction from methane. In methane pyrolysis in turn, ethyl is formed from methyl (CH_3) recombination (Equation (R3.12), reverse), which then leads to the production from ethylene. The acetylene formation is preceded by the formation of C_2H_3 in the reaction of ethylene with methyl radicals (Equation (R3.10))

$$C_2H_4 + CH_3 \rightleftharpoons C_2H_3 + CH_4 \quad \text{(R3.10)}$$

Methyl radicals are produced by the H-abstraction of methane, which is the start reaction of methane pyrolysis or by the unimolecular decomposition of ethane (Equation (R3.11) and (R3.12))

$$CH_4 + H \rightleftharpoons CH_3 + H_2 \quad \text{(R3.11)}$$
$$C_2H_6 (+M) \rightleftharpoons 2\ CH_4 (+M) \quad \text{(R3.12)}$$

As the reaction of ethane to ethyl after hydrogen abstraction is favored, methyl is produced less in ethane pyrolysis than in methane pyrolysis, where it is part of the start reaction. Thus, less methyl radicals are available to produce the intermediate C_2H_3, which is necessary for the path toward acetylene (Equation (R3.10)). A small amount of ethylene is still reacting to C_2H_3 and methane. The temperature in the ethane pyrolysis is too low to consume the methane again, so that it remains as a product. Although less ethylene is present in methane pyrolysis, significantly more of it is decomposed, so that significantly more acetylene is also formed. In ethane pyrolysis, the path toward benzene goes along C_4H_4 radicals, which are formed from acetylene. C_4H_4 further reacts again with acetylene to produce benzene. For methane pyrolysis, propyne (p-C_3H_4) and

C_3H_3 radicals are formed fast, and benzene is then produced from C_3H_3 radicals. The consumption of benzene toward light and heavy PAHs occurs at high temperatures in reactions with acetylene, C_3H_3 radicals, and CH_3 radicals. Thus, due to the higher temperatures and the increased presence of C_2H_2, C_3H_3 and CH_3, naphthalene ($C_{10}H_8$) and acenaphthylene ($C_{12}H_8$) as well as the lumped species such as $C_{20}H_{10}$ and $C_{20}H_{16}$ are products of the methane pyrolysis but not in the ethane pyrolysis.

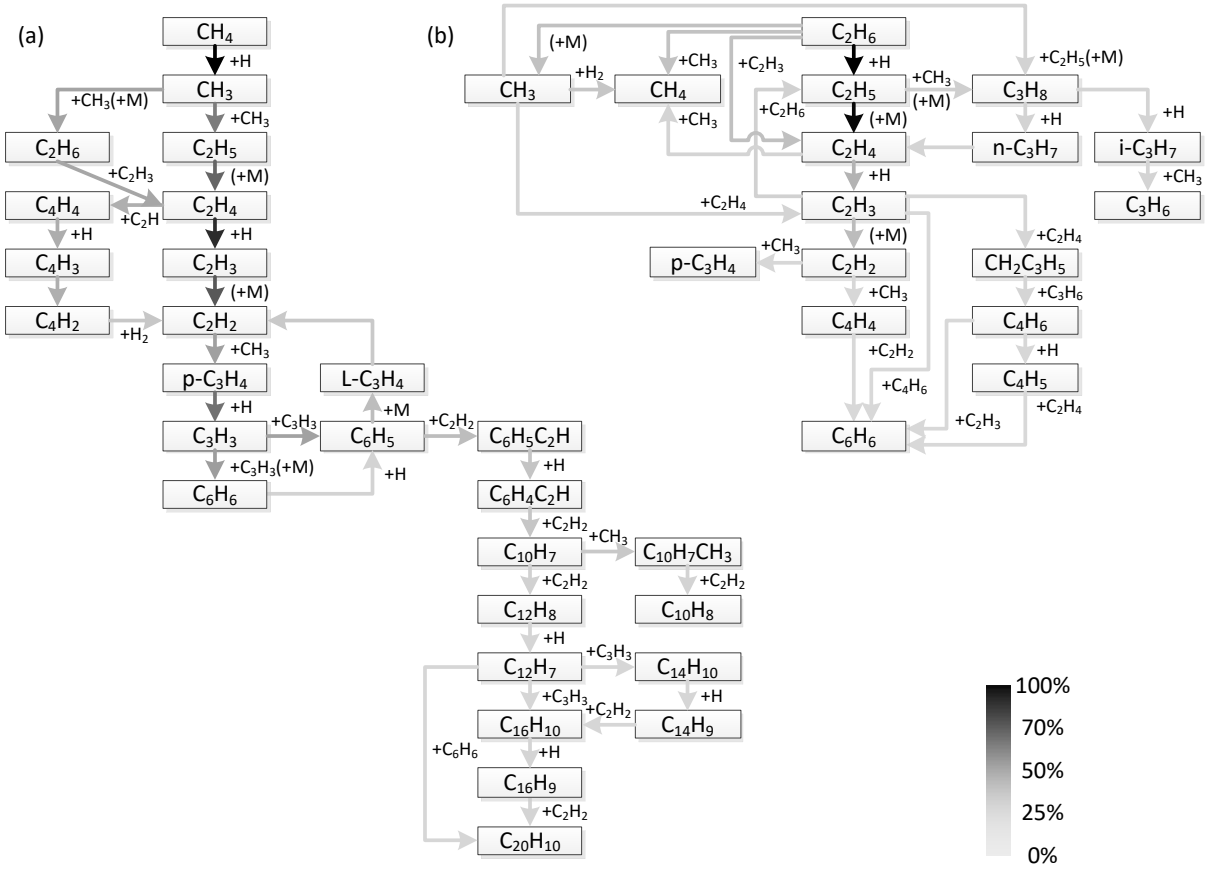

Figure 3.7. Reaction path for methane (a) and ethane (b) for an inlet temperature of 573 K, an inlet pressure of 1 bar and an inlet argon mole fraction of 0.93, performed at 50% conversion, respectively. The colors of the lines are related to the carbon fluxes according to the net reaction rates.

To identify the most sensitive reactions for the products of interest, a sensitivity analysis was performed and can be found in the electronic Supporting Information. The most important reaction for CH_4 and C_2H_4 formation for methane pyrolysis is the recombination of CH_3 to C_2H_5 (Equation (R3.13)).

$$2\ CH_3 \rightleftharpoons C_2H_5 + H \qquad \text{(R3.13)}$$

The H-radical released in (Equation (R3.13)) increases the conversion of CH_4 or C_2H_6. The ethyl radical C_2H_5 decomposes to C_2H_4 and H. In contrast, the most important reaction for the decomposition of C_2H_4 and formation of C_2H_2 is the H-abstraction from C_2H_4 by H radicals, forming C_2H_3 and H_2 (Equation (R3.14)), for methane and ethane pyrolysis. The fact that the same reaction is responsible for both the formation of C_2H_2 and the decomposition of C_2H_4 explains the trends of the mole fractions in Figure 3.5.

$$C_2H_4 + H \rightleftharpoons C_2H_3 + H_2 \quad \text{(R3.14)}$$

The higher amount of H-radicals available in methane pyrolysis, due to the favorable H/C ratio, could support the formation of C_2H_2. Regarding the formation of C_6H_6, the most important reaction with respect to methane pyrolysis is the recombination of propargyl radicals (C_3H_3).

$$2\ C_3H_3\ (+M) \rightleftharpoons C_6H_6\ (+M) \quad \text{(R3.15)}$$

As argon is the main compound in the gas phase, its influence as collision partner may be important and introduces some uncertainty. To investigate this, the collision efficiency of argon in the most important third-body reactions for ethene and acetylene formation were varied by a factor of 3, and the influence on the respective product gas was negligible; they changed by 0.4–2%.
For ethane pyrolysis, on the other hand, the reaction (Equation (R3.16)) is the most important reaction with respect to C_6H_6 formation.

$$C_2H_4 + C_4H_5 \rightleftharpoons C_6H_6 + H + H_2 \quad \text{(R3.16)}$$

The formation of the lumped species is mainly sensitive to the reactions (Equation (R3.17)) and (Equation (R3.18)).

$$C_{16}H_{10} + H \rightleftharpoons C_{16}H_9 + H_2 \quad \text{(R3.17)}$$
$$C_{16}H_9 + C_2H_2 \rightleftharpoons 0.5\ C_{16}H_{10} + H + 0.5\ C_{20}H_{10} \quad \text{(R3.18)}$$

3.3.4 Storage power and product gas

The influence of initial temperature, argon mole fraction, and pressure are investigated to find favorable operating points. Storage power and efficiency are shown in Figure 3.8 (left) for methane and ethane as a function of the inlet argon mole fraction for an

inlet temperature of 573 K and an inlet pressure of 1 bar. This condition was chosen with respect to the maximum storage power at which the most useful products for methane pyrolysis are produced. For a comparison, most parameters should remain unchanged; thus, this condition was also chosen for ethane pyrolysis. Overall, methane and ethane have a similar course of storage power and efficiency: for lower inlet argon mole fractions ($x_{Ar}<0.88$) both, storage power and efficiency are also low, as the temperature increase during the compression stroke is insufficient for a substantial educt consumption. With increasing inlet argon mole fractions, the storage power of methane increases strongly, whereas the storage power of ethane increases only slightly, which is a result of the overall higher conversion of ethane due to the higher reactivity. Therefore, the maximum storage power of ethane is 0.8 kW with an efficiency of 54% and is at 92 mol% argon, while that of methane is at a slightly higher argon load of 93 mol% but is significantly larger (0.99 kW, 58%). The higher maximum is mainly due to the lower exergy of methane, compared to ethane and the distribution of the product species, which are also shown in Figure 3.8 (right). For the operating conditions with the maximum storage power, the two main products are hydrogen and acetylene for methane as educt, and ethylene and methane for ethane as educt, respectively. Especially the high amount of methane in the product gas of ethane pyrolysis explains the overall lower storage power compared to methane pyrolysis. But not only the lower chemical exergy due to the product gas composition affects the lower storage power, also the lower temperatures and pressures over the complete cycle and at the end of the cycle reduces the physical exergy, which also influences the storage power. At high inlet argon mole fractions, the storage power and the efficiency of both is decreasing again, first due to the small amount of educt in the mixture and second due to change in the product gas composition. Although hydrogen and acetylene yields increase significantly, the yields of benzene and ethylene decrease. In addition, heavy PAHs and soot precursors are formed at these high temperatures. The storage power and the efficiency of ethane has a local minimum between $0.96<x_{AR}<0.98$: A second local maximum can be seen in $x_{AR} = 0.97$ as a result of the sharp increase in the acetylene yield and simultaneous reduction in the methane yield, which compensates the lower ethylene yield.

Considering now the course of the yields of the products as a function of the inlet argon mole fraction, it turns out that the maxima of 1) ethylene and 2) benzene are at low and medium inlet argon mole fractions (and thus, low and medium temperatures) and the maxima of hydrogen and acetylene are at the highest inlet argon mole fractions and the highest temperatures. As the formation of ethylene is the first step in the reaction paths of both, methane and ethane, ethylene is predominantly formed at low temperatures and low conversion rates, where not enough H and CH_3 radicals are

available for a further decomposition. With increasing inlet argon mole fractions, temperatures during compression increase and ethylene is decomposed to acetylene, which is unstable at these temperatures and further reacts to benzene via C_3H_3 for the methane case and C_4H_4 for the ethane case. Another product of ethane pyrolysis, which has its maximum in the same range ($0.93 < x_{Ar} < 0.95$) is methane. Methane is also produced by the decomposition of ethylene, but at medium temperatures it is not pyrolyzed itself. At high inlet argon mole fractions, several effects are superimposed due to the high temperatures, in both, methane and ethane pyrolysis. Significantly more acetylene and hydrogen are produced while the yields of ethylene and benzene continue to decrease. One reason for this is that methane as educt and as intermediate of ethane pyrolysis is almost completely converted and more radicals are available to form intermediates, such as CH_3 and C_2H_3, and thus, more acetylene is formed not only via C_2H_3 but also by the decomposition of benzene via C_6H_5. At these high temperatures in addition to PAHs and soot precursors, acetylene is retained in larger quantities. The decomposition of benzene and the increased presence of acetylene at higher temperatures in turn, leads to the unwanted formation of light and heavy PAHs, which require acetylene, benzene, or intermediates based on them as reaction partners.

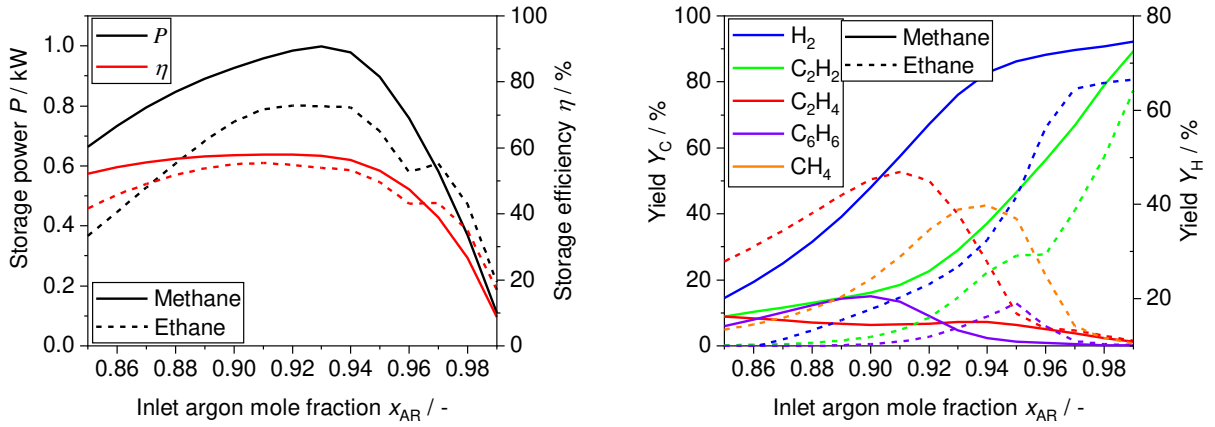

Figure 3.8. Left: Storage power (black lines, left axis) and storage efficiency (red lines, right axis) as a function of inlet argon mole fraction for an inlet temperature of 573 K and an inlet pressure of 1 bar for methane (solid lines) and ethane (dash lines). Right: Yields of main products as a function of inlet argon mole fraction for an inlet temperature of 573 K and an inlet pressure of 1 bar for methane (solid lines) and ethane (dash lines).

As there is a maximum storage power for inlet argon mole fractions near $x_{AR} = 0.93$, in the following, the variation of inlet temperature and inlet pressure are shown for both reactants at this fixed argon mole fraction. However, the optimum inlet argon mole fraction is slightly shifted toward lower values with increasing inlet pressures, with respect to the maximum storage power (compare Figure 3.8). First, the main products of methane pyrolysis: hydrogen, acetylene, ethylene, and benzene are shown in Figure

3.9a,b as a function of inlet temperature and inlet pressure. Figure 3.9c shows the species $C_{20}H_{10}$, representing PAHs, as a function of inlet temperature and inlet pressure. Regarding the temperature, the maximum yields for hydrogen and acetylene are achieved at the maximum inlet temperatures and the maximum yields for ethylene and benzene are attained at the lowest and medium inlet temperatures, as was already discussed in the previous section. An increasing inlet pressure leads to a higher amount of supplied work and a higher charge in the cylinder. Also, the TDC pressures and TDC temperatures rise up to 1100 bar and 2100 K, and the reaction rates rise, so that less hydrocarbons are formed but instead the equilibrium composition according to reaction (Equation (R3.2)) is progressively established. If such TDC pressures are reached, the technical feasibility is not given. In a realistic piston engine, this is a limiting factor. Thus, yields for ethylene and benzene are reduced and shifted toward lower temperatures. Acetylene, even at low temperatures, is converted completely to $C_{20}H_{16}$, which is the largest hydrocarbon in the mechanism prior to solid carbon. At high inlet pressures and low inlet temperatures, in addition to the formation of $C_{20}H_{16}$ from acetylene, the exothermal reaction back to methane is favored, due to the principle of Le Chatelier. The carbon of methane, which is not in the acetylene path, remains in a pathway, where methane is converted to ethane and back to methane via CH_3 and is therefore not available for other reactions. These reactions are pressure-dependent unimolecular reactions and reactions with H_2, both favored at high pressure, which is also needed for the formation of acetylene. The maximum hydrogen yield is up to 70% for the maximum inlet temperature (573 K) and inlet pressure (10 bar), where the maximum yield for acetylene is up to 30% for the maximum inlet temperature and the lowest inlet pressure (1 bar). Maximum yield for ethylene is up to 10% for the lowest inlet temperatures (323 K) and inlet pressures of 4 bar$<p_0<$10 bar and for benzene up to 16% for inlet temperatures of 373 K$<T_0<$423 K and inlet pressures of 2 bar$<p_0<$10 bar. The storage power and the efficiency as a function of inlet temperature and inlet pressure is shown in Figure 3.9d for methane pyrolysis. If only the temperature is increased at a constant pressure, a local maximum is observed. For an inlet pressure of 1 bar, it is at an inlet temperature of 423 K. Charge and reaction extent have opposite temperature dependencies. For higher inlet pressures, the storage power increases due to the cylinder charge and the faster reactions and is shifted to smaller inlet temperatures. The product gas contains mainly hydrogen and $C_{20}H_{16}$ as well as methane from the back reaction and less higher hydrocarbons. The maximum storage power for the engine of this study is 7.5 kW at the maximum inlet temperature and the maximum inlet pressure due to the high cylinder charge and the high chemical exergy of hydrogen compared to methane. At lower temperatures for the maximum inlet pressure, storage power is

decreased again, due to the exothermal reaction back to methane, even there is the highest cylinder charge.

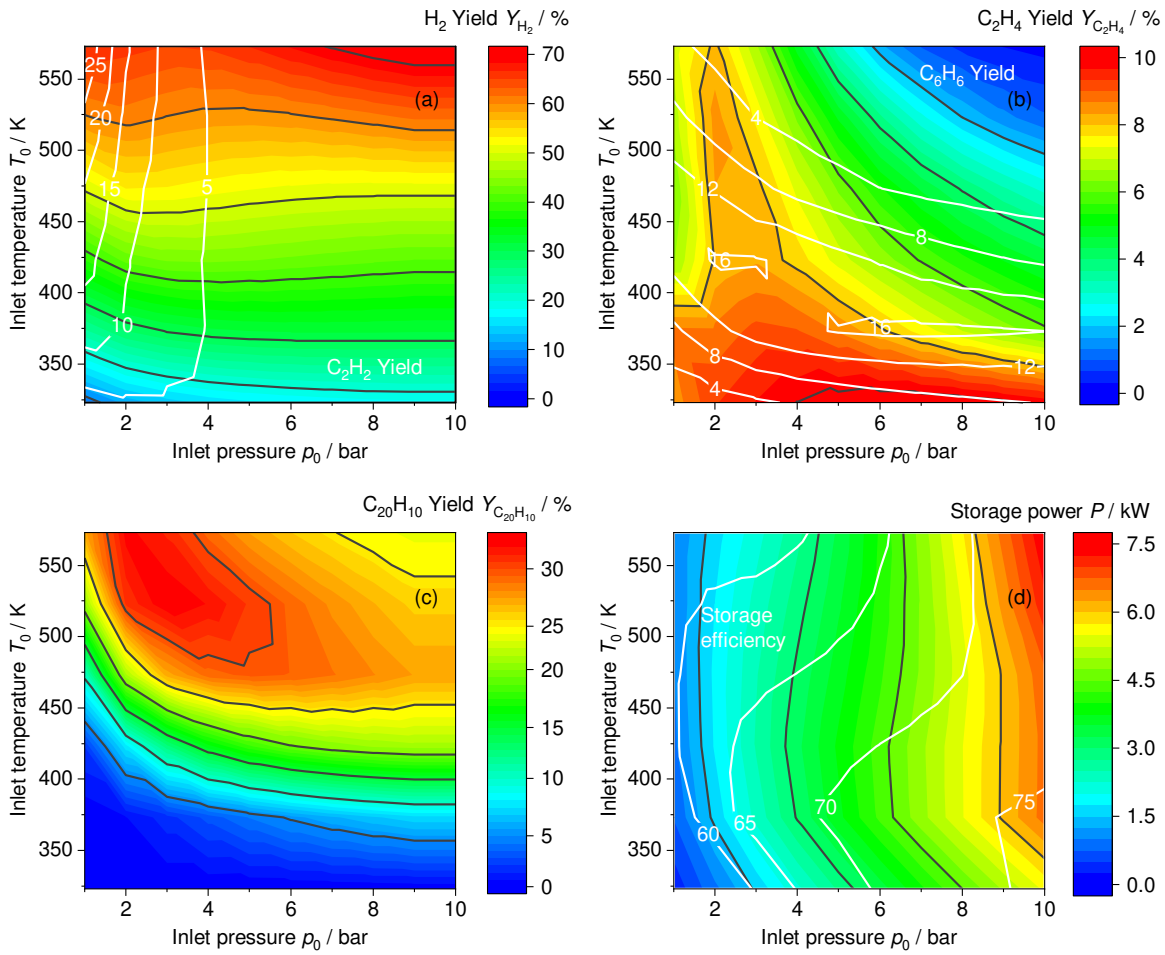

Figure 3.9. Methane pyrolysis as a function of inlet temperature and inlet pressure for an inlet argon mole fraction of 0.93. (a) H_2 yield (black lines, colored area) and C_2H_2 yield (white lines). (b) C_2H_4 yield (black lines, colored area) and C_6H_6 yield (white lines). (c) $C_{20}H_{10}$ Yield. (d) Storage power (black lines, colored area) and storage efficiency (white lines).

The efficiency is between 55%<η<75%, depending on inlet temperature and pressure. The temperature dependence is similar to the storage power dependence; the efficiency has a local maximum between 423 and 323 K. As the efficiency is the ratio of stored exergy to supplied work, also the supplied work has to be inspected. In general, the supplied work decreases with increasing temperatures, if no chemical reactions occur. If endothermal reactions occur, the supplied work in the compression stroke does not change noticeably until the reactions start. The resulting reduced temperature and pressure levels (see Section 3.3.1) results in a significant reduction of the work released in the expansion stroke. Thus, more work is required overall when endothermal reactions occur. Thus, two effects with opposite temperature dependencies influence the

supplied work, and consequently, the maximum efficiency is at medium inlet temperatures because the increase in the exergy due to the endothermal reactions is significantly higher than the increase in the supplied work. At low inlet temperatures, the efficiency decreases due to low conversion and at high inlet temperatures, the efficiency decreases due a strong increase of supplied work.
At higher inlet pressures, the efficiency is shifted toward lower temperatures and the maximum efficiency is located in the lower right quadrant of the diagram due to the reaction-accelerating effect of the high pressure and the small decrease in the supplied work caused by the small amount of exothermal reactions back to methane.

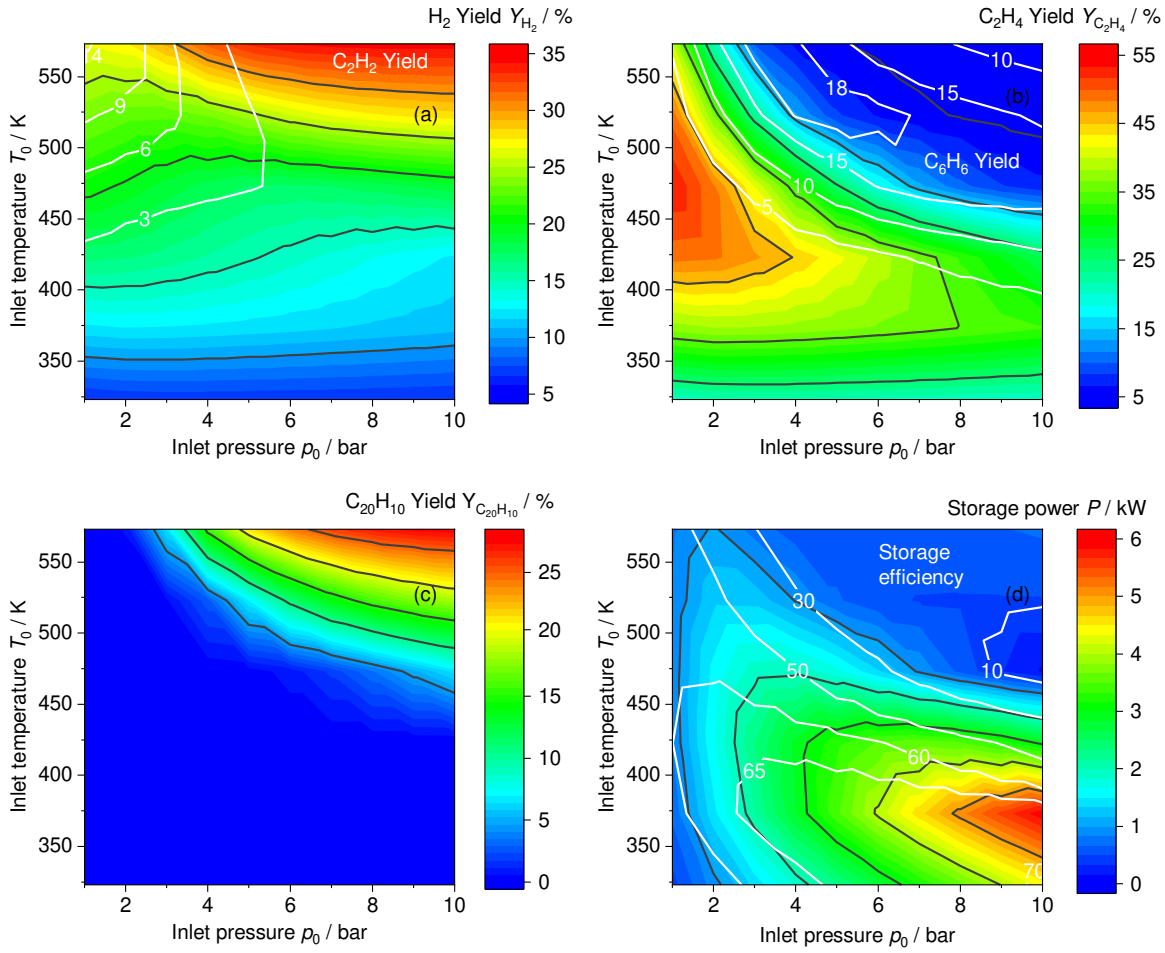

Figure 3.10. Ethane pyrolysis as a function of inlet temperature and inlet pressure for an inlet argon mole fraction of 0.93. (a) H_2 yield (black lines, colored area) and C_2H_2 yield (white lines). (b) C_2H_4 yield (black lines, colored area) and C_6H_6 yield (white lines). (c) $C_{20}H_{10}$ Yield. (d) Storage power (black lines, colored area) and storage efficiency (white lines).

For ethane pyrolysis, similar effects occur overall as ethane pyrolysis contains partly methane pyrolysis due to the decomposition from ethane to methane. In addition, the effect of increased reaction rates due to higher pressures also occurs. Figure 3.10a–c show the yields of the main products hydrogen, acetylene, ethylene, and benzene and

$C_{20}H_{10}$, representative for PAHs, as a function of inlet temperature and inlet pressure. Due to the overall lower temperatures and pressures, which are up to 1700 K and 850 bar in the TDC, the yields in hydrogen and acetylene as well as the mole fractions of light and heavy PAHs are significantly lower, whereas the yields of ethylene and benzene are higher. The maximum acetylene yield is only 14% and found for the highest inlet temperatures (573 K) and the lowest inlet pressures (1 bar), as the formation of acetylene is based on the previous formation of methane from ethane. For higher inlet pressures (6–10 bar), acetylene is mainly decomposed to $C_{20}H_{16}$, as it follows the path of methane pyrolysis and the main products are hydrogen (with a maximum yield of 35%) and $C_{20}H_{16}$ according to the equilibrium composition (hydrogen and solid carbon). Nevertheless, significantly less heavy PAHs are formed over the entire pressure and temperature range. The maximum yields for ethylene and benzene are 55% and 18% and they are shifted toward higher temperatures, due to the overall lower temperature level: The maximum ethylene yields are located at inlet temperatures of 423 K$<T_0<$523 K and inlet pressures of 1 bar$<p_0<$4 bar and the maximum benzene yields at inlet temperature 500 K$<T_0<$573 K and inlet pressures of 3 bar$<p_0<$7 bar. At higher inlet pressures (>6 bar) and intermediate inlet temperatures (373 K$<T_0<$423 K), the product gas mainly consists of ethylene and methane, and especially methane is not decomposed toward acetylene or PAHs due to the principle of Le Chatelier.

The storage power and the efficiency as a function of inlet temperature and inlet pressure for ethane pyrolysis are shown in Figure 3.10d. Overall, the storage power and the efficiencies in ethane pyrolysis are lower than in methane pyrolysis. Even at conditions, such as T_0 = 473 K and 2 bar$<p_0<$3 bar, where methane and ethane have similar efficiencies of ≈65%, the storage power in ethane pyrolysis is lower than in methane pyrolysis. Again, the temperature dependence and the pressure dependence can be analyzed separately. The storage power as a function of the temperature at a constant pressure has a maximum for an inlet temperature of 323 K$<T_0<$423 K, and with increasing pressure, the maximum value rises and is shifted toward lower temperatures, as seen and explained earlier. The maximum storage power is 6 kW and is found, in contrast to methane pyrolysis, at an inlet temperature of 373 K and the maximum inlet pressure (10 bar). The lower power is explained by the product gas composition: it contains larger quantities of ethylene together with small amounts of hydrogen and benzene and methane, which is not decomposed to form acetylene or heavy PAHs, whereas in the case of methane pyrolysis at the same operation points, methane and heavy PAHs are mainly present. Furthermore, this operating point (low inlet temperature and high inlet pressure) provides the highest cylinder charge. However, at inlet temperatures between 473 and 523 K and maximum inlet pressure, mainly $C_{20}H_{16}$ is produced from acetylene together with high amounts of methane (Y_{CH4} = 85%) and

only small amounts of hydrogen. The exothermal reaction to methane as well as the hydrogen which is stored in methane lead to the minimum storage power at this operating point. At the maximum inlet temperature (for the same pressure), methane decomposes; thus, the hydrogen yield increases and the product gas contains mainly $C_{20}H_{16}$ and hydrogen according to chemical equilibrium. Thus, the storage power increases again slightly. Compared to methane pyrolysis, there is considerably less hydrogen due to the lower H/C ratio; thus, the storage power at maximum inlet temperature and inlet pressure is lower.

The efficiency for ethane pyrolysis is between $10\% < \eta < 70\%$ and with a similar dependency as the storage power: The maximum efficiency of 70% is close to the maximum storage power as well as the minimum efficiency is close to the minimum storage power. For a constant inlet pressure, the efficiency has a maximum at a certain inlet temperature, as discussed for methane pyrolysis. With increasing pressure, the maximum is shifted toward lower temperatures due to faster reactions and a more favorable product gas composition.

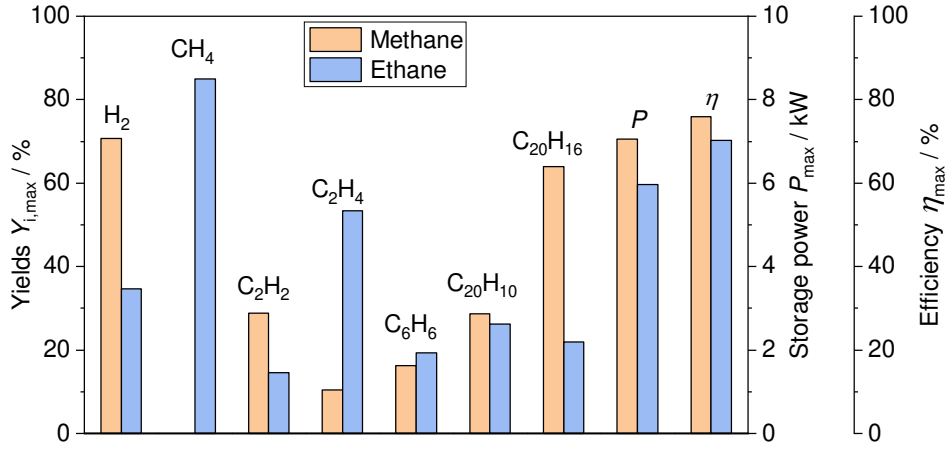

Figure 3.11. Maximum yields of H_2, CH_4, C_2H_2, C_2H_4, C_6H_6 and representative for heavy PAHs $C_{20}H_{10}$ and $C_{20}H_{16}$ (left axis), as well as maximum storage power and maximum efficiency (right axes) for an inlet argon mole fraction of 0.93 and at different T_0 and p_0 for methane and ethane pyrolysis. The yield of H_2 is related to H-atoms whereas the yields for the hydrocarbons are related to the C-atoms.

The observed maximum yields of interesting species, maximum storage power and maximum efficiency are summarized in Figure 3.11 for methane and ethane, respectively. The maxima are calculated for an inlet argon mole fraction of 0.93, where the maximum of the storage power is observed. In a direct comparison of methane and ethane as educt, the difference in both, product gas composition on one side and in storage power and efficiency on the other side becomes clear. Although methane pyrolysis results in significantly more hydrogen and acetylene, the main products of

ethane pyrolysis are methane and ethylene. Benzene production is moderate for both reactants. Methane pyrolysis of methane not only leads to a larger storage power and higher efficiencies but also to larger yields of soot precursors such as $C_{20}H_{10}$ and $C_{20}H_{16}$. For methane pyrolysis this is already observed at relatively low temperatures and a broad pressure range and is accompanied with a moderate conversion, whereas for ethane pyrolysis, soot precursors are mainly formed at the highest inlet temperatures and pressures.

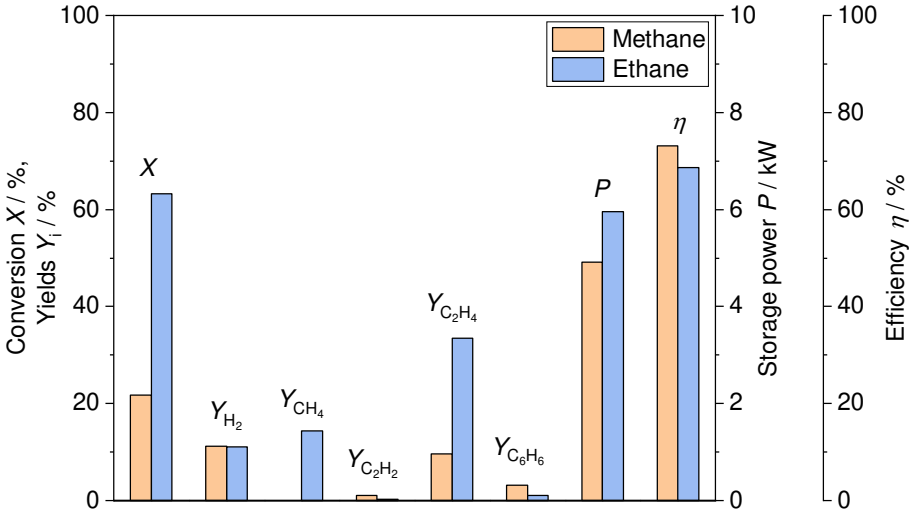

Figure 3.12. Conversion, yields of H_2, CH_4, C_2H_2, C_2H_4 and C_6H_6 (right axis) and storage power and efficiency (left axes) at yields of $C_{20}H_{10}$ and $C_{20}H_{10}$<10^{-4} for methane (373 K, 10 bar, 89 mol% argon) and ethane(373 K, 10 bar, 93 mol% argon), respectively. The yield of H_2 is related to H-atoms whereas the yields for the hydrocarbons are related to the C-atoms.

As the generation of soot and soot precursors is disadvantageous, Figure 3.12 shows the achievable educt conversion, yields of the most interesting species, as well as storage power and efficiency at which almost no heavy PAHs (Y_{C20H10}, Y_{C20H16}<10^{-4}) are formed. For methane, such conditions are found at T_0 = 373 K, p_0 = 10 bar, and x_{Ar} = 0.89, and for ethane at T_0 = 373 K, p_0 = 10 bar, and x_{Ar} = 0.93. Due to the low temperatures and high pressures, not only the PAH production is significantly reduced but also the methane conversion. Also, the yields of H_2, C_2H_2, and C_6H_6 from both, methane and ethane pyrolysis are lower. The ethane conversion is reduced to a considerably lesser extent. The formation of C_2H_4 is only slightly affected. Although the storage power and the efficiency of methane is relatively low, the storage power of ethane is at its maximum value as already shown in Figure 3.11. If soot precursor formation shall be avoided, ethane is the preferable reactant, as high educt conversions and high C_2H_4 yields can still be achieved, whereas methane has its advantages in the different product spectra at different operating conditions and often in a higher storage power and efficiency.

3.4 Conclusion

The pyrolysis of methane and ethane in a motored piston engine with a high but realistic compression ratio and engine speed (22:1, 3000 RPM) at inlet temperatures between 323 and 573 K, inlet pressures between 1 and 10 bar and an argon dilution between 85 and 99 mol% was investigated theoretically with respect to chemical energy storage. Therefore, the piston engine was modeled as a time-dependent reactor with a compression and expansion stroke but without gas-exchange strokes. The main products are hydrogen, acetylene, ethylene, benzene, and soot precursors depending on the operating conditions and used reactant. Due to the higher reactivity of ethane, lower temperatures are required to achieve a conversion, which also has the advantage of producing less PAHs and soot precursors. The formation of methane from ethane is rather disadvantageous for the process as it reduces the exergy of the mixture. The comparison with a previous equilibrium study [59] is interesting. There, it was found that, if equilibrium is reached, the usage of ethane is not useful for energy storage in piston engines. In the present work, it turns out that the kinetics of the process can be stopped in piston engines before the equilibrium is reached. In this case, ethane pyrolysis has several advantages compared to methane pyrolysis. For ethane–argon mixtures, significantly less methane and benzene as well as significantly more ethylene is produced if equilibration is not reached, as assumed in ref. [59]. In addition, PAH formation is only observed at very high temperatures and pressures and can be avoided more easily when ethane is used as reactant. In contrast, in methane pyrolysis, PAH formation can only be avoided at low initial temperatures, which also leads to a lower conversion and lower storage power. Nevertheless, both educts, can be used, because they lead to different product spectra, including the expected formation of soot due to the presence of heavy PAHs, and the process can run under different conditions (T_0 and p_0). Higher pressures lead to higher reactions rates, so that conversion and product formation starts at lower temperatures.

The thermodynamic analysis of this process showed that physical exergy losses are negligible and that very high exergetic efficiencies can be reached by the conversion of work to chemical exergy. The maximum storage power (increase in exergy) during the compression stroke is 7.5 kW for methane and 6 kW for ethane which is more than 70% of the work to be stored. These values for ethane pyrolysis can also be obtained without soot-precursor formation.

Overall, this engine process seems promising with respect to chemical energy storage or PtG conversion, although the theoretical investigation should be followed by an experimental one to prove the present predictions. As methane and ethane are present in different natural gas mixtures and sometimes in bio-gases, it is also interesting for

future investigations, to study the influence of the mixture composition on the outcome of such a piston engine energy storage process.
Further concepts to reduce the high argon content should be analyzed, because the separation from the products could reduce the storage efficiency considerably. In addition, the separation of the products should be investigated, including the design of an integrated process concept.

3.5 Outlook

In addition to the main process, some auxiliaries are required. To set the inlet conditions (temperature, pressure), a preheater and an inlet compressor are necessary. After the main process, the product gas should be separated, and the argon should be recirculated. The exergy input for the inlet conditions is represented by the physical exergy, which is low compared to the chemical exergy. For example, the physical exergy in the inlet state is 0.4 kW and the chemical exergy 15 kW for 573 K, 1 bar, and 93 mol% argon. To estimate the influence of the preheater and inlet compressor, the efficiency according to Equation (3.14) is extended by the physical exergy in the denominator. If now the components to reach the inlet conditions are included, the efficiency is decreased by 1–6%-points at low inlet pressures (1 bar$<p_0<$4 bar). At very high inlet pressures (10 bar), the efficiency strongly decreases (by up to 20% points) due to the increased exergy input. The product gas could be separated using a membrane, pressure swing adsorption, or condensation as this is already state-of-the-art for comparable processes [56]. The separation and recirculation of argon and unconverted methane could influence the efficiency of the process. The development of an entire process concept based on these estimations and approaches is part of our future work.

3.6 Acknowledgements

This work was supported by the Deutsche Forschungsgemeinschaft within the framework of the DFG research unit FOR 1993 ‘Multi-functional conversion of chemical species and energy’, Project-Number 229243862.

4 Effect of natural gas components and hydrogen

The content of this chapter was published in Energy:
C. Rudolph, B. Atakan, Investigation of natural gas/hydrogen mixtures for exergy storage in a piston engine, Energy 218, pp. 119375 (2021), DOI: 10.1016/j.energy.2020.119375.

Author contribution
My contribution embraced developing the concept, designing the computer code, conducting the simulations, analyzing and graphing the results, and writing the manuscript. Burak Atakan developed the concept and reviewed the manuscript. He also coordinated the project and acquired funding.

Highlights
- Chemical energy storage enables the long-term storage of renewable energies.
- Flexible energy conversion in a piston engine is investigated theoretically.
- The thermodynamics and kinetics within the piston engine are modelled.
- High energy products formed by natural gas pyrolysis using excess renewable energy.
- Hydrogen addition reduces the production of PAH's.

Abstract
The conversion of mechanical to chemical energy offers an option for long-term and versatile energy storage. It was already proven that piston engines can be used as flexible reactors for energy conversion. Here, a novel method for energy conversion in piston engines is investigated, the pyrolysis of natural gas/hydrogen mixtures for energy storage. The supplied energy is stored by chemical conversion into hydrogen and higher energy hydrocarbons. The storage efficiency and the product composition are addressed here. To reach sufficiently high temperatures after compression, a dilution with 85–99% argon is used. The main products are hydrogen, acetylene, ethylene and benzene but also soot precursors are formed. The piston engine is simulated as a time-dependent four-stroke single-zone model with detailed chemical kinetics. The intake pressure is kept constant at 2 bar, while intake temperature, intake argon mole fraction

and the hydrogen/natural gas ratio is varied. The hydrogen addition allows a reduction of the intake temperature and argon dilution but also reduces the storage power and efficiency. Yields of acetylene or ethylene are increased and the formation of soot precursors is suppressed. A storage power of 1.59 kW is reached with an efficiency of 52%.

4.1 Introduction

Since power generation with fluctuating renewable energies does not follow temporal and local power consumption demand, the need for energy storage systems is increased. Energy can be stored in mechanical energy (*e.g.*, pumped hydro storage (PHS), compressed air storage (CAES), flywheel storage), electrical energy (*e.g.*, capacitors and superconducting magnetic energy storage), electrochemical energy (batteries) and thermal energy (*e.g.*, latent and sensitive heat storage). A detailed review of selected energy storage systems was recently published [75]. Koohi-Fayegh et al. [75] compared electrochemical and battery energy storage, thermal energy storage, thermochemical energy storage, flywheel energy storage, compressed air energy storage, pumped hydro energy storage, magnetic and chemical energy storage and hydrogen energy storage in terms of functionality, capacity, efficiency, lifetime and costs and they also listed their advantages and disadvantages. Although most of these systems are technically matured, they are not designed to store energy for long time or to transport it. For long-term storage of highest capacities, chemical energy storage is the most important technology: Electrical excess energy is used to produce gaseous (Power-to-Gas) energy carriers, mainly hydrogen, and in a second step synthetic natural gas or liquid fuels (Power-to-Liquid) are produced. The hydrogen produced by the PtG process is then used in the chemical industry to produce methanol, ammonia or dimethyl ether (DME), in fuel cells to generate electricity with a high efficiency, in combustion engines or gas turbines for a clean combustion and for heating purposes [76].
Presently, hydrogen is mainly produced through steam methane reforming (SMR), where CH_4 and H_2O are converted into CO and H_2 according to Eq. (R4.1):

$$CH_4 + 2\ H_2O \rightleftharpoons CO + 3\ H_2 \qquad \Delta g^0 = 142\ \text{kJ/mol} \qquad \text{(R4.1)}$$

(The change in Gibbs energy Δg is given throughout for 298.15 K, if not stated differently.) The SMR is an endothermal reaction, which proceeds catalytically at temperatures of 850°C–900°C [16]. This method is economically advantageous since the actual costs for natural gas are low [36] and it offers the opportunity for large-scale hydrogen production with high efficiencies of up to 85% [16]. Other reforming processes are dry

methane reforming (DMR) and autothermal methane reforming (AMR) according to Eq. (R4.2) and Eq. (R4.3).:

$$CH_4 + CO_2 \rightleftharpoons 2\ CO + 2\ H_2 \qquad \Delta g^0 = 171\ \text{kJ/mol} \qquad \text{(R4.2)}$$

$$CH_4 + H_2O + 0.5\ O_2 \rightleftharpoons CO_2 + 3\ H_2 \qquad \Delta g^0 = 115\ \text{kJ/mol} \qquad \text{(R4.3)}$$

DMR is endothermal and needs significantly higher reaction temperatures. Gossler et al. [18] investigated DMR in an internal combustion engine and rapid compression machine and added oxygen to provide an autoignition and to ensure the necessary high temperatures for the CO_2 conversion. Carapellucci et al. [77] compared SMR with DMR and AMR in a thermodynamic equilibrium model, based on the minimization of the gibbs energy and they also found out that small amounts of oxygen are helpful to improve conversion and H_2 yield but also process efficiencies. Subsequently to SMR and DMR, the water-gas-shift reaction converts CO into CO_2 and generates additional H_2. Carbon-free hydrogen production by electrolysis uses electrical energy and heat to decompose water into hydrogen and oxygen according to Eq. (R4.4) [78].

$$H_2O(l) \rightleftharpoons H_2(g) + 0.5\ O_2(g) \qquad \Delta g^0 = 272\ \text{kJ/mol} \qquad \text{(R4.4)}$$

Different electrolysis technologies are employed: alkaline electrolysis, polymer electrolyte membrane (PEM) electrolysis and solid oxide electrolysis (SOE) and a detailed overview of the different technologies is given by Buttler et al. [19] while the production and hydrogen costs are discussed by El-Emam et al. [78]. The most matured technology is the alkaline electrolysis, which can achieve efficiencies of up to 80%. Higher efficiencies can be achieved by PEM electrolysis and SOE but at higher investment and H_2 production costs. Shiva-Kumar et al. [35] focused on PEM electrolysers and discussed different low cost electrocatalysts (for the hydrogen evolution reaction and oxygen evolution reaction) with respect to efficiency. Nevertheless, even alkaline electrolysers can actually compete with hydrogen production by SMR on an industrial scale because of the high costs and energy consumption.

Another technology for hydrogen production, which is perused in many ways due to the long range of methane or natural gas resources, is the pyrolysis of methane. It can also be regarded as a way to store energy. Methane is decomposed towards hydrogen, carbon and hydrocarbons like acetylene, ethylene or benzene according to Eqs. (R4.5)–(R4.8) in endergonic reactions. Due to the absence of oxygen or oxygen containing educts, no CO or CO_2 emission are produced.

$$CH4 \rightleftharpoons C + 2\ H_2 \qquad \Delta g^0 = 51\ \text{kJ/mol} \qquad \text{(R4.5)}$$

$CH4 \rightleftharpoons 0.167\ C_6H_6 + 1.5\ H_2$	$\Delta g^0 = 72$ kJ/mol	(R4.6)
$CH4 \rightleftharpoons 0.5\ C_2H_4 + H_2$	$\Delta g^0 = 85$ kJ/mol	(R4.7)
$CH4 \rightleftharpoons 0.5\ C_2H_2 + 1.5\ H_2$	$\Delta g^0 = 155$ kJ/mol	(R4.8)

Compared to other methods for hydrogen production, the efficiencies are low, between 35 and 50% [35] but the energy consumption is also significantly lower. The pyrolysis of methane has been studied many times. In early studies, the influence of temperature and residence time on the pyrolysis of methane and its products was investigated experimentally by Billaud et al. [79] in a flow reactor and theoretically by Gueret et al. [49] by calculating the thermodynamic equilibrium composition at the minimum Gibbs enthalpy. Wang et al. [80] measured the rate constant of the initial reaction of methane decomposition using a shock tube. The endothermal reaction of methane requires high temperatures to initiate and drive the decomposition, due to the stability of methane at low temperatures and all three authors named above agreed that a noticeable CH_4 conversion is only observed at temperatures of at least 1300 K–1500 K. At these temperatures, besides hydrogen, mainly benzene if formed. At temperatures above 1500 K, additionally acetylene and ethylene are produced. The net reactions towards these main species are formulated above (Eqs. (R4.6)–(R4.8)). To increase the reaction rate, methane pyrolysis is often either conducted using catalysts from different material, plasma reactors, molten metal reactors or bed reactors, which are described in several recent reviews, *e.g.*, in Ref. [81]. There, different assisted pyrolysis systems are compared with respect to green-house gas emissions and hydrogen production costs. In comparison with an unassisted methane pyrolysis, the reaction temperature of catalytic pyrolysis is reduced by 400 K–500 K [82]. Chen et al. [83] studied the methane decomposition using nickel-platinum catalysts and achieved conversion rates of 30%–60% at temperatures of 800 K–873 K. Using WO_3-ZrO_2 catalysts instead, conversion rates of up to 90% were achieved at 1073 K [84]. The plasma pyrolysis at room temperature was investigated by Zhang et al. [85] and despite of a methane conversion below 1%, they found hydrogen and unsatured alkenes and alkynes in the product gas. Higher conversion rates (up to 100%) and higher yields regarding acetylene (up to 80%) were achieved by An et al. [86] at temperatures of 1500 K and 2300 K. In order, not to produce only carbon black due to the high temperatures, the gas mixture was quenched at the end of the reactor and acetylene remains stable. To point out pathways towards intermediates and the formation of the main products, Nativel et al. [52] studied non-catalytic methane pyrolysis in a single-pulse shock tube and Keramiotis et al. [53] in a flow reactor at high temperatures to overcome the high activation energy. The major products detected were acetylene, ethylene, and benzene but also minor amounts of propene, propane, 1,3-butadiene, and soot were found.

Temperatures between 1500 K and 2400 K, were investigated in the flow reactor and in the shock tube, respectively, also due to the different residence times. The carbon black or soot formation within hydrocarbon and, in particular, methane pyrolysis is generally undesirable if gaseous hydrocarbons and hydrogen shall be produced. In this context, polycyclic aromatic hydrocarbons (PAH) were revealed as the main precursors for soot formation. The formation of soot increased with the residence time, as observed by Kang et al. [87] during propane pyrolysis at temperatures of up to 1250 K and by Bensabath et al. [88] during acetylene pyrolysis at temperatures of 1173 K in a plug flow reactor, respectively. Koike et al. [89] performed experiments to investigate the early stage of the pyrolysis of acetylene and ethylene in a shock tube and found out that hydrogen inhibits the decomposition of acetylene. Similar shock tube experiments [90] focused on the influence of additional hydrogen on the pyrolysis of acetylene and benzene. All these experiments lead to the same result that the addition of hydrogen prevents the formation of PAH's and inhibits the soot particle formation. Recent studies of hydrogen enrichment during pyrolysis or of flames confirm, that hydrogen has a soot or PAH preventing effect: Peukert et al. [91] studied the soot particle growth in a burnt-gas flow reactor during acetylene pyrolysis and achieved smaller particle diameters and lower soot volume fraction and Ezenwajiaku et al. [92] investigated PAH formation in methane diffusion flames and achieved a reduction of PAH's due to lower amounts of acetylene and propargyl as intermediate species. These results appear promising, so that the effect of hydrogen on such pyrolysis processes will be studied here theoretically in engines under non-isobaric conditions.

Combustion engines were already used as flexible reactors mainly for partial oxidations to produce syngas. The advantage is the production of work (electricity) or syngas on demand, only by varying the load and equivalence ratio of the combustion engine [60]. Lim et al. [14] investigated syngas production from methane via partial oxidation in a diesel engine. The energy input was due to the compression stroke and ignition from a spark plug and they achieved a methane conversion of 85%. Eyal et al. [93] performed an exergy analysis of a compression ignition engine with respect to fuel reforming to improve the efficiency. A recent review discusses different fuel reforming processes using internal combustion engines [94]. Instead of an exothermal reaction, such as partial oxidation, endothermal conversion processes like dry methane reforming, was also performed in a piston engine [18], as mentioned above. There, the needed energy for the endothermal reaction was provided by the compression stroke and some assisting partial oxidation. Using a piston engine for the pyrolysis of methane with respect to energy storage was proven to be feasible; it was investigated theoretically by Atakan [59] and Hegner et al. [95] and also experimentally by Hegner et al. [95]. A methane conversion of more than 70% could be achieved for reasonable intake conditions if the

educt is diluted with an atomic inert gas. The dilution causes a decrease of the heat capacity of the mixture leading to a higher temperature increase in the compression stroke. The main products are again acetylene, ethylene and benzene, which are energetically more valuable than the educt. The exergy of the mixture increases by more than 11% and exergetic efficiencies of up to 92% were predicted [59], so the process seems promising with respect to exergy storage. Besides the generation of wanted products, soot formation was also found in the experimental study. However, the existing studies of Atakan [59] and Hegner et al. [95] reveal some gaps. In the investigation of Atakan the thermodynamic equilibrium is calculated, ignoring kinetics within a mathematical optimization of engine and intake parameters. Hegner et al. [95] used a reaction mechanism with benzene as the largest molecule. Therefore, it cannot predict PAH's and soot precursors, although the experimental results show soot formation. To our knowledge, no other studies exist regarding methane or natural gas pyrolysis in piston engines with respect to energy storage. This gap is addressed here, with emphasis to the reduction of soot and its precursors.

Here the pyrolysis of natural gas in a piston engine with respect to energy storage and the influence of hydrogen addition is investigated systematically. First, the hydrogen addition is expected to lead to reduced PAH and soot formation. Second, the recent study investigates whether models which do not only rely on chemical equilibrium but include the detailed kinetics also predict considerable yields of useful, high-exergy products, reasonable storage capacities and efficiencies.

The concept is that excess energy from renewable sources can be used to motor a piston engine. The compression stroke provides the necessary activation energy to decompose gaseous hydrocarbons, here natural gas, towards hydrogen and higher exergy hydrocarbons. To ensure sufficiently high temperatures after compression, the natural gas/hydrogen mixture is diluted with argon to decrease the heat capacity. The exergy of the mixture increases due to the endothermal reaction. During the expansion stroke, the mixture cools down quickly. Chemical reactions should be quenched shortly after the top dead center due to the low temperatures and higher exergy hydrocarbons remain in the product gas. The exergy of the product gas is higher than the exergy of the educt gas. Therefore, the excess energy from the renewable sources is preserved to a large extent by producing high-exergy products. To investigate the feasibility of the process and to evaluate the process, the piston engine is simulated as a time dependent single zone model together with detailed chemical kinetics. Only the engine is modelled without gas pre-treatment, recirculation or gas separation, since these efforts would only be worthwhile when the central unit turns out to be favourable. The chosen modeling approach was already used in previous studies on oxidation under fuel-rich conditions in an HCCI engine [60]. In these studies, the agreement between

simulation and experiment was good: Products and favourable operating points are predicted well, but there are deviations in the exact pressure traces. The modelling procedure is shown in Fig. 4.1. A feasibility and parameter study are performed, varying intake temperature, argon dilution and hydrogen mole fraction. The results of different parameters are compared and evaluated, using a thermodynamic, exergetic and kinetic analysis, which is described in detail below. The kinetic analysis includes a reactions path analysis to understand the chemical processes.

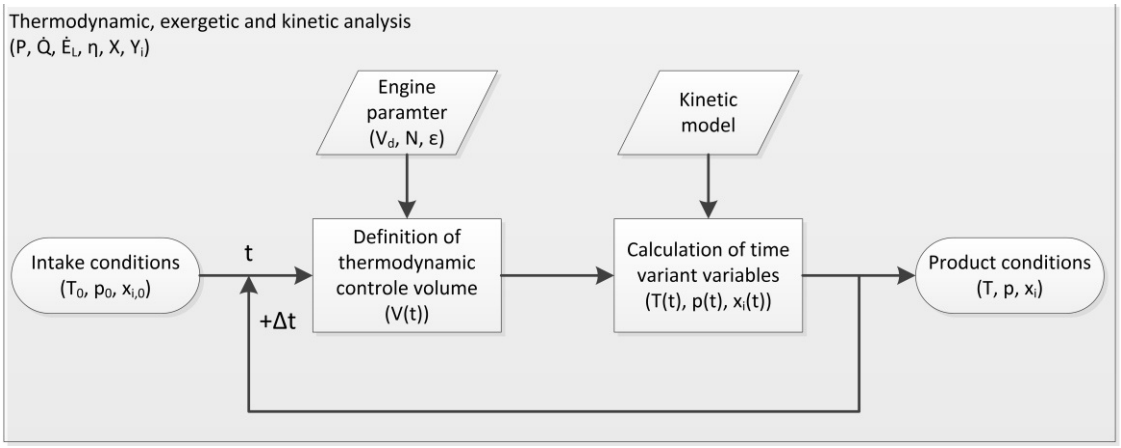

Figure 4.1. Modeling procedure.

4.2 Modeling

The simulation of the piston engine was performed using the module Cantera within Python [34]. For modelling a single-zone homogeneous time-variant volume is assumed. The energy equation is solved together with the detailed chemical kinetics to predict the chemical and energy conversion along the cycle. The engine model includes the compression and the expansion stroke as a closed system and the charge exchange strokes as open systems. The time-dependency is modelled by dividing the whole engine cycle into small time, or better crank angle, steps and calculating the position of the piston through the velocity sp from Eq. (4.1) [96]:

$$\frac{s_\mathrm{p}}{\bar{s}_\mathrm{p}} = \frac{\pi}{2} \cdot \sin(\Theta) \cdot \left(1 + \frac{\cos(\Theta)}{\sqrt{R^2 - \sin^2(\Theta)}}\right) \tag{4.1}$$

where Θ is the crank angle, s_p is the mean piston speed and R is the connecting rod length to crank radius ratio. For every time step, the energy and species conservation equations are solved. The energy balance accounts for the change of internal energy

U due to the volume work, the heat transfer and along the charge exchanges also for the enthalpy inflow and outflow h_{in} and h_{out} [61]:

$$\frac{\mathrm{d}U}{\mathrm{d}t} = -p\frac{\mathrm{d}V}{\mathrm{d}t} + \dot{Q} + \sum_{\mathrm{in}} \dot{m}_{\mathrm{in}} h_{\mathrm{in}} - \sum_{\mathrm{out}} \dot{m}_{\mathrm{out}} h_{\mathrm{out}} \tag{4.2}$$

Here, *p* is the pressure, *V* is the cylinder volume and $\dot{Q}$ the heat transfer rate. The heat transfer through the cylinder walls is calculated using the original Woschni correlation [63]:

$$\alpha = C \cdot d^{-0.2} \cdot p^{0.8} \cdot T^{-0.53} \cdot \left[C_1 \cdot \bar{s}_{\mathrm{p}} + C_2 \cdot \frac{V_{\mathrm{D}} \cdot T_{\mathrm{r}}}{V_{\mathrm{r}} \cdot p_{\mathrm{r}}} \cdot (p - p_{\mathrm{m}}) \right]^{0.8} \tag{4.3}$$

α is the heat transfer coefficient, *d* is the cylinder diameter, *T* and *p* are the instantaneous cylinder temperature and pressure, respectively. The indices d, m, and r describe the displacement, the motored conditions, and the reference conditions, respectively. The constants are C = 110, C_1 = 6.18 for the charge exchange stroke and C_1 = 2.28 for compression and expansion stroke. C_2 is set to zero, since no combustion takes place. The species conservation for each species k accounts the entering masses and the species generated in homogeneous phase reactions. It is expressed as [61]:

$$m \cdot \frac{\mathrm{d}y_{\mathrm{k}}}{\mathrm{d}t} = \sum_{\mathrm{in}} \dot{m}_{\mathrm{in}} \cdot \left(y_{\mathrm{k,in}} - y_{\mathrm{k}} \right) + V \cdot \dot{\omega}_{\mathrm{k}} \cdot M_{\mathrm{k}} \tag{4.4}$$

m is the mass, *y* is the mass fraction, *V* is the cylinder volume, ω̇ is the molar production rate and M is the molecular mass. The entering and exiting mass flows through the valves depend on the pressure difference between the pressure inside the cylinder and the pressure in the intake and exhaust ports. The molar production rate for each species and the elementary reactions are calculated with an elementary reaction mechanism, the complete Polimi mechanism [67], which includes 484 species up to C_{20} and 19341 reactions. The mechanism contains especially the formation of lumped species and the chemistry of PAH's and is validated for pyrolysis, partial oxidation and combustion of hydrocarbons and soot formation. Recently, the Polimi reaction mechanism was used to predict product species profiles during the oxidation of fuel-rich methane/n-heptane mixtures at equivalence ratios of up to 20 [97]. The simulation results were compared to results obtained from plug-flow reactor experiments and showed a reasonable agreement.

The engine parameters used in the model were chosen according to typical automotive parameters and are listed in Table 4.1. A high compression ratio and rotation speed are chosen, the first to increase the temperature at the end of compression stroke and the second to freeze the mixture fast in the expansion stroke. The rotation speed is kept constant because according to the concept the engine is motored by an external drive. Despite the relatively unusual engine parameters for gas engines, no knocking phenomena are expected as there is no ignition, due to the absence of oxygen. In opposite, due to the endothermal reactions pressure and temperature are lower than in a motored engine without chemical reactions. Since some residual gas remains in the cylinder in the exhaust stroke, there are small changes in the gas composition in successive cycles, especially in the first and second cycle. In order to reach steady-state conditions, four cycles are modelled, and the last cycle is used for the evaluation.

Table 4.1. Engine Parameter used for the simulation.

Parameter	Specification	Unit
Displacement V_D	400	cm^3
Bore d / Stroke s	79.5 / 80.5	mm
Compression ratio ε	22	-
Connection rod / crank radius R	3.5	-
Rotation speed N	3000	1/min
Coolant temperature T_{CW}	373	K

In this work, natural gas/hydrogen mixtures are used to evaluate the process. The composition of natural gas is taken to be 90% CH_4, 9% C_2H_6 and 1% C_3H_8. Additionally, the natural gas is mixed with up to 20% hydrogen. This value was chosen, since studies about the hydrogen concentration in natural gas pipelines show that the risk of ignition does not increase significantly when the hydrogen content in natural gas is below 20% [98]. The engine load for every inlet condition, respectively, is kept constant; start-up and shutdown are not considered. The intake temperatures T_0 are varied between 323 and 573 K and the intake pressure p_0 was set to 2 bar, since the exhaust gas pressure should not be lower than 1 atm, and the temperature drops due to the endothermal reaction, thus the pressure also falls below the initial values at the end of the cycle. Tuning the argon dilution was investigated, because the temperature after compression can be increased with an atomic inert gas with low heat capacity. The process parameters, described above, are summarized in Table 4.2. While in a real engine the intake state would have to be adjusted by a compressor and a preheater, in this study

that intake state is taken for granted. To realize such inlet conditions additional 10%–15% of the supplied power would be required.

Table 4.2. Process parameters used for the simulation.

Parameter	Range	Unit
Intake temperature T_0	323 – 573	K
Intake pressure (absolute) p_0	1 – 10	bar
Intake argon mole fraction	85 – 99	mol%
Intake hydrogen/natural gas ratio	0 – 20/80	mol/mol

The process leads to an increase of exergy of the mixture, which can be stored due to the supplied work. The specific exergy e of the mixture is the sum of the chemical and the physical exergy. The chemical exergy is calculated according to Refs. [59]. The gas mixture, whose exergy is to be determined, is chemically equilibrated with excess surrounding air in the ratio $1/f$ with $f = 10^6$. This factor is a good compromise: the final surrounding (air) composition is nearly unchanged after equilibration, while the numerical error is small. The surrounding air is present at standard conditions (298.15 K and 1.01325 bar) and has a relative humidity of 70% according to Ref. [71]. Afterwards, the specific chemical exergy e_{ch} is calculated using

$$e_{\mathrm{ch}} = \left(h_{\mathrm{sur}} + f \cdot h_{\mathrm{air}} - (f+1) \cdot h_{\mathrm{eq}}\right) - T_{\mathrm{sur}} \cdot \left(s_{\mathrm{sur}} + f \cdot s_{\mathrm{air}} - (f+1) \cdot s_{\mathrm{eq}}\right) \tag{4.5}$$

s is the entropy and the subscripts sur describes the mixture at surrounding conditions, air is used for surrounding air, as described above and eq describes the chemically equilibrated mixture. The specific physical exergy e_{ph} for an open system is calculated from

$$e_{\mathrm{ph}} = (h - h_{\mathrm{sur}}) - T_{\mathrm{sur}} \cdot (s - s_{\mathrm{sur}}) \tag{4.6}$$

The exergy produced per mass of the mixture Δe is the difference between the specific exergies of product and educt gas. The total amount of energy that can be stored through this process is described by the storage power P_{storage}, which is calculated for a 4-stroke engine from

$$P_{\mathrm{storage}} = m \cdot (e_{\mathrm{P}} - e_{\mathrm{E}}) \cdot \frac{N}{2} \tag{4.7}$$

The subscripts E and P stand for educt and product. To describe the efficiency of the process, the exergetic efficiency η is calculated as the ratio

$$\eta = \frac{P_{\mathrm{storage}}}{P_{\mathrm{mech}}} \tag{4.8}$$

Here, P_{mech} is the supplied power, needed to drive the engine. A thermodynamic analysis is conducted, including the calculation of supplied work, heat and exergy losses. The kinetic analysis includes an investigation of the product gas composition in the exhaust and a calculation of the conversion of the educt gas as well as of the yields of interesting species in the product gas from Eq. (4.9) and Eq. (4.10)

$$X = \frac{n_{\mathrm{E},0} - n_{\mathrm{E}}}{n_{\mathrm{E},0}} \tag{4.9}$$

$$Y_{\mathrm{k}} = \frac{n_{\mathrm{P},0} - n_{\mathrm{P}}}{\sum n_{\mathrm{E},0} \cdot \nu_{\mathrm{E}}} \cdot \nu_{\mathrm{P}} \tag{4.10}$$

where *n* is the molar amount of the species and the index 0 describes the intake state. The parameter n is the number of C or H atoms of the respective species. The yields of hydrocarbons are referred to the number of C-atoms in a species and the yield of hydrogen refers to the number of H-atoms. To identify the most important reactions, which are responsible for the differences in the product gas composition and PAH formation, a reaction path analysis was performed using the cantera module [61]. The largest carbon fluxes calculated from the net production rates for each reaction represent the most important reaction paths and are shown for a defined time during the engine cycle.

4.3 Results and Discussion

The conversion of the natural gas components and the generation of target species for neat natural gas without hydrogen addition for an intake temperature of 473 K and an intake argon mol fraction of 0.94 are shown in Fig. 4.2a. Only the compression and expansion strokes are plotted, since the influence of the gas exchange stroke on the temperature and the pressure curve, and on the outcome is negligible. Residual gas from the previous cycles remains in the cylinder and causes a hydrogen mole fraction of 0.003 at the beginning of compression stroke. First, propane and ethane are consumed at temperatures of 1230 K and 1290 K (35° before TDC and 32° before TDC) and small amounts of ethylene are produced. At 1500 K (24° before TDC), two percent methane conversion is observed, with all the propane and 40% of the ethane already

consumed. The temperature rise is reduced due to the endothermal reactions. At TDC, a temperature of 1790 K and a pressure of 177 bar is reached and mainly acetylene and benzene are formed from ethylene due to the higher temperatures. Shortly after the compression stroke, at 380°, the mixture is frozen and all reactions are slow, so the mixture is quenched. At the end of the expansion stroke, the temperature is 325 K and the pressure is 1.5 bar, which are both lower than the initial values due to the endothermal reactions and the conversion of work into chemical energy. The supplied power is 3.15 kW. Considering the whole process, 70% of methane was converted, while propane and ethane are consumed completely. Yields for hydrogen, acetylene, ethylene, and benzene of 54%, 13%, 8% and 9% but much of the carbon is converted into soot precursors, so that yields for lumped species, like $C_{20}H_{10}$ are up to 30%. As a result of the conversion to hydrocarbons with a higher enthalpy, the chemical exergy of the mixture is increased by 5%. Overall, a storage power of 1.7 kW with an efficiency of 54% is predicted. The physical exergy is low compared to the chemical exergy provided by the mixture and the supplied power (<1%). The necessary exergy to reach the inlet state is 300 W and corresponds to the physical exergy in the inlet state. If this was also included, the efficiency would be reduced by 5%-points. Nevertheless, this is not considered in the further process.

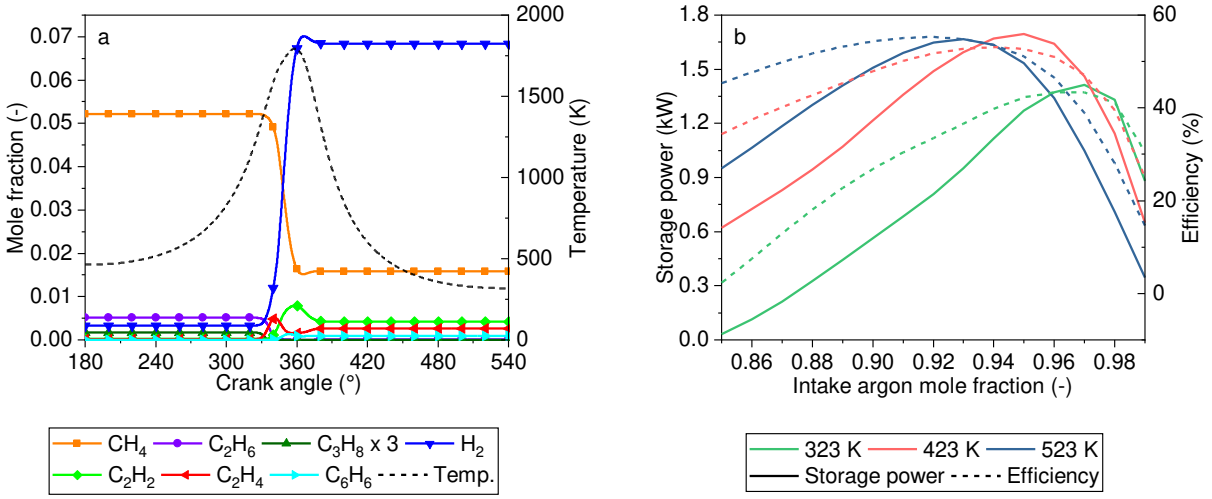

Figure 4.2. Mole fractions (left axis, solid lines) and temperature (right axis, dashed lines) as a function of crank angle for a compression and expansion stroke with $x_{Ar,0}$ = 0.94 and at T_0 = 473 K (a), and storage power (left axis, solid lines) and efficiency (right axis, dashed lines) as a function of intake argon mole fraction for different intake temperatures (b) without additional hydrogen.

A series of such simulations were performed to investigate the influence of the intake argon mole fraction and the intake temperature on the storage power and the efficiency; the results are shown in Fig. 4.2b. For every intake temperature, the storage

power as a function of argon mole fraction has the same trend, respectively. For intake argon mole fractions of $x_{Ar}<0.9$, the temperatures at the end of the compression stroke are not high enough, to achieve a reasonable conversion and to provide a formation of useful species, thus, the storage power and efficiency are low. At very high argon mole fractions $x_{Ar}>0.98$ the storage power decreases due to the lower fuel concentrations in the mixture. At higher intake temperatures, already lower argon mole fractions lead to a higher storage power. The local maximum of the storage power is located between x_{Ar} = 0.93 and x_{Ar} = 0.97 and shifts towards lower argon mole fractions with temperature. The maximum storage power of 1.69 kW is found at T_0 = 423 K and x_{Ar} = 0.95 and not, as expected, at T_0 = 523 K, where it is only 1.66 kW. The reasons for the lower maximum storage power at higher intake temperatures are 1) the lower charge in the cylinder due to the lower density of the mixture, 2) the increasing formation of soot precursors, and 3) the exothermal reaction back to methane and the decreasing generation of acetylene, ethylene and benzene due to the overall higher temperatures and faster reactions. Additionally, with increasing intake temperatures the transferred work in the compression stroke decreases slower than the storage power, and thus, the efficiency is positively affected. The maximum efficiency of 55% is found at 523 K and x_{Ar} = 0.92 and decreases to 43% at 323 K and x_{Ar} = 0.97.

A reaction path analysis was performed to visualize the most important reactions and the influence of hydrogen addition on these reactions. The reaction paths are shown in Fig. 4.3 for an intake temperature of T_0 = 473 K and an intake argon mole fraction of x_{Ar} = 0.94 for natural gas pyrolysis without additional hydrogen (Fig. 4.3a and 4.3c) and with 20% hydrogen in natural gas (Fig. 4.3b and 4.3d). The reaction path analysis was performed at 2% ethane conversion, respectively for 0% and 20% hydrogen in natural gas to show the influence on the initial reactions and at TDC, respectively for 0% and 20% hydrogen in natural gas, since most of PAH and soot production is expected there. An ethane conversion of 2% was chosen here because there is a distinct influence of hydrogen on the reactivity of the mixture and the reaction start. TDC was chosen to show the influence on the high temperature reactions. The addition of hydrogen to natural gas basically reduces the density and the heat capacity, which leads to a lower amount of supplied work and to higher temperatures and pressures at the end of the compression stroke, which helps to decompose methane and to form valuable species and also influences the storage power and the efficiency. The initial reactions in the pyrolysis of natural gas is the H-abstraction from methane and ethane, which proceed partially simultaneously and thus, compete for the H-radicals, which can be seen in Fig. 4.3a and 4.3b for 0% and 20% hydrogen in natural gas, respectively.

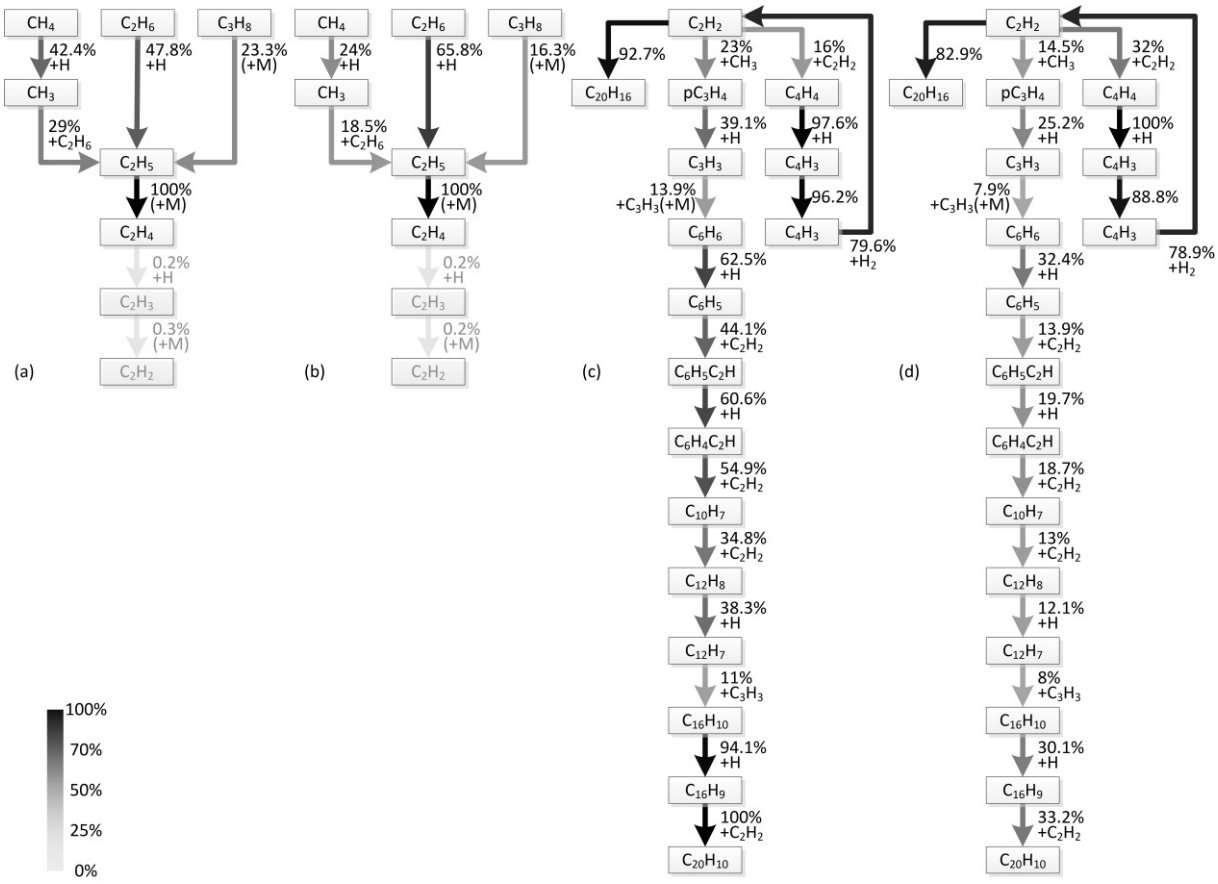

Figure 4.3. Reaction path analysis for natural gas pyrolysis at T_0 = 473 K and x_{Ar} = 0.94: (a) without additional H_2 at 2% C_2H_6 conversion (T = 1270 K, p = 38 bar, 33° BTDC), (b) with 20% H_2 in NG at 2% C_2H_6 conversion (T = 1260 K, p = 35 bar, 35° BTDC), (c) without additional H_2 at TDC and (d) with 20% H_2 in NG at TDC. The values of the lines are related to the carbon fluxes according to the net reaction rates and visualize the numbers next to the lines.

The presence of hydrogen in the mixture favours the formation of ethyl radicals by H-abstraction from ethane due to the higher temperatures. Ethane is completely consumed, when the conversion of methane starts with the increasing formation of methyl due to H-abstraction in the reaction with already present H-radicals, similar to the decomposition of ethane. The favourable effect of hydrogen continues along the entire pyrolysis pathway towards the formation of ethylene, acetylene and benzene. After benzene is produced, the reaction path towards the formation of PAH's is interrupted due to the additional hydrogen and the formation of soot is inhibited, as already explained in the literature [90,99]. The pathway towards PAH's and soot precursors, like $C_{14}H_{10}$, $C_{16}H_{10}$ and $C_{20}H_{10}$, contains several reactions with acetylene, for example Eq. (R4.9).

$$C_{16}H_{10} + C_2H_2 \rightleftharpoons 0.5\ C_{20}H_{10} + 0.5\ C_{16}H_{10} + H \qquad \text{(R4.9)}$$

The reaction flow analysis shows that the main reactant acetylene is consumed by the formation of ethylene due to the additional hydrogen, since the reactions Eq. (R4.10) and Eq. (R4.11) are favoured.

$$C_2H_3 + H_2 \rightleftharpoons C_2H_4 + H \quad \text{(R4.10)}$$

$$C_2H_3 + H_2 (+M) \rightleftharpoons C_2H_4 (+M) \quad \text{(R4.11)}$$

The unreacted acetylene follows the recombination pathway towards C_4H_4, which reacts with hydrogen radicals to form C_4H_3, C_4H_2 and subsequently acetylene again. Therefore, most of the carbon from acetylene remains in this loop. Thus, less acetylene is available for PAH formation. This effect can be seen in Fig. 4.3c and 4.3d.
Resulting temperatures and pressures at top dead center TDC, as well as the conversion and yields for some species for an intake temperature of 473 K and intake argon mole fraction of 0.94 for different hydrogen contents in the natural gas/hydrogen mixture are listed exemplary in Table B1 in Appendix B. The influence of the intake temperature and the hydrogen content in the natural gas for a fixed intake argon mole fraction of 0.94 on several outcomes are summarized in Fig. 4.4.
The methane conversion, as seen in Fig. 4.4a depends strongly on the intake temperature, due to the high activation energy of methane decomposition. The hydrogen addition shifts the conversion slightly towards lower intake temperatures. The influence of the hydrogen is more pronounced at higher temperatures. A methane conversion of at least 80% is recognized at 473 K and 20% hydrogen in natural gas or at 523 K without additional hydrogen. A methane conversion of more than 90% is observed in the upper right corner, at 573 K and between 5% and 20% hydrogen in natural gas. The main products are acetylene and benzene, as seen in Fig. 4.4b. The acetylene yield increases with intake temperature and with increasing hydrogen addition. While low hydrogen contents in natural gas result in a comparably low dependence of the acetylene yield on the intake temperature, higher hydrogen amounts have a stronger effect. The maximum acetylene yield is 22% and is predicted for the highest intake temperature of 573 K and 20% hydrogen in natural gas, since the highest temperature at the end of the compression stroke is also found at this condition. The maximum benzene yield is 14% and is observed between 373 K and 423 K without hydrogen addition. With increasing hydrogen content, the highest benzene yields are located in a smaller temperature interval. Besides acetylene and benzene, also a large amount of hydrogen with yields of up to 70% and ethylene with yields of up to 11% are found in the product gas, as well as soot precursors. The inhibition of PAH's due to the addition of hydrogen is seen Fig. 4.4c for naphthalene, as an example. Without hydrogen addition, the maximum naphthalene yield is 1.8% at an intake temperature of 373 K and decreases with

temperature due to the formation of larger PAH's. Hydrogen addition reduces the maximum naphthalene yield slightly, as well as the yields of other PAH's, as listed in Table B1. The maximum yield of ethylene is found at low intake temperatures (<373 K), where the methane conversion is lower, while ethane is already consumed completely. At higher intake temperatures, ethylene decomposes to acetylene and benzene, thus the ethylene yield decreases again.

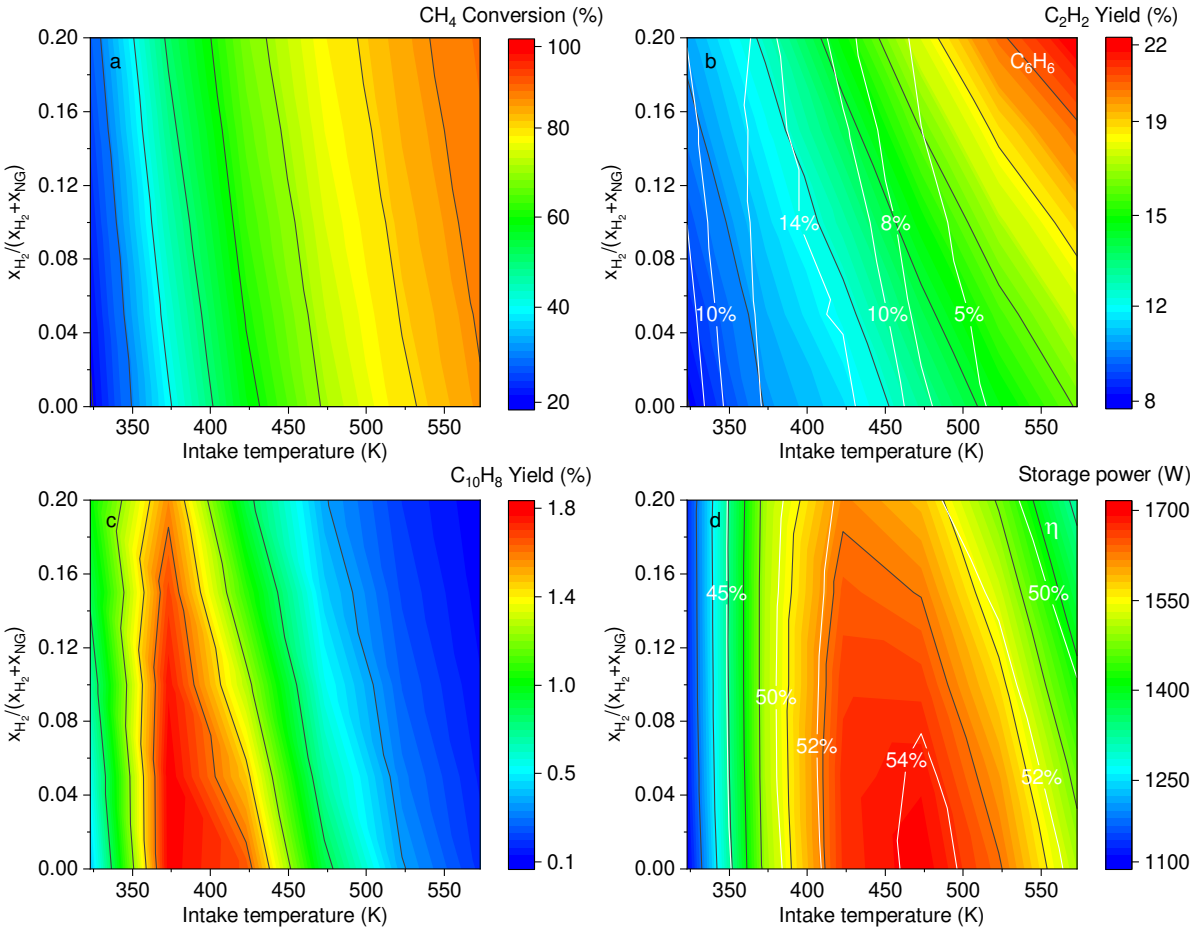

Figure 4.4. CH_4 Conversion (a), C_2H_2 Yield (black lines) and C_6H_6 Yield (white lines) (b), $C_{10}H_8$ Yield (c), and storage power (black lines) and efficiency (white lines) (d) as a function of intake temperature and hydrogen content in natural gas for x_{Ar} = 0.94.

The storage power and the efficiency of the process are presented in Fig. 4.4d. The maximum storage power is 1.7 kW with an efficiency of 54% for an intake temperature of 473 K and an intake argon mole fraction of 0.94 without additional hydrogen. The lower storage power at lower intake temperatures can be explained by the predominant conversion of ethane to ethylene while the conversion of methane is low. At higher intake temperatures, methane is also converted completely, but the product gas mainly contains acetylene, PAH's and soot precursors, which reduce the storage power again. The parameter range with the highest storage power lead to a product gas

composition, containing benzene, acetylene and ethylene with yields of 9% for benzene, 13% for acetylene and 8% ethylene with a reasonable methane conversion of 70%. The influence of each species becomes more apparent from Table 4.3, where the specific exergies of some important species are given.
At a hydrogen content of 20% in the natural gas/hydrogen mixture, the storage power reduces to 1.59 kW with a reduced efficiency of 52% at the previously mentioned parameters. The decrease of the storage power and the efficiency is to a smaller extent caused by the lower density leading to a lower mass in the cylinder and thus to a lower storage power. To a larger extent, the storage power is dependent on the composition of the product gas. According to Table 4.3 and the mole fractions in Table B1 in Appendix B, the reduction of the benzene yield from 9% to 4% has a greater impact on the storage power than the increase of the acetylene yield from 13% to 18% and the ethylene yield from 8% to 9% for ethylene, since the amount of benzene in the specific exergy is reduced by 1% but the amount of acetylene and ethylene in the specific exergy only increases by 0.48% and 0.1%.

Table 4.3. Specific exergies.

Mixture/Species	Spec. exergy / MJ/kmol
Natural gas (90% CH_4, 9% C_2H_6, 1% C_3H_8)	904.2
H_2	236.1
C_2H_2	1266.5
C_2H_4	1361.7
C_6H_6	3301.4

Although the results are promising, the simulated process is affected with some uncertainties. First, in the single-zone model it is assumed that the reactor volume is homogeneous. Thus, the conversion and the gas composition are identical at each point of the reactor volume. Typical problems of an internal combustion engine, such as cold combustion chamber walls or losses through crevices are not represented in a single-zone model, which may lead to a spatially distributed gas composition. Second, although the used reaction mechanism is validated for pyrolysis of hydrocarbons, reactions rates may vary along such a distribution. However, unlike to normal combustion, temperature peaks due to ignition are not expected here. The modeling of soot is still subject to uncertainties: The results show that soot will occur but not what type of soot it will be with respect to particle size, purity or C/H ratio and form. Third, the simulation predicts very high pressures at TDC due to the high argon dilution and soot formation. This may affect the durability of the engine, especially piston rings and valves can be

damaged and soot could settle in the exhaust tract. These technical limitations have to be considered in a practical implementation. Fourth, in this study it is not considered how the gas reaches the inlet state and how the mixture is separated at the outlet. A preheater and compressor as well as the separation of the gas will cause an additional energy input, which will reduce the efficiency of the process.

4.4 Conclusion

The influence of hydrogen on the pyrolysis of natural gas in an energy-storage piston engine was investigated theoretically. A four-stroke single-cylinder piston engine with detailed chemical kinetics was modelled in a single-zone model. To evaluate the process, the storage power expressed by the increase of exergy was calculated for different intake temperatures, intake argon mole fractions and hydrogen contents in the initial natural gas/hydrogen mixture.

The results show that excess energy from renewable sources can be stored by producing higher-exergy chemicals. The maximum predicted storage power is 1.7 kW for a 400 cm^3 cylinder with an intake temperature of 473 K, an intake argon mole fraction of 0.94 and a mixture without additional hydrogen. For these conditions the efficiency has a value of 54%. A methane conversion of 70% is achieved while ethane and propane were completely consumed. The product gas contains hydrogen, acetylene, ethylene and benzene with yields of 54%, 13%, 8% and 9%, respectively. The hydrogen addition influences several parameters: the temperature increases faster while the supplied work is reduced during the compression stroke. In addition, hydrogen leads to higher reaction rates and inhibits the reaction pathways towards benzene and PAH's. In total, this results in an increased methane conversion (77%) and higher yields of hydrogen (58%), acetylene (18%), and ethylene (9%) but to decreased yields of benzene (4%) and PAH's. Overall, this causes the reduction of storage power and efficiency by 6.5% and 2%-points, respectively.

In conclusion, the process of natural gas pyrolysis in a piston engine with respect to chemical energy storage seems feasible and an acceptable storage power and efficiency can be achieved. Even though the addition of hydrogen leads to a slightly decreased storage power, the increased formation of valuable species and the reduced formation of soot precursors seems promising. The hydrogen content in the natural gas grid is therefore not a disadvantage for this process. The piston engine is a technically mature technology that is widely used in large-scale plants. The efficiencies of the process presented here are lower compared to other energy storage technologies, but the low investment costs may compensate this disadvantage. This study also shows that a flexible provision of different forms of energy is possible and therefore this

concept should be further pursued and improved with respect to a sustainable and conscious use of energy.

4.5 Outlook

In this study the production of hydrogen and higher-exergy hydrocarbons in a piston engine was investigated. It turned out to be favourable and a further investigation of a comprehensive process beyond the engine seems worthwhile, but it is beyond the scope of this contribution. In such a concept, compressors and preheaters to reach the input state have to be included. The separation of the product gas mixture can, *e.g.*, be achieved by a membrane, by pressure swing adsorption or by condensation. The inert gas has to be recirculated back into the engine, while the hydrogen and higher hydrocarbons can be stored or used in chemical industry or for electricity generation. The development of such a process concept as well as the thermodynamic, exergetic and economic evaluation of the entire process is part of future work. In addition, the experimental validation of the used engine model and the associated kinetics is also important for further investigations, although it was already proved experimentally in an RCM that the generation of hydrogen and higher-exergy hydrocarbons from methane is possible [95].

4.6 Acknowledgements

This work was supported by the Deutsche Forschungsgemeinschaft within the framework of the DFG research unit FOR 1993 ‘Multi-functional conversion of chemical species and energy’ (Number: 229243862).

5 Exergy storage and CO_2 utilization: A combined approach

The content of this chapter is accepted in Energy Technology:
C. Rudolph, B. Atakan, Dry methane reforming in a piston engine for chemical energy storage and carbon dioxide utilization: Kinetic modeling and thermodynamic evaluation, Energy Technology, (2023), DOI: 10.1002/ente.202201252.

Author contribution
My contribution embraced developing the concept, designing the computer code, conducting the simulations, analyzing and graphing the results, and writing the manuscript. Burak Atakan developed the concept and reviewed the manuscript. He also coordinated the project and acquired funding.

Abstract
The flexible energy conversion in piston engines may offer one possibility for storing energy from renewable sources. This work theoretically explores the engine-based dry methane reforming to convert mechanical energy into chemical energy, achieving a net negative CO_2 balance for this step. The endothermic, endergonic reforming process is activated by the temperature increase during the compression stroke, assisted by a reduction of the heat capacity through dilution with an atomic inert gas, namely argon. This leads to an increase in chemical exergy, as higher-exergy species are produced with small exergy losses while simultaneously consuming CO_2. In this work, the engine-based homogenous dry reforming serves as an flexible power-to-gas process and energy storage solution, presenting an alternative to catalytic processes.
The piston engine is simulated using a time-dependent single-zone model with detailed chemical kinetics, followed by an analysis of thermodynamics and kinetics. With inlet temperatures ranging from 423–473 K and argon dilutions of 91–94 mol%, CH_4 and CO_2 conversion are between 50–90% and 30–80%, respectively, resulting in synthesis gas yields of 45–55% with an H_2/CO ratio ranging 1 to 5. Additionally, higher

hydrocarbons such as C_2H_2, C_2H_4, and C_6H_6 are produced with yields of up to 20%, 10%, and 10%, benefiting the overall process. So, this power-to-gas process allows for exergy storage of up to 3.35 kW/l per cycle with an efficiency of up to 75%.

5.1 Introduction

The world's global warming and the resulting environmental impact are among the most significant challenges to be overcome in future. Therefore, the reduction of CO_2 emissions and the use of alternative energy sources, such as renewable energies or hydrogen as an energy carrier, gain in importance. Carbon capture and utilization technologies can contribute to the decarbonization of the energy system and green energy provision. In this context, dry methane reforming (DMR) is promising since synthesis gas, *i.e.*, hydrogen and carbon monoxide is produced with a negative CO_2 balance for the storage step. This process is CO_2 neutral, even when the gas is released to the atmosphere again [100]. The production of hydrogen is of major interest to the chemical industry and for electricity generation using technologies such as fuel cells or grid balancing applications. Hydrogen production from methane or natural gas (NG) pyrolysis (R5.1) is a CO_2-free method that requires energy input to overcome the reaction energy since it is an endothermic and endergonic reaction.

$$CH_4 \rightleftharpoons C(s) + 2H_2 \qquad \Delta h^0 = 75\ \text{kJ/mol} \qquad \Delta g^0 = 51\ \text{kJ/mol} \qquad \text{(R5.1)}$$

The decomposition of methane or NG can be achieved thermally or catalytically in reactors [81]. These processes often exhibit comparably small efficiencies in industrial scale (<50%) [35]. Also, these processes often encounter challenges associated with undesirable soot deposits [101]. Most of the world's hydrogen is produced by steam methane reforming (SMR) (R5.2) or coal gasification because these technologies are available at industrial scales. The production is quite efficient, with energetic efficiencies above 80% and low costs [36,39,102,103].

$$CH_4 + H_2O \rightleftharpoons CO + 3H_2 \qquad \Delta h^0 = 205\ \text{kJ/mol} \qquad \Delta g^0 = 114\ \text{kJ/mol} \qquad \text{(R5.2)}$$

The conversion of methane and water vapor is also an endothermic and endergonic process, requiring a catalyst to increase the reaction rate. The subsequent water-gas-shift reaction further increases the hydrogen yield (R5.3).

$$CO + H_2O \rightleftharpoons CO_2 + H_2 \qquad \Delta h^0 = -41\ \text{kJ/mol} \qquad \Delta g^0 = -29\ \text{kJ/mol} \qquad \text{(R5.3)}$$

However, unlike DMR where CO_2 is consumed, the SMR process produces CO_2. DMR (R5.4) has thermal efficiencies (< 92%) comparable to SMR, although the energy demand is even higher [100] because both CH_4 and CO_2 have high bond dissociation energies.

$$CH_4 + CO_2 \rightleftharpoons 2CO + 2H_2 \qquad \Delta h^0 = 247\ \text{kJ/mol} \qquad \Delta g^0 = 171\ \text{kJ/mol} \qquad \text{(R5.4)}$$

The reaction can be catalytically activated, and recent investigations have shown promising results with Ni-catalysts despite technical limitations due to coking and catalyst deactivation [103,104]. The development of commercial-scale applications is still in its beginning. Recently, Gossler and Drost et al. [18] investigated the usage of a piston engine for DMR combined with exothermal partial oxidation to produce hydrogen and carbon monoxide. Kinetic simulations were compared with rapid compression machines (RCM) experiments. The initial stage involved optimizing the inlet temperature and pressure, and the gas composition (CO_2, CH_4 and dimethyl ether, and O_2 as an oxidizer to allow a high conversion) to maximize CO_2 conversion. The optimization predicted 50% CO_2 conversion at intake conditions of 462 K and 1 bar and an equivalence ratio of 2.7 for 20 mol% CO_2 in the initial mixture. The addition of O_2 leads to the partial oxidation of CH_4, providing high temperatures to overcome the activation energy. The results were validated through RCM experiments. The authors mentioned the positive effect of the heat loss during the hold time, which lead to quenching of the reaction. However, they also noted that the expansion stroke in an internal combustion engine (ICE) would further increase the CO_2 conversion. A similar study was recently conducted by Drost et al. [105], employing again mathematical optimization to explore CH_4-CO_2 conversion in a piston engine aiming for synthesis gas formation. As presented by Gossler and Drost et al. [18], exothermic reactions lead to a temperature increase, resulting in CH_4 and CO_2 conversion. So, the reasonable equivalence ratio range of 2.5 - 3.5 for CH_4-CO_2 conversion, as found by Gossler and Drost et al. [18], was confirmed by Drost et al. [105]. However, due to the presence of exothermic reactions and the introduction of oxygen within the equivalence ratios of 2.5 – 3.5, the overall process exhibits a negative enthalpy of reaction and a negative Gibbs energy, thus, energy or exergy is not stored in the products.

The flexibility of energy conversion on demand using IC engines, made possible by variable cylinder charges, offers the possibility to use piston engines as chemical reactors for chemical production. This can be achieved through homogeneous partial oxidation, pyrolysis, or dry reforming, presenting an alternative to the catalytic route. The homogeneous process can often convert gas mixtures containing compounds which poison the catalyst (*e.g.*, sulphur-containing compounds) without pre-cleaning. The

feasibility of an IC engine for polygeneration processes and exergy storage has been proven in several publications [58,60,106,107], considering thermodynamics, kinetics, and economics. In polygeneration, methane is partially oxidized at equivalence ratios of up to 7; for exergy storage, methane is pyrolyzed. The products were synthesis gas and higher hydrocarbons. It was shown that exergetic efficiencies of up to 79% were achieved in polygeneration processes and up to 75% in exergy storage processes. The hydrogen costs were calculated for the polygeneration process, showing that they are competitive with SMR processes. Thus, both processes seem quite promising.

The present study ties up in both, the work presented by Gossler and Drost et al. [18] and by Drost et al. [105] and the previous research on polygeneration: Firstly, since the reforming process presented by Gossler and Drost et al. [18] is activated through an exothermic reaction, it should be assigned as autothermal reforming. In the present study, DMR according to (R5.4: $CH_4 + CO_2 \rightleftharpoons 2\ CO + 2\ H_2$) is investigated. The activation energy is overcome at high temperatures after compression. To increase the temperature, an inert gas is used as a dilutant, reducing the heat capacity of the methane and CO_2 containing gas mixture.

Additionally, the relevance of an exergetic analysis gains importance when developing novel concepts such as engine-base dry reforming. The significance of the exergetic analysis is reflected by the fact that all valuable outputs, *e.g.*, heat, work and chemicals are accounted using thermodynamically sound assessment. This implies the first and second law of thermodynamics and includes the differences in the quality of the different energy forms involved in the analysis. While analyzing the engine-based polygeneration concept, as done by Atakan et al. [60] and Banke et al. [58], the comparison of the thermal efficiency and the exergetic efficiency shows that only the latter provides meaningful insights. According to Atakan et al. [60] and Banke et al. [58], fuel-rich driven engines exhibit a thermal efficiency below 20% whereas their exergetic efficiency is above 70%. This leads to the conclusion that engine-based polygeneration is an interesting concept. So, the concept of exergetic analysis will be utilized in this work as well.

The authors in [18] and in [105] focused on the kinetics but did not perform an exergetic analysis. To evaluate the process in the context of polygeneration and exergy storage, it is necessary to consider thermodynamic parameters such as work, exergy loss, and exergetic efficiencies. This gap is addressed here. A parameter study is performed using a time-dependent single-zone model with detailed chemical kinetics. The process is evaluated based on the predicted formation of synthesis gas and higher hydrocarbons, as well as the storage capacities and efficiencies. To achieve this, the inlet temperature, inlet argon mole fraction, and the inlet CO_2/CH_4 ratio were varied. A

kinetic, exergetic, and thermodynamic analysis was performed to compare the results and to evaluate the process.

A schematic of the process is illustrated in Figure 5.1. The system considered in this work primarily focuses on the piston engine as a chemical reactor, as indicated by the system boundary line (red). The piston engine is motored by an electric motor powered by surplus renewable energy. It should be noted that the overall process consists of several subsystems, including the pre-process for providing the feedstock and preheating, the separation process of the product gases involving argon recirculation and heat integration. Separation of the large amounts of argon could be accomplished via a multi-bed pressure-swing adsorption unit [108]. For the separation of H_2, H_2 membranes or pressure swing adsorption units have already proven successful [106]. The separation of higher hydrocarbons like benzene could be realized by a cold trap. To evaluate the potentials of the piston engine as the key process, this work does not evaluate or discuss the pre-processes, the subsequent processes, and the energy supply for motoring the piston engine.

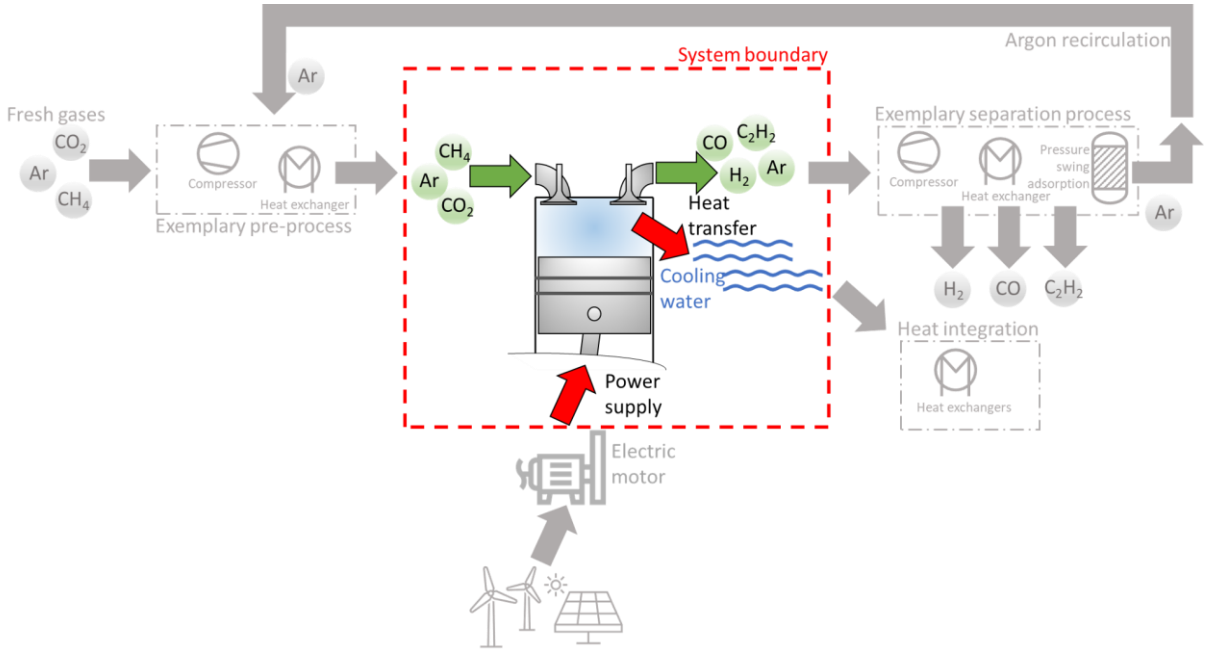

Figure 5.1. Schematic of the process. The system boundary (red) indicates the system evaluated in this work. Grayed-out areas represent superordinate process steps not included in this work.

5.2 Methodology

The simulation of the piston engine was performed using Cantera [61] within Python. The engine model is a time-dependent single-zone model including gas exchange and

working strokes. The piston velocity s_p as a function of time t is determined by equation (5.1):

$$s_p(t) = \bar{s}_p \cdot \frac{\pi}{2} \cdot \sin(2 \cdot N \cdot \pi \cdot t) \cdot \left(1 + \frac{\cos(2 \cdot N \cdot \pi \cdot t)}{\sqrt{R^2 - \sin^2(2 \cdot N \cdot \pi \cdot t)}}\right) \tag{5.1}$$

Here, $\bar{s}_p$ is the mean piston velocity, N is the rotation speed, and R is the ratio of connecting rod length to crank radius.

For every time-step, the energy and species conservation equations for an open system are solved according to eqns. (5.2) and (5.5) using an ODE solver [61]. According to the first law of thermodynamics (equation (5.2)), the change of internal energy U is equal to the work transfer caused by volume change $\frac{dV}{dt}$, heat transfer $\dot{Q}_{HT}$ to the walls and the inflowing and outflowing enthalpies h multiplied by the associated mass flow rates $\dot{m}$.

$$\frac{dU}{dt} = -p\frac{dV}{dt} + \dot{Q}_{HT} + \sum_{in} \dot{m}_{in} \cdot h_{in} - h\sum_{out} \dot{m}_{out} \tag{5.2}$$

The heat transfer through the cylinder walls is determined using Newton's law of cooling (equation (5.3)). The area of the cylinder walls and the cylinder head is indicated by A, and the temperature of the cooling water is indicated by T_{cw}.

$$\dot{Q}_{HT} = \alpha \cdot A \cdot (T_{CW} - T) \tag{5.3}$$

The convective heat transfer coefficient is computed according to the Woschni [63] correlation (equation (5.4)).

$$\alpha = C \cdot d^{-0.2} \cdot p^{0.8} \cdot T^{-0.53} \cdot \left[C_1 \cdot \bar{s}_p + C_2 \cdot \frac{V_d \cdot T_{ref}}{V_{ref} \cdot p_{ref}} \cdot (p - p_{motored})\right]^{0.8} \tag{5.4}$$

Here, the characteristic constants C and C_1 are set according to Woschni [63], and the constant C_2 is set to zero as no combustion occurs. It must be noted that for the simulation of the polygeneration-based biogas combustion in chapter 5.3.4, the constant C_2 is chosen according to the original literature [63]. The index ref indicates a reference condition, following Woschni [63] when the inlet valve is closed.

The change of the mass of each species i ($m\frac{dy_i}{dt}$) is calculated by the generated species through homogeneous gas phase reactions, expressed by $V \cdot \dot{\omega}_i \cdot W_i$, and the inflowing and outflowing mass of the species i ($\sum_{in} \dot{m}_{in}(y_{i,in} - y_i)$). Here, V is the cylinder volume, y is

the mass fraction of the corresponding species, $\dot{\omega}$ is the molar production rate, and W is the molar mass of each species i.

$$m\frac{\mathrm{d}Y_\mathrm{i}}{\mathrm{d}t} = \sum_{\mathrm{in}} \dot{m}_{\mathrm{in}}(y_{\mathrm{i,in}} - y_i) + V \cdot \dot{\omega}_\mathrm{i} \cdot W_\mathrm{i} \tag{5.5}$$

A detailed description of the engine model can be found in previous publications [107,109,110]. The state of the homogenous cylinder charge is calculated for every time-step assuming ideal gas behavior. The thermodynamic gas properties and production rates for each species are calculated using the elementary reaction mechanism PolyMech 2.1 from Zhao et al. [111], based on the work of Porras et al. [17]. The reaction mechanism is validated for fuel-rich oxidation in HCCI engines, emphasizing the formation of synthesis gas and C_2 species. Additionally, the PolyMech 2.1 is comparably small, containing 192 species and 948 reactions up to C_3, which is favorable for comprehensive parameters studies. Nevertheless, a PAH sub-mechanism is included in the PolyMech 2.1 [111] to estimate benzene and soot precursor formation.
The engine and process parameters used in the model are listed in Table 1. The inlet temperature and the inlet argon mole fraction were both varied over a wide range between 298 K and 1273 K and 70 and 99 mol% to determine the optimum conditions with respect to reactant conversion and exergetic efficiency. The inlet pressure was set to 1.2 bar because a lower intake pressure would lead to outlet pressures below 1 bar due to the endothermic reactions and exergy losses, as found in previous studies [107,109]. The CO_2/CH_4-ratio was varied up to 1.5, leading to a changing CO/H_2-ratio in the product gas and effecting work demand, entropy production and product spectrum, shown in the results section.

Table 5.1. Modeling parameter.

Parameter	Value
Inlet temperature T_0 [K]	298 - 1273
Inlet pressure p_0 [bar]	1.2
Inlet argon mole fraction x_{Ar} [mol%]	70 - 99
Inlet CO_2/CH_4 ratio x_{CO2}/x_{CH4} [-]	0/1 – 0.6/0.4
Bore/Stroke [mm/mm]	170/210
Compression ratio ε [-]	22
Rotation speed N [min^{-1}]	1500, 3000

The engine size (see Table 5.1) was chosen according to a typical industrial gas engine [112], which is already used for conventional combined heat and power plants. The engine speed was varied between 1500 and 3000 min^{-1} as the rotation speed affects the flow rate and the time at top dead center (TDC) and thus the time available for the chemical kinetics or chemical equilibrium, as found in [111]. Herein, a relatively high compression ratio of 22 was used for the benefit of the endothermic and endergonic pyrolysis process.
The thermodynamic analysis contains the calculation of the work or power $\dot{W}$, the transferred heat $\dot{Q}_{HT}$ (equation (5.3)), and the entropy production rate $\dot{S}_{irr}$, as explained in previous works [109,110]. As mentioned before, the work transfer is caused by or leads to volume change, so the work is calculated using equation (5.6).

$$\frac{\mathrm{d}W}{\mathrm{d}t} = -p\frac{\mathrm{d}V}{\mathrm{d}t} \tag{5.6}$$

The entropy production rate is determined using the second law of thermodynamics. Entropy production results from the imbalance of the entropy change in the system due to chemical conversion, and entropy change due to heat transfer to the cylinder walls (equation (5.7)).

$$\dot{S}_{\mathrm{irr}} = \dot{m} \cdot (s_{\mathrm{out}} - s_{\mathrm{in}}) - \frac{\dot{Q}_{\mathrm{HT}}}{T_{\mathrm{cw}}} \tag{5.7}$$

Additionally, the exergetic analysis of the process is based on the exergies of heat and work, the exergy losses, and the specific exergy of the reactant and the product gas, respectively [71]. The exergy of work $\dot{E}_W$ is essentially the work or power done or the work or power supplied ($\dot{W}$). In contrast, the exergy of heat $\dot{E}_Q$ is calculated by multiplying the transferred heat $\dot{Q}_{HT}$ to the cylinder walls with the Carnot efficiency (5.8). The temperature of the heat sink is the cooling water temperature T_{cw} of 373 K, and the temperature T is the temperature of the gas mixture at the respective time step.

$$E_{\mathrm{Q}} = \left(1 - \frac{T_{\mathrm{cw}}}{T}\right) \cdot Q_{\mathrm{HT}} \tag{5.8}$$

Irreversibilities of the process due to heat transfer and chemical reactions as well as temperature and pressure changes are quantified by calculating the exergy loss rates (also named exergy destruction rates) via equation (5.9)

$$E_{\mathrm{Loss}} = 298\ \mathrm{K} \cdot S_{\mathrm{irr}} \tag{5.9}$$

The chemical and thermodynamic exergy of each species is calculated using a method presented in [59,107], evaluating the chemical and thermodynamic valence of species i or j at a temperature *T* and a pressure *p*. The stored exergy $\Delta\dot{E}$ is calculated by equation (5.10)

$$\Delta E = m \cdot (e_{out} - e_{in}) \tag{5.10}$$

Here, e_{in} and e_{out} are the specific exergies of reactant and product gas, respectively. It must be noted that the mentioned exergies in the discussion are related to the displacement volume. The exergetic efficiency of the process is defined as the ratio of stored exergy to work demand *W* (eq. 5.11), both integrated along the complete cycle.

$$\eta = \frac{\Delta E}{W} \tag{5.11}$$

The product gas is analyzed by calculating the conversion of CO_2 and CH_4 and the yields of the target species.
The conversion X_j and the yields $Y_{i,j}$ of the respective species are calculated according to eqns. (12) and (13), respectively.

$$X_{\mathrm{j}} = \frac{n_{\mathrm{j,E,0}} - n_{\mathrm{j,E}}}{n_{\mathrm{j,E,0}}} \tag{5.12}$$

$$Y_{\mathrm{i,j}} = \frac{n_{i,1} - n_{i,0}}{\sum_{\mathrm{i}}\left(n_{\mathrm{j,E,0}} \cdot \nu_{\mathrm{j,E}}\right)} \tag{5.13}$$

Here, *n* is the molar amount of each species i or j, and the subscripts E, 0, and 1 are used for educt, inlet, and outlet state, respectively. Also, ν is the number of C or H atoms of each species i or j, whereby all yields except H_2 being referred to C atoms, and the H_2 yield being referred to H atoms.

5.3 Results and discussion

Firstly, a description of the conversion of CH_4 and CO_2 as a function of the inlet temperature, inlet argon mole fraction, and CO_2 fraction is provided. This is followed by a discussion of limits for the inlet parameters. Subsequently, the species formation, exergetic performance, stored exergy and efficiency under the most promising conditions, and their variation along the CO_2 fraction are discussed. Furthermore, the

influence of the rotational speed is shown. Chapter 5.3.4 compares the approach presented here with similar processes already presented in the literature.

5.3.1 Reactant conversion and limitation of the inlet parameters

The conversion of CH_4 and CO_2 is linked to the prevailing TDC temperature, which in turn is affected by various engine and inlet parameters. The effect of the inlet temperature and the inlet argon mole fraction on the TDC temperature and the associated CH_4 conversion are shown in Figure 5.2 (left) for a representative mixture (50% CH_4, 50% CO_2). The selected engine parameters result in TDC temperatures ranging from 1000 K to 5000 K. This corresponds to a CH_4 conversion of 30% to 50% in the range of 1700 K to 1750 K, a CH_4 conversion between 75% and 85% in the range of 1750 K to 1850 K, and a conversion of up to 95% in the range of 1850 K to 2000 K. Similarly, the CO_2 conversion reaches ~30% at temperatures around 1800 K and ~85% at temperatures around 2000 K. These CO_2 conversions align with the results of the experimental work of Rudolph et al. [113], which shows CO formation at temperatures between 1900 K and 2700 K with reaction times of 1.5 to 3 ms. According to Figure 5.2 (left), if a CH_4 conversion of 80% and a CO_2 conversion (not shown) of 50% is targeted, the necessary inlet temperature and the inlet argon mole fraction vary between 298 K and 1000 K and 70% and 97%, respectively. For higher conversions, the necessary inlet temperature and inlet argon mole fraction are shifted almost parallel towards higher inlet temperatures and higher inlet argon mole fractions. High inlet temperatures lead to large irreversibilities, *e.g.*, due to heat losses during the compression-expansion process resulting in much lower outlet temperatures and pressures. High inlet argon mole fractions reduce the mixture's absolute reactant content and, thus, of products. So, the appropriate range of argon mole fraction and inlet temperature to store exergy per mass of CH_4 and the resulting efficiencies are analyzed, as shown in Figure 5.2 (right).
It is seen that the specific stored exergy per CH_4 mass has a maximum between 298 K and 623 K and argon mole fractions between 90 and 99%. Instead, the specific stored exergy (per total mass, not shown) has a maximum between 773 K and 1273 K inlet temperature and argon mole fractions between 86 and 70%. This is because higher inlet temperatures lead to an overall higher temperature level throughout the entire cycle, promoting the formation of higher-exergy species. The described increase of specific stored exergy per CH_4 mass becomes even more evident when considering the stored exergy along the isothermal lines of the TDC temperature and the corresponding constant CH_4 conversion. However, at high inlet temperatures and small argon amounts the physical exergy change and the irreversibly produced entropy are up to 15 times higher compared to small inlet temperatures and high argon amounts. To

provide numerical values for this statement: for an inlet temperature of 473 K and an argon dilution of 0.91, the change in physical exergy and the irreversible entropy-production are Δe_{phys} = -13.5 kJ/kg ($\Delta \dot{E}_{phys}$ = -0.42 kW/l per cycle) and $\dot{S}_{irr}$ = 3.71 W/K/l per cycle. The percentage of entropy production attributed to entropy change of the system due to chemical reaction is 20% and by heat transfer 80%. For an inlet temperature of 973 K and an argon mole fraction of 0.72, the change in physical exergy and the irreversible produced entropy are considerably greater, with Δe_{phys} = -162.8 kJ/kg ($\Delta \dot{E}_{phys}$ = -2.35 kW/l per cycle) and $\dot{S}_{irr}$ = 4.57 W/K/l per cycle. This contrasts with the smaller inlet temperatures, where the fraction of entropy production attributed to entropy change of the system is 28% and due to heat transfer is 72%. This justifies the consideration of the limitation of the inlet argon mole fraction and the inlet temperatures to values between 0.9 and 0.97 and 373 K and 573 K, respectively. Also, this contradictory behavior of the change of the physical exergy and the irreversibly produced entropy between the different conditions is particularly noticeable when regarding the efficiencies ($\eta = \Delta e/w$ (equation 5.11)). Since proportionally less work must be supplied at lower inlet temperatures, the efficiency has a maximum between 298 K and 873 K and 95 mol% and 76 mol% argon. So, the efficiency is slightly shifted to smaller inlet temperatures than the stored exergy.

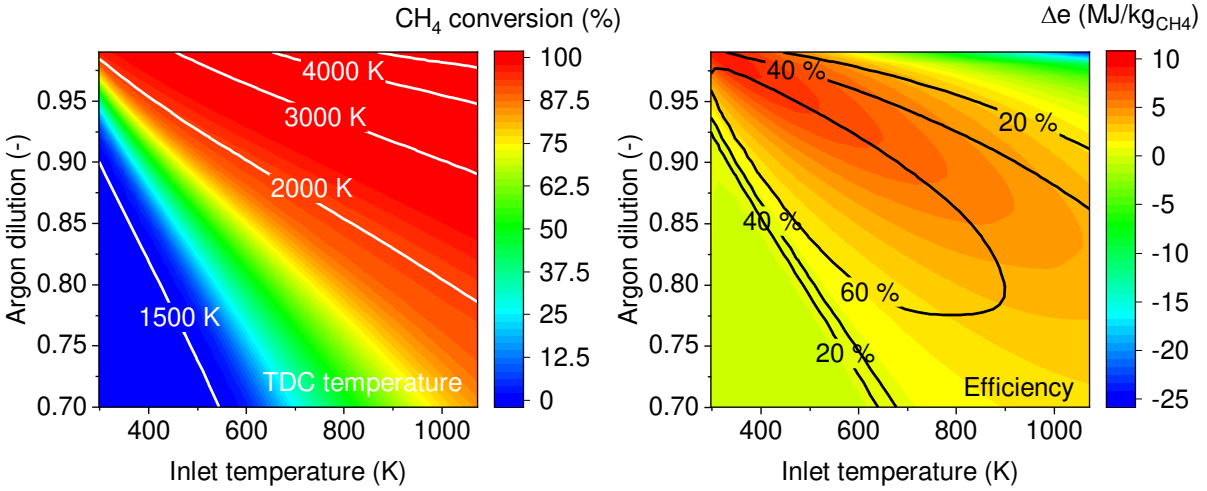

Figure 5.2. Left: CH_4 conversion (colored contour) and TDC temperature (white lines). Right: Specific stored exergy per mass of CH_4 (colored contour) and efficiency (white lines). The results are shown as a function of the inlet argon mole fraction and inlet temperature for a rotation speed of 3000 min^{-1} and 50% CO_2 in the CH_4-CO_2 mixture.

It must be noted that the calculations mentioned above do not consider the required heat of the preheating process to achieve the respective inlet temperature. But an estimation using the change of enthalpy in a non-reacting open system reveals that the efficiency would decrease from ~55% to ~25 when using inlet temperatures above

900 K. In comparison, the efficiency would be relieved only from ~65% to ~58% at inlet temperatures below 473 K.

Figure 5.3 illustrates the resulting optimum of the inlet temperature and the inlet argon mole fraction leading to the overall maximum of the exergetic efficiency for each CO_2 fraction. The large symbols represent the points with the highest efficiencies and the different blue shades and symbols represent the varying CO_2 fractions for each combination of inlet temperature and argon dilution. The most promising inlet conditions in terms of exergetic efficiency are between 423 K and 473 K and 0.91 and 0.94, yielding very high conversions of more than 80% CH_4 and 50-80% CO_2, as shown in Figure 5.3. The most promising conditions are summarized in Table 5.2.

Table 5.2. Most efficient conditions.

CO_2 fraction in CH_4-CO_2 →	0	0.1	0.2	0.3	0.4	0.5	0.6
Inlet temperature T_0 [K]	423	423	448	448	448	448	473
Inlet argon mole fraction x_{Ar} [mol%]	94	94	94	93	93	92	91

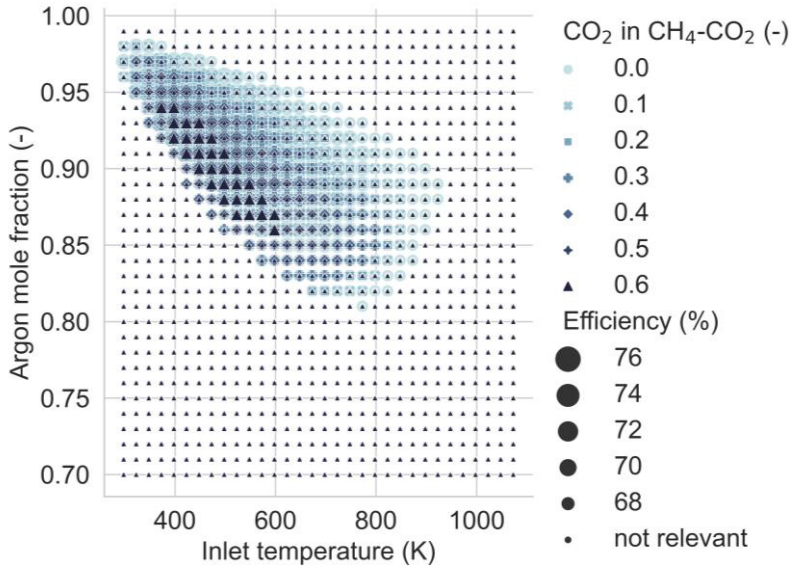

Figure 5.3. Argon mole fraction as a function of inlet temperature for varying CO_2 fractions (blue shades) and varying exergetic efficiencies (symbol size) at a rotation speed of 3000 min^{-1}.

The maximum exergetic efficiencies are between 74% (without CO_2) and 68% (60% CO_2 in CH_4-CO_2). Also, it can be observed that the maximum efficiency without CO_2 addition tends to occur at lower inlet temperatures (423 K) and higher argon mole fractions (0.94). At higher CO_2 fractions (0.5, 0.6), the maximum efficiencies are shifted towards higher temperatures (473 K) and lower argon fractions (0.91). It must be noted that the

volumetric heat capacity at the inlet state varies between 752 J/m³/K and 698 J/m³/K due to changing CO_2 fractions, argon mole fractions, and temperatures. Also, the decrease of the volumetric heat capacity as a function of the temperature along the compression cycle is more pronounced for higher CO_2 fractions, causing the shift towards a smaller required argon mole fraction for higher CO_2 fractions.
The comparison of the conditions found in this work to those in a previous study [107] is summarized in Table 5.3. It must be noted that the engine size plays a significant role with respect to key values such as the storable exergy or the efficiency. However, despite these variations, the comparison reveals the most efficient conditions remain consistent as well as the CH_4 conversion and the H_2 yield.

Table 5.3. Comparison of the present conditions with those in Ref. [107].

	[107]	This work	
T_0 (K)	573	423	573
p_0 (bar)	1	1.2	1.2
d/*s* (mm/mm)	79.5/80.5	170/210	170/210
ε (-)	22	22	22
N (1/min)	3000	3000	3000
x_{Ar} (%)	93	94	93
X_{CH4} (%)	85	71	85
Y_{H2} (%)	63	53	63
Δ*E* (E_{store}) (kW/l)	2.4	2.9	3.1
η (%)	63	74	71
Δe (e_{store}) (MJ/kg_{CH4})	4	3.5	4.4
m_{H2} / m_{CH4} (kg_{H2}/kg_{CH4})	0.16	0.133	0.16
Reaction mechanism	Creck 1412 [114]	PolyMech2.1 [111]	PolyMech2.1 [111]

5.3.2 Product spectra

The conversions, yields, and the resulting distribution of exergy flow rates of the products after the engine cycle as a function of the CO_2 amount in the CH_4-CO_2 mixture, obtained under the conditions shown in Figure 5.3, are depicted in Figure 5.4 (top). As the amount of CO_2 increases, the yields of H_2O and CO increase. In contrast, higher

hydrocarbons, such as C_2H_2, C_2H_4, and C_6H_6, are mainly formed at low CO_2 fractions. Consequently, the C_2H_4 and C_6H_6 yields decrease steadily with increasing CO_2 fractions. However, the C_2H_2 and the H_2 yields show a maximum at 20% CO_2 in the CH_4-CO_2 mixture. This maximum coincides with the higher conversion of CH_4 at that point, shifting the product distribution towards C_2H_2 and H_2. The oxygen atoms from the CO_2 conversion are mainly bound in H_2O. With increasing CO_2 fraction, less hydrogen is available, and more oxygen atoms are bound in CO and H_2O. This reduced availability of C and H limits the C_2H_2 and H_2 formation. Among the changing product gas distribution, the conversion of CH_4 is overall enhanced as oxidation reactions enable the CH_4 decomposition via additional pathways: These pathways include unimolecular decomposition reactions, and reactions with H-atoms versus oxidation reactions as reactions with OH radicals or O atoms. CO_2 decomposition mainly occurs via CO_2 + H, as revealed by a reaction path analysis, so the CO_2 decomposition decreases with increasing CO_2 fraction in the CH_4-CO_2 mixture. It must be noted that no oxygenated product species, such as methanol or formaldehyde, are observed.

The product gas distribution is reflected in the distribution of exergy fluxes of the product gas species, as shown in Figure 5.4 (bottom). The exergy flow rates of CH_4, H_2, and the higher hydrocarbons, C_2H_2, C_2H_4, and C_6H_6, decrease with increasing CO_2 fraction according to the species yields. Similarly, the exergy flow rates of CO_2 and CO increase with increasing CO_2 fraction. As a result of the maximum C_2H_2 yield at 20% CO_2, the stored exergy also exhibits a maximum of 20% CO_2. Moreover, the stored exergy also tends towards lower exergy flow rates with increasing CO_2 fractions. The same tendency is observed, to a lesser extent, in the work supplied, leading to an overall decrease in efficiency from 74% to 68% as the CO_2 fraction increases. In addition, exergy losses increase with increasing CO_2 fraction, primarily due to increased heat transfer and secondly due to greater irreversibilities of the endothermic reactions.

These observations are further confirmed in Figure 5.5, showing a comparison of the relative exergy distribution at inlet and outlet state for each CO_2 fraction. Emphasis is given here on the possibility of storing chemical exergy due to work input, but it also opens the discussion of re-using the unconverted CH_4. In addition, the low exergy losses in this process are emphasized. A key feature is that exergy losses are comparatively low due to the production of entropy by changing the entropy of the system in chemical reactions. In this process, exergy losses are mainly due to heat transfer, with over 80% of the exergy losses attributed to heat transfer. It is also observed that exergy losses increase with increasing CO_2 content, which is due to the increasing occurrence of exothermic reactions. Considering the corresponding proportions of exergy losses due to the chemical reactions in the system and heat transfer, only 4% of the exergy losses are associated with the entropy change of the system when no CO_2 is present in

the initial mixture. Thus, the remaining 96% of the exergy losses are due to heat transfer. When CO_2 levels reach 30% and 50%, the proportion of exergy losses due to entropy change of the system increases to 15% and 19%, respectively, and the remaining 85% and 81% are attributed to heat losses.

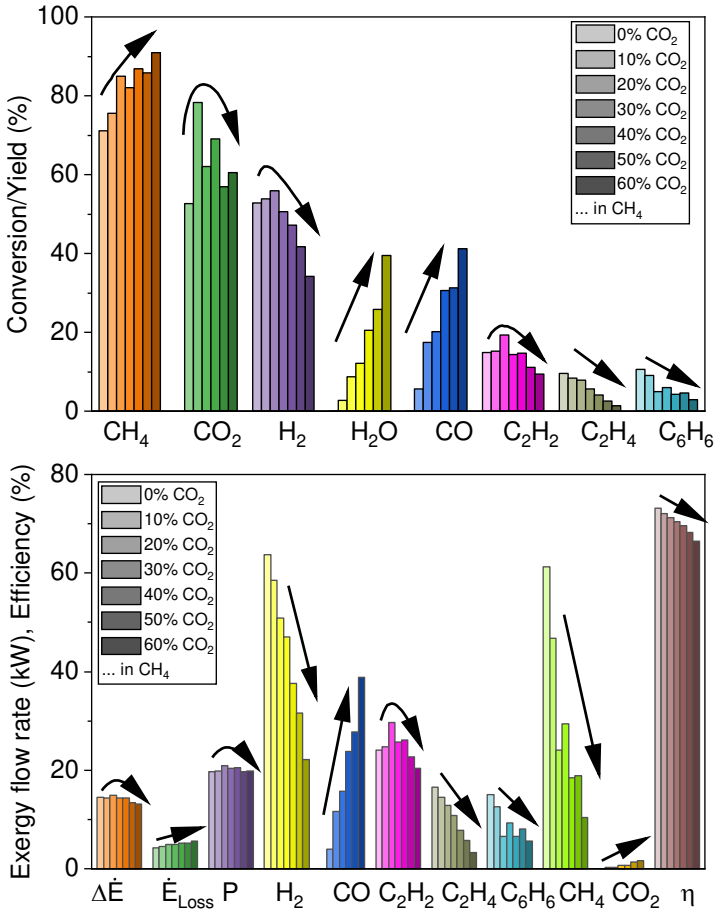

Figure 5.4. Top: Conversion of reactants and yields of target species (H_2, CO, C_2H_2, C_2H_4, and C_6H_6) and H_2O. Bottom: Exergy flow rates of stored exergy $\Delta\dot{E}$, exergy loss $\dot{E}_{Loss}$, power, chemical exergies of species present in the product gas (H_2, CO, C_2H_2, C_2H_4, C_6H_6, CH_4, CO_2) and efficiency. The results are shown as a function of the CO_2 amount in the CH_4-CO_2 mixture for inlet argon dilution and inlet temperature according to Table 5.2, and a rotation speed of 3000 min^{-1}.

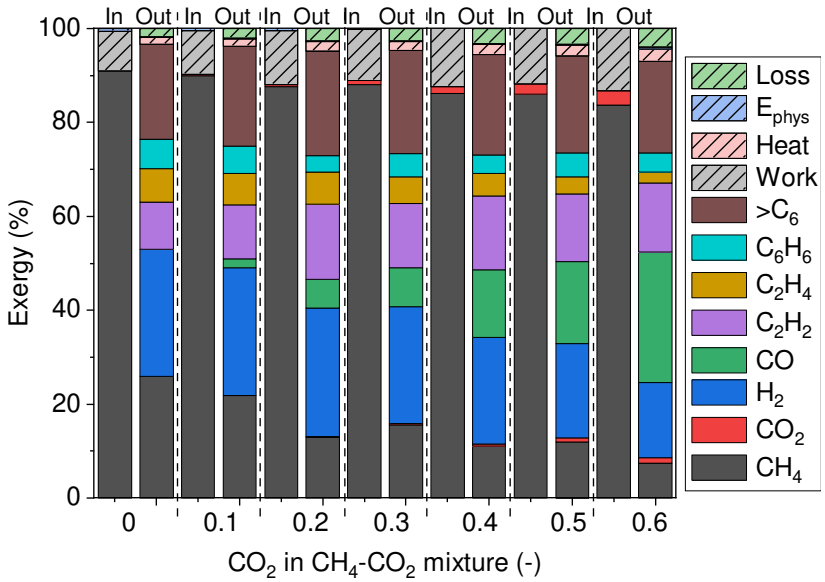

Figure 5.5. Distribution of exergy as a function of CO_2 fraction for the inlet state ("in") and the outlet state ("out"). The results are shown for a rotation speed of 3000 min^{-1}.

Figure 5.6 shows the conversion of the reactants (Fig. 5.6 top-left) and the formation of the target species (Fig. 5.6 top-right and bottom-left), as well as the stored exergy, efficiency, and exergy losses (Fig. 5.6 bottom-right) as a function of inlet temperature and CO_2 fraction for an argon dilution of 93%. The aim is to identify the most interesting conditions for the respective target. Figure 5.6 (top-left) confirms the strong influence of temperature on the conversion of both reactants. The inlet temperature above 423 K is required to achieve adequate conversion of at least 50% CO_2 and 80% CH_4. With increasing CO_2 fraction, a shift towards lower inlet temperatures can be observed due to the increasing exploitation of oxidation pathways. This trend contradicts the findings in Figure 5.3, as the constant argon dilution in this case keeps the temperature-dependent volumetric heat capacity constant. So, the increasing amount of exothermic oxidation reactions result in higher temperatures and pressures at TDC. If the argon dilution and the inlet temperature vary according to the maximum efficiency, as in Figure 5.3, the temperature at TDC increases while the pressure at TDC decreases. This is due to the combined effect of a decreased heat capacity, a higher inlet temperature and the exothermic oxidation reactions. The target species H_2 and CO, depicted in Figure 5.6 (top-right), are the main equilibrium products and their yields reaching a maximum at the maximal temperature. According to Eq. (R5.4: $CH_4 + CO_2 \rightleftharpoons 2\ CO + 2\ H_2$), the maximum H_2 yield is obtained at a CO_2 fraction of 50%. At higher CO_2 amounts, the H_2 yield decreases due to the formation of water in chemical equilibrium. This occurs because there are not enough C atoms available to only form CO, thus, the free O-Atoms are bound in water. In contrast, the CO yield increases with increasing CO_2 fraction and is limited only by the conversion of CO_2. The resulting H_2/CO ratio varies

between 1.4 and infinity for all values, and between 1.4 and 5 if only viable H_2 and CO yields are considered. At 423 K, promising H_2/CO ratios of 4 or 2 are achieved with CO_2 fractions of 0.4 or 0.5, respectively.

The formation of higher hydrocarbons as high-exergy species contributes significantly to the overall feasibility of the process in the context of chemical energy storage. Figure 5.6 (bottom left) illustrates the temperature and CO_2-content dependent formation of these higher hydrocarbons. Generally, their formation is coupled to the absence of oxidation reactions and higher energy input, as their formation reactions are mainly endothermal. Nevertheless, not only high temperatures lead to their formation. Decomposition and recombination reactions of stable "intermediate-temperature" species such as C_2H_4 and C_6H_6 impact the product spectra by transforming into C_2H_2 or PAHs. Hence, the maximum yields of C_2H_4 and C_6H_6 of 15% and 13%, respectively, are found for neat CH_4 mixtures (with argon) at inlet temperatures of 698 K and 423 K, respectively. With increasing CO_2 fraction, their yields decrease to less than 5% due to the dominance of oxidation reactions and the increased formation of CO, H_2, and water (yields up to 45%). The maximum C_2H_2 yield of 85% is located at maximum inlet temperatures and zero CO_2 fractions. Generally, the C_2H_2 yields decrease with increasing CO_2 fraction. Similar to Figure 5.4, the C_2H_2 yield has a local maximum at intermediate temperatures between 400 K and 600 K, and a CO_2 fraction of 0.3 in the CH_4-CO_2 mixture as PAH building reactions and CO building reactions compete for the C_2H_2 consumption at lower or higher CO_2 fractions, respectively.

As key quantities for this process, Figure 5.6 (bottom-right) shows the stored exergy, the exergy loss, and the exergetic efficiency as a function of the CO_2 fraction and the inlet temperature. High inlet temperatures lead to elevated exergy losses due to irreversibilities of the endothermic reactions and high heat losses through the cylinder walls. Also, these endothermic reactions cause a reduction in temperature and pressure at the outlet compared to the inlet state, leading to a reduction of the physical exergy of the cylinder charge. Overall, this leads to a reduction of the storable exergy and efficiency at high temperatures (>800 K) compared to intermediate temperatures (400–800 K). Temperatures below 400 K do not lead to reactant conversion, resulting in small storable exergy values as exergy losses dominate the process through heat losses. The maximum storable exergy of up 3.35 kW/l and the maximum efficiency of up to 75% can be found in an intermediate temperature range (400–800 K) and CO_2 fractions below 0.5 in the CH_4-CO_2 mixture. The location of the maximum is attributed to the formation of high-exergy species in this regime, coupled with comparatively small exergy losses and small reductions in physical exergy. With increasing CO_2 fraction, the storable exergy and the efficiency decrease because of the changing product gas composition and the associated shift to CO and H_2. However, the exergy losses increase

with increasing CO_2 fraction as the elevated occurrence of exothermic oxidation reactions leads to slightly higher in-cylinder temperatures and corresponding heat losses.

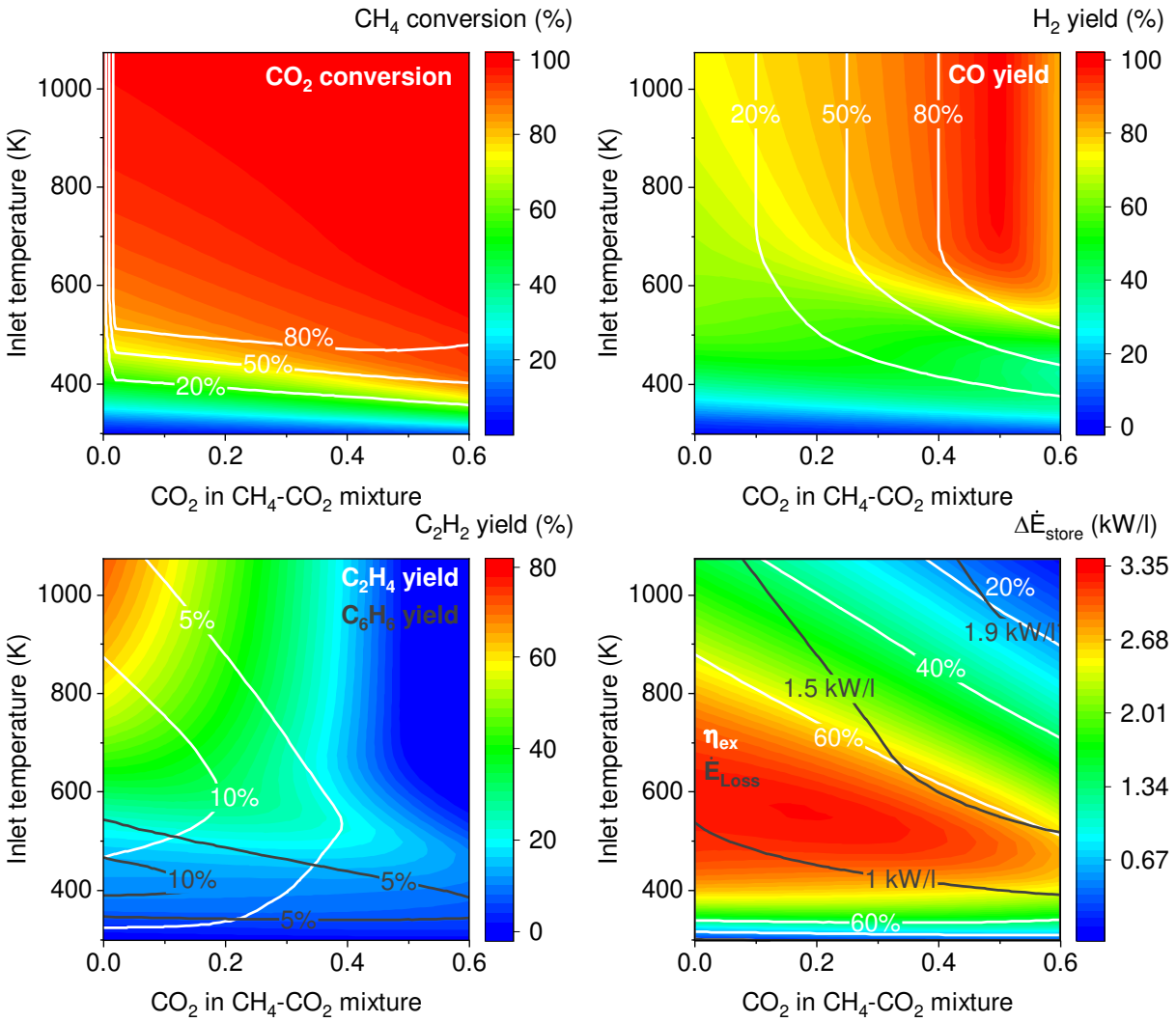

Figure 5.6. Top-left: CH_4 conversion (colored contours) and CO_2 conversion (white lines). Top-right: H_2 yield (colored contours) and CO yield (white lines). Bottom-left: C_2H_2 yield (colored contours), C_2H_4 yield (white lines) and C_6H_6 yield (grey lines). Bottom-right: Stored exergy per displacement volume (colored contours), efficiency (white lines) and exergy losses (grey lines). The results are shown as a function of the inlet temperature and the CO_2 amount in the CH_4-CO_2 mixture for an inlet argon dilution of 93 mol% and a rotation speed of 3000 min^{-1}.

The aforementioned results and maps (*i.e.*, Figure 5.6) are shown for a constant argon dilution of 93 mol%. Figure 5.7 depicts the maximum values for the product yields of H_2, CO, C_2H_2, C_2H_4, and C_6H_6 along with the storable exergy and the exergetic efficiency across all modeled conditions (x_{Ar}, x_{CO_2}, T_0). These values are presented as a function of the TDC temperature and the CO_2 fraction in the CH_4-CO_2 mixture. Overall, the general principles found above can be affirmed by Figure 5.6. The TDC temperature regime between 2000 K and 3000 K is favorable for various applications (energy storage,

power-to-gas processes, or homogeneous dry reforming), targeting species formation, storage capacity (stored energy), or CO_2 decomposition.

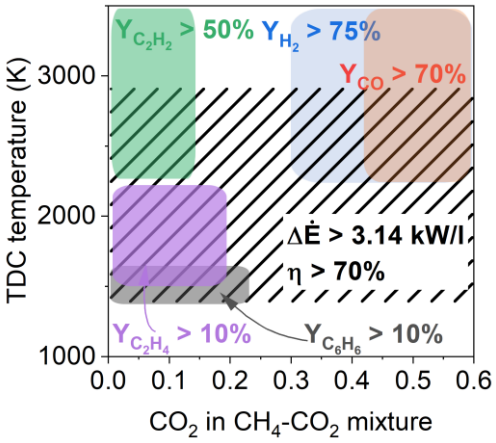

Figure 5.7. Maximum products (H_2, CO, C_2H_2, C_2H_4, C_6H_6), stored exergy and efficiency as a function of CO_2 fraction and TDC temperature for various inlet temperatures and argon dilutions. Different colors represent different species: green C_2H_2, blue H_2, red CO, purple C_2H_4, grey C_6H_6, and hatched stored exergy and efficiency. The maximum yields for each species are C_2H_2 > 50%, H_2 > 75%, CO > 70%, C_2H_4 > 10%, C_6H_6 > 10% and the maximum stored exergy and efficiency are > 3.14 kW/l and > 70%.

5.3.3 Influence of the rotation speed

Figure 5.8 left and right, respectively, shows the influence of the inlet argon dilution and the rotation speed on the CO_2 and the CH_4 conversion, the stored exergy, the efficiency, and the product yields for an intake temperature of 473 K and a CO_2 amount of 50 % in the CH_4-CO_2 mixture. As shown before, the conversion of CO_2 and CH_4 mainly depends on the in-cylinder temperature and the argon dilution, with a minor influence of the rotation speed. The conversion of CH_4 and CO_2 increases with increasing argon dilution. A maximum conversion of > 90% can be achieved with at least 95 mol% argon due to the increasing temperature rise during compression. However, reasonable high conversions of >80% (CH_4) and >50% (CO_2) is achieved for 90 mol% argon. Comparing the rotation speed of 1500 min^{-1} and 3000 min^{-1}, the conversion of CH_4 and CO_2 is higher at the lower rotation speed due to longer reaction times at TDC. The stored exergy and the efficiency have a maximum at 92 mol% argon because of the low conversion at lower levels and the decreasing fuel/dilutant ratio at higher levels. Lower rotation speeds lead to increased stored exergy caused by the increased conversion and the associated formation of useful species. However, this causes an increase in the amount of work required for compression, which leads to a reduction in efficiency at lower speeds.

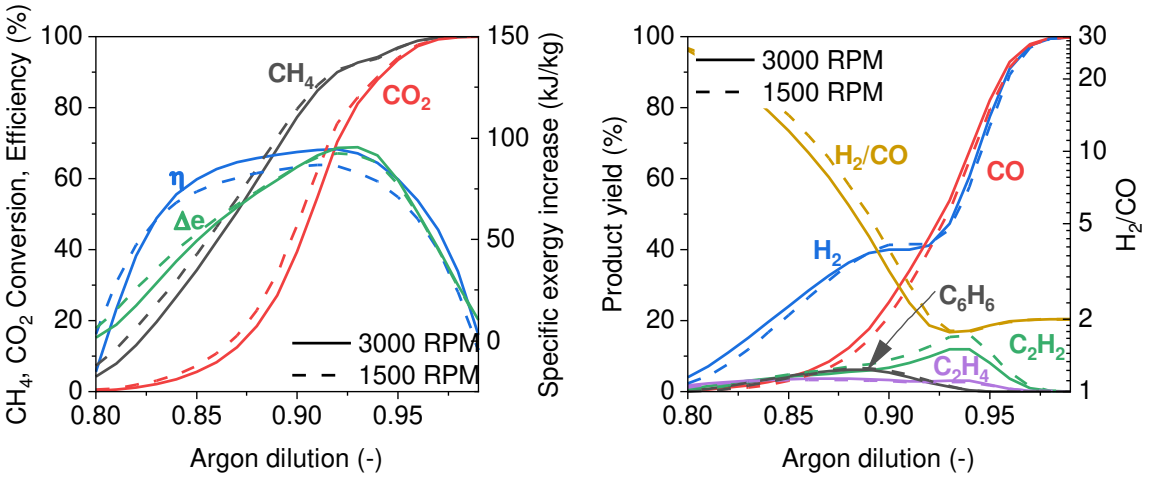

Figure 5.8. Left: CH_4 and CO_2 conversion, and efficiency (left axis) and stored exergy (right axis). Right: Yields of target species and H_2/CO ratio (right axis). The results are shown as a function of the inlet argon mole fraction and for different rotation speeds (3000 min^{-1} (solid line) and 1500 min^{-1} (dashed line)), for an intake temperature of 473 K and a CO_2 amount of 50% in the CH_4-CO_2 mixture.

As depicted in Figure 5.8 right, the formation of H_2 and CO increases with increasing argon dilution. This is, because at higher in-cylinder temperatures the product gas composition is shifted towards the equilibrium composition according to reaction (R5.4: $CH_4 + CO_2 \rightleftharpoons 2\ CO + 2\ H_2$). At 87 mol% argon dilution, the H_2 yield exhibits a peak influenced by the maxima of C_2H_4 and C_6H_6 and the increased formation of C_2H_2, binding the available H atoms. The formation of C_2H_2 and C_6H_6 have maxima at 94 mol% and 89 mol%, respectively. At low to medium temperatures, C_2H_4 and C_6H_6 are more stable and persist, while C_2H_2 decomposes. At high temperatures, C_2H_2 is increasingly formed due to the decomposition of C_2H_4 and C_6H_6. The H_2/CO ratio is between 30 and 10 for an intake argon dilution up to 87 mol% argon due to the low conversion and H_2 and CO formation. With further increase in conversion, the H_2/CO ratio decreases until it reaches nearly 2 for >93 mol% argon, which is quite favorable for some processes. Increasing the rotation speed from 1500 min^{-1} to 3000 min^{-1} slightly shifts the higher hydrocarbons towards lower argon dilutions, as their decomposition is inhibited due to faster quenching. But especially the formation of C_2H_2 at high argon dilutions undergoes an increase at lower rotation speeds. Overall, the effect of the rotation speed on the reaction kinetics is negligible, but the increased flow rate at higher rotational speeds can be utilized.

5.3.4 Comparison with alternative processes

To compare the dry reforming process in this work with reforming processes presented by Gossler et al. [18], and Banke and Kaiser [115], engine simulations were performed for two mixtures: CH_4-CO_2-air and CH_4-CO_2-oxygen. The simulations covered equivalence ratios Φ between 1 and 100 with a constant CH_4-CO_2 ratio of 1 and air defined as 21% O_2 and 79% N_2. The CH_4-CO_2-air mixture did not contain argon to initiate the reaction. However, the inlet temperatures were varied between 323 K and 773 K to ensure the ignition. Also, as Gossler et al. [18] proposed, a comparably low rotation speed of 600 min^{-1} is used for the air-enriched reforming simulations. The results of the air-enriched reforming were analyzed according to the exergetic analysis described above. The exergy distribution contains the work done, the exergy of heat, the exergy losses, and the chemical exergies of the species present at the outlet after the engine cycle. These exergy distributions are compared with those received by the engine-based conversion of 50% CH_4/50% CO_2 mixtures diluted with 93 mol% argon at T_0 = 423 K and 3000 min^{-1}. The comparison is depicted in Figure 5.9a. At equivalence ratios of 1, the process mainly provides work, but significant exergy losses are observed due to the heat release during combustion and heat losses through cylinder walls. With increasing equivalence ratio, both, exergy loss and work output decrease, consistent with the findings explained by Atakan [116]. At equivalence ratios above 3, the exergy distribution includes syntheses gas (H_2 and CO) as well as higher hydrocarbons and PAHs. However, the exergetic portion of the unconverted reactant, particularly CH_4, becomes more significant as the equivalence ratio increases. At the latest, at equivalence ratios of 5, it accounts for about half of the total exergy, diminishing the effectiveness of the air-enriched reforming process.

According to Banke and Kaiser [115], substituting air with oxygen is promising as stable operation can be achieved over a wide range of CO_2 fractions. This is because flame velocities are sufficiently high to enable stable spark ignition. Since the use of CH_4-CO_2-oxygen mixtures under fuel-rich conditions, allows the very fuel-rich operation in SI engines, the exergetic outcome is also compared. The results are shown in Figure 5.9b. Generally, there is a slight shift of the synthesis gas yield towards higher equivalence ratios along with a shift of the PAH region towards equivalence ratios above 3. However, beyond equivalence ratios of 3, there are no other differences between the exergy distributions of CH_4-CO_2-air mixtures and CH_4-CO_2-oxygen mixtures. While there are only minor differences observed from an exergetic perspective, the economic perspective may lead to different results.

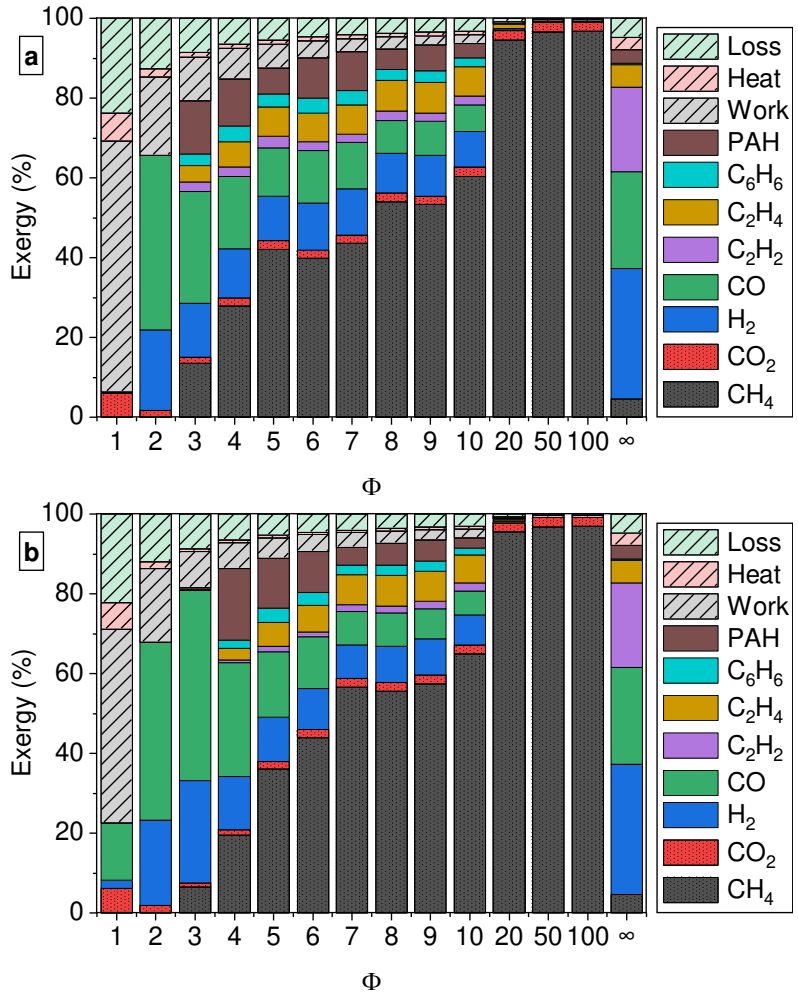

Figure 5.9. Distribution of exergy during engine-based conversion of 50% CH_4/50% CO_2 mixtures with addition of air (a) or oxygen (b) as a function of equivalence ratio (x_{Ar} = 0, 323 K<T_0<773 K, 600 min^{-1}) (comparable with [18]) compared to engine-based conversion of 50% CH_4/50% CO_2 mixtures presented in this work (assigned as Φ = ∞, x_{Ar} = 0.93, T_0 = 423 K, 3000 min^{-1}).

In contrast, the typical dry reforming process (without air) is characterized by comparatively low exergy losses and remarkable contributions of the chemical exergies of H_2, CO, C_2H_2, and C_2H_4 along with less chemical exergy of the unconverted reactant. This interesting exergy distribution makes the process presented here an attractive alternative to the approach suggested by Gossler et al. [18] and Banke and Kaiser [115].
Overall, the engine-based dry reforming presented in this work seems promising 1) due to the on-demand formation of H_2, CO, and interesting amounts of higher hydrocarbons, 2) the consumption of CO_2 with up to 80% conversion and 3) this process is associated with significantly lower exergy losses than comparable processes. However, one challenge to overcome is the reduction of argon without incurring high chemical irreversibilities or heat/exergy losses.

5.4 Conclusions

Homogeneous dry methane reforming in a piston engine, driven by excess energy from renewables, was theoretically investigated as a novel approach in the context of energy storage coupled with carbon capture and storage technologies. The piston engine was modeled as a time-dependent single-zone model with detailed chemical kinetics. A detailed kinetic, thermodynamic, and exergetic analysis was performed to assess the feasibility of the process with respect to stored exergy, efficiency, methane conversion and CO_2 usage. The conversion of the reactants, CH_4 and CO_2, and the yields of the target species, H_2, CO, C_2H_2, C_2H_4, and C_6H_6, along with exergy flow rates of work, heat transfer, exergy losses, and chemical exergy, were calculated. Inlet parameters such as temperature and composition of the inlet mixture were varied between 298 and 1273 K, 70 – 99 mol% argon, and 0 – 60 mol% CO_2, respectively, to gain a thorough understanding of engine-based dry reforming.

A respective minimum TDC temperature is required to initiate the reaction during compression. By contrast, excessively high TDC temperatures lead to large exergy losses. So, a reasonable TDC temperature range is limited to 1700-3000 K. Considering the CH_4 conversion, CO_2 conversion, and efficiency, suitable inlet temperatures and argon dilutions range between 91 mol% and 94 mol% and 423 K and 473 K, respectively. These values vary with the CO_2 fraction in the initial mixture.

The CO_2 addition shifts the product gas composition from H_2 and higher hydrocarbons (no CO_2, pure CH_4 pyrolysis) towards H_2, CO, and water. In this context, C_2H_2 has a key function, contributing to the formation of PAHs or soot precursors at small CO_2 fractions (≤ 0.1) and the formation of CO at high CO_2 fractions (≥ 0.4). At intermediate CO_2 fractions (0.2, 0.3), the carbon from C_2H_2 remains in a loop of decomposition and formation of C_2H_2.

The CH_4 conversion is enhanced with increasing CO_2 fraction, as the presence of O-atoms or OH radicals promote oxidation reactions. The CO_2 conversion mainly occurs via CO_2 + H, so the presence of H-atoms limits the CO_2 conversion, and a maximum CO2 conversion is found for intermediate CO_2 fractions (0.2, 0.3). Also, on-demand production of species is possible by choosing the appropriate conditions: Maximum yields for H_2, CO, C_2H_2, C_2H_4, and C_6H_6 are presented, and their most promising formation-conditions are identified using a product map that considers various conditions of argon dilution, inlet temperature, and CO_2 fraction. The formation of products with higher exergy than the reactants increases the exergy of the cylinder charge by up to 3.35 kW/l (up to 185 kJ/kg), resulting in storable exergy (per supplied work) efficiencies of up to 75%. The storable exergy and the efficiency are slightly reduced with increasing CO_2 fraction as the product spectra are shifted towards H_2 and CO. In addition, exergy

losses are increased. Despite the lower storable exergy, a promising CO_2 conversion of 85 % can be achieved. Finally, a compromise between these two possible targets must be found.

A comparison with alternative approaches proposed by Gossler et al. [18] and Banke and Kaiser [115], showed that this process could be an attractive alternative due to its low exergy losses and simultaneously promising high exergy throughputs of H_2, CO, C_2H_2, and C_2H_4. But, the needed high amount of argon is challenging with respect to a subsequent separation of H_2 and CO. Overall, this novel approach could be promising in terms of flexible species production, storable exergy, and efficiency with simultaneous CO_2 utilization. However, experimental verification and economic assessment is necessary next.

5.5 Acknowledgements

This work was supported by the Deutsche Forschungsgemeinschaft within the framework of the DFG research unit FOR 1993 “Multi-functional conversion of chemical species and energy”, Project Number 229243862.

6 Kinetics of dry methane reforming: Experimental validation

The content of this chapter was published in Proceedings of the Combustion Institute: *C. Rudolph, C. M. Grégoire, S. P. Cooper, S. A. Alturaifi, O. Mathieu, E. L. Petersen, B. Atakan, Shock-tube study on high-temperature CO formation during dry methane reforming, Proceedings of the Combustion Institute, (2022), DOI: 10.1016/j.proci.2022.08.005.*

Author contribution

My contribution embraced developing the concept, performing and post-processing the experiments, processing the raw data, conducting the simulations, analyzing and graphing the results and writing the manuscript. Claire M. Grégoire contributed significantly to the conduction of the experiments and the analysis of the raw data. Claire M. Grégoire, Sean P. Cooper, S. A. Alturaifi, Olivier Mathieu, Eric L. Petersen and Burak Atakan contributed to the interpretation of the results and reviewed the manuscript. Eric L. Petersen and Burak Atakan developed the concept, coordinated the project, provided the laboratories, and acquired funding.

Abstract

The use of natural-gas-fueled combustion engines at unusual operating conditions to provide electrical and/or chemical energy on demand emphasizes the need for fundamental research on decomposition and formation of base chemicals at these conditions. In this work, the CO formation behind reflected shock waves from the pyrolysis of CO_2/CH_4 mixtures was investigated for the first time in the context of engine-based dry methane reforming, to understand the interaction of CO_2 and CH_4 at high temperatures and to test the validity of literature reaction mechanisms. Different CO_2/CH_4 mixtures at atmospheric pressure and temperatures between 1900 K and 2700 K were investigated. Time-resolved CO measurements were performed by laser absorption using a quantum cascade laser.

With increasing CO_2 addition later reaction onset was observed, showing a reduction

in the overall reactivity. Rate of production and sensitivity analyses highlight competing reactions in the pyrolysis and oxidation pathways and that the number of available H radicals is limited, which is attributed to the reduced reactivity. However, the analysis shows that CO_2 is also a source for OH radicals (via $CO_2 + H \rightleftharpoons CO + OH$), which enhance methane decomposition. The comparison with literature reaction mechanisms showed that none of the tested mechanisms can perfectly predict the time-resolved CO formation, highlighting the need for the validation of detailed kinetics models under nontypical conditions.

6.1 Introduction

Global warming and the resulting impacts on the environment are among the greatest current challenges of our civilization. Accordingly, goals such as the reduction of CO_2 emissions and the use of alternative energy sources, *e.g.*, renewable energy or hydrogen as an energy carrier, gain importance. Innovative processes are under development to create a sustainable and (net) CO_2-free future. However, one solution for the transition process could be the use of natural gas-fueled internal combustion engines under polygeneration [14,58] or energy storage [107] conditions. As described in a recent review by Atakan et al. [60], the advantages include technical maturity and durability, as well as flexibility, since the cylinder charge can be adjusted to the energy demand only by varying the equivalence ratio (Φ). This flexibility leads to the possibility of providing power ($\Phi \leq 1$); power, heat and syngas simultaneously in a polygeneration process ($\Phi > 1$); or storable chemical energy in high-energy chemicals ($\Phi \rightarrow \infty$).
Additionally, reforming processes can be considered. With the net reaction equation ($CH_4 + CO_2 \rightleftharpoons 2CO + 2H_2$) and the prospective free enthalpy at standard conditions (Δg^0 = 172 kJ/mol), the reforming process is an endergonic process, producing syngas while at the same time having net negative CO_2 production. Therefore, it can be associated with energy storage processes (similar to [107]) that convert mechanical energy to storable chemical energy. Unfortunately, there is a limited number of studies following this approach, however, most research on dry reforming is based on catalytic- or plasma-activated dry reforming. Gossler et al. [18] investigated the dry reforming combined with partial oxidation of methane in a rapid compression (expansion) machine. To assess the general feasibility of the process and to find promising initial conditions, an optimization, targeting the CO_2 conversion, was carried out before the experiments. The optimization yielded 50% CO_2 conversion at ~2000 K for a mixture with a 40%/20% CH_4/CO_2 ratio (molar) at Φ = 2.8. The additional oxygen is used to initiate the oxidation of methane providing an increase in temperature and radicals to enhance the CO_2

conversion. Additionally, the optimized conditions were tested in RCM experiments, and general agreement was observed.

However, the modeling of such processes is always limited to the accuracy of the kinetics and thermodynamics of the model. In particular, kinetic models are often not validated for engine-based energy storage and reforming processes. While the kinetics of the partial oxidation of methane and methane/additive mixtures with respect to polygeneration was investigated several times, and a comprehensive understanding was gained [117,118], only a few kinetic-focused studies are available for methane pyrolysis or dry methane reforming in the context of energy storage. Nativel et al. [52] investigated the methane pyrolysis related to energy storage in a shock tube and provided profiles of target species such as C_2H_2 at engine-like conditions. Comparison of their experimental data with various elemental reaction mechanisms showed good agreement for CH_4 decomposition by all mechanisms, but greater scatter in the prediction of the products. Overall, the authors stated that the mechanism of Cai and Pitsch [119] delivers the best performance.

The kinetics of CO_2 formation have been widely investigated since it is one of the most common combustion products. In contrast, in the context of oxy-fuel combustion, the chemical effect of CO_2 in the fuel has also been addressed. Bagheri et al. [120] recently published a kinetic study on oxy-methane combustion, targeting the understanding of combustion characteristics and pathways. They pointed to an important role of the bath gas (CO_2), through its effect on boundary conditions such as reaction initiation (*e.g.*, by generating low-reactivity radicals), but also through its effect on retarded ignition delay times and flame speeds. Similar findings were also presented by Koroglu et al. [121], who investigated ignition delay times of oxy-methane in shock tubes. They also observed slower burning rates and longer ignition delay times caused by a reduced OH formation via $O_2+H \rightleftharpoons OH+O$ since the CO_2 decomposition via $CO_2+H \rightleftharpoons CO+OH$ competes for the H radicals; it is also caused by the increased heat capacity.

However, recent studies on oxy-methane combustion are related to fuel-lean combustion processes and therefore are not comparable with the methane dry reforming process at piston-engine-like conditions. The extent to which the chemical kinetic effect of CO_2 on methane can be compared must be determined. To close this gap, we performed a shock-tube study on the CO formation during the thermal decomposition of CO_2/CH_4 mixtures with different CO_2 blends, at atmospheric pressure and temperatures between 1900 K and 2700 K. The scope of this study was to address and to understand the interactions of CO_2 and CH_4 at temperature conditions encountered in engine-based reforming processes, and to identify key reactions which have the greatest impact on modeling results. Additionally, several elementary reaction mechanisms were

tested with respect to their validity at these conditions. Provided first is a summary of the experimental apparatus and measurement techniques, followed by details on the chemical kinetic model calculations. The results from the experiments are presented and discussed, including an analysis of the important chemical kinetic pathways and future work that is needed.

6.2 Experimental methods

6.2.1 Shock tube

A stainless-steel shock tube was used to perform atmospheric pressure CO laser absorption measurements at elevated temperatures. The driver section has an inner diameter of 7.62 cm and a length of 3.15 m and is separated from the driven tube by the diaphragm section. The driven section has an inner diameter of 16.2 cm and a length of 7.88 m. The diaphragm used in this study was a 0.25-mm-thick polycarbonate diaphragm providing pressures behind the reflected shock wave of 1±0.2 atm. Also in the diaphragm section on the driven side is a cross-shaped cutting blade, which supports diaphragm opening and prevents diaphragm fragments. To ensure the most efficient formation and propagation of the shock wave, helium was used as the driver gas. Along the driven tube up to sidewall measurement location, four piezoelectric pressure transducers (PCB P113A22) detected the pressure of the incident shock wave, allowing the calculation of the incident shock wave speed. The sidewall is located 1.6 cm from the endwall and has an additional piezoelectric pressure transducer to measure the sidewall pressure. The incident-shock velocity at the endwall is extrapolated using the previously determined incident shock wave velocities via a curve-fit. This determination of the shock speed allows for the calculation of T_5 and P_5, the temperature and pressure behind the reflected shock wave, using the one-dimensional shock wave equations within uncertainties of ±0.8% and ±1%, respectively [122]. Additionally, at the sidewall location two sapphire optical window ports enable CO laser absorption measurements. Test times between 1.75 and 3 ms were observed due to changing arrival times of the expansion wave and variable contact surface interactions.

Before performing experiments, the whole shock tube facility is evacuated to 10–5 Torr using a turbomolecular turbopump (Agilent Turbo V1001 Navigator). To obtain a homogeneous premixed gas mixture, the test gas mixture is manometrically prepared in a separate tank. The test-gas mixture consisted of high-purity gases with purities of 99.999% (Ar, He), 99.97% (CH_4) and 99.99% (CO_2) provided by Praxair. The dilutant consisted of 20% He and 80% Ar which enabled rapid collisional relaxation for CO, as described in detail in [123]. Different CO_2 blends in CH_4 were used to understand the kinetics of the CO_2 influence on the CO formation in the dry methane reforming

process and to validate elementary reaction mechanisms specified in Section 6.3. The CO_2 fractions investigated herein were chosen according to two considerations: 1) According to the net reaction and the associated Gibbs energies, up to 50% CO_2 seems to be reasonable with respect to energy input and CO_2 conversion. 2) This work is connected to engine-based polygeneration and energy storage processes working with natural gas and biogas, which usually consist of 25–50% CO_2 and 50–70% CH_4. The targeted temperature range was between 1937 K and 2676 K at atmospheric pressure to find both the reaction onset and the maximum CO formation, which is directly linked to the maximum CO_2 conversion. Atmospheric pressure experiments were performed to start the investigation under these unusual conditions at a simpler stage and for the benefit of the laser absorption measurements. The investigated conditions can be found in detail in Table 6.1.

Table 6.1. Mixture compositions and measurement conditions.

Mixture (CH_4/CO_2)	Mole fractions (%)				Temperature T_5 (K)	Pressure P_5 (atm)
	Ar	He	CH_4	CO_2		
90/10	79.000	20.252	0.673	0.075	2002–2450	1.11–0.92
75/25	79.333	19.916	0.564	0.187	2008–2561	1.12–0.81
50/50	79.436	19.820	0.372	0.372	1937–2676	0.78–1.13

6.2.2 CO Laser diagnostic

The CO laser absorption measurements were performed using a quantum cascade laser. The wavelength was set to 4.8 µm, which enables the monitoring of the P(20) line of the 1←0 band at 2059.91 cm^{-1}. To obtain the maximum absorption strength, a removable cell containing a CO/Ar mixture (10% CO and 90% Ar) is used to center the laser beam to the peak of the P(20) line using the following controller conditions: 30°C and ~196 mA. This method was used according to the work from Spearrin et al. [124]. The laser beam is split when it passes a 50/50 beam splitter: a part of the laser beam with its incident intensity I_0 is directly detected, while the second part of the laser beam passes through the reactive mixture within the shock tube, where the transient intensity I_t is also detected. It must be noted that both beams pass a bypass filter, irises, and lenses before being detected. The Beer-Lambert law (Eqn. 6.1) is used to calculate the CO mole fraction x_{CO} based on the time-resolved intensities I_0 and I_t:

$$\frac{I_t}{I_0} = \exp(-k_\nu \cdot x_{CO} \cdot P \cdot L). \tag{6.1}$$

Here, k_ν is the absorption coefficient, P is the total gas pressure, and L is the path length or rather the distance between the sapphire window ports. The temperature-dependent absorption coefficient equation for k_ν was determined with a typical calibration method using 2000 ppm CO in 20% He and 80% Ar within the temperatures 1180 K to 2709 K.

$$k_\nu = 23.9 \cdot \exp\left(-0.000649 \cdot T_5\right). \tag{6.2}$$

The corresponding pressure ranges from 0.87 to 1.38 atm, which is in the range of the present experiments as the same diaphragm type was used. Additionally, the effect of pressure variation on the absorption coefficient is considered in the uncertainty. Uncertainties of the CO mole fraction result is 5%. Additional information on the spectroscopic diagnostic can be found in the supplemental material.

6.3 Modeling

The shock-tube simulation was performed using the zero-dimensional batch reactor model in Chemkin Pro 21.2 [125] with a constant-volume assumption. Five different elementary reaction mechanisms were used in this study, and a summary of these can be found in Table 6.2. The selection of these mechanisms was made because they are all very different (among others: reduced to very comprehensive, different chemistry data sets, etc.) and yet could provide good predictions based on their validation for the experimental data in this study.

Table 6.2. Elementary reaction mechanisms used in this study.

Name	Species	Reactions	Ref.
PolyMech2.1	192	948	[111]
FFCM	38	291	[126]
NUIGMech1.1	923	5966	[127]
CRECK C_1-C_3	114	1999	[67]
Cai&Pitsch	335	1610	[119]

The PolyMech2.1 [111] is an elementary reaction mechanism based on the mechanism from Porras et al. [17] containing C_0-C_6 species and additionally incorporates a PAH sub-mechanism. This mechanism was developed for fuel-rich polygeneration and energy storage processes and is widely validated for species profiles and ignition delay

times using plug-flow reactors, shock tubes, rapid compression machines, and flames, showing reliable results. The Foundational Fuel Chemistry Model (FFCM) [126] is a reduced fundamental reaction mechanism containing C_0-C_2 species for the prediction of the fuel-lean or stoichiometric combustion of foundational fuels such as methane, syngas, or hydrogen and is validated against species profiles in flow reactors and shock tube, ignition delay times, and flame speeds.
The NUIGMech1.1 mechanism developed by Wu et al. [127] is a very comprehensive mechanism for a wide range of different fuels from H_2 and syngas to n-heptane, especially for high-temperature chemistry. Also, the validation covers a wide range of fuels and equivalence ratios (0.1-100) in all established types of validation experiments. The elementary reaction mechanism from Ranzi et al. [67] (CRECK C_1-C_3) contains high-temperature chemistry for C_1-C_3 fuels such as syngas or natural gas surrogates or oxygenated species. The reaction mechanism from Cai and Pitsch [119] is a reduced mechanism, developed for the combustion of primary reference fuels especially for the prediction of PAHs and validated against ignition delay times and flame speeds. Although this mechanism seems inappropriate at first glance, it has nevertheless shown to make good predictions in similar studies such as the investigation of the energy storage related methane pyrolysis in shock tubes performed by Nativel et al. [52].

6.4 Results and discussion

In this section, the CO formation as a function of temperature and time is presented and compared to model predictions. A reaction path analysis was performed to understand the influence of different CO_2 blends on the species formation. The pressure and CO time histories of each data point presented in this work can be found in the supplementary material. Selected representative conditions are shown here for comparability.
Figure 6.1 shows representative experimental CO time histories along with the corresponding computed profiles for a low- (~2000 K), medium- (~2210 K) and high-temperature (~2460 K) regime for all investigated CO_2 blends. In the low-temperature regime, the CO mole fraction increases nearly linearly after a short time lag, but does not reach chemical equilibrium during the respective test time. This behavior occurs for every CO_2 blend, however, the higher the CO_2 amount, the later the reaction onset can be observed. According to the models, no CO_2-to-CO conversion would be observed for a 100% CO_2 blend, which implies an enhancement of the CO_2 decomposition through CH_4 addition. Therefore, the 100% CO_2 blend was not measured as this condition is not of interest to engine-based energy storage and reforming concepts. This result is also in accordance with the later reaction onset. With increasing temperature,

the reaction onset occurs earlier, and the CO curve approaches a logarithmic behavior, reaching an asymptotic value. However, the increasing CO_2 amount still leads to a later reaction onset, which is detailed below. The obtained CO mole fraction increases with higher CO_2 amounts (because CO_2 is the only source for O atoms) as well at any temperature.

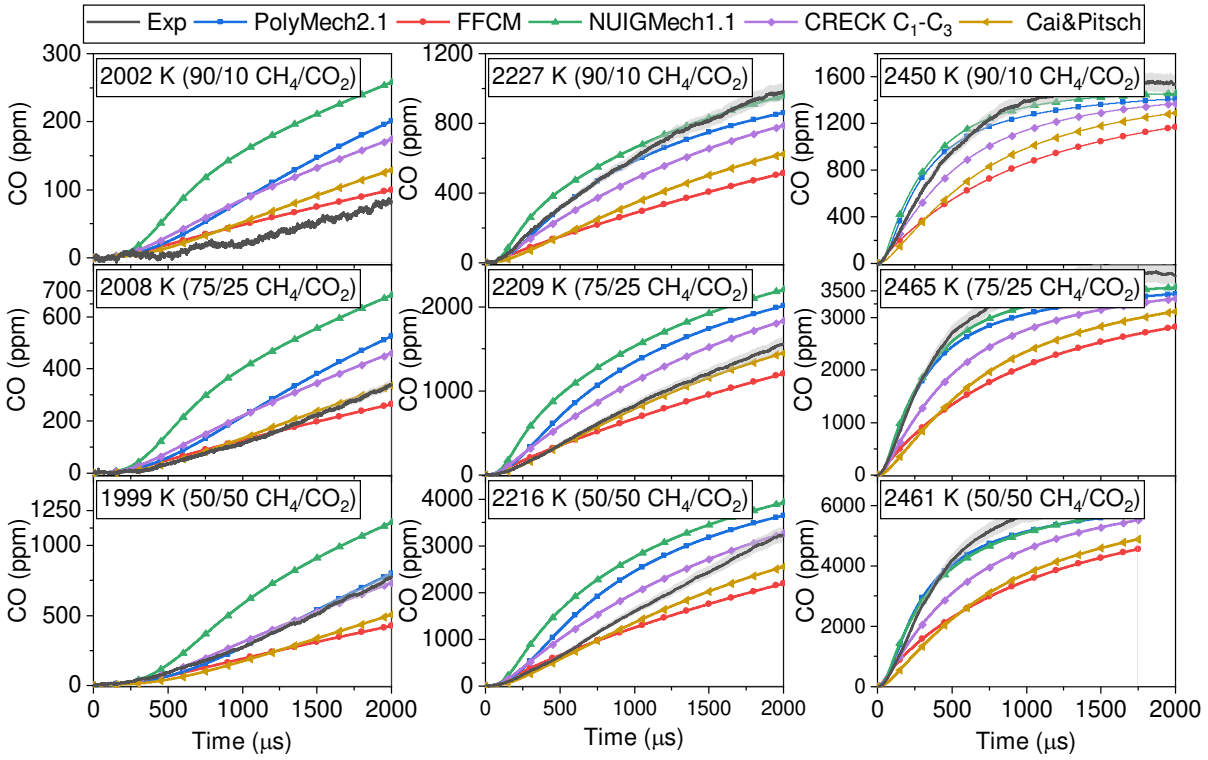

Figure 6.1. CO time histories for different CO_2 blends (top down; 10% CO2, 90% CH_4; 25% CO_2, 75% CH_4; 50% CO_2, 50% CH_4) and different temperatures T_5 (left to right; ~2000 K, ~2210 K, ~2460 K). Shaded areas represent uncertainties.

The modeling prediction using the different mechanisms leads to very different results in onset, progression, and achievable plateau. In addition, no systematics can be discerned. The reduced reaction mechanisms, FFCM and Cai and Pitsch, predict the CO profile in the low- and medium- temperature regime quite well. Note, the good agreement using the Cai and Pitsch mechanism is in accordance with the results from Nativel et al. [52]. However, there are two exceptions: at ~2000 K, 50% CO_2 and ~2210 K, 10% CO_2. These experiments, and the experimental results in the high-temperature regime are in a general good agreement with the modeling using PolyMech2.1, but the NUIGMech1.1 and the CRECK models also show good to acceptable results. To give an overview of the predictive ability of CO formation of the different reaction mechanisms and to reveal the one that leads to the best agreement with experiments and simulations at each condition, Table 6.3 shows the best reaction mechanism with their coefficients of determination (R^2) in each case in a matrix. According to this matrix, the

PolyMech2.1, the NUIGMech1.1 and the CRECK model have the best agreement at high temperatures or high CO_2 blends. In the low-temperature or low CO_2-blend regime, the FFCM or the Cai and Pitsch model better predict the CO formation.

Table 6.3. Matrix of best prediction of literature reaction mechanisms.

	LT	MT	HT
90/10 CH_4/CO_2	FFCM (R^2 = 0.4)	PolyMech (R^2 = 0.96)	NUIGMech (R^2 = 0.96)
75/25 CH_4/CO_2	Cai&Pitsch (R^2 = 0.99)	Cai&Pitsch (R^2 = 0.99)	NUIGMech (R^2 = 0.93)
50/50 CH_4/CO_2	PolyMech (R^2 = 0.99)	CRECK (R^2 = 0.76)	PolyMech (R^2 = 0.93)

Figure 6.2 shows the CO mole fraction at the end of the respective test time as a function of the temperature T_5 for different CO_2 blends and gives an overview of the CO formation and also the CO_2 conversion since they are directly linked. Information about the test time can be found in the supplementary material. Additionally, the maximum possible CO mole fraction obtained from the atom balance of the limiting atom (here O) is shown. As it can be seen from the figure, the CO formation increases with increasing temperature and the maximum CO mole fraction is only reached at temperatures above 2500 K for each CO_2 blend, showing that chemical equilibrium is not reached at temperatures below 2500 K. All mechanisms predict the same trends; however, the level of the result is slightly different. For all three CO_2 blends, the low temperature regime (<2150 K) is reproduced well from the PolyMech2.1 and CRECK mechanisms while the NUIGMech1.1 mechanism slightly overestimates and the FFCM and the Cai and Pitsch mechanisms slightly underpredict the CO mole fraction. At higher temperatures, all mechanisms underpredict the CO mole fraction.

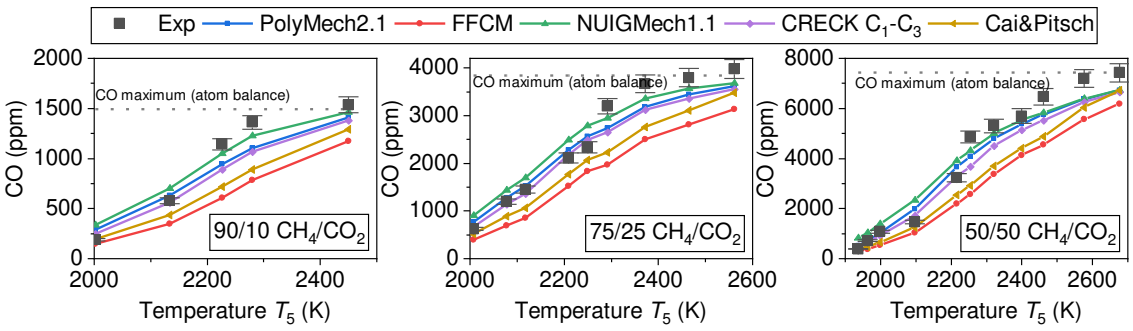

Figure 6.2. CO mole fraction at the end of the respective test time as a function of temperature T_5 for different CO_2 blends (left 10% CO_2, 90% CH_4; middle 25% CO_2, 75% CH_4; right 50% CO_2, 50% CH_4).

The later reaction onset with increasing CO_2 blend, which was already pointed out in connection with the CO time histories (Fig. 6.1) and the associated decrease in

reactivity of the total mixture becomes clear by forming the ratio CO/CO_{max} and defining the CO delay time τ_{20}. Here, the CO delay time τ_{20} describes the time needed to reach 20% of the ratio CO/CO_{max}. Figure 6.3 shows the logarithm of the CO delay time as a function of the inverse temperature for every measured CO_2 blend. It should be noted that only experimental results and associated regression lines are presented to identify the general tendencies.
The experimental results are slightly scattered but already indicate the increasing CO delay time with increasing CO_2 fraction. From the regression lines, it can be seen that the CO delay time increases with higher CO_2 fraction by 5 to 25% at lower temperatures and by ~24% at higher temperatures. Also, in the investigated temperature range from ~2000 K to ~2450 K (0.5 to 0.41 10^3/K), the CO delay time decreases with an exponential behavior.

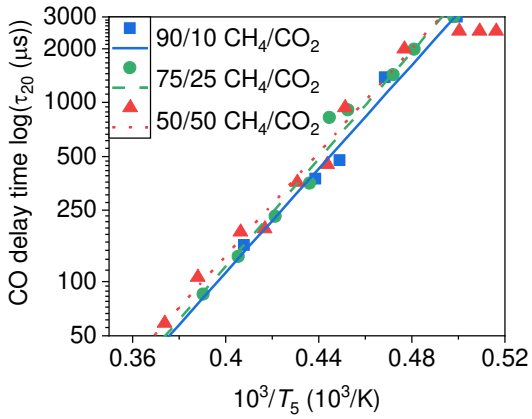

Figure 6.3. Logarithmic CO delay time τ_{20} as a function of the temperature $10^3/T_5$ for different CO_2 blends (blue 10% CO_2, 90% CH4; green 25% CO_2, 75% CH_4; red 50% CO_2, 50% CH_4). Symbols represent experiments with additional linear regression lines.

From Figs. 6.2 and 6.3 and the comparison of the different CO_2 blends, some general statements can be made. Note that while some statements are obvious, they should still be expressed.

1) The CO formation increases with increasing temperature and shows no unsteady behavior along the investigated temperature range.
2) The higher the CO_2 blend up to the 50% CO_2 blend, the higher the CO mole fraction. Although no experiments were performed with higher CO_2 blends, modeling results confirm this statement as less CO would be formed with 75% or 100% CO_2 in the CH_4/CO_2 mixture.
3) The maximum CO mole fraction can be found at temperatures >2500 K for a fixed CO_2 fraction.
4) With increasing CO_2 blend, the ratio of CO/CO_{max} at temperatures above 2000 K is decreasing and the CO delay time τ_{20} is increasing. This indicates a decreasing CO_2

conversion with increasing CO_2 blend at these temperatures due to the need to overcome higher activation energies.

6.4.1 Reaction path and sensitivity analysis

To gain understanding of the process and to reveal general principles, the most important reaction patterns, which are involved in the decomposition of the reactants and the formation of CO, are identified. It also helps in understanding the differences in mechanisms predictions. The reaction path analysis shown in Figure 6.4 was performed using the PolyMech2.1 reaction mechanism because it shows mostly good and always acceptable results for all CO time histories. As PolyMech2.1 was developed for these kinds of conditions, one objective of this study was to explore the chemical pathways described by PolyMech2.1 and to suggest possible improvements. It should be noted that all conditions were considered for the analysis, but only selected conditions are shown in the manuscript.

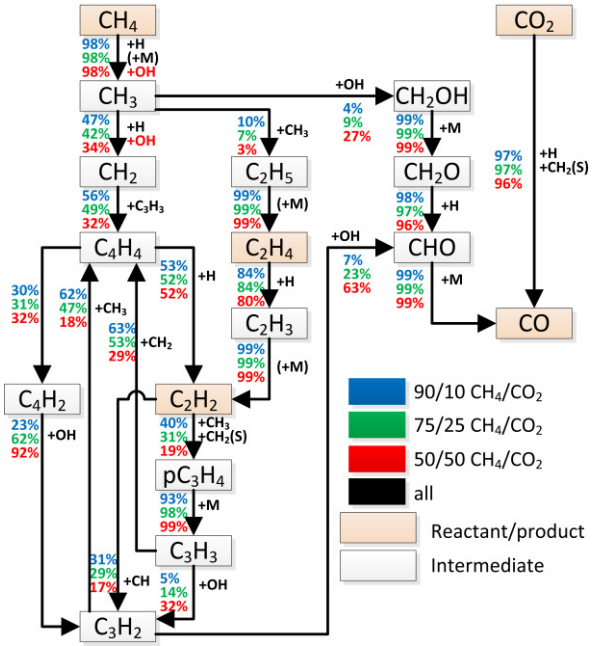

Figure 6.4. Reaction path analysis using PolyMech2.1 for different CO_2 blends at ~2210 K. The numbers are denoted to the carbon flux related to the respective reactant at 50% CO_2 conversion.

Figure 6.4 depicts the reaction pattern for different CO_2 blends at ~2210 K. It should be noted that only the most important pathways are shown.
CO_2 decomposes mainly via the reverse reaction of (R6.1):

$$CO + OH \rightleftharpoons CO_2 + H\,, \qquad \text{(R6.1)}$$

where the collision with hydrogen radicals leads to the abstraction of O from CO_2, forming OH radicals and CO. This reaction is the most important reaction for the whole process since it leads not only to the direct decomposition of CO_2, but also to the formation of OH and, due to the absence of additional oxygen, it is the only source for OH formation. This sequence can be observed for any CO_2 blend and temperature. However, the absolute rate increases at higher temperatures and decreases with higher CO_2 amount because fewer H atoms are available and the H radical consumption via reaction (R6.3) is favored. This decrease with higher levels of CO_2 also explains why lower CO_2 conversion is observed for higher CO_2 blends. It is interesting to note that the unimolecular decomposition reaction of CO_2 ($CO_2+M \rightleftharpoons CO+O+M$) has a negligible influence at the conditions herein, even if the mixture contains only 50% CH_4 (instead of 90%).
The consumption of CH_4 differs strongly for the different mixtures. For low CO_2 content it occurs via reaction (R6.2) and reaction (R6.3), forming H and CH_3 radicals.

$$CH_4 (+ M) \rightleftharpoons CH_3 + H (+ M) , \quad \text{(R6.2)}$$
$$CH_4 + H \rightleftharpoons CH_3 + H_2 . \quad \text{(R6.3)}$$

For the two mixtures with low CO_2 mole fractions (≤25%), the pyrolysis pathway from CH_3 to C_2H_4, C_2H_2, C_4H_4, and C_3H_3 via several H abstraction and recombination reactions is favored due to the absence of OH radicals. For the mixtures with 50% CO_2, oxidation reactions are favored, starting with the decomposition of CH_4 via reaction (R6.4)

$$CH_4 + OH \rightleftharpoons H_2O + CH_3 , \quad \text{(R6.4)}$$

and following the oxidation pathway towards CO. However, compared to reaction path analysis from CH_4 oxidation at fuel-rich conditions in previous studies [118], the formation of CH_3O (methoxy) is negligible. Instead, the formation of CH_2O (formaldehyde) occurs by the H abstraction of CH_2OH (hydroxymethyl) via reaction (R6.6) and its preliminary formation via reaction (R6.5)

$$CH_3 + OH \rightleftharpoons CH_2OH + H , \quad \text{(R6.5)}$$
$$CH_2OH + M \rightleftharpoons CH_2O + H + M . \quad \text{(R6.6)}$$

Additionally, and in contrast to [118], the following formation of CO via CH_2O and CHO proceeds without O or OH addition but with H abstraction or unimolecular

decomposition (R6.7) because at this time, O and OH radicals are already consumed under our conditions.

$$CHO + M \rightleftharpoons CO + H + M \,. \qquad \text{(R6.7)}$$

But below 2200 K, CO_2 directly forms CO and CH_2O by recombination with $CH_2(S)$:

$$CH_2(S) + CO_2 \rightleftharpoons CH_2O + CO \,. \qquad \text{(R6.8)}$$

Moreover, the pyrolysis pathway to C_2 and C_3 hydrocarbons is also affected by additional OH radicals: as with increasing CO_2 amount, CH_3 and CH_2 (and $CH_2(S)$) are increasingly used to form CH_2OH and CH_2O, and fewer of those radicals are available to form C_2H_4 and C_2H_2. It should also be noted that the formation of benzene and PAHs via C_3H_3 (via self-recombination of C_3H_3 towards C_6H_6 or C_6H_5, not shown in Fig. 6.4) is negligible because reactions (R6.9) and (R6.10) are favored due to the presence of OH.

$$C_3H_3 + OH \rightleftharpoons C_3H_2 + H_2O \,, \qquad \text{(R6.9)}$$
$$C_3H_2 + OH \rightleftharpoons CHO + C_2H_2 \,. \qquad \text{(R6.10)}$$

Rate of production analyses, which are the basis of reaction flow analyses, were performed for all mechanisms, plots are shown in the supplemental material. They reveal the reactions having the biggest share in CO production for all tested reaction mechanisms. These steps are mainly reactions (R6.1), (R6.7), and (R6.8), for which different reaction rate coefficients are used among the models. The predictions by the FFCM and Cai and Pitsch mechanisms are consistently the lowest due to the lowest reaction rates for (R6.7) and (R6.8). Accordingly, the general overprediction by NUIGMech1.1 is due to it having the highest reaction rates. However, some mechanisms contain similar reaction rates (*e.g.*, (R6.1): PolyMech2.1 and CRECK, (R6.7) and (R6.8): PolyMech2.1 and NUIGMech1.1), explaining the similar CO predictions at low temperatures for the PolyMech2.1 and the CRECK reaction mechanisms and at high temperatures for PolyMech2.1 and NUIGMech1.1.

To identify the reactions whose change would cause the greatest response in the CO time history in the predictions of the PolyMech2.1 model, sensitivity analyses were performed. Figure 6.5 shows the CO sensitivity of the respective reactions as a function of time for different CO2 blends and an average temperature of ~2210 K, which are mainly (R6.1), (R6.2), (R6.3), (R6.8), (R6.11), and (R6.12)

$$CH_3{+}CH_3 \rightleftharpoons C_2H_5 + H \,, \qquad \text{(R6.11)}$$

$CH_3 + CH_2 \rightleftharpoons C_2H_4 + H$. (R6.12)

As expected, the CH_4 decomposition reactions (R6.2) and (R6.3) have the greatest influence on reaction onset, and (R6.1) has the greatest influence on CO formation in the plateau. In the supplemental sensitivity analyses for all conditions are found. Interestingly, this behavior occurs for all investigated temperatures and CO_2 blends, but, with increasing temperature, the plateaus of (R6.2), (R6.3), and (R6.8) are shifted towards earlier times and are less important, whereas (R6.1) gains importance at higher temperatures. This shift is due to the faster decomposition of CH_4 at higher temperatures, providing enough H radicals to initiate the CO_2 decomposition. With increasing CO_2 amount, sensitivity is only slightly affected, and the most distinct influence is observed for the lowest temperatures due to the reduced reactivity as discussed above. Here, (R6.2), (R6.3), and (R6.8) are slightly less important, while the sensitivities of (R6.1) und (R6.9) are unchanged. Since the compression stroke in combustion engines typically leads to pressures above 1 atm, sensitivity analyses at respective conditions at 30 atm were performed to investigate the pressure-dependent differences, shown in the supplemental material. As expected, the reactions are much faster, and especially the third-body reactions such as (R6.2) gain importance, but also the oxidation reactions of CH_4 and CH_3 (R6.4) and (R6.5) are getting faster.

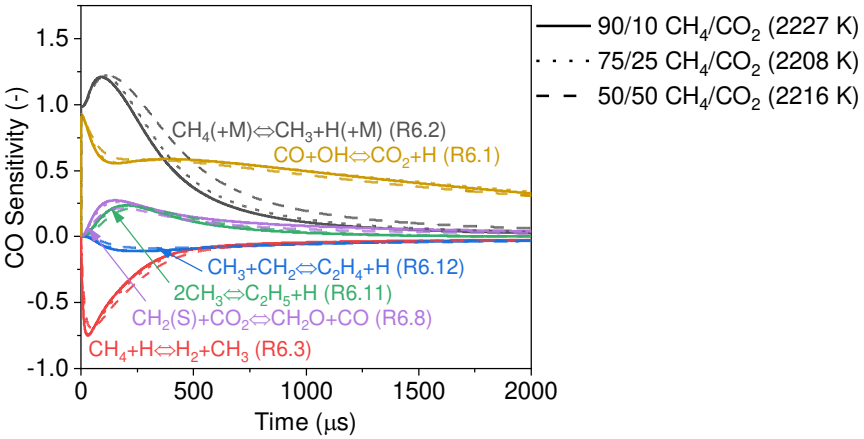

Figure 6.5. Sensitivity analysis for CO formation as a function of the time using PolyMech2.1. The sensitivity analysis is performed at ~2210 K and different CO_2 blends.

Since reactions (R6.1), (R6.2), and (R6.3) were unraveled as key reactions for the CO formation, the reaction rate expressions (in $cm^3/mol/s$) implemented in PolyMech2.1, as given below for these reactions, their pre-exponential factors were modified separately within their uncertainties (uncertainty factor f_k), plotted in Figure 6.6:

$k_{1.1} = 7.046 \cdot 10^4 T^{2.053} e^{179.1\ K/T}$ (f_k = 1.2) [128],

$k_{1.2} = 5.757 \cdot 10^{12} T^{-0.664} e^{-167.1\ K/T}$ (f_k = 1.5) [128],
$k_2 = 2.1 \cdot 10^{16} e^{-52800\ K/T}$ (f_k = 1.25) [80],
$k_3 = 3.072 \cdot 10^{5} T^{2.5} e^{-4825\ K/T}$ (f_k = 1.4) [129].

It should be noted that (R6.2) is a third body reaction, for which the collision partners and associated efficiencies may affect the reaction rate, but this is not further investigated herein.

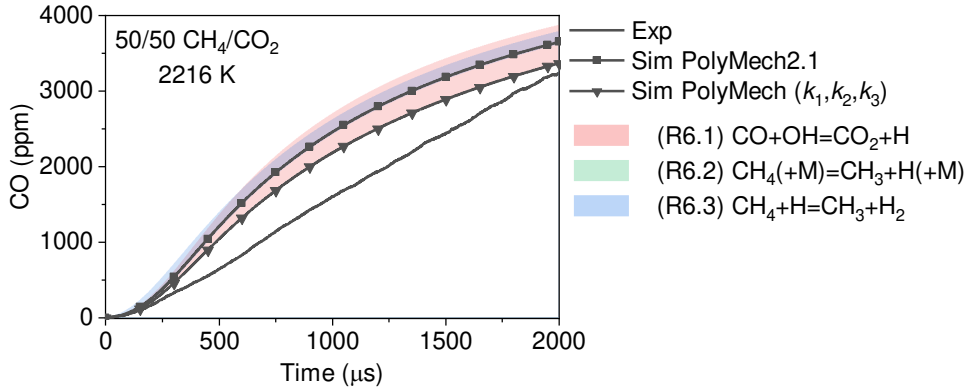

Figure 6.6. CO time history for 50% CO_2, 50% CH_4 and ~2216 K. Colored shaded areas are denoted to the changes occurred by varied reaction rates of R6.1(red), R6.2 (green) and R6.3 (blue).

Figure 6.6 shows the influence of these reaction rates on the predictions after the rate coefficients are changed separately within their uncertainties. It must be noted that an increase of the respective reaction rate for (R6.1) and (R6.2) leads also to an increase of the CO mole fraction. In contrast, the modification of reaction (R6.3) has an opposite effect, and an increase of its reaction rate leads accordingly to a decrease of the CO mole fraction because the preliminary generated H radicals are preferably consumed by the CH_4 decomposition reaction instead of the CO_2 decomposition reaction. It can be noted that the variation of the various (R6.1) rate constants within their uncertainties shows the biggest influence on the CO mole fraction, while (R_2)'s uncertainties have a very small effect.
Adapting all rate coefficients (k_1, k_2, k_3) within their maximum or minimum uncertainties to reduce the overprediction of the PolyMech2.1 leads to smaller overprediction for low and medium temperatures, while the high-temperature regime is only slightly affected, showing a small underprediction. To have a better expression along the whole temperature range, the activation energy might need to be reevaluated. However, a significant improvement of the mechanism prediction could not be achieved. To improve mechanisms like PolyMech2.1 also for reforming and energy storage processes, the mentioned reactions should be reassessed for such conditions.

6.5 Conclusion

In this work, the CO formation behind reflected shock waves during the pyrolysis of CO_2/CH_4 was investigated for the first time in the context of engine-based energy storage and reforming processes. The shock-tube facility at Texas A&M University was used to pro-vide conditions as ~1 atm and 1900-2700 K; CO time histories were obtained using a quantum cascade laser. Different mixtures, 750–3720 ppm CO_2 and 6730–3720 ppm CH_4 (10–50% CO_2 in CH_4) in Ar/He, were assessed to understand the interaction of CH_4 and CO_2 at these conditions. The experimental results were compared to literature reaction mechanisms.

A larger CO_2 addition leads to a reduced reactivity of the whole mixture which results in a reaction start at higher temperatures and the competition for H radicals between CO_2 and CH_4. Once the reaction starts, CH_4 consumption via OH is enhanced as CO_2 provides OH radicals, while CO_2 conversion is slightly inhibited. Rate of production and sensitivity analysis revealed that the reaction $CO+OH \rightleftharpoons CO_2+H$ is the most important reaction for all conditions. CH_4 decomposition ($CH_4(+M) \rightleftharpoons CH_3+H(+M)$ and $CH_4+H \rightleftharpoons CH_3+H_2$) also has great influence, providing or consuming the needed H radicals. The PolyMech2.1, NUIGMech1.1 and CRECK mechanisms show an acceptable-to-good agreement for mainly high temperatures or high CO_2 blends, while the predictions of the FFCM and the Cai and Pitsch reaction mechanism have larger deviations. However, none of the tested mechanisms can precisely predict CO formation. Adapting the rate coefficients of the most important reactions within their uncertainties in PolyMech2.1 was not sufficient to improve predictions. Since no reaction mechanism can perfectly predict CO formation at "simpler conditions", *i.e.*, atmospheric pressure, the need to study CO formation at high pressure is also apparent.

To develop new processes such as engine-based polygeneration, energy storage or reforming processes, numerical models including kinetics and thermodynamics based on the knowledge of works like these are helpful to predict promising conditions.

6.6 Acknowledgements

This work was supported by the Deutsche Forschungsgemeinschaft within the framework of the DFG research unit FOR 1993 “Multi-functional conversion of chemical species and energy”, Project-Number 229243862. Additional support for the experiments came from the Texas A&M Engineering Experiment Station (TEES) and the TEES Turbomachinery Laboratory. Additional support was provided by King Fahd University of Petroleum & Minerals through the Saudi Arabian Cultural Mission in the form of fellowship funding for coauthor SAA (Fellowship No. 1440/10079/9)

7 Behavior of higher alkanes in the dry reforming process

The content of this chapter was published in Applications in Energy and Combustion Science:
C. Rudolph, C. M. Grégoire, S. P. Cooper, S. A. Alturaifi, O. Mathieu, E. L. Petersen, B. Atakan, Spectroscopic study of CO formation from CO_2-enriched pyrolysis of C_2H_6 and C_3H_8 under engine-relevant conditions, Applications in Energy and Combustion Science (2023), DOI: 10.1016/j.jaecs.2023.100123.

Author contribution

My contribution embraced developing the concept, performing and post-processing the experiments, processing the raw data, conducting the simulations, analyzing and graphing the results and writing the manuscript. Claire M. Grégoire contributed significantly to the conduction of the experiments and the analysis of the raw data. Claire M. Grégoire, Sean P. Cooper, S. A. Alturaifi, and Olivier Mathieu, Eric L. Petersen and Burak Atakan contributed to the interpretation of the results and reviewed the manuscript. Eric L. Petersen and Burak Atakan also developed the concept, coordinated the project, provided the laboratories, and acquired funding.

Highlights

- Dry reforming of ethane and propane was investigated behind reflected shock waves.
- Temperatures between 1830 and 2950 K were studied, as they occur in piston engines.
- CO formation was measured using a quantum cascade laser.
- The analysis aims at a fundament understanding of the reforming process.
- Tested literature reaction mechanisms cannot correctly predict the CO formation.

Abstract

To address the challenges of climate change, technologies and processes that contribute to reducing net CO_2 emissions are key. Herein, engine-based dry reforming combines the possibility of storing excess energy and converting unwanted CO_2 into syngas. To fundamentally investigate this process at simpler, but engine-like conditions, the pyrolysis of CO_2/C_2H_6 and CO_2/C_3H_8 mixtures behind reflected shock waves was studied. The targeted conditions were especially temperatures of 1830–2590 K, as they are encountered in piston engines, and atmospheric pressure. The time-resolved CO formation was measured using a quantum cascade laser, providing a unique experimental dataset. In addition, laser absorption data at temperatures above 2500 K reveal physically unattainable CO mole fractions, so these experiments are discussed separately. This phenomenon is shown and briefly discussed.

A detailed chemical kinetics analysis reveals the interaction of linear alkanes and CO_2, and the influence of the respective linear alkane on CO formation. The decomposition of all linear alkanes leads to radical formation, initiating CO_2 decomposition via, *e.g.*, $CO_2+H \rightleftharpoons CO+OH$ and $CH_2(S)+CO_2 \rightleftharpoons CH_2O+CO$. Overall, the C_2H_6/CO_2 blends exhibit smaller τ_{20} (the time at which 20% of maximum CO mole fraction is reached based on the atom balance) since the C-C chain cleavage of C_2H_6 decomposes to CH_3, enhancing $CH_2(S)$ formation and also the subsequent enhanced C_1-oxidation path. In contrast, the C-C-C chain of C_3H_8 leads to C_2H_5 and CH_3 and to faster H-radical formation via $C_2H_5(+M) \rightleftharpoons H+C_2H_4(+M)$. As C_2H_2 is one of the key species with respect to the high-temperature pyrolysis of alkanes, its formation and decomposition has a great influence on the whole process because its respective reactions compete for H-radicals, also needed for CO_2 decomposition. A comparison was made with results predicted from literature reaction mechanisms. It was reported that all tested models need improvement, underlining the limitation of chemical kinetics mechanisms and validation data at untypical conditions.

7.1 Introduction

Today's challenges to substantially reducing greenhouse gas emissions include strategies to avoid anthropogenic pollutants, such as transitioning the energy system to renewable energy, and strategies to use or store these greenhouse gases [130,131]. The important role of carbon dioxide utilization and storage in the development of technologies required to achieve the climate goals was recently reviewed by Kleijne et al. [132]. In this context, dry reforming of hydrocarbons should be mentioned. Dry reforming of, *e.g.*, methane is an endothermic, endergonic reaction ($CH_4+CO_2 \rightleftharpoons 2CO+2H_2$, Δg^0 = 172 kJ/mol), having a net-negative CO_2 balance and producing valuable

synthesis gas, as needed in the chemical industry. Due to the high endothermicity, high temperatures are needed to overcome the activation energy. Dry reforming is typically performed in plasma-activated [133–136] or catalytic reactors [136–139]. There are a couple of recent reviews, giving comprehensive overviews on this topic (*e.g.*, Shi et al. [136]), and describing the latest developments (*e.g.*, Abdulrasheed et al. [138]). Among others, Abdulrasheed et al. [138] presented the recent progress of synergistic interplay of catalyst components used for dry reforming. Catalytically assisted dry reforming of methane requires temperatures of 650–850°C, depending on the catalyst [138]. Various materials, such as Ni or bimetallic catalysts, have widely been investigated to overcome challenges like coke deposition [137,139] and are already commercially available. To circumvent the challenges like coking, and to still achieve high selectivity, plasma-activated dry reforming was widely investigated. Uytdenhouwen et al. [134] performed experiments with various CO_2/CH_4 mixtures at temperatures below 50°C in a SiO_2-packed plasma reactor to achieve partial chemical equilibrium. They found higher reaction rates when CH_4 is added because new chemical pathways are pursued. The products are mainly CO and H_2, however, unsaturated and oxygenated hydrocarbons up to C_7 and C_4-OH were also detected. The same group performed experiments on this topic using an atmospheric-pressure glow discharge reactor [133], achieving a high conversion above 90% of CO_2 and CH_4.

Since the C-H bond of methane has a higher bond dissociation energy compared to the C-C bonds of ethane or propane, dry reforming of higher linear alkanes seems to be thermodynamically favorable. Catalysts are also readily used in the dry reforming of ethane and propane, as described in the work of Tsiotsias et al. [140] or Ahadzadeh et al. [141]. Among others, Ni catalysts supported with Al_2O_3 were studied for ethane [140] and propane [142] dry reforming, providing syngas with H_2/CO ratios between 0.3–0.6 at temperatures between 400–600°C. Li et al. [143] investigated the dehydrogenation of ethane on different catalysts using CO_2 as an oxidant at 650°C. These authors found that Pd-doped catalysts achieve a high C_2H_4 selectivity, while the usage of Ni monometallic catalysts lead to enhanced CO_2 conversion and CO formation. Råberg et al. [142] did experiments focusing on propane dry reforming on Ni catalysts at 600°C, achieving a CO selectivity above 90% and a CO_2 conversion of up to 60%.

Non-catalytic dry reforming usually requires very high temperatures, so this approach is rarely pursued. Cao et al. [144] followed a thermodynamic equilibrium approach, varying the CH_4/CO_2 ratio, temperature, and pressure. They revealed high H_2 and CO selectivities of up to 90% for temperatures above 800 K and pressures below 0.1 MPa. Also, the undesirable formation of carbon black is inhibited by adapting the CH_4/CO_2 ratio towards ≤1. Another approach is to use piston engines as chemical reactors for various purposes, such as partial oxidation [60] or pyrolysis [109], to produce syngas

and unsaturated hydrocarbons, in addition to on-demand work or heat. The input energy for these processes is provided by the compression stroke, promoting high-temperature reactions. The recent reviews by Atakan et al. [60] and Ashok et al. [145] show the variety and flexibility of this application. This approach can also be extended for the dry reforming processes, as shown by Gossler et al. [18]. Gossler et al. [18] used mathematical optimization to find promising conditions at which dry reforming of methane can be conducted in piston engines. Their main objective was the CO_2 conversion, which was up to 50% at 2000 K [18]. To initiate the process, small amounts of oxygen were added (up to an equivalence ratio (Φ) of 2.8) so that methane is partially oxidated, leading to higher temperatures and higher CO_2 conversion. The predicted conditions with large CO_2 conversion were confirmed in RCM experiments. As the authors pointed out, one challenge was to overcome the higher activation energy in the CO_2-containing mixtures, compared to the partial oxidation of methane, as studied in [146], or the pyrolysis of methane, as studied in [109]. This higher activation energy goes along with the findings from Bagheri et al. [120] and Koroglu et al. [121], who analyzed the effect of CO_2 with respect to oxy-fuel combustion, ascertaining longer ignition delay times and lower flame speeds due to the presence of CO_2.
To gain a better understanding of the processes of interest, such as engine-based dry reforming introduced by Gossler et al. [18], and to fill the knowledge gap of the chemical interactions of CO_2 and methane or natural gas components at these conditions, kinetic investigations in a high-temperature regime with various, thermodynamically favorable CO_2/alkane mixtures are performed in this study. In this context, we recently analyzed CO_2/CH_4 blends with varying ratios and the associated CO formation at temperatures between 1900 K and 2700 K near atmospheric pressure behind reflected shock waves [113]. To complete the experimental data available in the literature and to comprise the knowledge on C_2 and C_3 linear alkanes/CO_2 mixtures, shock-tube experiments at temperatures between 1830 K and 2450 K were carried out, and the resulting CO formation is addressed. The experimental results are compared to results of literature reaction mechanisms to gauge their ability to predict CO formation. To understand the difference of the respective alkane, the most important reactions were unraveled, and reaction pathways were analyzed. Based on sensitivity analyses, key reactions with the greatest impact on the results are identified.

7.2 Experimental methods

7.2.1 Shock tube

The pyrolysis of CO_2/C_2H_6 and CO_2/C_3H_8 mixtures at high temperatures was investigated in a low-pressure shock tube paired with a quantum cascade laser for CO

detection, shown in Fig. 7.1. Detailed information about the shock tube is given elsewhere [147], and only the most important aspects are described here. The driven tube has a large inner diameter of 16.2 cm, minimizing boundary-layer effects amplified by the presence of CO_2. A 0.25-mm-thick polycarbonate diaphragm separates the driven section from the driver section, which has an inner diameter of 7.62 cm and a length of 3.15 m. Diaphragm opening is supported by a cross-shaped cutting blade, also preventing diaphragm fragments. To achieve optimal shock wave propagation, helium was used as the driver gas. The driven section is evacuated to pressures below 10–5 Torr using a turbo-molecular turbopump (Agilent Turbo V1001 Navigator), and the driver section is evacuated using a rough pump before filling with the driver and test gases. Four piezo-electric pressure transducers (PCB P113A22) were used along the last 1 m of the 7.88 m driven section to monitor the pressure changes and, thus, the passage of the incident shock wave. The velocity of the incident shock wave was determined by the time of passage of the incident shock wave and the exact positions of those pressure transducers. The endwall shock velocity is then extrapolated via a linear curve-fit, allowing for the calculation of the temperature T_5 and pressure P_5 behind the reflected shock wave using the 1D shock wave equations. The uncertainties of T_5 and P_5 are ± 0.8% and ± 1%, respectively, according to the method presented in Mathieu et al. [122]. To perform CO laser absorption measurements, two sapphire optical window ports are located at the sidewall, 1.6 mm upstream from the endwall. The sidewall pressure is detected using an additional piezo-electric pressure transducer. The design, *i.e.*, the large internal volume and length, and the driver gas, enables test times between 1.75 and 3 ms depending on changing arrival times of the expansion wave and contact surface interaction.

Test gas preparation was conducted in a mixing tank by manometrically filling high-purity gases using MKS Baratron pressure transducers (0–1333.2 Pa, 0–133.32 kPa). The pure gases were provided by Praxair with purities between 99.99% (CO_2), 99.97% (C_2H_6, C_3H_8), and 99.999% (He, Ar). For the benefit of the CO laser absorption measurements, a diluent composed of 20% He and 80% Ar was used to ensure rapid vibrational equilibrium as described by Mathieu et al. [123]. The premixing and the high dilution also allow for the assumption of a homogeneous mixture and the neglection of local temperature and pressure gradients within the test time. To understand the kinetic effect of CO_2 on the thermal decomposition of C_2 and C_3 hydrocarbons, 25% and 50% CO_2 blends in the CO_2/C_2H_6 or CO_2/C_3H_8 mixtures were investigated. Due to the high activation energy needed for the endothermic decomposition of the CO_2/C_2H_6 and CO_2/C_3H_8 mixtures, temperatures between 1832 and 2590 K at near atmospheric pressure were investigated. The respective conditions, which are discussed in detail later,

are summarized in Table 7.1. Note that experiments above 2500 K are discussed separately.

Table 7.1. Mixture compositions and measurement conditions.

Mixture	Mole fractions (mol%)				Temperature T_5 (K)	Pressure P_5 (atm)
	Ar	He	C_2H_6 C_3H_8	CO_2		
25/75 CO_2/C_2H_6	79.33	19.92	0.563	0.187	1996 – 2588	1.07 – 0.82
25/75 CO_2/C_3H_8	79.33	19.92	0.563	0.187	1996 – 2564	1.09 – 0.83
50/50 CO_2/C_2H_6	79.44	19.82	0.372	0.372	1832 – 2594	1.17 – 0.85
50/50 CO_2/C_3H_8	79.33	19.92	0.374	0.374	1890 – 2572	1.10 – 0.81

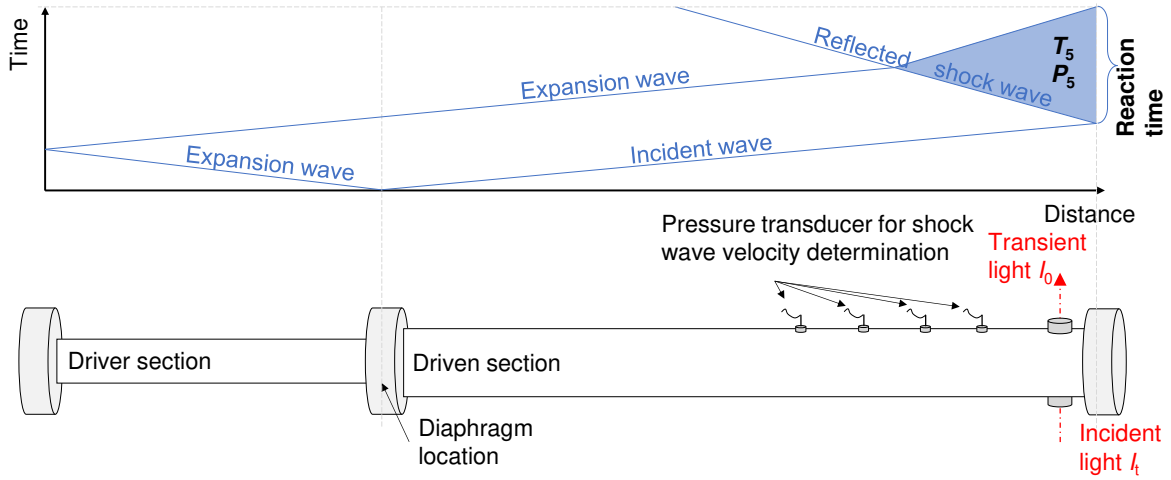

Figure 7.1. Experimental shock tube setup.

7.2.2 CO Laser absorption measurements

The quantum cascade laser presented in Mathieu at al. [147] was used to perform time-resolved CO measurements in the range of 10–10000 ppm that benefit the investigation of reaction start and course as well as the validation of intermediate reactions. The emitted light has a wavelength of 4.8 µm, matching the P(20) transition of the 1←0 band, centered at 2059.91 cm^{-1} for the stable laser operation at 30°C with a current of ~196 mA. The laser is located on a stabilization plate with a constant temperature of 20°C to prevent overheating. The laser beam is centered before each run using a removable cell, containing 10% CO and 90% Ar, according to a method presented by Spearrin et al. [124]. This laser setup allows a high repeatability of CO-measurements withing 3.8% [148]. The laser alignment is verified by preceding argon experiments so

that broadband losses such as beam steering do not occur. Due to the high dilution of argon in the experiments presented and discussed here, this aspect can be neglected. Additional experiments were performed with the laser blocked to identify and prevent further effects of broadband sources. The incident and transmitted intensities, I_0 and I_t, are monitored by two InSb detectors after passing bypass filters, irises, and lenses. Time-resolved CO mole fractions x were calculated using the Beer-Lambert law (Eq. 7.1):

$$\frac{I_t}{I_0} = \exp(-k_\nu \cdot x_{CO} \cdot P \cdot L). \tag{7.1}$$

with k_ν being the absorption coefficient, P the absolute gas pressure, and L the path length, which is the distance between the optical sapphire windows (*i.e.*, the shock-tube inner diameter). The spectral absorption coefficient k_ν ($cm^{-1}atm^{-1}$) is strongly temperature dependent, given by Eq. 2:

$$k_\nu = 23.9 \cdot \exp\,(-0.000649 \cdot T_5). \tag{7.2}$$

This equation is derived by measuring the incident and transient intensities I_0 and I_t with a well-known CO concentration of 2000 ppm in a 20% He and 80% Ar diluent, at temperatures between 1180 and 2709 K. Also, the pressure during the calibration experiments varies between 0.087 and 0.138 MPa – similar to the pressures in the pyrolysis experiments presented later. The pressure dependence is not of interest here, since the same pressure P_5 (within 5% uncertainty) is established by gas dynamics and the high dilution at the appropriate temperature T_5, in both the actual experiments and the calibration measurements. Considering temperature changes during the measurements due to endothermic or exothermic reactions, obtained from 0D batch-reactor simulations, and a weak pressure dependency of k_ν as well as the repeatability of the laser measurements, the overall uncertainty in the CO mole fraction is 5%. However, it must be noted that P_5 and T_5 serve as input parameters for the simulation, and the computed time-dependent pressure and temperature profiles are used for the Beer-Lambert Law. The measured absorption coefficients can be found in the supplementary material (Fig. D1). Detailed information about the quantum cascade laser and the calibration method can be found in Mathieu et al. [147]. Experiments were also carried out at temperatures above 2500 K, but led to unphysical results, as is explained below. Although these results were not included in the mechanistic discussion, they may be interesting for other researchers, thus they are briefly presented.

7.3 Modeling

The chemistry behind the reflected shock is modeled using the zero-dimensional, constant-volume batch-reactor model in ChemKin Pro 21.2 [125]. Energy and species conservation equations are solved to predict the time-resolved temperature, pressure, and species profiles for each condition. The conservation equations were given in [125]. To analyze the chemical kinetics, rate-of-production and sensitivity analyses were performed. Herein, the relative rate of production (*ROP*) and relative sensitivity (*S*) related to a species i and a reaction r are calculated according to Eq. 7.3 and Eq. 7.4, respectively.

$$ROP_{\mathrm{i,r}} = \frac{\max\left(\nu''_{\mathrm{i,r}} - \nu'_{\mathrm{i,r},0}\right) q_{\mathrm{i}}}{\sum_{\mathrm{j}} \max\left(\nu''_{\mathrm{i,r}} - \nu'_{\mathrm{i,r},0}\right) q_{\mathrm{i}}} \tag{7.3}$$

$$S_{\mathrm{i,r}} = \frac{\delta x_{\mathrm{i}} k_{\mathrm{r}}}{\delta k_{\mathrm{r}} x_{\mathrm{i}}} \tag{7.4}$$

Here, ν is the stochiometric coefficient of forward (') and reverse ('') reactions and q_{i} is the rate of progress as the difference between forward and reverse reaction rate k for each species i. However, generated reaction paths, as shown below, are based on the absolute rate of production using time-integrated rates of production.

To model the CO formation, several elementary reaction mechanisms, as shown in Table 7.2, were selected. All kinetic models used here contain at least the kinetics for species sized of up to C_3 and were tested against combustion data. The PolyMech2.1 model [111], based on the work of Porras et al. [17], was developed for fuel-rich polygeneration and energy storage processes, and shall now be validated for engine-based reforming processes such as the thermal decomposition of C_1-C_3 hydrocarbon-CO_2 mixtures, as presented here. Also, the prediction of the CO mole fractions in CH_4/CO_2 pyrolysis is in good agreement with experimental results over a wide range of conditions, as found in our previous work [113].

Table 7.2. Elementary reaction mechanisms used in this study.

Name	Species	Reactions	Ref.
NUIGMech1.1	923	5966	[127]
PolyMech2.1	192	948	[111]
CRECK C_1-C_3	114	1999	[114]
Burke	113	710	[149]
USC	111	784	[150]

Also, the experimental results were compared with several mechanisms from different working groups: high-temperature chemistry is included in the comprehensive elementary reaction mechanism of Wu et al. [127] (NUIGMech1.1) and Ranzi et al. [114] (CRECK C_1-C_3). The Burke model [149] and the USC model [150] are comparatively small and were built for CH_4/DME combustion and synthesis gas combustion, respectively.

7.4 Results and discussion

Before presenting the experimental CO time histories and kinetic simulations, CO formation in chemical equilibrium is briefly discussed. For all mixtures, the equilibrium compositions at temperatures above 1800 K contain mainly CO, H_2 and C_2H_2. The CO amount in chemical equilibrium corresponds to the maximum possible CO mole fraction $x_{CO,max}$ according to the net reaction and depends only on the CO_2 blend in the initial mixture and is within 0.15% constant for temperature changes within 1800 K and 2500 K. Since CO_2 is the only source for O atoms, the CO mole fractions measured give a direct indication on the CO_2 conversion.
In the following, CO time histories of experiments are discussed and compared with simulations. To gain understanding of the effect of CO_2 addition on the thermal decomposition of C_2H_6 and C_3H_8, and of the resulting CO formation, rate of production analyses were performed, and reaction paths were generated. Additionally, key reactions are unraveled in sensitivity analyses that would improve the tested mechanisms in terms of predicting CO formation.

7.4.1 Experimental results and model comparison

CO time histories of 25% CO_2 and 50% CO_2 in C_2H_6 and C_3H_8, respectively, are given in Fig. 7.2 for representative low, intermediate, and high temperatures T_5 of ~2000 K, ~2260 K, and ~2450 K. Experiments are compared with simulations using the mentioned reaction mechanisms (Burke [149], USC [150], PolyMech2.1 [111], NUIGMech1.1 [127], and CRECK [114]). All raw pressure signals and CO time histories, including the specified conditions (T_5, P_5 and test time), are provided in the supplementary material (Fig. D2 – Fig. D4). Also, further simulations compared with experiments for each condition are presented in Fig. D5 – Fig. D9 in the supplementary material.
In the low temperature-regime, a sharp increase of the CO mole fraction can be observed for all mixtures within the first 250 µs, followed by a nearly linear increase until the arrival of the expansion wave (~2500 µs). At the end of the respective test times, chemical equilibrium is not reached. Since CO_2 is the only source for CO, the achieved CO mole fraction increases with increasing CO_2 content. In the intermediate- and high-

temperature regimes, the sharp increase remains, followed by a logarithmic increase after 250 µs. While the CO mole fraction does still not reach the maximum value at the intermediate temperatures, a plateau at the maximum value is obtained at temperatures of ~2450 K within the observable reaction time. Also, more CO is formed at higher initial CO_2 content at medium temperatures, while this effect is negligible at high temperatures. At temperatures above 2200 K, the CO formation rate is higher in C_3H_8-containing mixtures compared to the ethane mixtures.

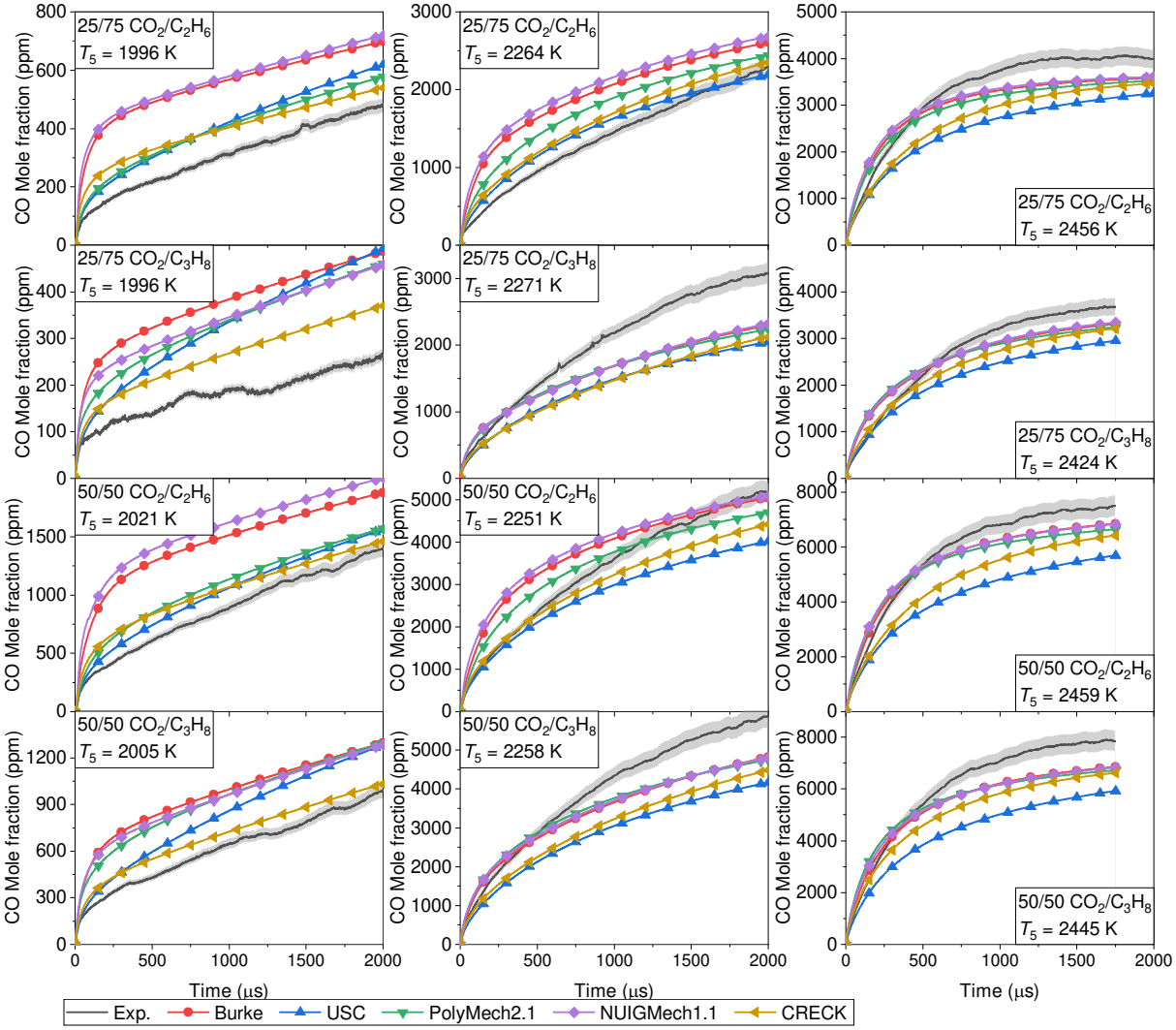

Figure 7.2. Time dependent CO mole fractions for 25% and 50% CO_2 blends (top down) in C_2H_6 and C_3H_8 and temperatures T_5 of ~2000 K, ~2260 K, and ~2450 K (left to right), respectively. Black lines correspond to the experiments, and the shaded areas are experimental uncertainties of 5%. Colored lines with symbols are simulations.

All presented reaction mechanisms are generally capable of predicting the qualitative trends. However, the quantitative predictions differ significantly from the experimental values and are generally outside the experimental uncertainties. Especially in the low-temperature regime the predicted CO mole fraction is up to 1.9-times the experimental CO mole fraction. The CRECK model and the USC model predict throughout less CO

than found experimentally. The results from the Burke model and the NUIGMech1.1 model resemble each other and predict the fastest rise and the highest values for the CO mole fraction, because the Burke and the NUIGMech1.1 have many similar reactions. The PolyMech2.1 does not reveal a systematic behavior. At temperatures below ~2260 K, all models predict CO mole fractions that are too high. Overall, the prediction quality gets better at higher temperatures.

To quantify the ability to predict the CO formation, a modified coefficient of determination P^2 was calculated using Eq. 5; $P^2 = 1$ is achieved when $x_{CO,exp} = x_{CO,sim}$.

$$P^2 = \frac{\sum(y_i - \hat{y}_i)^2}{\sum(y_i - \bar{y})^2}, \tag{7.5}$$

y is the experimental CO mole fraction at each time step i, $\bar{y}$ being the average experimental CO mole fraction, and $\hat{y}$ being the CO mole fractions from the simulations. An P^2 value of one, indicates a perfect prediction, while negative P^2 values imply a poor prediction of the CO formation. However, no statement can be made as to whether CO formation is overestimated or underestimated. The P^2 is determined for every mixture and every condition and shown in Fig. 7.3 as a function of the temperature T_5 for every mixture and every kinetic model used in this work. However, only values between 1 and 1.5 are shown in Fig. 7.3 since values below this are not of substantial interest. Therefore, if P^2 for conditions/mechanisms are missing in Fig. 7.3, their values are below 1.5 but were considered in the evaluation.

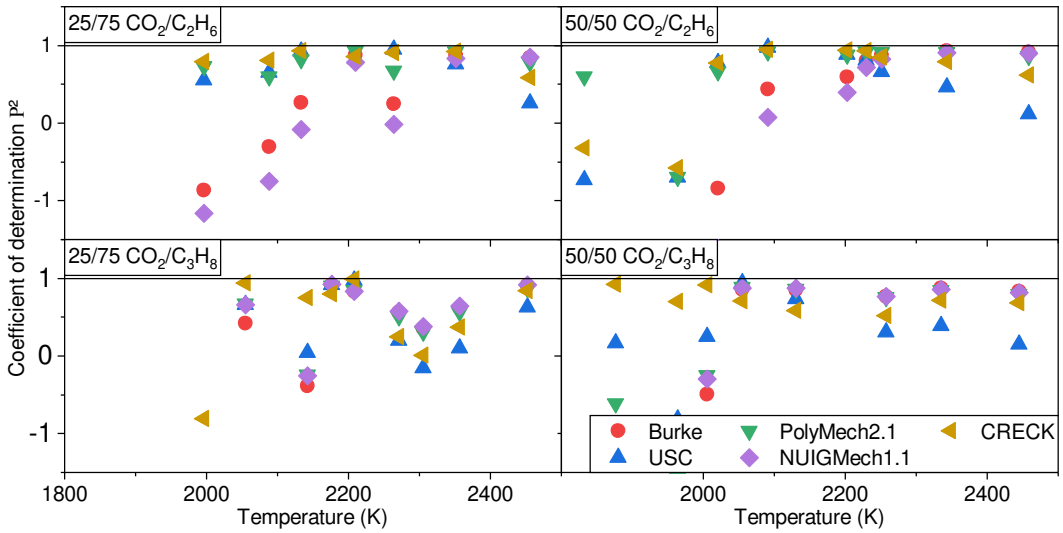

Figure 7.3. Coefficient of determination P^2 as a function of temperature T_5 for 25% and 50% CO_2 blends (left to right) in C_2H_6 and C_3H_8 (top down) for different reaction mechanisms: Burke [149] (red dot), USC [150] (blue triangle), PolyMech2.1 [111] (green triangle, downward), NUIGMech1.1 [127] (purple diamond), CRECK [114] (yellow triangle, sideward). The horizontal line indicates the identical mole fractions in experiment and simulation.

As already observed from Fig. 7.2, the prediction of the CO mole fractions at temperatures above 2300 K is in relatively good agreement with the experiments, confirmed by P^2 values between 0.6 and 0.93 for the Burke, PolyMech2.1, NUIGMech1.1, and CRECK models; only for the USC model, the P^2 values range from 0.1 to 0.5. At temperatures between 2100 K and 2260 K, P^2 varies from 0.4 for Burke and NUIGMech1.1 to 0.93 for the CRECK mechanism. Generally, the predictions for C_2H_6 mixtures are better than those for the C_3H_8 mixtures for both CO2 blends, when using the USC, CRECK and PolyMech2.1 models. For the C_3H_8 mixtures, the Burke and the NUIGMech1.1 predictions are mostly better. At temperatures below 2100 K, the prediction quality differs strongly; when using the Burke and the NUIGMech1.1 model P^2 levels below 7 are observed, while the PolyMech2.1 and the CRECK still attain values of up to 0.7 and 0.9, respectively.

Taking the average P^2 over all conditions, the PolyMech2.1 and the CRECK reaction mechanisms have values of 0.40 and 0.60, respectively, while USC has a P^2 of 0.18 and Burke and NUIGMech1.1 have P^2 values of -0.27 and -0.24, respectively. So, the use of the PolyMech2.1 and the CRECK mechanisms for the following analyses seems justified. However, since the PolyMech2.1 was developed for engine-based polygeneration and energy storage processes, the focus of the analysis is on the performance of the PolyMech2.1 under these unusual conditions. It should be noted, however, that the production rates and sensitivity analyses of the other mechanisms presented here are given in the supplementary material.

7.4.2 Effect of mixture composition on the reactivity

To visualize the influence of the CO_2 blend and the selected linear alkane (C_2H_6, C_3H_8) on the reactivity associated with the CO_2 conversion and the CO formation, the relative mole fraction of CO defined as the CO mole fraction relative to the maximum CO mole fraction which could be reached in chemical equilibrium in each experiment $x_{CO,rel} = x_{CO}/x_{CO,max}$ was studied. Also, to illustrate the changes in reactivity quantitatively, a CO delay time (τ_{20}) is defined as the time when 20% of the maximum CO mole fraction $x_{CO,max}$ is reached. The relative mole fraction $x_{CO,rel}$ and the CO delay time are presented in Fig. 7.4 (left and right, respectively) for a broad range of temperatures. Note that the results shown in Fig. 7.4 are experimental results, and no simulations are shown therein.

Not unexpectedly, the reactivity of ethane and propane increases with the initial carbon dioxide fraction, as seen in Fig. 7.4, which contrasts with our finding for methane reaction with carbon dioxide [113]. Here, the delay-time curves for higher CO_2 content are

shifted to lower temperatures (or higher inverse temperatures). For methane, we argued that the high activation energies and the competition for H radicals, which are needed for the decomposition of both CH_4 and CO_2 (via (R7.1), see below), lead to this finding. From the ratio $x_{CO,rel}$, it is observed that an increased CO_2 content (up to the investigated 50% blend) promotes the CO formation at low and intermediate temperatures. Although the initial increase in CO mole fraction is greater for the C_3H_8 mixtures, the absolute and relative CO yield are higher in the C_2H_6 containing mixtures. So, for ethane and propane, higher CO_2 concentration leads to faster formation of CO, especially at low and intermediate temperatures.

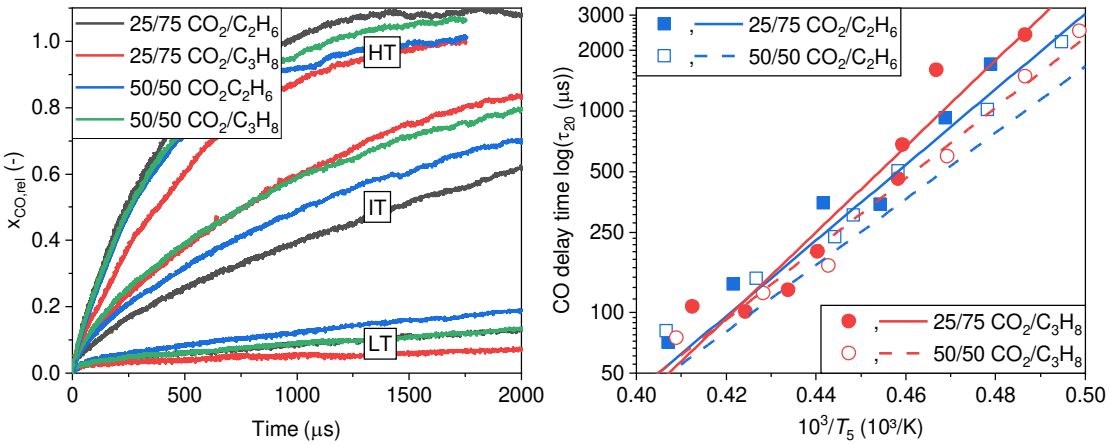

Figure 7.4. (left) Relative CO mole fraction $x_{CO,rel}$, as a function of reaction time for 25% and 50% CO_2 blends in C_2H_6 and C_3H_8 for low temperature (LT: 1996 K, 1996 K, 2021 K, 2005 K, respectively), intermediate temperature (IT: 2264 K, 2271 K, 2251 K, 2258 K, respectively), and high temperature (HT: 2456 K, 2424 K, 2459 K, 2445 K, respectively). (right) logarithmic CO delay time τ_{20} as a function of inverse temperature $10^3/T$ for 25% (filled symbols, solid lines) and 50% (blank symbols, dashed lines) CO_2 blends in C_2H_6 (blue squares) and C_3H_8 (red circles).

At high temperatures, the influence is difficult to discern, since at high temperature a fast decomposition of the reactants along other channels will probably dominate the CO formation. The CO delay time is less informative at temperatures 10^3 K/T>0.5 (T_5<2000 K) and 10^3/T<0.44 (T_5>2260 K) because τ_{20} is at the end of the test time or rather is not reached at all, or is hardly distinguishable due to the temperature-induced sharp increase in the CO mole fraction. However, a clear tendency is visible in the intermediate-temperature range: τ_{20} values are up to 40% smaller for 50% CO_2 blends in C_2H_6 and C_3H_8 than those for the 25% CO_2 blends in C_2H_6 and C_3H_8 (*e.g.*, 1012 µs versus 1711 µs at ~2090 K for C_2H_6, or 1475 µs versus 2454 µs at 2055 K for C_3H_8). The difference in τ_{20} for the different hydrocarbons is more visible for the 25% CO_2 blends: τ_{20} values for C_3H_8 mixtures are up to 42% higher than for C_2H_6 mixtures (*e.g.*, 1589 µs at 2142 K versus 924 µs at 2133 K), so the rate of C_3H_8 reforming to CO is astonishingly

lower than for the normally less-reactive C_2H_6. A limit is found at ~2260 K, where the rate of CO formation in the C_3H_8 mixtures seems not to be affected by CO_2 concentration, while that for the C_2H_6 mixtures still does. A similar effect for the C_2H_6 mixtures is observed at ~2350 K. To get additional insight into these complex and unexpected findings, the reaction paths were investigated in the following.

7.4.3 Reaction path and sensitivity analyses

A reaction path analysis offers insight into the most important reaction patterns involved in the decomposition of the reactants and the formation of the products. The reaction path analysis is discussed along with the carbon fluxes predicted by the PolyMech2.1 at a temperature of ~2260 K, and 25% and 50% CO2 blends. The corresponding rate-of-production analysis for LT, IT, and HT for every mixture is presented in the supplementary material using the PolyMech2.1 and the CRECK reaction mechanism (Fig. D10 and Fig. D11).

Figure 7.5 shows the reaction path analysis for the C_2H_6/CO_2 blends at the time of 50% CO_2 conversion. Note that only the most important pathways are shown, and less distinctive pathways might also occur.

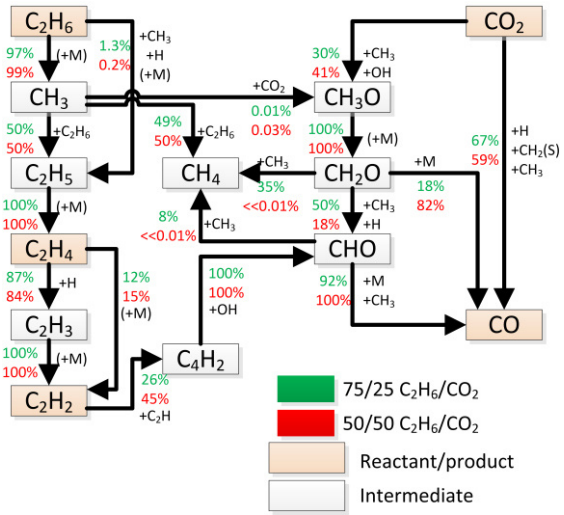

Figure 7.5. Reaction path analysis using PolyMech2.1 [111] at ~2260 K for 25% and 50% CO_2 blends in C_2H_6. The numbers are denoted to the carbon flux related to the respective reactant at 50% CO_2 conversion.

On the right side of the diagram is the path of CO_2 consumption, which mainly reacts directly to form CO via the reverse reaction of (R7.1), which forms OH radicals and consumes H radicals and, via reaction (R7.2), consumes the singlet state methylene $CH_2(S)$. This sequence is also in accordance with Rudolph et al. [113], showing a similar path of CO_2 decomposition in the dry reforming of methane. A first inspection of the

numbers in the figure shows that the paths on the left side for ethane consumption are negligibly influenced by the mixture composition. Thus, the CO_2-consumption path must be regarded in more detail.

$$CO + OH \rightleftharpoons CO_2 + H \quad \text{(R7.1)}$$
$$CH_2(S) + CO_2 \rightleftharpoons CH_2O + CO \quad \text{(R7.2)}$$

The reverse reaction with CH_3 (R7.3), which is present in large quantities, is also important for CO_2 consumption; here methoxy radicals (CH_3O) and CO are formed.

$$CH_3O + CO \rightleftharpoons CH_3 + CO_2 \quad \text{(R7.3)}$$

The decomposition of C_2H_6, shown on the left side of the diagram, occurs via reverse reaction (R7.4) and reaction (R7.5), forming CH_3 and C_2H_5. Oxidation reactions of C_2H_6 are not observed since most OH radicals are consumed by the formation of $CH_2(S)$ (via $CH_3+OH \rightleftharpoons CH_2(S)+H_2O$, not shown in Fig. 7.5.) and H_2O (via $H_2O+H \rightleftharpoons OH+H_2$).

$$CH_3 + CH_3 (+M) \rightleftharpoons C_2H_6 (+M) \quad \text{(R7.4)}$$
$$C_2H_6 + H \rightleftharpoons C_2H_5 + H_2 \quad \text{(R7.5)}$$

The formation of unsaturated hydrocarbons, such as C_2H_4 and C_2H_2, proceeds via H abstraction reactions (reverse reaction R7.6 and reactions R7.7 and R7.8). Also, since the temperatures are greater than 2000 K, C_2H_4 is nearly completely decomposed to C_2H_3 and C_2H_2. Large quantities of H radicals are consumed in reaction (R7.7) and reverse reaction (R7.12), forming the intermediate C_2H_3 and stable CH_4. Especially the formation of CH_4 binds many H atoms, which are then not available for reverse reaction (R7.1). Therefore, compared to the methane conversion discussed in Rudolph et al. [113], pathways with $CH_2(S)$ and CH_3 are much more important for CO formation in the dry reforming of ethane.

$$H + C_2H_4 (+M) \rightleftharpoons C_2H_5 (+M) \quad \text{(R7.6)}$$
$$C_2H_4 + H \rightleftharpoons C_2H_3 + H_2 \quad \text{(R7.7)}$$
$$C_2H_3 (+M) \rightleftharpoons C_2H_2 + H (+M) \quad \text{(R7.8)}$$

Large quantities of C_2H_2 are further decomposed to CHO via C_4H_2, making reaction (R7.9) one of the most important reactions for CO formation, which is again similar to the methane conversion path discussed in Rudolph et al. [113].

$$CHO + M \rightleftharpoons CO + H + M \quad \text{(R7.9)}$$

At lower temperatures, the CO_2 decomposition via (R7.2) is favored because $CH_2(S)$ radicals are increasingly formed from CH_3, which again is formed in C_2H_6 decomposition. Also, since H radicals are consumed in the reaction with C_2H_6 forming C_2H_5 in (R7.5) and with C_2H_4 in (R7.7), they cannot contribute to CO_2 conversion. Conversely, at higher temperatures, reverse reactions (R7.1) and (R7.3) are favored, forming also methoxy (CH_3O) radicals. With increasing CO_2 fractions, less H is available for reverse reaction (R7.1) and reaction (R7.2). However, the oxidation pathway, forming CH_3O and CHO, is promoted as the concentrations of O and OH in the mixture increase, leading to faster CO formation with increasing CO_2 fraction.
The reaction pathway of C_3H_8/CO_2 blends has a similar structure and is presented in Fig. 7.6. An inspection of the numbers reveals that there are no large differences along any path due to the CO_2-fraction. But a comparison of the CO_2 consumption path for the two hydrocarbons reveals that the CO_2 reaction along the right path (with H, singlet methylene, and methyl) strongly dominates in the propane system. The decomposition of CO_2 occurs via similar reactions: reverse reaction (R7.1) and reactions (R7.2) and (R7.9). In the propane mixture, these reactions are slightly enhanced (observed in the rate-of-production analyses in the supplementary material, Fig. D10. And Fig. D11.) compared to C_2H_6 because C_3H_8 decomposes directly to C_2H_5 (via (R7.10)) which further reacts to C_2H_4 via reverse reaction (R7.6), providing more H radicals than C_2H_6.

$$C_3H_8 (+M) \rightleftharpoons C_2H_5 + CH_3 (+M) \quad \text{(R7.10)}$$

The formation of unsaturated species, such as C_3H_6 and C_2H_2, and CH_4, does not consume or bind any radicals or atoms. As the path along reverse reaction (R7.1) dominates, more OH radicals are also formed in the first steps, leading to an increased formation of $CH_2(S)$ (via $CH_3 + OH \rightleftharpoons CH_2(S) + H_2O$) and providing more $CH_2(S)$ for (R2).
The previously described effect that the CO formation at low temperatures (~2000 K) is faster for the C_2H_6 mixture than for the C_3H_8 mixture can be explained based on the previous analysis: at low temperatures, CO formation via (R7.2) is favored. The singlet state radical $CH_2(S)$, however, is formed in CH_3 reactions, which is formed in larger amounts in C_2H_6 decomposition than in C_3H_8 decomposition, leading to smaller reaction rates for reaction (R7.2) for the C_3H_8/CO_2 blends at low temperatures. At intermediate and high temperatures, the effects described above become more relevant.

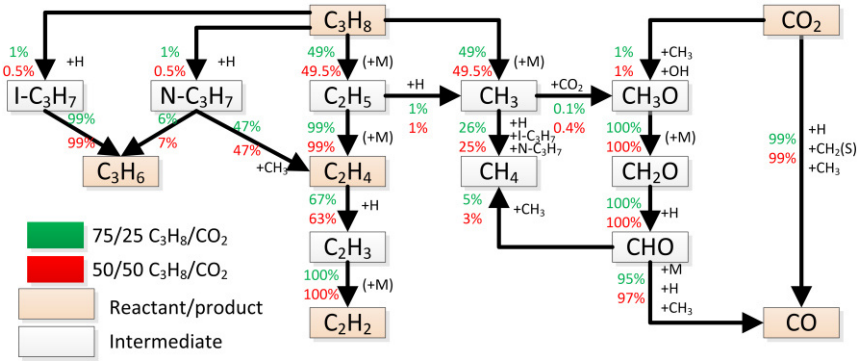

Figure 7.6. Reaction path analysis using PolyMech2.1 [111] at ~2260 K for 25% and 50% CO_2 blends in C_3H_8. The numbers are denoted to the carbon flux related to the respective reactant at 50% CO2 conversion.

The rate of production analysis performed with the CRECK model shows similar trends, as can be seen in Fig. D11 in the supplementary material. The reactions rates for (R7.1), (R7.2) and (R7.9) are the same, but since the predicted CO mole fractions are different, the rates of the hydrocarbon decomposition reactions have a large influence. A sensitivity analysis was performed using PolyMech2.1 to unravel the key reactions needing improvement for a better prediction of the CO formation at these conditions. The sensitivity analysis is shown in Fig. 7.7 for all investigated mixtures and three representative temperatures, namely ~2000 K, ~2260 K, and ~2450 K. To show the variation of the sensitivity along the reaction time, the analysis for three times 50 µs, 500 µs, and 1500 µs are presented here. Complete sensitivity analyses for the PolyMech2.1, CRECK, Burke, USC, and NUIGMech1.1 models can be found in the supplementary material (Fig. D12.-Fig. D16.).

The most sensitive reaction for CO formation is reverse reaction (R7.1) for each condition, temperature, and test time. Along the test time, reverse reaction (R7.1) gains importance for the low and intermediate temperature for all C_2H_6 and C_3H_8 blends. For the high-temperature regime, the trends are cluttered. For the 25% CO_2 blend in C_2H_6, reverse reaction (R7.1) becomes more important along the test time, finally being nearly the only sensitive reaction at 1500 µs. In contrast, all other mixtures show a maximum sensitivity at 500 µs in the high-temperature regime. In the first 500 µs, which is the most relevant part, the sensitivity of reverse reaction (R7.1) increases with increasing temperature, and the sensitivity distribution is slightly shifted from (R7.2) (sensitive at low temperatures) to (R7.1). The sensitivity of the decomposition reactions of the hydrocarbons, *e.g.*, reaction (R7.5) and (R7.10), is comparably small. In the 50% CO_2 blends, oxidation reactions such as (R7.11) gain in sensitivity since more O and OH radicals are available and produce H radicals, converted in reverse reaction (R7.1).

$$CH_3 + OH \rightleftharpoons CH_2OH + H \qquad (R7.11)$$

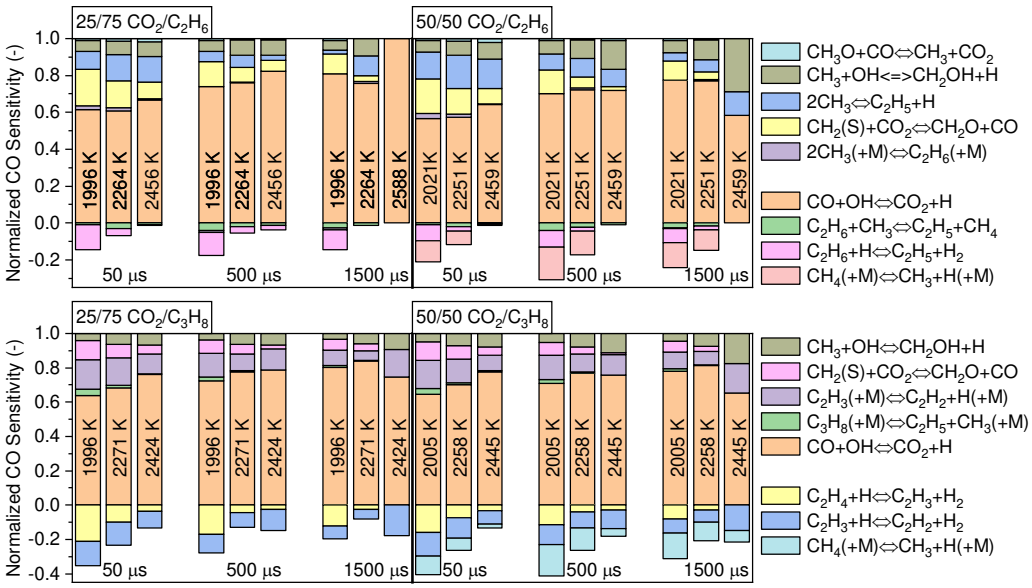

Figure 7.7. Sensitivity analyses using PolyMech2.1 [111] for 25% and 50% CO_2 blends (left to right) in C_2H_6 and C_3H_8 (top down) at different temperatures (~2000 K, ~2260 K, and 2450 K). The sensitivities are presented for 50 µs, 500 µs, and 1500 µs along the total test time.

In C_2H_6 blends, the CO formation is mainly sensitive to the rates of C_2H_6 decomposition reactions and of CO formations reactions. The CO formation in C_3H_8 blends is also sensitive to the rates of reactions with higher hydrocarbons, such as reactions (R7.7) and (R7.8). This result is due to the enhanced formation of C_2H_5, which reacts directly to the unsaturated hydrocarbons. Interestingly, the formation of CH_4 via the reverse reaction (R7.12) is also very sensitive with a negative sensitivity coefficient, because the CO formation is precluded, since H-atoms are required for this reaction.

$$CH_4 (+M) \rightleftharpoons CH_3 + H (+M) \qquad (R7.12)$$

The sensitivity analyses performed with the CRECK, the NUIGMech1.1, the Burke and the USC models, shown in the supplementary material (Figs. D13.-D16.), lead to qualitatively similar results. The most important reactions are the decomposition reactions of CO_2 (reverse reaction (R7.1) and reaction (R7.2)) and the hydrocarbon formation reactions (reverse reaction (R7.7) and reaction (R7.8)). For the C_2H_6 mixtures, the decomposition of C_2H_6 via reverse reaction (R7.4) and the recombination of CH_3 to release H-atoms ($CH_3 + CH_3 \rightleftharpoons C_2H_5 + H$) affect mostly the CO formation. Similarly, for the C_3H_8 mixtures, the decomposition reactions of C_3H_8 (R7.10 and reverse reaction *i*-$C_3H_7 + H \rightleftharpoons C_3H_8$ and $C_3H_8 + H \rightleftharpoons H_2 +$ *n*-C3H7 are the most sensitive reactions. To understand the different predictions of the reaction mechanisms, the reaction rates of the above reactions are regarded. These are shown in the supplementary material. The

reaction rates for reaction (R7.1) and (R7.2) are mostly identical with an exception for (R7.1) implemented in the NUIGMech1.1 is slightly smaller at low temperature, so for the NUIGMech1.1 model, (R7.2) gains more importance at low temperatures. The reaction rates for the hydrocarbon containing reactions (C_2H_6 and C_3H_8 decomposition as well as C_2H_2 and C_2H_4 formation) vary between the different mechanisms. Similar, the sensitive reaction i-C_3H_7 + H ⇌ C_3H_8 is not even included in the PolyMech2.1 and the USC model. These variations and the not included reaction cause the deviating prediction capability of the reaction mechanisms. Special emphasis is taken on the reaction (R7.2) as this reaction is very sensitive on CO formation, however, it has been the subject of only a moderate number of studies, *e.g.*, [151–154]. The reaction rate of CO_2 + CH_2(S) ⇌ CH_2O + CO (R7.2), implemented in all models presented here and various models beyond them (e.g., Aramco3 [68], GRI3.0 [155] or the Cai&Pitsch model [119]) was determined experimentally at ambient conditions (298 K, 1 atm) by Koch et al. [154] in 1990. An alternative is the reaction rate of Miller et al. [156] from 1992, which is obtained by detailed kinetic and thermodynamic modeling. This reaction rate [156] is implemented in, *e.g.*, the mechanisms of Petersen et al. [157], Marinov et al. [158], and the SanDiego model [159]. Since this reaction is of great importance for systems such as the one studied here, kinetic models could benefit tremendously from an updated reaction rate of the reaction (R7.2).
To summarize, the interaction between the alkane and CO_2 in gas phase dry reforming is dominated by the provision of H-containing radicals, such as H, CH_3, CH_2(S) and CHO, supporting the CO formation without consumption of the reactants themselves. The most important and sensitive reactions for CO formation are reverse reaction (R7.1) CO+OH ⇌ CO_2+H and reaction (R7.2) CH_2(S)+CO_2⇌CH_2O+CO, and, depending on the alkane, the formation reactions of further products such as C_2H_2, C_2H_4 or CH_4. As it is one of the key species, the formation of C_2H_2 plays an important role in the whole process for all alkane/CO_2 blends.

7.4.4 Shock-tube measurements above 2500 K

Shock-tube experiments were also carried out at temperatures above 2500 K but led to results in need of further investigation with respect to the laser absorption. Experiments were performed at temperatures above 2500 K in C_2H_6/CO2 and C_3H_8/CO_2 blends. Also, to extend the data, CO time histories at similar conditions (>2500 K) derived from CH_4/CO_2 blends were taken from Rudolph et al. [113]. Throughout, it was found that the determined fraction $x_{CO,rel}$ was above 1 at longer reaction times, as shown in Fig. 7.8.

Figure 7.8 depicts the relative mole fraction $x_{CO,rel}$ as a function of the reaction time for different CO_2 fractions and different hydrocarbon blends at temperatures above 2500 K. As it can be seen, the theoretical maximum is exceeded by up to 30%, which is significantly larger than the standard uncertainty of 5%, as determined for all other measurements. The offset increases with the order of the hydrocarbon and the smaller the CO_2 amount. In particular, the offset of C_3H_8 blends is significantly larger.

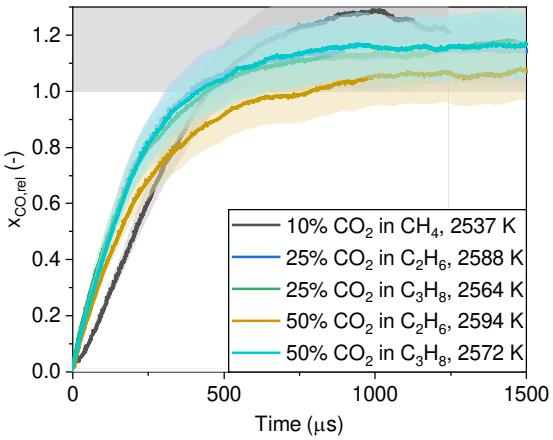

Figure 7.8. Relative mole fraction $x_{CO,rel}$ as a function of test time for 10%, 25% and 50% CO_2 blends in CH_4, C_2H_6, C_3H_8, respectively, at temperatures above 2500 K. Shaded areas are experimental uncertainties.

To rule out possible error sources, further measurements were carried out. First, new mixtures were prepared, and new experiments were performed, showing good reproducibility. Off-line measurements were also performed to check whether other species like soot or higher hydrocarbons may be responsible for this reproducible effect at high temperatures, but no light absorption was observed. Experiments to measure the emission were performed (laser light blocked) but no emission was detected. To figure out the influence of the hydrocarbon, CO formation from H_2/CO_2 blends with a ratio of 50%/50% being diluted in 99.25% Ar/He were investigated at temperatures of 2600 and 2700 K. Using H_2 blends did not lead to a similar phenomenon, and CO mole fractions therefrom did not exceed the theoretical maximum, obtained from the atom balance, showing that the spectroscopy works well at these high temperatures and for high amounts of CO to be measured. Also, extending the calibration of the absorption coefficient to higher amounts of CO does lead to a decrease of the absorption coefficient k_ν along the temperature range, which in turn rather increases the CO mole fractions obtained from the raw data. Also, to the best of the authors' knowledge, no other species absorb at 2059.91 cm^{-1} of the P(20) transition line. It is however possible that a species formed at such high temperature, most likely involved in the formation of larger species leading to soot, can absorb at this specific wavelength.

Another possibility for the unphysical results is the calculation of the mole fractions from the signals I_t and I_0. As already described, the temperature and pressure from the simulations are used for those calculations. However, since the temperature profiles are strongly dependent on the reactions occurring as well as on the thermo-chemistry of the reactants, the products and the intermediates, uncertainties in the thermo-data of the models could cause large temperature differences. These temperature differences strongly influence the calculated mole fraction and can account for the 30%-overshoot at temperatures T_5 above 2500 K. Since such behavior was only seen in the hydrocarbon/CO_2 mixtures, it can be assumed that it concerns the thermo-data of the hydrocarbons and their intermediates. These deviations in the CO mole fraction due to uncertainties in the thermodynamics data and modeled time-resolved temperature profiles could also occur at low or intermediate temperatures T_5 (below 2500 K). However, processing the raw data using different datasets of thermodynamic data to calculate the absorption coefficient and the CO mole fraction does not lead to increased uncertainties. Herein, in-situ temperature measurements could help to avoid this problem associated with the varying temperature profiles from the modeling. However, the importance of improving the thermo-data from the main species and the intermediates at very high temperatures should be emphasized. Detailed information can be found in the supplementary material.

Another plausible explanation could be that the CO formed at high temperature is at least in part not in thermal equilibrium. Calculating the vibrational partition function at 2600 K reveals that nearly 30% of the CO molecules are in the first vibrationally excited state (v = 1) in equilibrium. If the reaction dynamics of the most important reactions (R7.1) are regarded, it is known that the product distribution is based to the vibrational ground state of CO, at least for certain initial energies of the reacting H-atoms [160]. If a smaller fraction of CO would be in the v = 1 state, the absorption coefficient would increase, leading to an overestimation of the CO mole fraction. This outcome would also be in agreement with the stronger effect in propane mixtures, where the reaction path towards CO is dominated much more strongly by reverse reaction (R7.1) than for ethane, as discussed above. However, this hypothesis needs further experimental verification in future work. The measurements below 2500 K presented in this work and in Rudolph et al. [113] do not exceed the theoretical maximum, and should be reliable, although some bias cannot be excluded. Note that such non-equilibrium effects are generally not included in elementary reaction mechanisms.

7.5 Conclusion

In this work, the pyrolysis of CO_2/C_2H_6 and CO_2/C_3H_8 mixtures and the associated CO formation behind reflected shock waves were studied for the first time in the context of dry reforming in piston engines. The reaction times and temperatures in shock tubes are quite relevant for typical piston engines, so that some transfer of the results can take place. To investigate first the fundamental kinetics in this process, shock-tube experiments connected to laser absorption measurements using a quantum cascade laser were performed at ~1 atm and 1830 K–2450 K. The scope of this study was to gain better understanding of the influence of different linear alkanes on CO_2 decomposition. In addition to the provision of experimental data to complete literature datasets, the experimental data were compared with the prediction of literature reaction mechanisms. A statistical analysis sets out the best agreement with the CRECK [114] model and the PolyMech2.1 [111] and still acceptable agreement with the USC [150] model, while the Burke [149] and the NUIGMech1.1 [127] models have insufficient agreement. Such a statistical analysis is not often used in the literature, but may be a better approach than just comparing species time histories in reacting systems qualitatively.
The following analysis using the PolyMech2.1 model revealed that the CO_2 decomposition is initiated due to the consumption of the linear alkanes, leading to early radical formation. Herein, CO_2 is directly converted to CO via $CO_2+H \rightleftharpoons CO+OH$ and $CH_2(S)+CO_2 \rightleftharpoons CH_2O+CO$, which appeared to be the most important reactions according to rate-of-production and sensitivity analyses. The linear chains of C_2H_6 and C_3H_8 first decay via unimolecular reactions towards CH_3, and $CH_3+C_2H_5$, leading further to the formation of H and $CH_2(S)$, respectively. In particular, the CO formation in the C_2H_6/CO_2 mixtures is faster than in the C_3H_8/CO_2 mixtures, as evidenced by a smaller τ_{20} (defined as the time needed to reach 20% of the theoretical maximum CO mole fraction), because of increased CH_3 formation, being needed for $CH_2(S)$ and the C_1-oxidation pathway. Also, the H-radical provision via, *e.g.*, $H+C_2H_4(+M) \rightleftharpoons C_2H_5 (+M)$ is generally slower than the oxidation reactions, justifying the higher τ_{20} for the C_3H_8 mixtures. An increasing CO_2 amount in the mixture leads to the increasing availability of O atoms and OH radicals, respectively, thus, oxidation pathways forming CH_3O or CH_2OH are favored, and overall CO formation is increased. Since the pyrolysis of linear alkanes results in the formation of unsaturated hydrocarbons, such as C_2H_2 at very high temperatures, their formation and decomposition reactions contribute significantly to H radical consumption (*i.e.*, via $C_2H_4+H \rightleftharpoons C_2H_3+H_2$) and thus influence the consumption of CO_2 and the associated formation of CO. These general principles, found by rate-of-production and sensitivity analyses using PolyMech2.1, were supported by those of the CRECK model, yielding similar results. However, none of these models are able to

predict the CO formation from C_2H_6/CO_2 or C_3H_8/CO_2 pyrolysis, which shows the necessity for improvement of often-investigated reaction rates for untypical conditions, such as those needed for engine-based dry reforming.
Only at temperatures above 2400 K is CO formation complete within 2 ms, which would also be the preferable time in usual piston engines, where the whole cycle takes 10–200 ms. Thus, compression ratios or pre-heating must be selected accordingly. From the results above 2500 K, it seems that CO is not in thermal equilibrium, which is worth further investigation, and perhaps is also part of the discrepancy between the model predictions and the experimental findings for temperatures above 2500 K. Additionally, the importance of improving thermochemistry at temperatures above 2500 K is highlighted.
To extend the knowledge about dry reforming processes, additional investigations should be carried out on the formation of hydrogen and unsaturated hydrocarbons, *e.g.*, C_2H_2, in future work. To investigate this process also for conditions more suitable for combustion engines, high-pressure experiments would be desirable.

7.6 Acknowledgements

Financial support by the Deutsche Forschungsgemeinschaft within the framework of the DFG research unit FOR 1993 “Multifunctional conversion of chemical species and energy” (Project number 229243862) is gratefully acknowledged. Additional support for the experiments came from the Texas A&M Engineering Experiment Station (TEES) and the TEES Turbomachinery Laboratory in the form of a Ralph-James Fellowship (for CMG). Additional support was provided by King Fahd University of Petroleum & Minerals through the Saudi Arabian Cultural Mission in the form of fellowship funding for coauthor SAA (Fellowship No 1440/10079/9)

8 Conclusion and Outlook

8.1 Conclusion

The ambitious goal to halve greenhouse gas emissions within the next eight years is based on the indispensable need to build a net-zero-emissions energy system to keep the 1.5°-target. This requires a technological change, accomplished in the shortest time possible. The key to managing the technological change within the targeted eight years could lie in technically matured and socially accepted technologies, such as combustion engines, with alternative operating strategies. In this context, the use of combustion engines could accelerate the technological change. Combustion engines exhibit a high degree of flexibility to guarantee a sector-wide and readily available energy supply by renewable primary energies. Because the flexibility of these engines is based on the fact that the cylinder charge of the combustion engine can be varied according to the demand: a fuel-lean operated combustion engine provides mainly mechanical/electrical power. In contrast a fuel-rich operated combustion engine simultaneously provides mechanical/electrical energy, heat, and important chemicals, a process known as polygeneration. The use of combustion engines in terms of polygeneration has been intensively studied within the research unit FOR1993 [60] from theoretical ideas to practical implementation and economic considerations. An alternative process is to operate an internal combustion engine in the form of a power-to-gas process. In this case, the combustion engine would be a compressor rather than a chemical reactor. The engine-based, power-to-gas process relies on endothermic, endergonic pyrolysis, or dry reforming of methane or natural gas forced by the energy input during the compression stroke. In conjunction with exergy storage, this involves the conversion of surplus energy from renewable sources into storable, chemical exergy. In that process, chemicals are produced that have a high energetic value (*e.g.*, calorific value) or can be used as base chemicals for subsequent processes (*e.g.*, Fischer-Tropsch synthesis).
This work addresses the chemical and thermodynamic evaluation of engine-based exergy storage to clarify whether the process is practical and exergetically feasible, as well as to identify operating principles and appropriate conditions. For this purpose, thermodynamic-kinetic simulations and fundamental validation experiments were performed. The focus is on the unconventional concept of performing pyrolysis and dry

reforming of hydrocarbons in a homogeneous high-temperature gas-phase process instead of the usual catalytic process. High temperatures at the end of compression help to overcome the high activation energies. The reactants are diluted with a monoatomic inert gas to reduce the high heat capacity of the mixture.
Previous thermodynamic evaluations under the simplified assumptions of reversible, adiabatic compression and complete conversion of the reactants have already shown that engine-based exergy storage is both practical and exergetically favorable [59]. These assessments are complemented by a fundamental and detailed investigation based on simulations of the engine cycle. Engine simulations make it possible to define operating ranges and uncover undesirable behavior before conducting expensive experiments or implementing the process into an existing system. In addition, the comprehensive analysis of the result indicates whether the process is exergetically feasible under engine conditions.
The engine simulations were performed with Cantera [161] within python using a single-zone model. The single-zone model was chosen because the assumption of a homogeneous temperature, pressure, and species distribution inside the cylinder provides a compromise between accurate results and short computation times. The kinematics were also implemented so that the energy, species, and mass balances can be solved according to the laws of thermodynamics for each piston position over several cycles. The simulation includes the exergetic analysis of the process and the product gas composition based on the 2nd law of thermodynamics. The target results are product gas yields, chemical exergy change, exergetic and energetic values (among others, work, heat, irreversible entropy, exergy loss), and exergetic efficiency. Various literature heat transfer models and reaction mechanisms were used to model the heat transfer and the chemical kinetics, and their influence on the simulation results was analyzed.
The investigated parameters can essentially be divided into two different groups: geometric and kinematic engine parameters, which include the engine size (bore, stroke), the compression ratio, and the engine speed, and thermodynamic conditions, which include the intake temperature, the intake pressure, and the mixture composition. The range of each parameter was chosen according to typical values, but the optimal parameters emerged from the analysis of the simulation results. A total of four different reactants or reactant mixtures were investigated with respect to engine-based exergy storage and carbon capture and utilization: neat methane, neat ethane, natural gas /hydrogen, and methane/CO_2.

Influence and limitation of inlet parameters

Varying engine sizes were considered (*i.e.*, an 0.4 l engine up to a 4.8 l engine) resulting in a smaller cylinder surface to cylinder volume ratio and, thus, less heat losses per

volume with increasing engine size. Heat losses lead to a temperature decrease inside of the cylinder compared to adiabatic compression and to more local gradients, making them unfavorable for temperature-driven chemical processes. Exergetically, increasing heat losses lead to increasing exergy losses or, more precisely, exergy destruction, even if part of the heat transferred to the surrounding medium can be used. In addition, it must be mentioned that industrial-scale gas engines used in combined heat and power plants, for example, tend to be in the range of the 4.8 l engine. The compression ratio is crucial for the temperature and pressure at the end of compression and the work supplied to the piston engine by surplus renewable energies. This justifies the choice of compression ratios of 20 and 22, which are in the range of the technical upper limit. The engine speed affects the available reaction time for the chemical processes and the exergy and product flow rates. Here, small engine speeds allow for reaching chemical equilibrium before the expansion stroke quenches the mixture. At high engine speeds, the mixture is quenched immediately, allowing unstable products or intermediates to persist. In the pyrolysis of hydrocarbons, it is desirable that intermediates such as acetylene, ethylene, and benzene remain, as they have high specific exergies and are chemically valuable. On the other hand, soot, or species such as methane (as a product), occurring mainly in chemical equilibrium at high temperatures, are undesirable. Those species have a lower exergy and are chemically less valuable than the initial reactant. Thus, a high engine speed (here, 3000 min^{-1}) is recommended for the engine-based pyrolysis, leading to a fast quenching of the mixture. In contrast, the dry reforming of hydrocarbons can lead to the formation of synthesis gas if chemical equilibrium is reached and, similarly, enables the formation of higher molecular weight hydrocarbons when the mixture is quenched fast enough. However, the latter happens to the detriment of CO_2 conversion. Accordingly, a relatively high engine speed (here, 3000 min^{-1}) or a relatively low engine speed (here, 1500 min^{-1}) can be beneficial for the dry reforming process, depending on the demand.

The variation of the inlet pressure initially ranged from 1 atm to 10 atm, but it was shown that increasing inlet pressures are detrimental to the chemical process according to the principle of "Le Chatelier". An inlet pressure of 1 atm leads to pressures below 1 atm at the outlet valve. Therefore, the inlet pressure was set to 1.2 atm in subsequent studies.

The required argon mole fraction (to reduce the heat capacity) and inlet temperature are coupled in terms of achieving a particular compression temperature which is already implied by the isentropic law for ideal gases ($T_{compression} = T_0 \cdot \varepsilon^{cp/cv}$). High argon fractions should be avoided to favor absolute reactant and, thus, product amounts in the mixture so that high inlet temperatures are required. The exergetic analysis shows that inlet temperatures above 900 K lead to high exergy losses during the compression

and expansion strokes and an increased work supply. Consequently, the exergetic efficiency of the process decreases significantly. Entropy production occurs mainly due to temperature and pressure change, chemical reactions, and heat transfer. Because of the endothermic process and the entropy production, the temperature and pressure at the outlet are significantly lower than at the inlet. Assuming the preheating of the mixture to temperatures above 900 K is done by recirculating the hot (or rather "cold") product gas, the exergetic efficiencies would be halved. Despite high inlet temperatures, an argon mole fraction of ~70% would still be required. Therefore, the needed argon mole fraction and inlet temperatures are in the range of 90-97% and 373-573 K, respectively. For the pyrolysis of methane, for example, the optimum conditions in terms of chemical exergy change are 93% argon, 10 bar and 573 K. For the pyrolysis of ethane, the optimum conditions tend to be 93% argon, 10 bar, and 373 K. The addition of hydrogen leads to a slight shift towards lower inlet temperatures, from 473 K (no hydrogen) to 423 K (20% hydrogen) at 1 bar and 94% argon, with maximum exergetic efficiencies achieved because of the increased reactivity. In contrast, the addition of CO_2 leads to the need for higher inlet temperatures and similarly smaller argon mole fractions, from 94% argon (no CO_2) to 91% argon (60% CO_2) caused by smaller volumetric heat capacities with increasing CO_2 fraction. However, these parameters are narrowed down depending on the current demand.

Methane and CO_2 conversion

The required end-of-compression temperatures vary for the different reactants. For methane pyrolysis, the maximum temperatures needed to achieve a methane conversion of 75% are ~1900 K. For ethane pyrolysis, significantly lower temperatures (~1400 K) are required for an ethane conversion of 75%, as ethane is much more reactive. Considering the natural gas/hydrogen mixture, a significant reduction in the temperature required to achieve 75% methane conversion is expected; however, only a decrease of 50 K was observed. This is due to the early consumption of reactive radicals such as H, CH_3, and C_2H_5 by ethane and propane. The dry reforming of methane requires slightly lower maximum temperatures of 1800 K to achieve a methane conversion of 75%, compared to methane pyrolysis. This lower temperature can be attributed to the fact that although CO_2 is very inert, the presence of O-atoms is the basis for the formation of very reactive OH radicals and exothermic oxidation reactions. The CO_2 conversion in the methane/CO_2 is slightly shifted towards higher temperatures so that maximum temperatures of ~1850-1900 K are needed to achieve a conversion of 75%.

Products

The target products are hydrogen, acetylene, ethylene, and benzene, and if CO_2 is added to the reactants, CO. The formation of the products depends strongly on the

composition of the initial mixture and the reactants, but also on the initial conditions (*i.e.*, temperature, pressure, and argon mole fraction). In other words, this also means that the desired chemicals can be produced on demand. The main product is hydrogen, which is inevitably produced by the decomposition of the reactants to species with a smaller H/C ratio. Because of the beneficial H/C ratio of methane, the maximum yields of up to 80% are found for methane pyrolysis and dry reforming of methane at maximum temperatures above 2500 K. CO is only formed in the dry reforming process due to the presence of O-atoms in CO_2. Maximum yields of up to 80% are achieved when chemical equilibrium is reached at temperatures above 2500 K.
An energetically and chemically important chemical is ethylene. The formation of ethylene mainly occurs via the C_2-pathway from ethane pyrolysis. Here, maximum yields of up to 60% at low to intermediate temperatures of 1300-1600 K are promising. Ethylene originating from methane decomposition and subsequent recombination reactions is usually only an intermediate product to acetylene, so only a small amount remains. If acetylene is targeted, methane-based mixtures (methane, natural gas/hydrogen, methane/CO_2) and maximum temperatures above 2000 K are promising with yields between 20 and 50%. The most promising result in terms of acetylene formation is obtained with the natural gas/hydrogen mixture because the hydrogen addition forces the needed carbon to remain in a loop of decomposition and formation of acetylene by +H or +H_2 reactions. Additionally, acetylene is the precursor for the formation of C_3H_3, PAHs, and thus soot. These findings make acetylene the target chemical for methane pyrolysis and dry reforming of methane. The formation of benzene is based on the decomposition of acetylene. Thus, maximum benzene yields of up to 16% are achieved by methane pyrolysis at intermediate temperatures around 1600-1700 K. As benzene is a PAH precursor, it becomes evident that soot formation occurs to a greater extent during methane pyrolysis. However, these studies have shown that adding H_2 or CO_2 reduces benzene, larger PAH, and soot formation as the carbon remains in acetylene (H_2 addition) or CO (CO_2 addition). Although no soot is predicted during the pyrolysis of ethane, there are also unwanted products such as methane, which strongly reduce the chemical exergy increase. The methane formation from ethane pyrolysis occurs mainly via two pathways, first, directly from ethane decomposition and second, from ethylene decomposition. Also, methane formation is favored when the maximum temperatures exceed 1600 K. Overall, certain products can be produced on demand, but undesirable soot or methane formation must be avoided.

Exergetic analysis

The exergetic analysis discloses that for all processes (pyrolysis and dry reforming), only small exergy losses occur. The exergy losses are mainly the result of heat losses and

only to a small extent caused by the entropy production associated with the chemical reactions. Overall, exergy losses are less than 5% of the total exergy of the system (on the output side). Exceptions are the dry reforming process, when high CO_2 fractions are used, or ethane pyrolysis, when large amounts of methane are formed. Here, exothermic reactions, *i.e.*, oxidation reactions of methane (dry reforming) or exothermic decomposition of ethane to methane (ethane pyrolysis), lead to a proportionally increased entropy production by the chemical reactions. In this case, exergy losses account for up to 10% of the total exergy amount of the system (on the output side). The largest exergy input is derived from the chemical exergies of the reactants (up to 90% of the total exergy) and the work supply. On the output side, the largest exergy amounts come from the chemical exergies of the products. In particular, the formation of hydrogen, acetylene, and ethylene contributes significantly to the total exergy. The chemical exergy increase due to the formation of higher hydrocarbons, is about 10%. The exergetic efficiency as the ratio of the chemical exergy increase to work input is one of the decisive parameters for evaluating the possibility of chemical exergy storage. Overall, maximum exergetic efficiencies of up to 75% are achieved. The formation of higher hydrocarbons significantly increases the efficiency because of their high specific chemical exergies. Even if the exergy of the initial mixture is increased by the addition of hydrogen or by using ethane, this is at the expense of the chemical exergy increase, and the exergetic efficiencies drop to 54% (H_2 addition) and 70% (ethane pyrolysis), respectively. In general, engine-based exergy storage has been shown to be associated with promisingly high exergetic efficiencies and low exergy losses. Interestingly, a comparison of the polygeneration and the exergy storage process shows that exergy storage performs comparably well in terms of exergy losses and product formation.

From theoretical to experimental investigations

The simulations mentioned above help to gain a general understanding of the process and provide information about possible product spectra. However, the particular outcome may change depending on the use of various models. In this regard, the heat transfer models, and the reaction mechanisms are to be mentioned in particular. It was shown that the accuracy of those models affects the temperature and pressure at each piston position, the conversion of the reactants, and the formation of intermediates and target species, highlighting the need for their validation. In this work, the accuracy of various reaction mechanisms was specifically investigated to evaluate the predictive capability of the engine simulations and to make suggestions for improvements of the respective reaction mechanism. Additionally, these validation experiments helped in understanding the underlying chemical processes.

High-temperature CO formation from dry reforming of alkanes: Experimental validation

For this purpose, shock-tube/CO laser absorption experiments were performed with respect to dry reforming of C_1-C_3 alkanes. The temperatures and time scales of the shock tube experiments were similar to the maximum temperatures required in the piston engine (1700–2700 K) and reaction times given by the engine speed (500 µs-5 ms). Generally, it was shown that the hydrocarbons and CO_2 were converted at these temperatures and within these time scales as the measurement of CO allowed for tracking the reaction progress and the conversion of the reactants. Of the three alkanes studied here, propane is the hydrocarbon with the longest chain length and should therefore be the most reactive. However, the calculation of CO formation time τ_{20} yielded that ethane is the most reactive hydrocarbon in terms of dry reforming, followed by propane and methane. The low τ_{20} for ethane is due to the enhanced CO formation via the C_1-oxidation pathway starting from CH_3 by C-C bond cleavage. The hydrocarbon decomposition benefits from the CO_2 addition because of the presence of O-atoms. There are two main pathways for CO formation for all hydrocarbons. The first pathway is based on the release of H radicals by the decomposition of methane and the C_2-formation pathway up to acetylene followed by the key reaction $CO_2+H \rightleftharpoons CO+OH$. The second pathway is based on the C_1-oxidation pathway, forming $CH_2(s)$ and CH_2OH followed by the key reactions $CO_2+CH_2(s) \rightleftharpoons CH_2O+CO$ and $CHO+M \rightleftharpoons CO+H+M$. The comparison of the experimental results and model predictions indicates that no reaction mechanism is capable of perfectly predicting the CO mole fraction for every condition. Sensitivity analyses revealed the potential for improvement in the reaction rates of the reactions $CO_2+H \rightleftharpoons CO+OH$ and $CO_2+CH_2(s) \rightleftharpoons CH_2O+CO$, as well as in the thermodynamic data of the hydrocarbons and their intermediates for all mechanisms. However, the general trends could be predicted well by the reaction mechanism created in the framework of the research unit FOR1993 by Porras et al. [17] and Zhang et al. [111]. Indeed, the PolyMech [17,111] and the CRECK Models [64,114] appear suitable for predicting reliable trends, so the engine simulation results for exergy storage and dry reforming are useful for process assessment and predicting feasible operating ranges.

Final remarks

Overall, engine-based exergy storage and dry reforming are efficient homogenous high-temperature power-to-gas processes to complement our future transitional energy system. It was shown that these processes offer the opportunity to provide particular chemicals on demand with simultaneously small exergy losses and high

exergetic efficiencies. This work closes the gap between simplified thermodynamic considerations, piston engine experiments, and economic assessments.

8.2 Outlook

The results showed that the process is generally feasible and trends regarding promising operating conditions, exergetic efficiencies and on-demand product formation could be predicted well by the engine simulations. Accuracy can be improved with better heat transfer correlations tailored to these unusual conditions and well-validated reaction mechanisms. While validation experiments are used to verify the reliability of reaction mechanisms, piston engine experiments need to be performed to investigate heat transfer models and the viability of the process itself. In this regard, the first steps were performed experimentally at Karlsruhe Institute of Technology by pyrolysis of methane, ethane, propane, and natural gas, highly diluted in argon, in a rapid compression machine. The associated simulations were performed in the framework of this work. These investigations will help to understand the behavior of the process under experimental conditions (*i.e.*, the temperature and pressure histories and the linked formation of species). Also, these experiments enable the development of more appropriate heat transfer models for pyrolysis or dry reforming in piston engines.

Secondly, it was shown that high amounts of argon are needed to reduce the heat capacity of the mixture and to achieve the required temperature increase for the conversion of the reactants. These high amounts of argon reduce the absolute amount of the reactant, the products, and consequently, the storable chemical exergy. At the same time, it is difficult and inefficient to separate small amounts of different products from the product gas. To that end, the process would benefit from reduced amounts of argon, which would not be at the expense of the exergetic efficiency and would not cause higher exergy losses. Adding small amounts of an oxidizer like O_2, O_3, or H_2O_2 could lead to a heat release-induced temperature increase when small amounts of the reactant are oxidized. This could be coupled to alternative engine concepts, such as membrane-piston reactors, similar to the concept introduced by Anderson et al. [162].

Thirdly, due to the high dilution, the resulting product gas from the engine cycle is a mixture of several chemicals in only small amounts. Specific products must be separated from the total mixture to be used as base chemicals in subsequent processes. Current concepts include condensing benzene or higher hydrocarbons, which have a comparatively high vapor pressure at surrounding temperature, using a cold trap. Hydrogen, ethylene, and acetylene could be separated using hydrogen membranes or multistage pressure swing absorption. Initial estimates showed that a separation, recirculation of argon, and a preheating concept by coupling the heat flows would reduce

the efficiency by about 10-15 percentage points. Therefore, it is necessary to optimize this separation process.

Appendix

A Supplementary material for "Pyrolysis of methane and ethane in a compression-expansion-process as a new concept for chemical energy storage – A kinetic and exergetic investigation"

1 Sensitivity analysis for methane pyrolysis (T_0 = 573 K, p_0 = 1 bar, 93 mol% Ar)

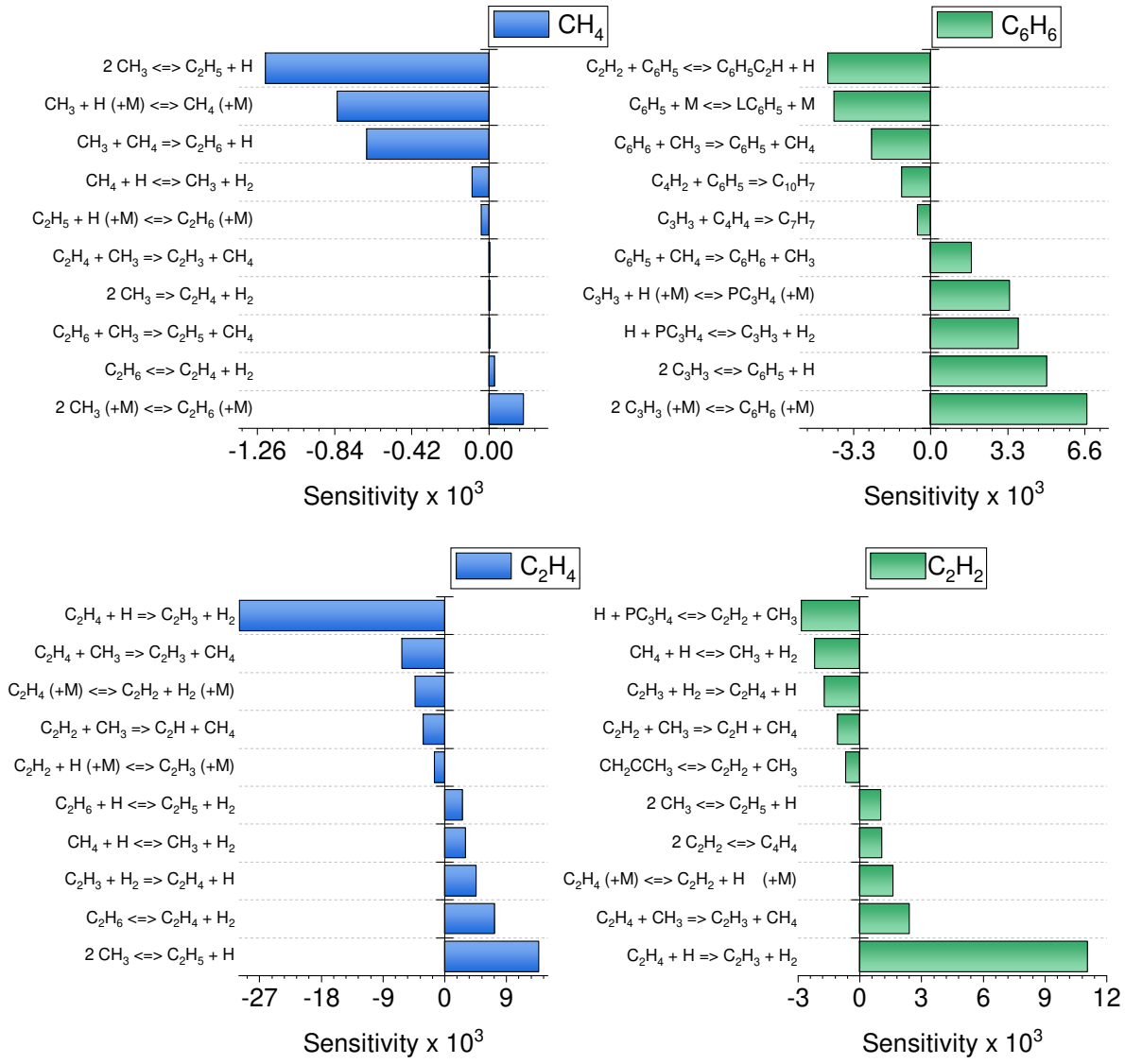

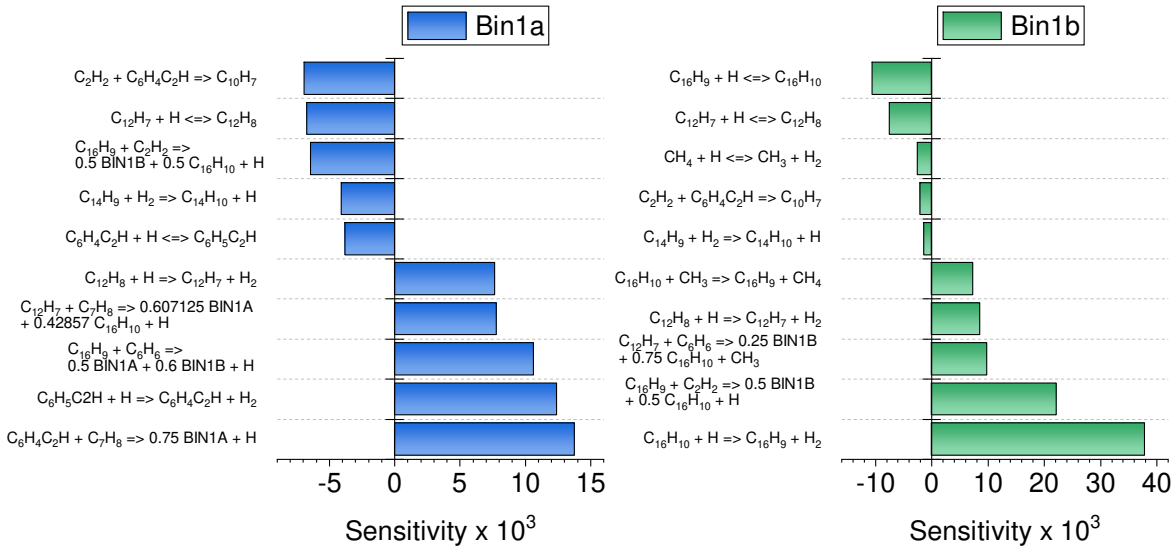

2 Sensitivity analysis for ethane pyrolysis (T_0 = 573 K, p_0 = 1 bar, 93 mol% Ar)

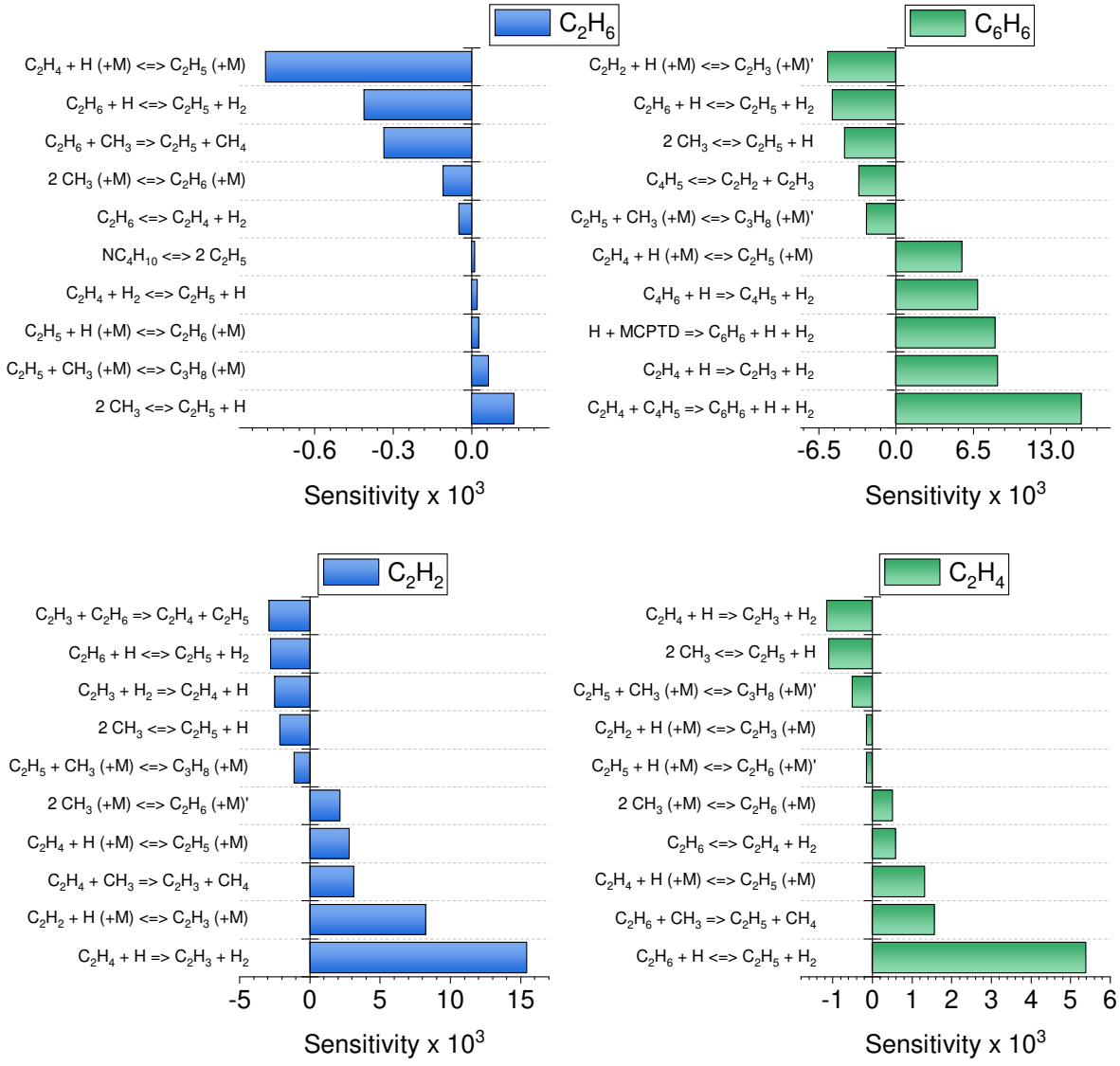

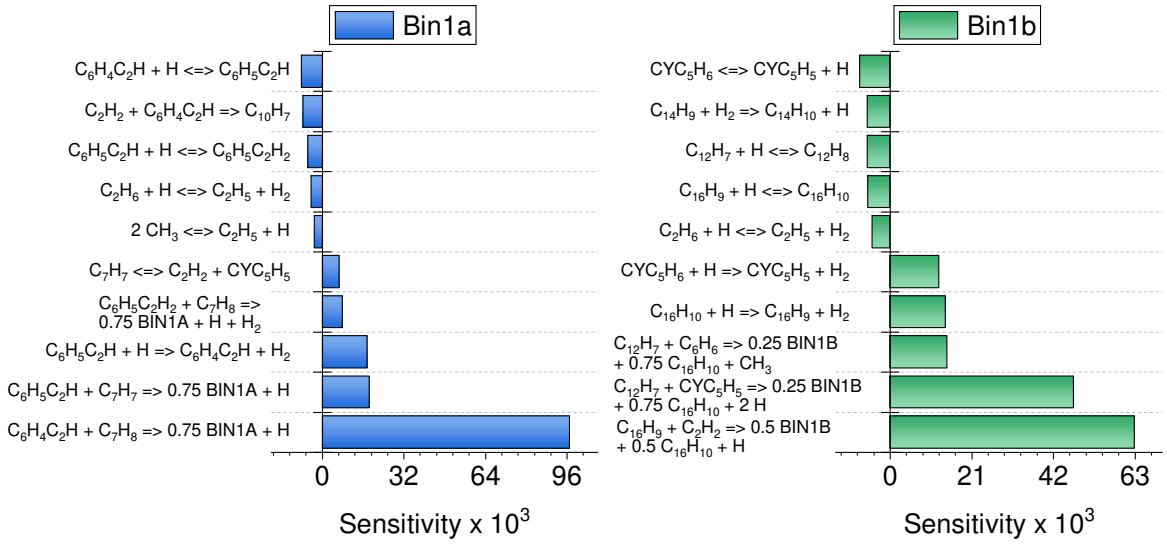
Bin1a
$C_6H_4C_2H + H <=> C_6H_5C_2H$
$C_2H_2 + C_6H_4C_2H => C_{10}H_7$
$C_6H_5C_2H + H <=> C_6H_5C_2H_2$
$C_2H_6 + H <=> C_2H_5 + H_2$
$2\ CH_3 <=> C_2H_5 + H$
$C_7H_7 <=> C_2H_2 + CYC_5H_5$
$C_6H_5C_2H_2 + C_7H_8 =>$ $0.75\ BIN1A + H + H_2$
$C_6H_5C_2H + H => C_6H_4C_2H + H_2$
$C_6H_5C_2H + C_7H_7 => 0.75\ BIN1A + H$
$C_6H_4C_2H + C_7H_8 => 0.75\ BIN1A + H$
0
32
64
96
Sensitivity x 10^3
Bin1b
$CYC_5H_6 <=> CYC_5H_5 + H$
$C_{14}H_9 + H_2 => C_{14}H_{10} + H$
$C_{12}H_7 + H <=> C_{12}H_8$
$C_{16}H_9 + H <=> C_{16}H_{10}$
$C_2H_6 + H <=> C_2H_5 + H_2$
$CYC_5H_6 + H => CYC_5H_5 + H_2$
$C_{16}H_{10} + H => C_{16}H_9 + H_2$
$C_{12}H_7 + C_6H_6 => 0.25\ BIN1B$ $+ 0.75\ C_{16}H_{10} + CH_3$
$C_{12}H_7 + CYC_5H_5 => 0.25\ BIN1B$ $+ 0.75\ C_{16}H_{10} + 2\ H$
$C_{16}H_9 + C_2H_2 => 0.5\ BIN1B$ $+ 0.5\ C_{16}H_{10} + H$
0
21
42
63
Sensitivity x 10^3

B Appendix for "Investigation of natural gas/hydrogen mixtures for exergy storage in a piston engine"

Table B1. Mole fractions in the product gas of main products, methane conversion and yields of main products, temperature and pressure at TDC for T0 = 473 K and xAr = 0.94 depending on hydrogen content in natural gas.

	Hydrogen content in natural gas/hydrogen mixture: $x_{H_2} / (x_{H_2} + x_{NG})$				
	0	0.05	0.1	0.15	0.2
Ar Mole fraction	0.9058	0.9065	0.9075	0.9086	0.9099
H_2 Mole fraction	0.0684	0.0696	0.0704	0.0709	0.0711
C_2H_2 Mole fraction	0.0042	0.0043	0.0044	0.0046	0.0047
C_2H_4 Mole fraction	0.0027	0.0027	0.0026	0.0026	0.0025
C_6H_6 Mole fraction	0.0009	0.0007	0.0006	0.0005	0,0004
CH_4 Conversion	70.4%	72.5%	74.3%	75.9%	77.4%
H_2 Yield	54.1%	55.4%	56.5%	57.5%	58.3%
C_2H_2 Yield	12.7%	13.7%	14.8%	16.1%	17.5%
C_2H_4 Yield	8.0%	8.4%	8.8%	9.1%	9.4%
C_6H_6 Yield	8.7%	7.2%	6.0%	5.0%	4.3%
$C_{10}H_8$ Yield	0.9%	0.7%	0.6%	0.5%	0.4%
$C_{20}H_{10}$ Yield	30.86%	28.85%	26.53%	23.89%	21.01%
$C_{20}H_{16}$ Yield	9.26%	10.29%	11.31%	12.43%	13.58%
TDC Temperature	1793.8 K	1813.4 K	1834.1 K	1857.5 K	1883.5 K
TDC Pressure	176.5 bar	178.6 bar	180.5 bar	182.7 bar	185.2 bar
TDC Temperature (motored)	2171.0 K	2197.3 K	2224.5 K	2252.7 K	2282.0 K
TDC Pressure (motored)	205.1 bar	207.6 bar	210.2 bar	212.8 bar	215.6 bar

C Supplementary material for "Shock-tube study on high-temperature CO formation during dry methane reforming"

1 CO Laser absorption diagnostic

To characterize k_ν over a temperature range of 1200–2700 K at atmospheric pressure, separate experiments were performed. In these experiments, 2000 ppm CO in a Helium/Argon dilution of 20/79.8 were used as an input for the Beer-Lamber law to derive an absorption coefficient k_ν, associated with the measured intensities I_0 and I_t. The derived values for k_ν are shown in Fig. C1 together with the best fit of the data, from which the temperature dependence of the absorption coefficient is obtained. During the experiments, the temperature T_5 changes within the measurement time due the characteristic of the reactive mixture (endothermic or exothermic). This temperature change is computed using a zero-dimensional batch reactor with the measured pressure as input and an elementary reaction mechanism. The resulting temperature profile is used to calculate a time-variant absorption coefficient for each measurement. It leads to a small uncertainty in the CO mole fraction of about 5%.

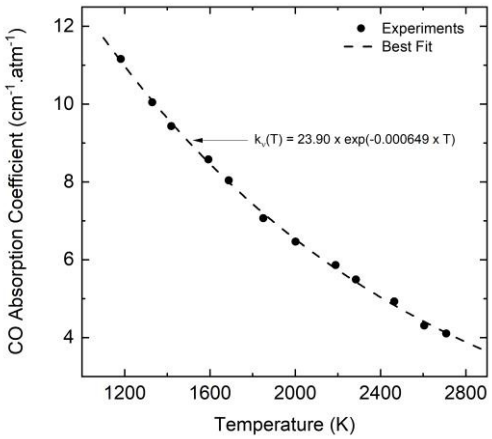

Figure C1. Spectral absorption coefficient of 2000 ppm CO in 0.20/0.798 He/Ar. Dashed line represents the best fit used to calculate k_ν.

2 CO Time histories

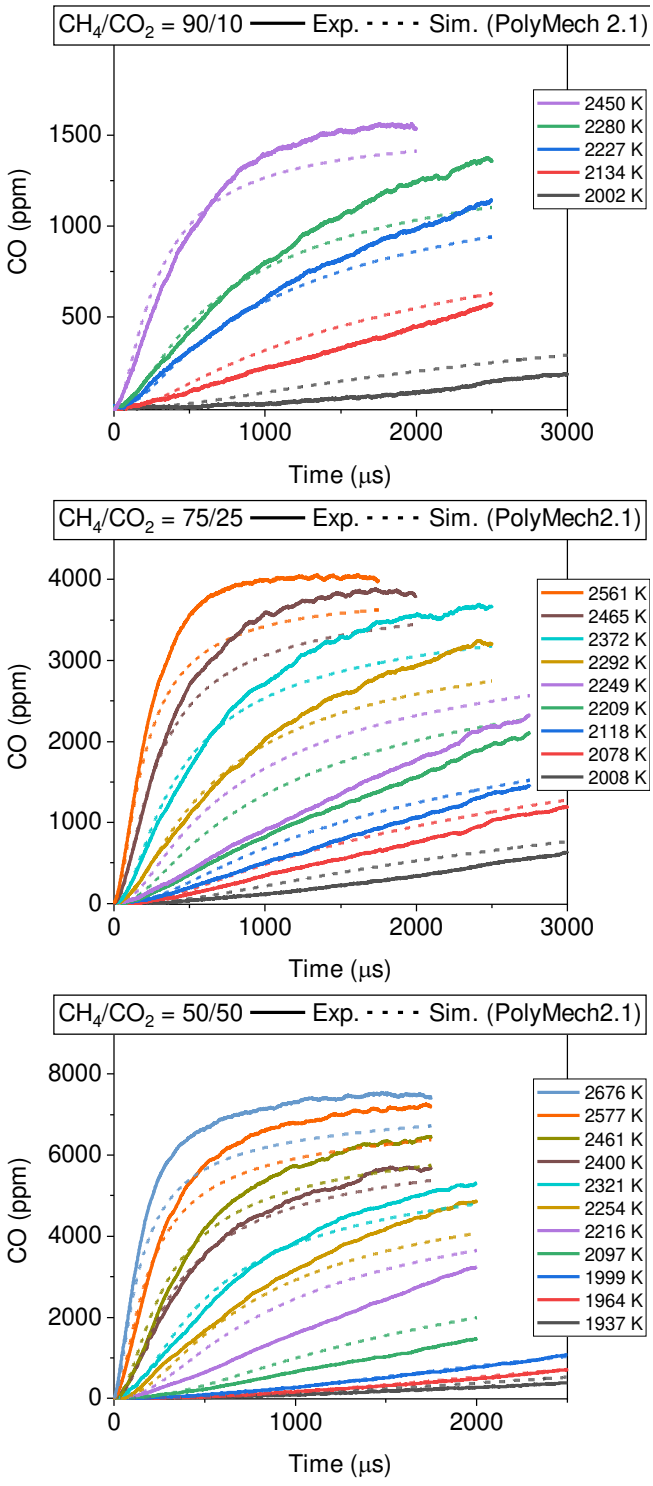

Figure C2. CO time histories for different CO_2 blends ((left 10% CO_2, 90% CH_4; middle 25% CO_2, 75% CH_4; right 50% CO_2, 50% CH_4) and for all investigated temperatures. The solid lines are the experiments, the dashed lines are simulations using the PolyMech2.1 [111] reaction mechanism.

3 Pressure Profiles

In this section, all measured pressure and CO profiles are presented. Note that a full range (up to 3.5 ms) is given, but the respective test time is dependent on changing arrival times of the expansion wave and variable contact surface interactions. Test times between 1.75 and 3 ms were observed. Table C1. gives the test times for each data point.

Table C1. Experimental conditions and respective test times.

T_5 (K)	P_5 (atm)	Test time (ms)	CO_2 blend in CH_4
1937	1.13	2.5	
1964	1.07	2.5	
1999	1.046	2.5	
2097	1.06	2	
2216	1	2	
2254	0.939	2	50%
2321	0.93	2	
2400	0.97	1.75	
2461	0.85	1.75	
2577	0.826	1.75	
2676	0.781	1.75	
2008	1.117	3	
2078	1.074	3	
2118	1.028	2.75	
2209	1.037	2.75	
2249	1.03	2.75	25%
2292	0.93	2.5	
2372	0.901	2.5	
2465	0.861	2	
2561	0.804	1.75	
2002	1.105	2.5	
2134	1.002	2.5	
2227	0.946	2.5	10%
2280	0.943	2.5	
2450	0.924	2	

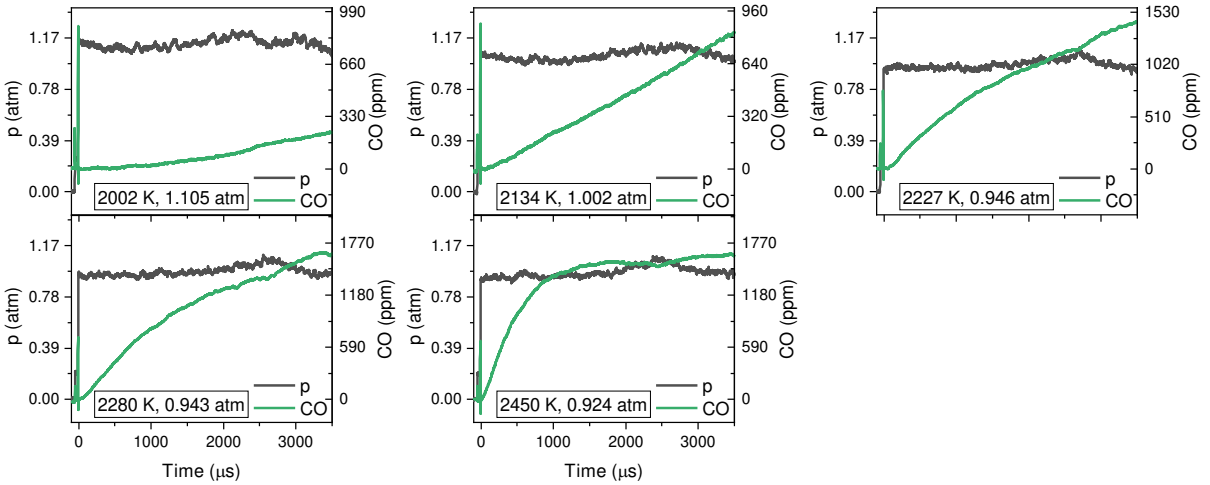

Figure C3. Measured pressure profiles (black lines) and CO profiles (green lines) for a CO_2 blend of 10% at respective temperatures.

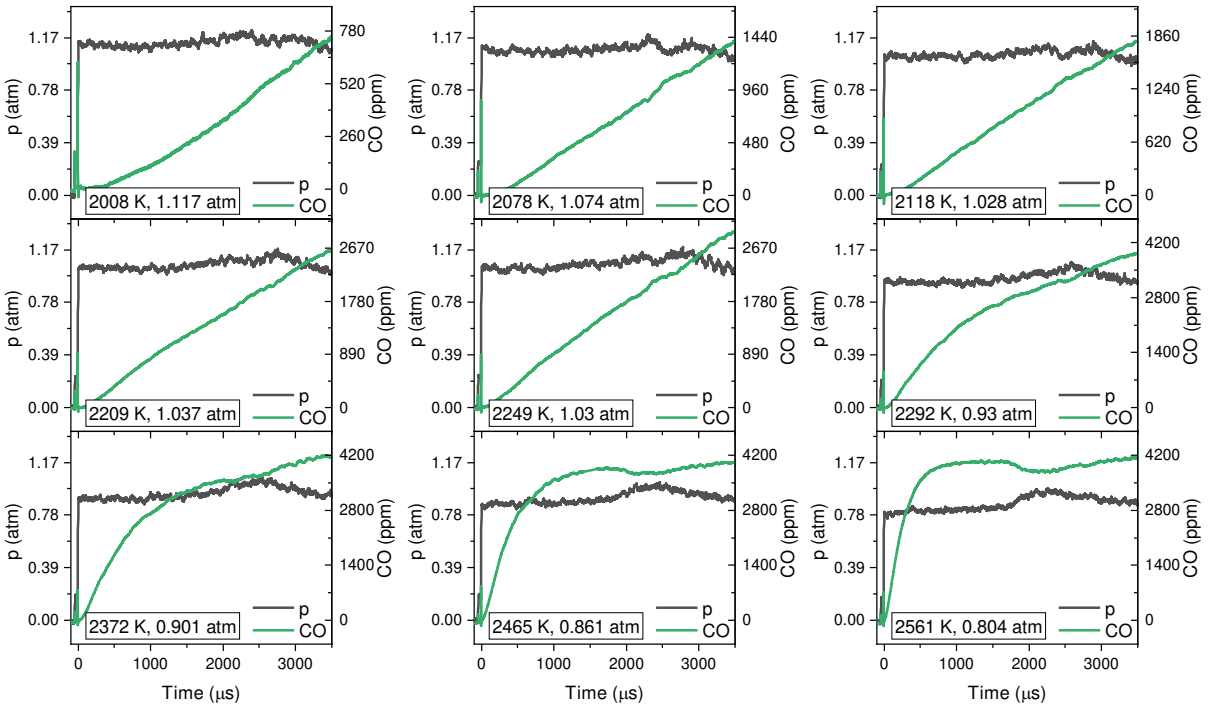

Figure C4. Measured pressure profiles (black lines) and CO profiles (green lines) for a CO_2 blend of 25% at respective temperatures.

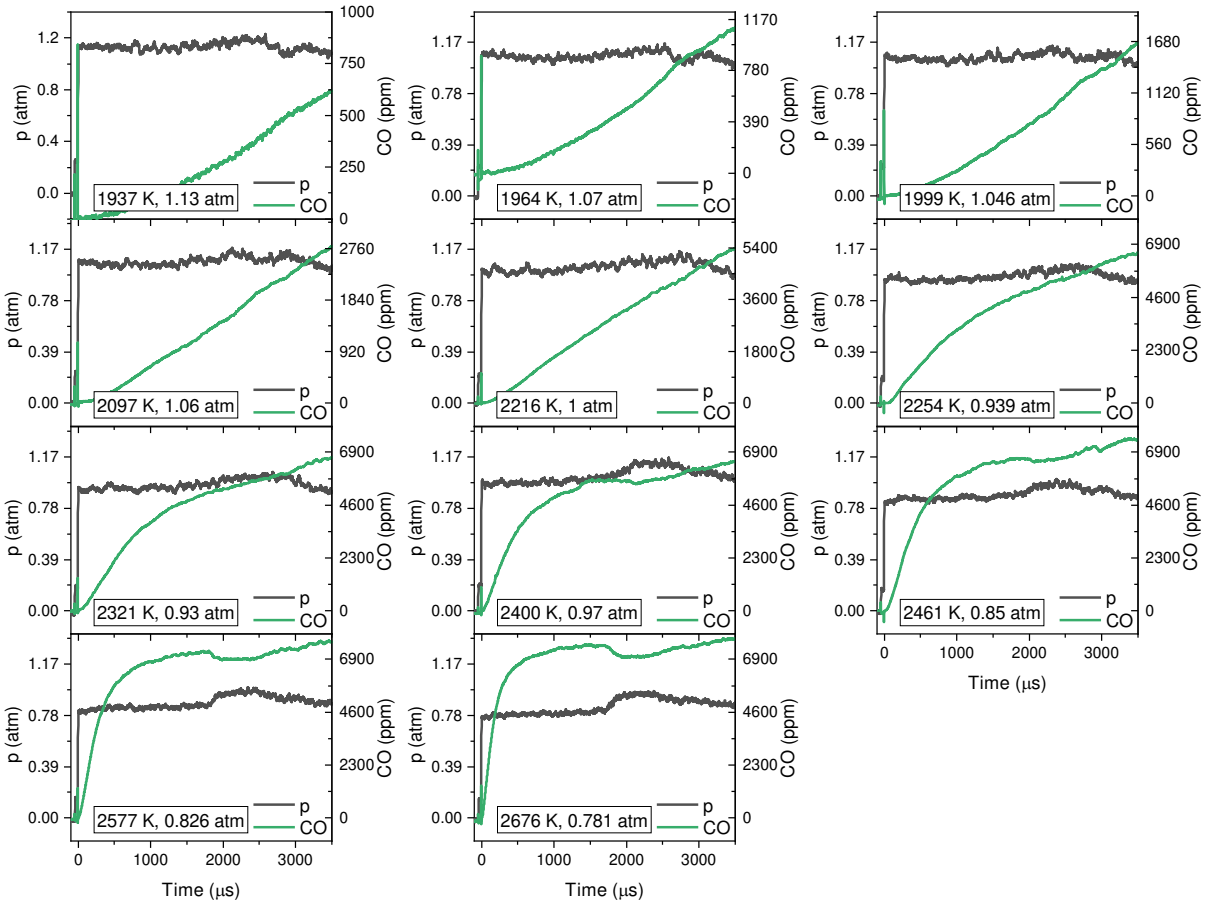

Figure C5. Measured pressure profiles (black lines) and CO profiles (green lines) for a CO_2 blend of 50% at respective temperatures.

4 Rate of Production and Sensitivity Analysis for all Presented Mechanisms

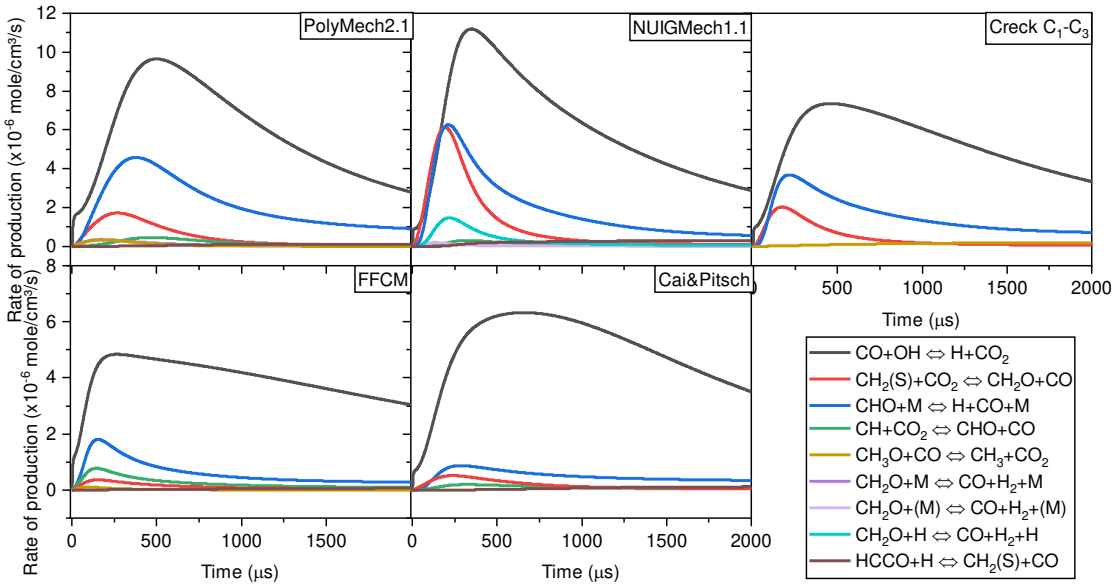

Figure C6. Rate of production analysis for CO formation for an illustrative data point of 2216 K and 50% CO_2 and 50% CH_4 using all presented reaction mechanisms (PolyMech2.1 [111], NUIGMech1.1 [127], CRECK [67], FFCM [126], Cai and Pitsch [119]).

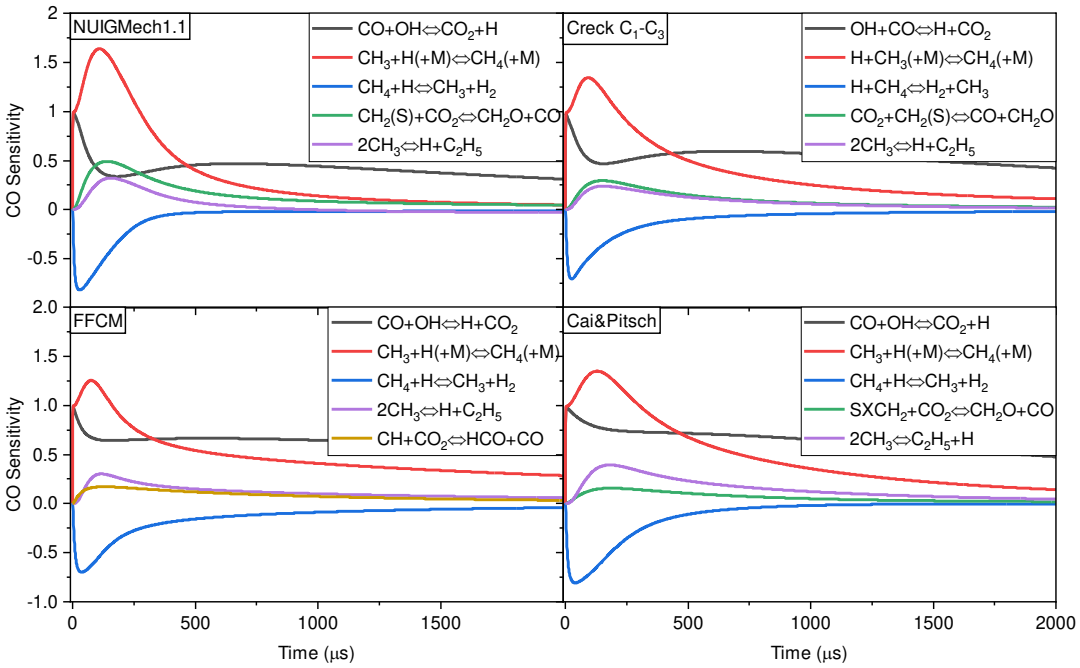

Figure C7. Sensitivity analysis for CO formation for an illustrative data point of 2216 K and 50% CO_2 and 50% CH_4 using all presented reaction mechanisms (NUIGMech1.1 [127], CRECK [67], FFCM [126], Cai and Pitsch [119]).

5 Sensitivity Analysis

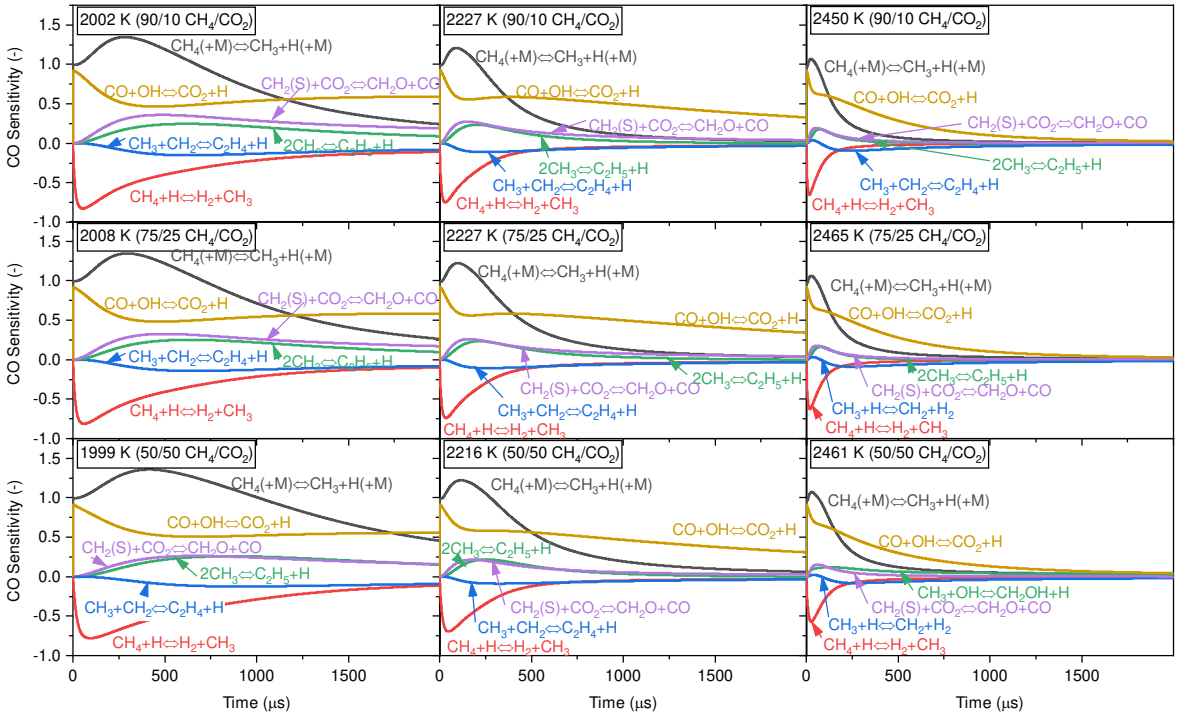

Figure C8. CO Sensitivity for different CO_2 blends (top down; 10% CO_2 and 90% CH_4; 25% CO_2 and 75% CH_4; 50% CO_2 and 50% CH_4) and different temperatures T_5 (left to right; ~2000 K, ~2215 K, 2460 K). Different colors represent different reactions. The PolyMech2.1 [111] was used for the sensitivity analysis.

6 CO Time Histories with Adapted Rate Coefficients

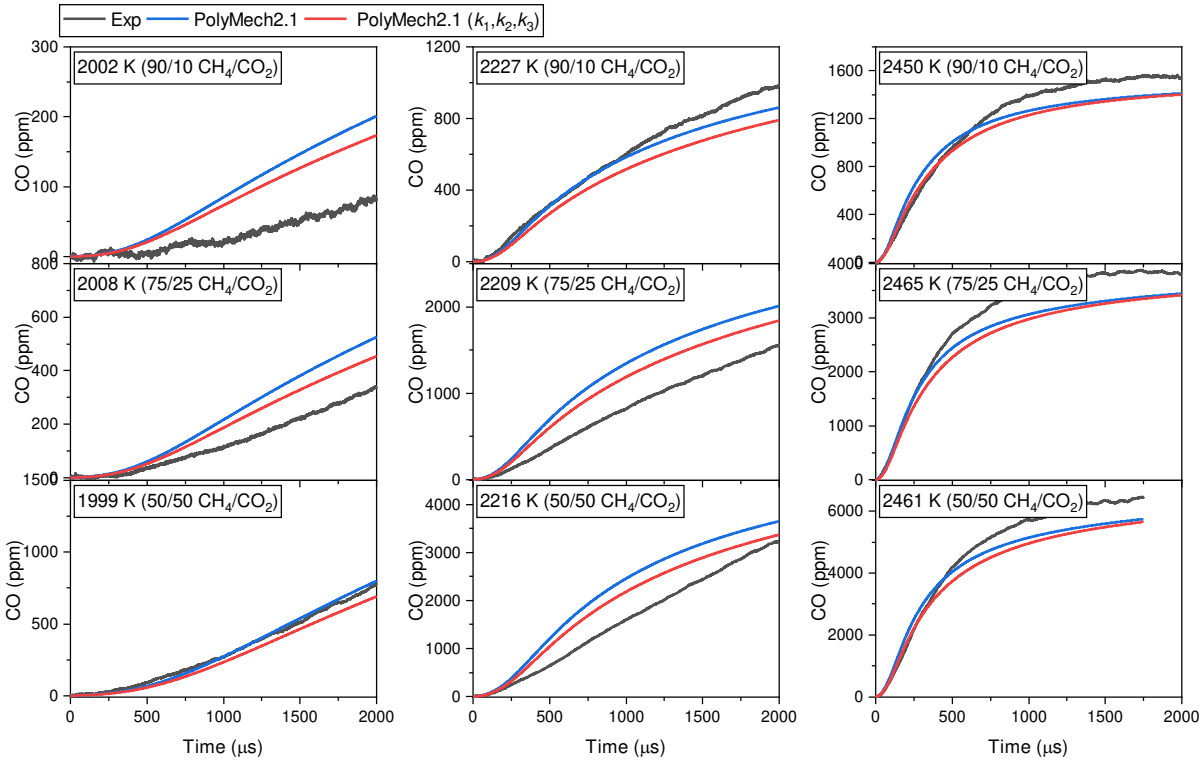

Figure C9. CO time histories for different CO_2 blends (top down; 10% CO_2 and 90% CH_4; 25% CO_2 and 75% CH_4; 50% CO_2 and 50% CH_4) and different temperatures T_5 (left to right; ~2000 K, ~2215 K, 2460 K). Black lines represent experiments, colored lines represent simulations (blue PolyMech2.1 [111], red PolyMech2.1 with adapted rate coefficients within their uncertainties).

7 CO Time Histories and Sensitivities for 30 atm

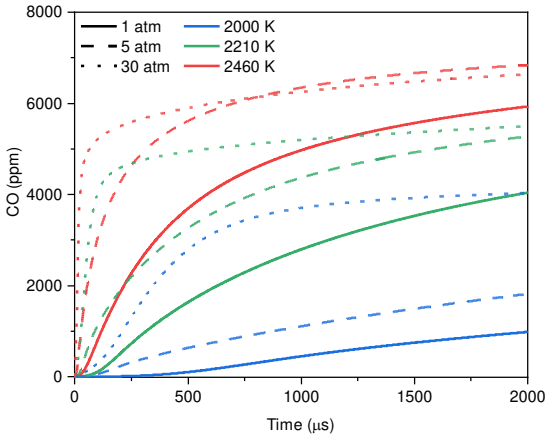

Figure C10. Illustrative CO time histories different temperatures T_5 and 50% CO_2 and 50% CH_4 and 30 atm. The PolyMech2.1 [111] was used for the simulation.

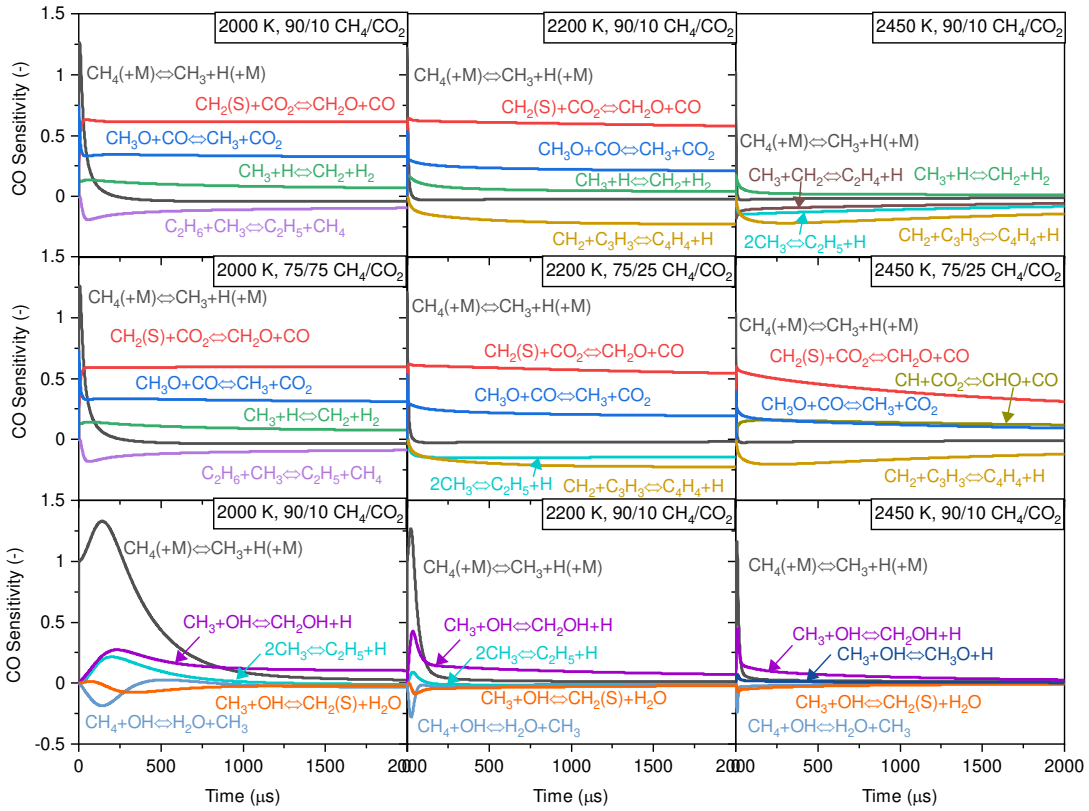

Figure C11. CO Sensitivity for different CO_2 blends (top down; 10% CO_2 and 90% CH_4; 25% CO_2 and 75% CH_4; 50% CO_2 and 50% CH_4) and different temperatures T_5 (left to right; 2000 K, 2200 K, 2450 K) and 30 atm. Different colors represent different reactions. The PolyMech2.1 [111] was used for the sensitivity analysis.

D Supplementary material for "Spectroscopic study of CO formation from CO_2-enriched pyrolysis of C_2H_6 and C_3H_8 under engine-relevant conditions"

1 CO Laser absorption diagnostic

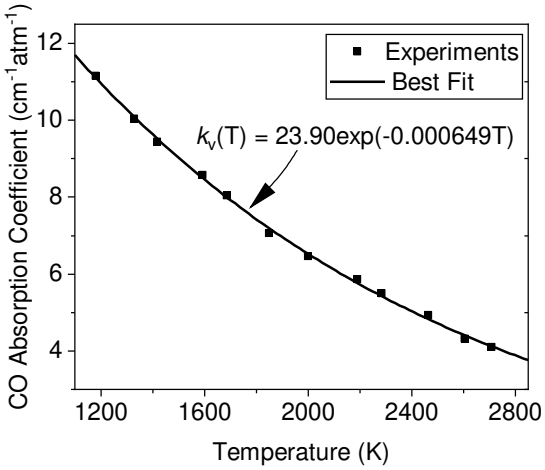

Figure D1. CO absorption coefficient as a function of the temperature (experiments and best fit) using 2000 ppm CO dilute in 20% He and 80% Ar.

2 Measurement data and pressure profiles

Table D1. Experimental conditions and respective test times.

Mixture	Temperature T_5 (K)	Pressure P_5 (atm)	Test time (ms)
25/75 CO_2/C_2H_6	1996	1.074	3
	2088	1.052	3
	2133	1.018	2.5
	2201	0.975	2.5
	2264	0.956	2.25
	2370	0.92	2
	2456	0.88	2
	2588	0.816	1.75
25/75 CO_2/C_3H_8	1996	1.093	2.5
	2055	1.023	2.5
	2142	1.017	2.5
	2177	0.972	2.5
	2244	0.979	2.5
	2271	0.913	2.25
	2305	0.805	2.25
	2357	0.899	2
	2424	0.896	1.75
	2564	0.819	1.75

Table D 2. Continued. Experimental conditions and respective test times.

Mixture	Temperature T_5 (K)	Pressure P_5 (atm)	Test time (ms)
50/50 CO_2/C_2H_6	1832	1.17	3
	1964	1.025	3
	2021	1.048	3
	2091	1.005	3
	2182	0.972	2.75
	2230	0.955	2.75
	2251	0.945	2.75
	2343	0.903	2.25
	2459	0.87	1.75
	2594	0.851	1.75
50/50 CO_2/C_3H_8	1890	1.107	2.5
	1964	1.113	2.5
	2005	1.087	2.5
	2055	1.009	2.5
	2131	0.99	2.5
	2258	0.945	2.5
	2335	0.907	2
	2445	0.87	1.75
	2572	0.805	1.75

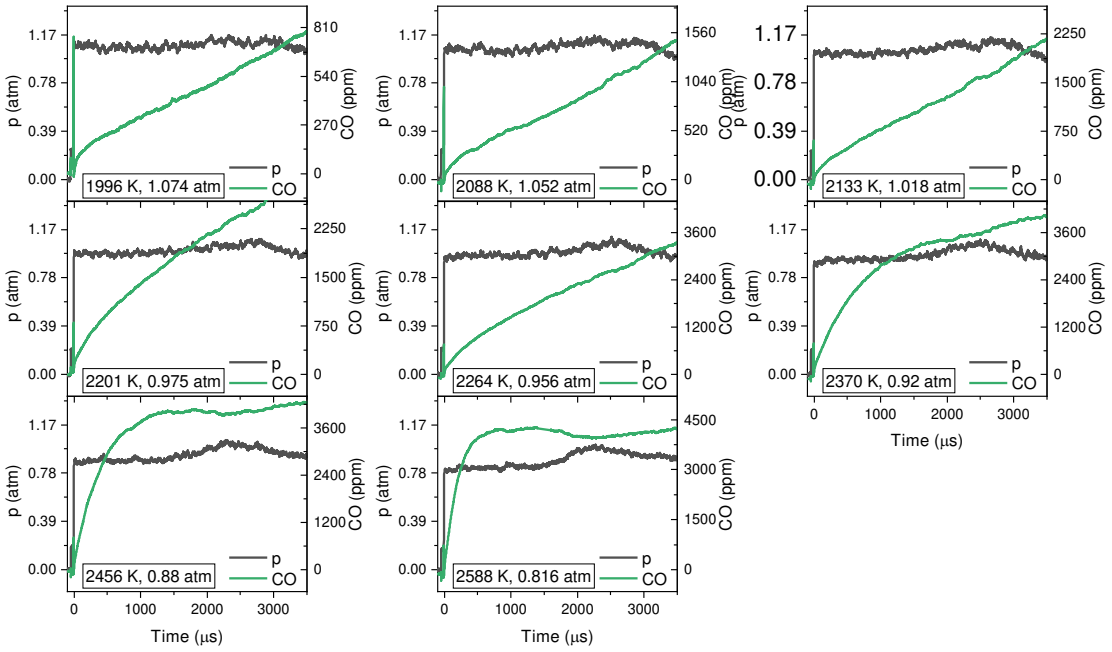

Figure D2 Measured pressure profiles (black lines) and CO profiles (green lines) for 25/75 CO_2/C_2H_6.

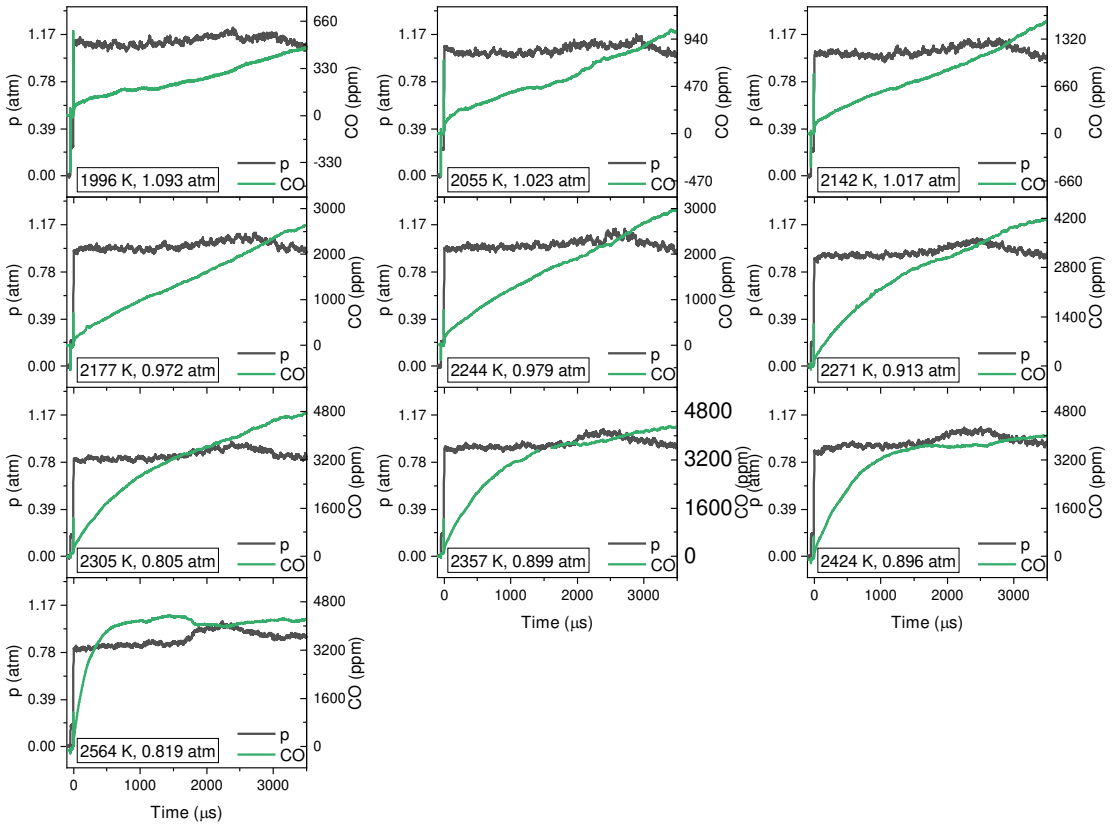

Figure D3. Measured pressure profiles (black lines) and CO profiles (green lines) for 25/75 CO_2/C_3H_8.

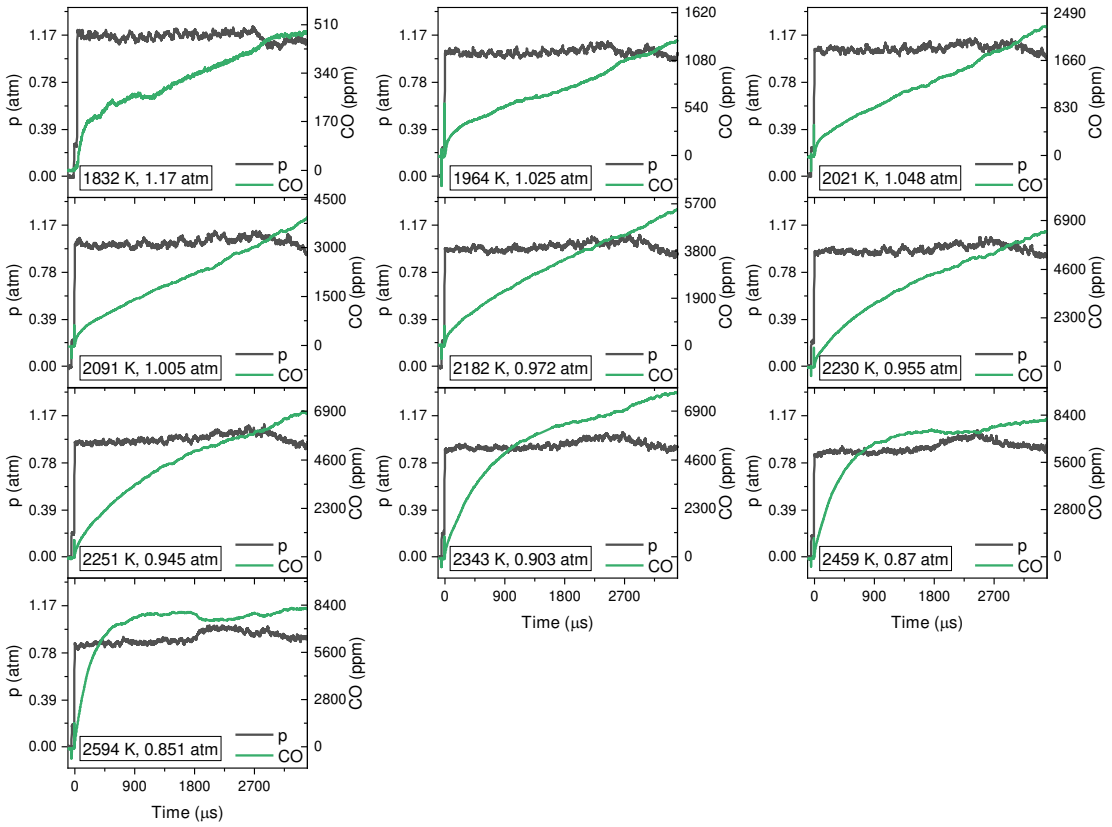

Figure D4. Measured pressure profiles (black lines) and CO profiles (green lines) for 50/50 CO_2/C_2H_6.

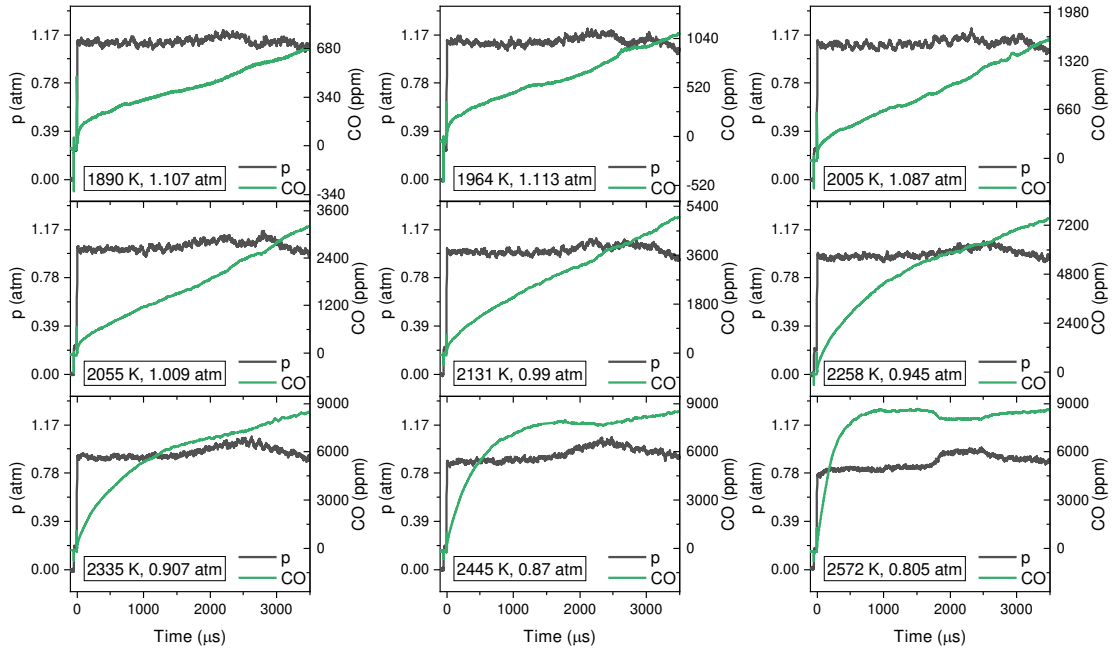

Figure D5. Measured pressure profiles (black lines) and CO profiles (green lines) for 50/50 CO_2/C_3H_8.

3 Overview CO time-histories: Experiments vs. simulations

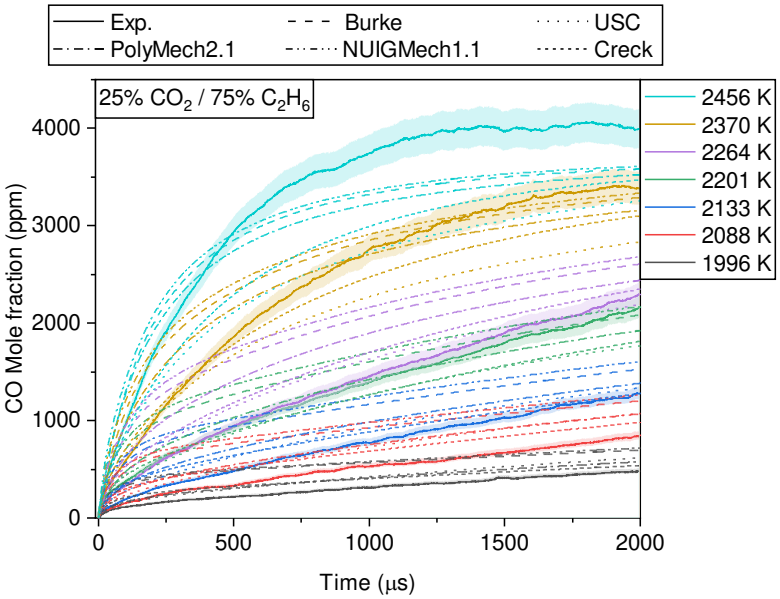

Figure D6. Overview of CO time-histories for the 25% CO_2 and 75% C_2H_6 mixture: Solid lines are experiments, dashed, dotted, or dash-dotted lines are simulations using different models (Burke [149], USC [150], PolyMech2.1 [111], NUIGMech1.1 [127], Creck [114]). Shaded areas are measurement deviations. Different colors represent different temperatures.

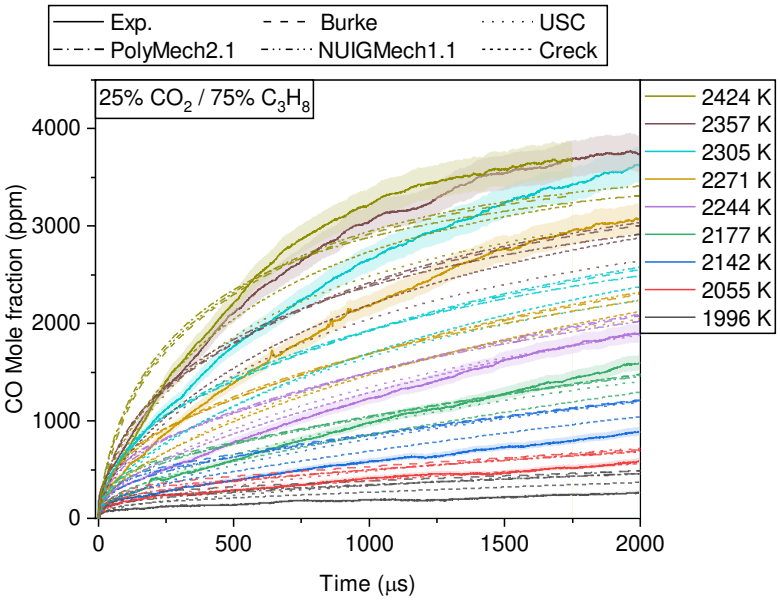

Figure D7. Overview of CO time-histories for the 25% CO_2 and 75% C_3H_8 mixture: Solid lines are experiments, dashed, dotted, or dash-dotted lines are simulations using different models (Burke [149], USC [150], PolyMech2.1 [111], NUIGMech1.1 [127], Creck [114]). Shaded areas are measurement deviations. Different colors represent different temperatures.

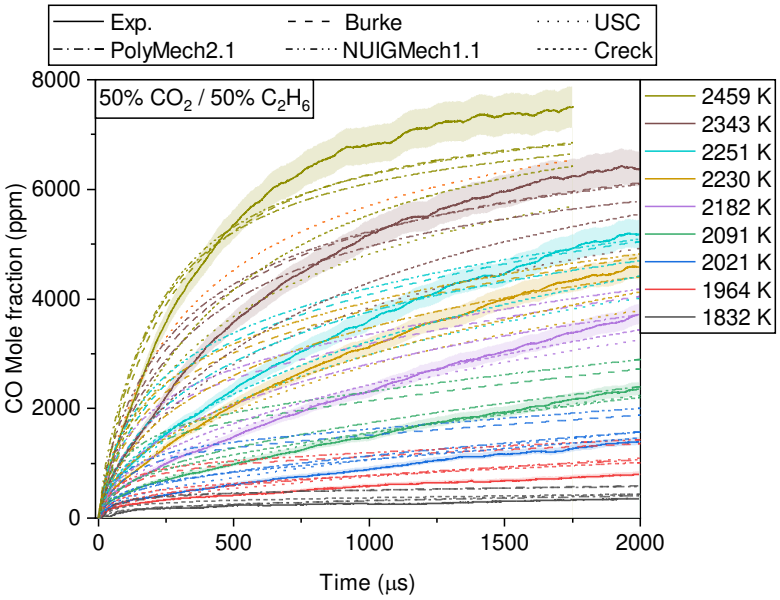

Figure D8. Overview of CO time-histories for the 50% CO_2 and 50% C_2H_6 mixture: Solid lines are experiments, dashed, dotted, or dash-dotted lines are simulations using different models (Burke [149], USC [150], PolyMech2.1 [111], NUIGMech1.1 [127], Creck [114]). Shaded areas are measurement deviations. Different colors represent different temperatures.

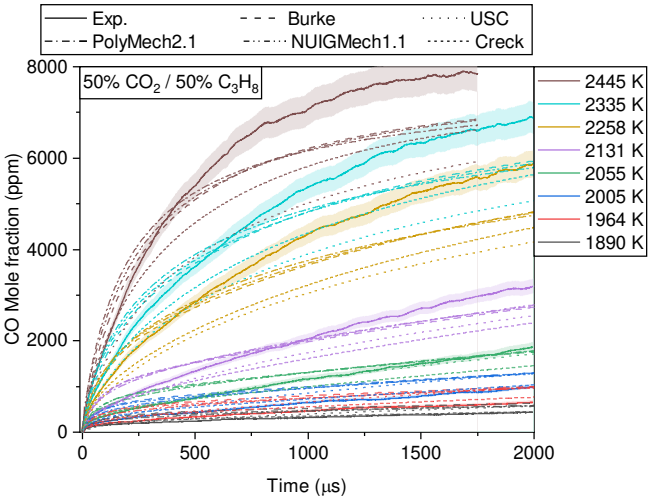

Figure D9. Overview of CO time-histories for the 50% CO_2 and 50% C_3H_8 mixture: Solid lines are experiments, dashed, dotted, or dash-dotted lines are simulations using different models (Burke [149], USC [150], PolyMech2.1 [111], NUIGMech1.1 [127], Creck [114]). Shaded areas are measurement deviations. Different colors represent different temperatures.

4 Rate-of-production analysis

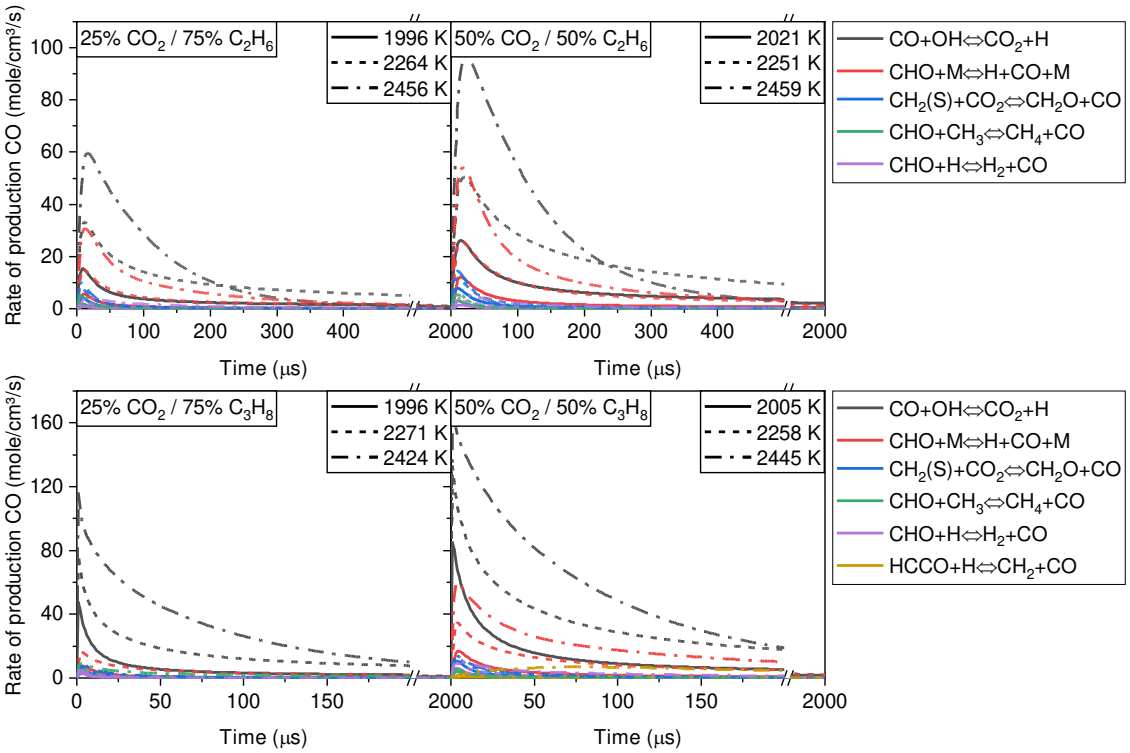

Figure D10. Rate of production analyses generated with PolyMech2.1 [111] for 25% CO_2/75% C_2H_6 (upper left), 50% CO_2/50% C_2H_6 (upper right), 25% CO_2/75% C_3H_8 (lower left), and 50% CO_2/50% C_3H_8 (lower right) for ~2000 K, ~2255 K, and ~2450 K, respectively.

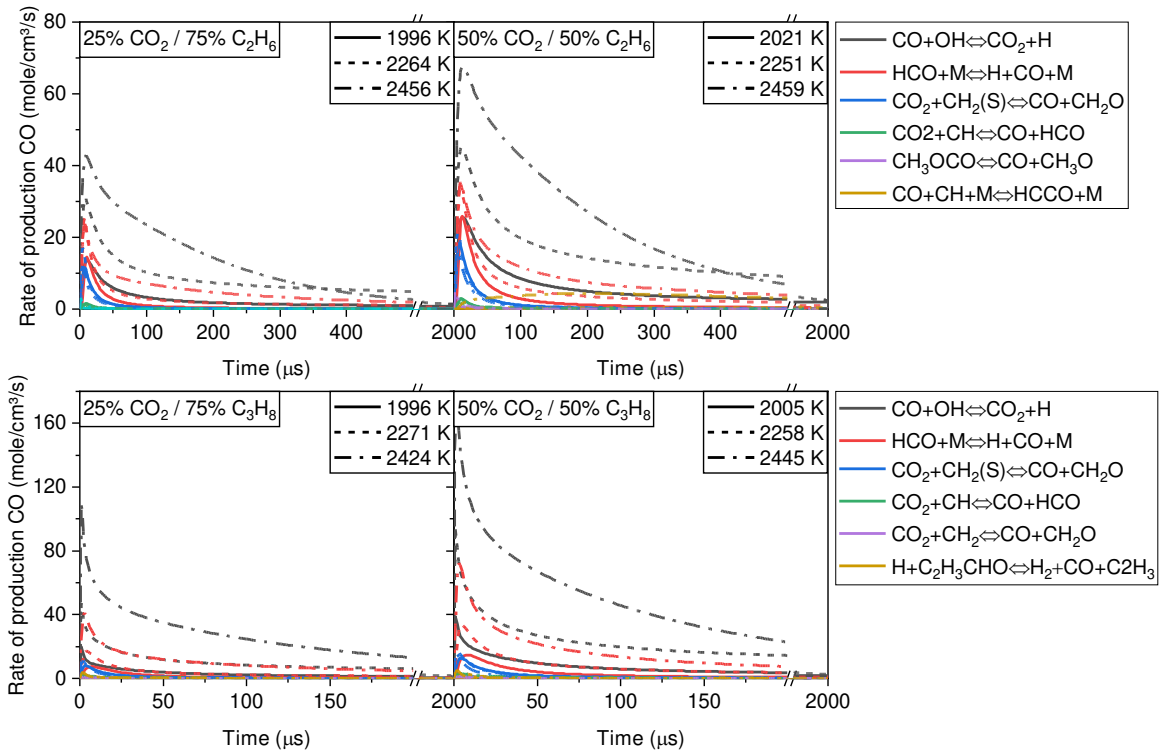

Figure D11. Rate of production analyses generated with Creck [114] for 25% CO_2/75% C_2H_6 (upper left), 50% CO_2/50% C_2H_6 (upper right), 25% CO_2/75% C_3H_8 (lower left), and 50% CO_2/50% C_3H_8 (lower right) for ~2000 K, ~2255 K, and ~2450 K, respectively.

5 Sensitivity analysis

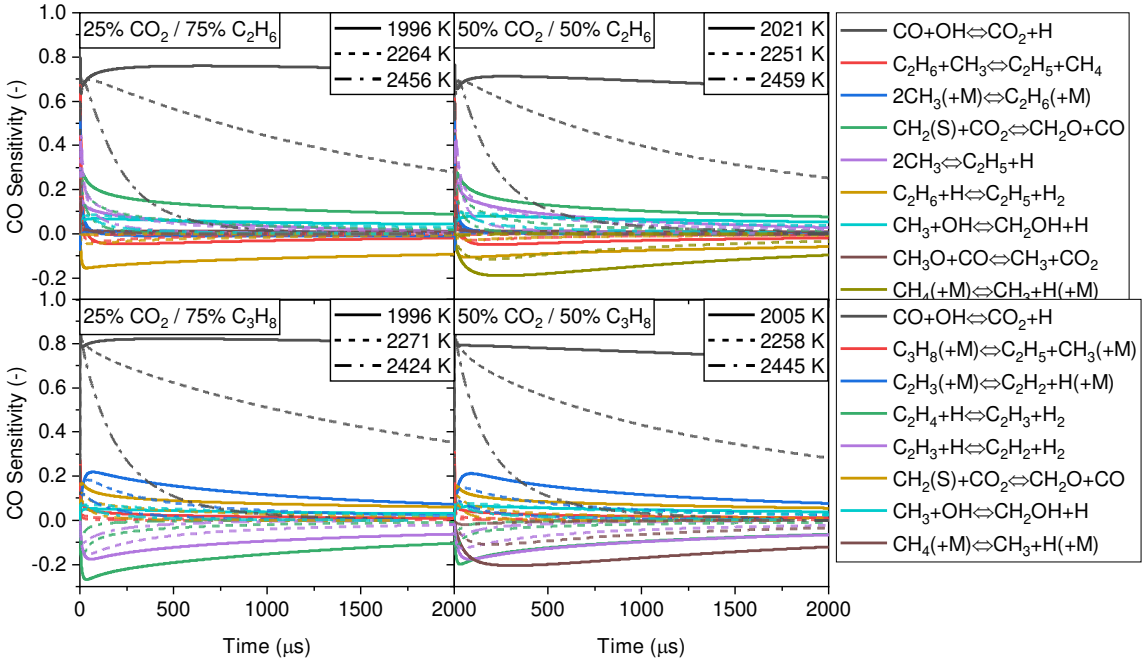

Figure D12. Sensitivity analyses for CO generated with PolyMech2.1 [111] for 25% CO_2/75% C_2H_6 (upper left), 50% CO_2/50% C_2H_6 (upper right), 25% CO_2/75% C_3H_8 (lower left), and 50% CO_2/50% C_3H_8 (lower right) for ~2000 K, ~2255 K, and ~2450 K, respectively.

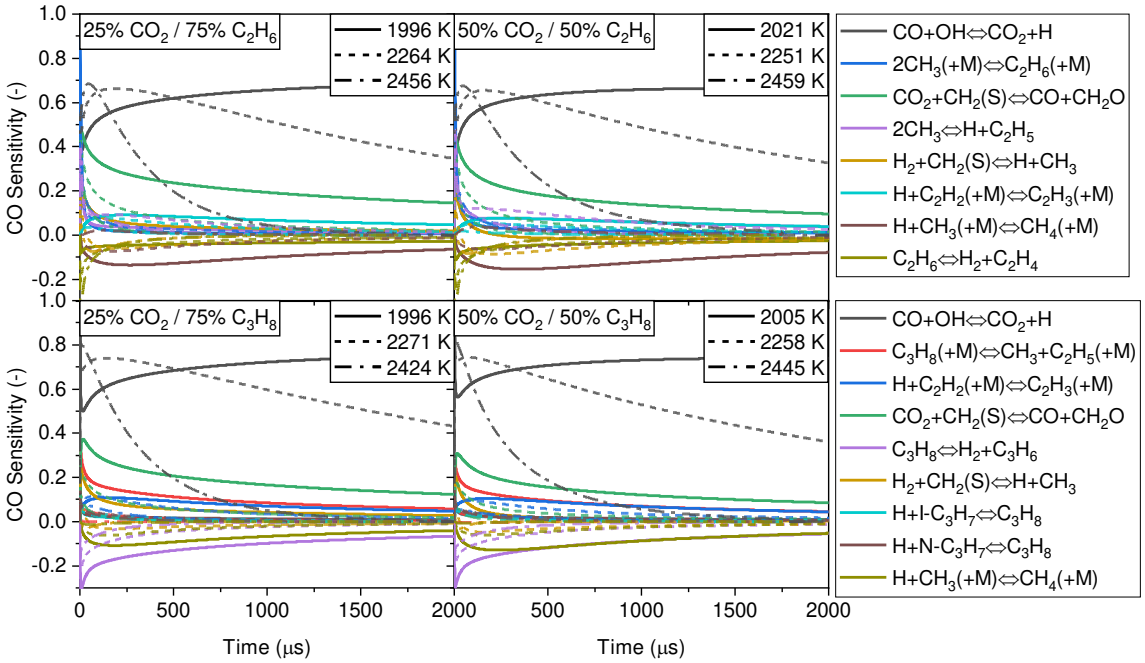

Figure D13. Sensitivity analyses for CO generated with Creck [114] for 25% CO_2/75% C_2H_6 (upper left), 50% CO_2 / 50% C_2H_6 (upper right), 25% CO_2/75% C_3H_8 (lower left), and 50% CO_2/50% C_3H_8 (lower right) for ~2000 K, ~2255 K, and ~2450 K, respectively.

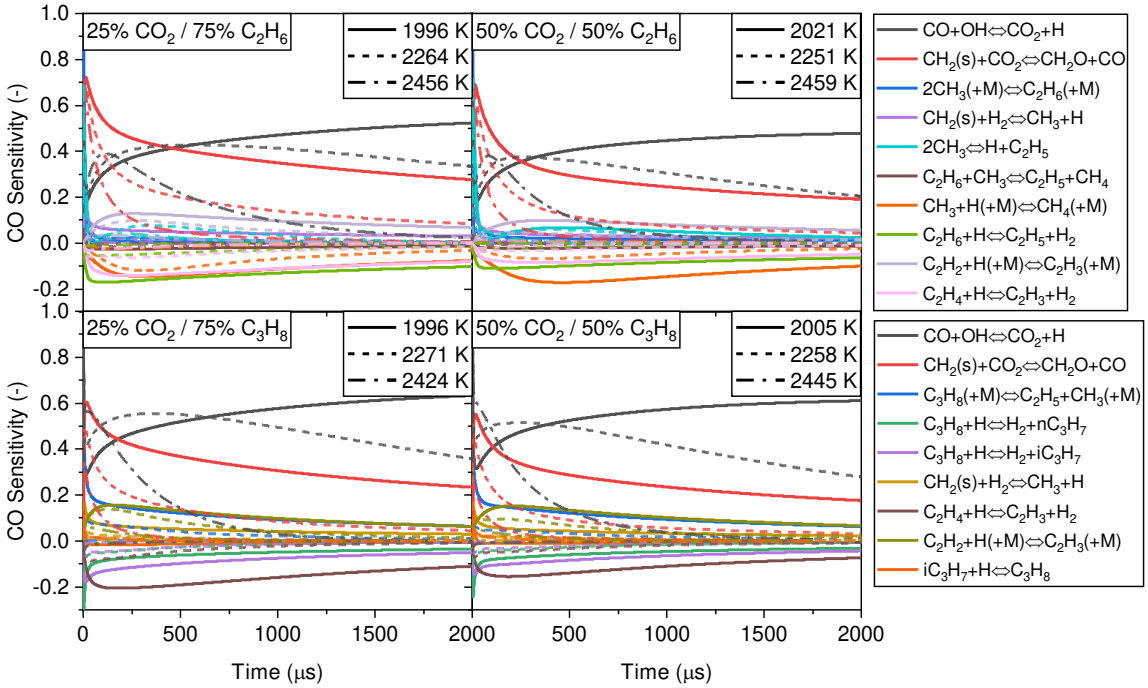

Figure D14. Sensitivity analyses for CO generated with NUIGMech1.1 [127] for 25% CO_2/75% C_2H_6 (upper left), 50% CO_2/50% C_2H_6 (upper right), 25% CO_2/75% C_3H_8 (lower left), and 50% CO_2/50% C_3H_8 (lower right) for ~2000 K, ~2255 K, and ~2450 K, respectively.

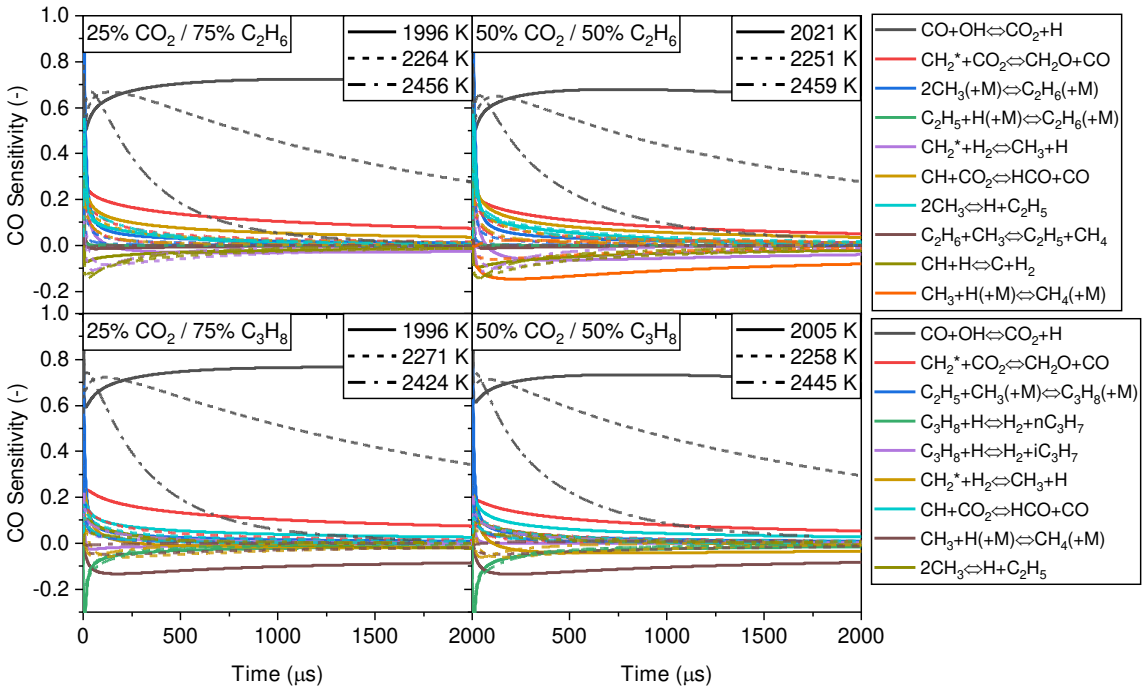

Figure D15. Sensitivity analyses for CO generated with USC [150] for 25% CO_2/75% C_2H_6 (upper left), 50% CO_2/50% C_2H_6 (upper right), 25% CO_2/75% C_3H_8 (lower left), and 50% CO_2/50% C_3H_8 (lower right) for ~2000 K, ~2255 K, and ~2450 K, respectively.

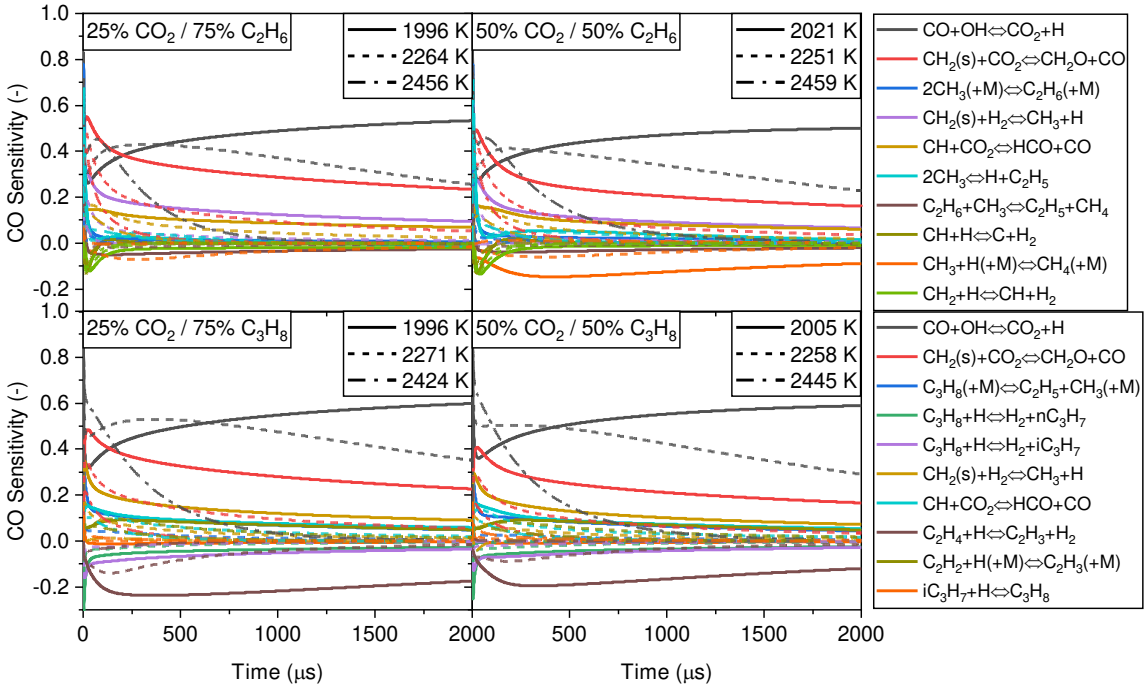

Figure D16. Sensitivity analyses for CO generated with Burke [149] for 25% CO_2/75% C_2H_6 (upper left), 50% CO_2/50% C_2H_6 (upper right), 25% CO_2/75% C_3H_8 (lower left), and 50% CO_2/50% C_3H_8 (lower right) for ~2000 K, ~2255 K, and ~2450 K, respectively.

Table D3. Rate constants for rate expression of the form $k = AT^{B}exp(-E_A/(RT))$. Units are mol, cm, K, s, and cal.

Mechanism	Type	A	B	E_A
$CO + OH \rightleftharpoons CO_2 + H$				
PolyMech2.1	duplicate	7.05E+04	2.053	-355.88
		5.76E+12	-0.664	331.98
Creck	duplicate	7.02E+04	2.053	-355.7
		5.76E+12	-0.664	331.8
NUIGMech1.1	p-log	2.30E+07	1.35	9.74E+02
USC	duplicate	7.05E+04	2.053	-355.67
		5.76E+12	-0.664	331.83
Burke	duplicate	7.02E+04	2.053	-355.7
		5.76E+12	-0.664	331.8
$CH_2(S) + CO_2 \rightleftharpoons CH_2O + CO$				
PolyMech2.1		1.40E+13	0	0
Creck		1.40E+13	0	0
NUIGMech1.1		1.40E+13	0	0
USC		1.40E+13	0	0
Burke		1.40E+13	0	0
$CH_4 (+M) \rightleftharpoons CH_3 + H (+M)$				
PolyMech2.1	Troe*	2.10E+16	0	104919
Creck**	Troe*	1.27E+16	-0.63	383
NUIGMech1.1**	Troe*	6.47E+13	0.185	-54
USC**	Troe*	1.27E+16	-0.63	383
Burke**	Troe*	1.27E+16	-0.63	383
Mechanism	Type	A	B	EA
$CH_3 + CH_3 \rightleftharpoons C_2H_5 + H$				
PolyMech2.1		1.50E+12	0.1	10607.1
Creck	p-log	4.74E+12	0.105	10664.3
NUIGMech1.1	p-log	103.2	3.23	11236.1
USC		4.99E+12	0.1	10600
Burke	p-log	4.74E+12	0.105	10664.3
$CH_3 + CH_3 (+M) \rightleftharpoons C_2H_6 (+M)$				
PolyMech2.1	Troe*	9.46E+14	-0.538	135.14
Creck	Troe*	2.28E+15	-0.69	174.9
NUIGMech1.1	Troe*	2.28E+15	-0.69	174.9
USC	Troe*	2.12E+16	-0.97	620
Burke	Troe*	2.28E+15	-0.69	174.9
$i\text{-}C_3H_7 + H \rightleftharpoons C_3H_8$				
PolyMech2.1	not available			
Creck		1.00E+14	0	0
NUIGMech1.1		1.66E+13	0.22	0
USC	not available			
Burke		1.00E+14	0	0

Table D4. Continued. Rate constants for rate expression of the form $k = AT^{B}exp(-E_A/(RT))$. Units are mol, cm, K, s, and cal.

Mechanism	Type	A	B	E_A
C_3H_8 (+M) ⇌ C_2H_5 + CH_3 (+M)				
PolyMech2.1	Troe*	1.55E+24	-2.034	90388
Creck	Troe*	1.29E+37	-5.84	97380
NUIGMech1.1	Troe*	1.55E+24	-2.034	90388
USC**	Troe*	4.90E+14	-0.5	0
Burke	Troe*	1.29E+37	-5.84	97380
C_3H_8 + H ⇌ H_2 + n-C_3H_7				
PolyMech2.1		1.30E+14	0	9703
Creck		1.75E+05	2.69	6450
NUIGMech1.1	duplicate	1.29E+04	2.93	5245.68
		1.47E+10	1.31	10300
USC		1.30E+06	2.54	6756
Burke		3.49E+05	2.69	6450
C_2H_3 (+M) ⇌ C_2H_2 +H (+M)				
PolyMech2.1	Troe	7.800E+08	1.62	37059.3
Creck**	Troe	1.7100E+10	1.266	2709
NUIGMech1.1**	Troe	1.7100E+10	1.266	2709
USC	Troe	3.860E+08	1.620	37048.2
Burke**	Troe	1.7100E+10	1.266	2709
C_2H_4 + H ⇌ C_2H_3 + H_2				
PolyMech2.1		1.266E+05	2.752	11649
Creck		5.0700E+07	1.930	12950
NUIGMech1.1		6.189E+06	2.31	12829.9
USC		5.070E+07	1.9	12950
Burke		5.070E+07	1.930	12950

*For Troe-reactions, only the high-pressure limit is shown here. The low-pressure limit and the Troe parameters can be found in the respective reaction mechanism file.

**Reaction rate coefficients are presented for the reverse reaction based on the respective reaction mechanism.

6 Shock-tube measurements above 2500 K

Fig. D17. shows temperature profiles using a sample of three different models (NUIGMech1.1, CRECK C_1-C_3, and PolyMech2.1). It can be observed that the profiles are not matching either during the first sharp decrease, nor at the secondary plateau. At low and intermediate temperatures, the variation amongst models is negligible and the temperature decrease due to endothermic reactions is less than 100 K. However, for high temperatures (*i.e.*, 2500 K), temperature profiles diverge amongst models and predict a temperature decrease due to endothermic reactions by up to 250 K.

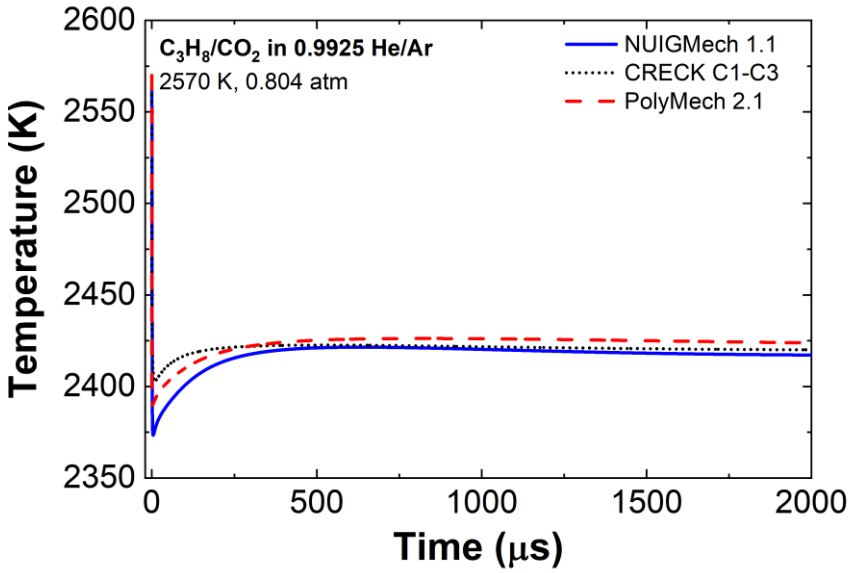

Figure D17. Temperature profiles from the numerical predictions using NUIGMech1.1, CRECK C_1-C_3, and PolyMech2.1 with temperature T_5 = 2570 K for the 50/50 C_3H_8/CO_2 mixture.

To show the influence of a varying dT/dt from 150 K up to 350 K on the CO mole fraction for the measurement at 2570 K of the 50/50 C_3H_8/CO_2 mixture, the temperature profiles used for the processing of the raw data were estimated to satisfy the dT/dt assumptions. The time-resolved CO mole fractions are shown in Fig. D18. They demonstrate that the CO mole fraction will not exceed the theoretical maximum if temperature profiles with a dT/dt of 350 K were predicted. This variation seems to indicate that the thermodynamic data at temperatures of ~2500 K require improvement to predict temperature profiles more precise.

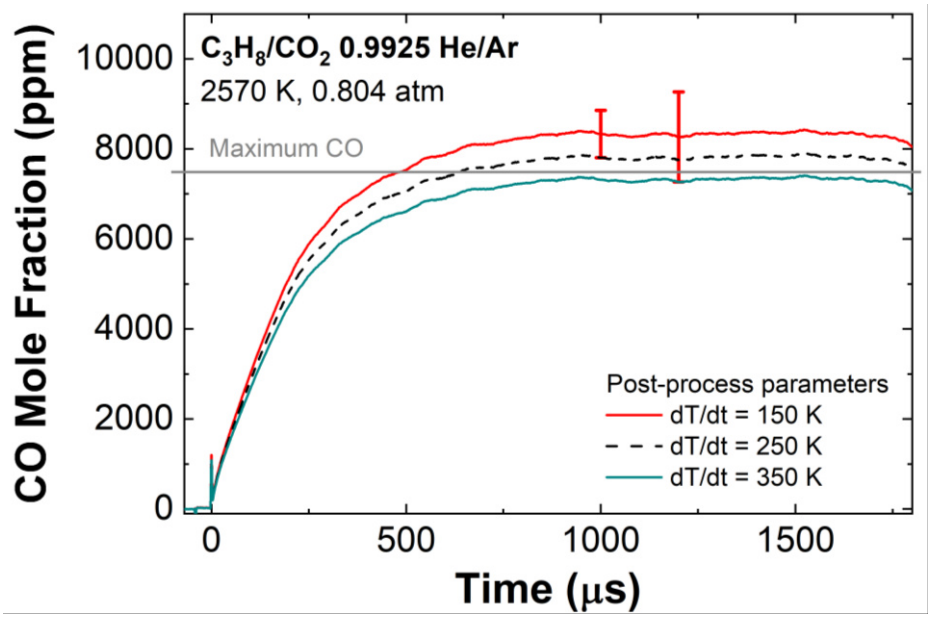

Figure D18. Time-dependent CO mole fractions for the 50/50 C_3H_8/CO_2 mixture, at 2570 K, processed using different dT/dt parameters.

References

[1] H.-O. Pörtner, D.C. Roberts, M. Tignor, E.S. Poloczanska, K. Mintenbeck, A. Alegría, M. Craig, S. Langsdorf, S. Löschke, V. Möller, A. Okem, B. Rama (eds.). Cambridge University Press. Cambridge University Press, Cambridge, UK and New York, NY, USA (2022) pp. 3056.

[2] Paris Agreement, adopted 12 Dec 2015, Session COP 21, Report FCCC/CP/2015/10/Add.1, https://unfccc.int/sites/default/files/resource/docs/2015/cop21/eng/10a01.pdf, retrieved 22 Nov 2022.

[3] United Nations Environment Programme (2021). Emissions Gap Report 2021: The Heat Is On – A World of Climate Promises Not Yet Delivered. Nairobi.

[4] Paris Agreement, adopted 12 Dec 2015, Session COP 22, Report FCCC/CP/2016/2, https://unfccc.int/resource/docs/2016/cop22/eng/02.pdf, retrieved 22 Nov 2022.

[5] A. Tay, *Nature* (2022).

[6] The White Hourse, FACT SHEET: President Biden Sets 2030 Greenhouse Gas Pollution Reduction Target Aimed at Creating Good-Paying Union Jobs and Securing U.S. Leadership on Clean Energy Technologies, 22 April 2021, https://www.whitehouse.gov/briefing-room/statements-releases/2021/04/22/fact-sheet-president-biden-sets-2030-greenhouse-gas-pollution-reduction-target-aimed-at-creating-good-paying-union-jobs-and-securing-u-s-leadership-on-clean-energy-technologies/, retrieved 22 Nov 2022.

[7] The European Commission, The European Green Deal Brussels, 11 Dec 2019, https://eur-lex.europa.eu/legal-content/EN/TXT/?uri=COM:2019:640:FIN, retrieved 22 Nov 2022.

[8] G. Vaidyanathan, *Nature* (2021).

[9] Inger Andersen, Clean, affordable, equitable: The energy systems we need, Speech on High-Level Dialogue on Energy, 23 Sep 2021, https://www.unep.org/news-and-stories/speech/clean-affordable-equitable-energy-systems-we-need, retrieved 22 Nov 2022.

[10] W. Wang, B. Yuan, Q. Sun, R. Wennersten, *Journal of Energy Storage* 52 (8) (2022) 104812.

[11] E. Bellos, Z. Said, P. Lykas, C. Tzivanidis, *Thermal Science and Engineering Progress* 34 (5) (2022) 101435.

[12] A.S. Mehr, A. Lanzini, M. Santarelli, M.A. Rosen, *Energy* 228 (2021) 120613.
[13] Y. Zhang, Y. Lin, F. Lin, K. Yang, *Energy Conversion and Management* 260 (2) (2022) 115609.
[14] E.G. Lim, E.E. Dames, K.D. Cedrone, A.J. Acocella, T.R. Needham, A. Arce, D.R. Cohn, L. Bromberg, W.K. Cheng, W.H. Green, *Can. J. Chem. Eng.* 94 (4) (2016) 623–635.
[15] S. Mohankumar, P. Senthilkumar, *Renewable and Sustainable Energy Reviews* 80 (12) (2017) 1227–1238.
[16] H. Nazir, C. Louis, S. Jose, J. Prakash, N. Muthuswamy, M.E.M. Buan, C. Flox, S. Chavan, X. Shi, P. Kauranen, T. Kallio, G. Maia, K. Tammeveski, N. Lymperopoulos, E. Carcadea, E. Veziroglu, A. Iranzo, A.M. Kannan, *International Journal of Hydrogen Energy* 45 (27) (2020) 13777–13788.
[17] S. Porras, D. Kaczmarek, J. Herzler, S. Drost, M. Werler, T. Kasper, M. Fikri, R. Schießl, B. Atakan, C. Schulz, U. Maas, *Combustion and Flame* 212 (2020) 107–122.
[18] H. Gossler, S. Drost, S. Porras, R. Schießl, U. Maas, O. Deutschmann, *Combustion and Flame* 207 (2019) 186–195.
[19] A. Buttler, H. Spliethoff, *Renewable and Sustainable Energy Reviews* 82 (2018) 2440–2454.
[20] M.A. ALDER, *Water & Environment J* 1 (3) (1987) 271–277.
[21] A. Alengebawy, B.A. Mohamed, N. Ghimire, K. Jin, T. Liu, M. Samer, P. Ai, *Environmental research* 213 (2022) 113632.
[22] G.L. Kyriakopoulos, G. Arabatzis, *Renewable and Sustainable Energy Reviews* 56 (2016) 1044–1067.
[23] X. Luo, J. Wang, M. Dooner, J. Clarke, *Applied Energy* 137 (2015) 511–536.
[24] B. Zakeri, S. Syri, *Renewable and Sustainable Energy Reviews* 42 (2015) 569–596.
[25] H. Chen, T.N. Cong, W. Yang, C. Tan, Y. Li, Y. Ding, *Progress in Natural Science* 19 (3) (2009) 291–312.
[26] X. Tan, Q. Li, H. Wang, *International Journal of Electrical Power & Energy Systems* 44 (1) (2013) 179–191.
[27] M.M. Rahman, A.O. Oni, E. Gemechu, A. Kumar, *Energy Conversion and Management* 223 (2020) 113295.
[28] Z. Zhou, M. Benbouzid, J. Frédéric Charpentier, F. Scuiller, T. Tang, *Renewable and Sustainable Energy Reviews* 18 (2013) 390–400.
[29] M. Budt, D. Wolf, R. Span, J. Yan, *Applied Energy* 170 (2016) 250–268.
[30] S. Karellas, N. Tzouganatos, *Renewable and Sustainable Energy Reviews* 29 (2014) 865–882.
[31] J.P. Deane, B.P. Ó Gallachóir, E.J. McKeogh, *Renewable and Sustainable Energy Reviews* 14 (4) (2010) 1293–1302.

[32] S. Rehman, L.M. Al-Hadhrami, M.M. Alam, *Renewable and Sustainable Energy Reviews* 44 (2015) 586–598.
[33] W.F. Pickard, D. Abbott, *Proc. IEEE* 100 (2) (2012) 317–321.
[34] M. Fasihi, D. Bogdanov, C. Breyer, *Energy Procedia* 99 (2016) 243–268.
[35] S. Shiva Kumar, V. Himabindu, *Materials Science for Energy Technologies* 2 (3) (2019) 442–454.
[36] B. Parkinson, M. Tabatabaei, D.C. Upham, B. Ballinger, C. Greig, S. Smart, E. McFarland, *International Journal of Hydrogen Energy* 43 (5) (2018) 2540–2555.
[37] M. STEINBERG, *International Journal of Hydrogen Energy* 23 (6) (1998) 419–425.
[38] L. Tock, F. Maréchal, *International Journal of Hydrogen Energy* 37 (16) (2012) 11785–11795.
[39] J.D. Holladay, J. Hu, D.L. King, Y. Wang, *Catalysis Today* 139 (4) (2009) 244–260.
[40] M.A. Ancona, G. Antonioni, L. Branchini, A. de Pascale, F. Melino, V. Orlandini, V. Antonucci, M. Ferraro, *Energy Procedia* 101 (2016) 854–861.
[41] M. Gruber, P. Weinbrecht, L. Biffar, S. Harth, D. Trimis, J. Brabandt, O. Posdziech, R. Blumentritt, *Fuel Processing Technology* 181 (2018) 61–74.
[42] N.Z. Muradov, *Energy Fuels* 12 (1) (1998) 41–48.
[43] M. Karaismailoglu, H.E. Figen, S.Z. Baykara, *International Journal of Hydrogen Energy* 44 (20) (2019) 9922–9929.
[44] E.K. Lee, S.Y. Lee, G.Y. Han, B.K. Lee, T.-J. Lee, J.H. Jun, K.J. Yoon, *Carbon* 42 (12-13) (2004) 2641–2648.
[45] E. Tezel, H.E. Figen, S.Z. Baykara, *International Journal of Hydrogen Energy* 44 (20) (2019) 9930–9940.
[46] N. MURADOV, *Catalysis Communications* 2 (3-4) (2001) 89–94.
[47] E. Bartholomé, *Chemical Engineering Science* 3 (1954) 94–104.
[48] G. Fau, N. Gascoin, P. Gillard, J. Steelant, *Journal of Analytical and Applied Pyrolysis* 104 (2013) 1–9.
[49] C. Guéret, M. Daroux, F. Billaud, *Chemical Engineering Science* 52 (5) (1997) 815–827.
[50] F.P. Larkins, A.Z. Khan, *Aust. J. Chem.* 42 (10) (1989) 1655.
[51] A. Holmen, *Catalysis Today* 142 (1-2) (2009) 2–8.
[52] D. Nativel, B. Shu, J. Herzler, M. Fikri, C. Schulz, *Proceedings of the Combustion Institute* 37 (1) (2019) 197–204.
[53] C. Keramiotis, G. Vourliotakis, G. Skevis, M.A. Founti, C. Esarte, N.E. Sánchez, A. Millera, R. Bilbao, M.U. Alzueta, *Energy* 43 (1) (2012) 103–110.
[54] C.V. Naik, A.M. Dean, *Proceedings of the Combustion Institute* 32 (1) (2009) 437–443.
[55] G.F. Glasier, P.D. Pacey, *Carbon* 39 (1) (2001) 15–23.

[56] R. Hegner, B. Atakan, *International Journal of Hydrogen Energy* 42 (2) (2017) 1287–1297.
[57] S. Wiemann, R. Hegner, B. Atakan, C. Schulz, S.A. Kaiser, *Fuel* 215 (2018) 40–45.
[58] K. Banke, R. Hegner, D. Schröder, C. Schulz, B. Atakan, S.A. Kaiser, *Fuel* 243 (2019) 97–103.
[59] B. Atakan, *Energies* 12 (17) (2019) 3332.
[60] B. Atakan, S.A. Kaiser, J. Herzler, S. Porras, K. Banke, O. Deutschmann, T. Kasper, M. Fikri, R. Schießl, D. Schröder, C. Rudolph, D. Kaczmarek, H. Gossler, S. Drost, V. Bykov, U. Maas, C. Schulz, *Renewable and Sustainable Energy Reviews* 133 (2020) 110264.
[61] D.G. Goodwin, H.K. Moffat, R.L. Speth, *Cantera: An Object-Oriented Software Toolkit For Chemical Kinetics, Thermodynamics, And Transport Processes. Version 2.3.0*, Zenodo, 2017.
[62] A.C. Hindmarsh, P.N. Brown, K.E. Grant, S.L. Lee, R. Serban, D.E. Shumaker, C.S. Woodward, *ACM Trans. Math. Softw.* 31 (3) (2005) 363–396.
[63] G. Woschni, in: *SAE Technical Paper Series*, vol. 670931, National Fuels and Lubricants, Powerplants, Transportation Meetings, OCT. 30, 1967, SAE International400 Commonwealth Drive, Warrendale, PA, United States, 1967.
[64] A. Cuoci, A. Frassoldati, T. Faravelli, E. Ranzi, *Combustion and Flame* 156 (10) (2009) 2010–2022.
[65] T. Faravelli, *Combustion and Flame* 132 (1-2) (2003) 188–207.
[66] A. Frassoldati, T. Faravelli, E. Ranzi, *Combustion and Flame* 135 (1-2) (2003) 97–112.
[67] E. Ranzi, A. Frassoldati, R. Grana, A. Cuoci, T. Faravelli, A.P. Kelley, C.K. Law, *Progress in Energy and Combustion Science* 38 (4) (2012) 468–501.
[68] C.-W. Zhou, Y. Li, U. Burke, C. Banyon, K.P. Somers, S. Ding, S. Khan, J.W. Hargis, T. Sikes, O. Mathieu, E.L. Petersen, M. AlAbbad, A. Farooq, Y. Pan, Y. Zhang, Z. Huang, J. Lopez, Z. Loparo, S.S. Vasu, H.J. Curran, *Combustion and Flame* 197 (2018) 423–438.
[69] Z. Wang, G. Du, Z. Li, X. Wang, D. Wang, *Fuel* 255 (2019) 115701.
[70] M. Pochet, H. Jeanmart, F. Contino, *Front. Mech. Eng.* 6 (2020) 52.
[71] T. J. Kotas, *The exergy method of thermal plant analysis*, Krieger Publishing company, Malabar, Florida, 1995.
[72] G.F. Hohenberg, in: *SAE Technical Paper Series*, 1979 SAE International Off-Highway and Powerplant Congress and Exposition, SEP. 10, 1979, SAE International400 Commonwealth Drive, Warrendale, PA, United States, 1979.
[73] W.J.D. Annand, *Proceedings of the Institution of Mechanical Engineers* 177 (1) (1963) 973–996.

[74] J. Chang, O. Güralp, Z. Filipi, D.N. Assanis, T.-W. Kuo, P. Najt, R. Rask, in: *SAE Technical Paper Series*, 2004 Powertrain & Fluid Systems Conference & Exhibition, OCT. 25, 2004, SAE International400 Commonwealth Drive, Warrendale, PA, United States, 2004.

[75] S. Koohi-Fayegh, M.A. Rosen, *Journal of Energy Storage* 27 (2020) 101047.

[76] H. Nazir, N. Muthuswamy, C. Louis, S. Jose, J. Prakash, M.E.M. Buan, C. Flox, S. Chavan, X. Shi, P. Kauranen, T. Kallio, G. Maia, K. Tammeveski, N. Lymperopoulos, E. Carcadea, E. Veziroglu, A. Iranzo, A. M Kannan, *International Journal of Hydrogen Energy* (2020).

[77] R. Carapellucci, L. Giordano, *Journal of Power Sources* 469 (2020) 228391.

[78] R.S. El-Emam, H. Özcan, *Journal of Cleaner Production* 220 (2019) 593–609.

[79] F.G. Billaud, F. Baronnet, C.P. Gueret, *Ind. Eng. Chem. Res.* 32 (8) (1993) 1549–1554.

[80] S. Wang, D.F. Davidson, R.K. Hanson, *The journal of physical chemistry. A* 120 (28) (2016) 5427–5434.

[81] S. Timmerberg, M. Kaltschmitt, M. Finkbeiner, *Energy Conversion and Management: X* 7 (2020) 100043.

[82] N. MURADOV, T. VEZIROLU, *International Journal of Hydrogen Energy* 30 (3) (2005) 225–237.

[83] Q. Chen, A.C. Lua, *Chemical Engineering Journal* 389 (2020) 124366.

[84] A.S. Al-Fatesh, S.O. Kasim, A.A. Ibrahim, A.S. Al-Awadi, A.E. Abasaeed, A.H. Fakeeha, A.E. Awadallah, *Renewable Energy* 155 (2020) 969–978.

[85] R. Zhang, H. Liao, J. Yang, X. Fan, B. Yang, *Proceedings of the Combustion Institute* 37 (4) (2019) 5577–5586.

[86] H. An, Y. Cheng, T. Li, Y. Li, Y. Cheng, *Fuel Processing Technology* 172 (2018) 195–199.

[87] J. Kang, J. Ran, J. Niu, J. Shi, J. He, Z. Yang, *International Journal of Hydrogen Energy* 44 (41) (2019) 22904–22918.

[88] T. Bensabath, M.D. Le, H. Monnier, P.-A. Glaude, *Chemical Engineering Science* 202 (2019) 84–94.

[89] T. Koike, K. Morinaga, *BCSJ* 54 (2) (1981) 530–534.

[90] A. Eremin, E. Gurentsov, E. Mikheyeva, *Combustion and Flame* 159 (12) (2012) 3607–3615.

[91] S. Peukert, A. Sallom, A. Emelianov, T. Endres, M. Fikri, H. Böhm, H. Jander, A. Eremin, C. Schulz, *Proceedings of the Combustion Institute* 37 (1) (2019) 1125–1132.

[92] C. Ezenwajiaku, M. Talibi, N.A.K. Doan, N. Swaminathan, R. Balachandran, *International Journal of Hydrogen Energy* 44 (14) (2019) 7642–7655.

[93] A. Eyal, L. Tartakovsky, *Applied Energy* 263 (2020) 114622.

[94] L. Tartakovsky, M. Sheintuch, *Progress in Energy and Combustion Science* 67 (2018) 88–114.
[95] R. Hegner, S. Drost, M. Werler, R. Schießl, U. Maas, B. Atakan (2017).
[96] J.B. Heywood, *Internal combustion engine fundamentals*, McGraw-Hill, New York, N.Y., 1988.
[97] D. Kaczmarek, B. Atakan, T. Kasper, *Combustion and Flame* 205 (2019) 345–357.
[98] M.W. Melaina, O. Antonia, M. Penev, *Blending Hydrogen into Natural Gas Pipeline Networks. A Review of Key Issues*, 2013.
[99] A. Drakon, A. Eremin, E. Mikheyeva, B. Shu, M. Fikri, C. Schulz, *Combustion and Flame* 198 (2018) 158–168.
[100] R.K. Parsapur, S. Chatterjee, K.-W. Huang, *ACS Energy Lett.* 5 (9) (2020) 2881–2885.
[101] S. Schneider, S. Bajohr, F. Graf, T. Kolb, *Chemie Ing. Techn.* 92 (8) (2020) 1023–1032.
[102] R. Yukesh Kannah, S. Kavitha, Preethi, O. Parthiba Karthikeyan, G. Kumar, N.V. Dai-Viet, J. Rajesh Banu, *Bioresource technology* 319 (2021) 124175.
[103] P.M. Mortensen, I. Dybkjær, *Applied Catalysis A: General* 495 (2015) 141–151.
[104] D. Li, Y. Nakagawa, K. Tomishige, *Applied Catalysis A: General* 408 (1-2) (2011) 1–24.
[105] S. Drost, W. Xie, R. Schießl, U. Maas, *Proceedings of the Combustion Institute* 133 (October 2018) (2022) 186.
[106] D. Schröder, R. Hegner, A. Güngör, B. Atakan, *Energy Conversion and Management* 203 (2020) 112085.
[107] C. Rudolph, B. Atakan, *Energy Technol.* 56 (2021) 2000948.
[108] M. Luberti, H. Ahn, *Separation and Purification Technology* 261 (2021) 118254.
[109] C. Rudolph, B. Atakan, *Energy* 218 (53) (2021) 119375.
[110] C. Rudolph, D. Freund, D. Kaczmarek, B. Atakan, *Combustion and Flame* 9 (2022) 112063.
[111] H. Zhang, D. Kaczmarek, C. Rudolph, S. Schmitt, N. Gaiser, P. Oßwald, T. Bierkandt, T. Kasper, B. Atakan, K. Kohse-Höinghaus, *Combustion and Flame* 237 (2022) 111863.
[112] Rolls-Royce Group, Gas system Series 4000 Natural Gas, *https://www.mtu-solutions.com/content/dam/mtu/products/power-generation/may-2021/3234731_PG_spec_8V12V16V20V4000GS_3A_NG_NOx500_50Hz.pdf/_jcr_content/renditions/original./3234731_PG_spec_8V12V16V20V4000GS_3A_NG_NOx500_50Hz.pdf*.
[113] C. Rudolph, C.M. Grégoire, S.P. Cooper, S.A. Alturaifi, O. Mathieu, E.L. Petersen, B. Atakan, *Proceedings of the Combustion Institute* 243 (2022) 97.

[114] E. Ranzi, A. Frassoldati, A. STAGNI, M. Pelucchi, A. CUOCI, T. Faravelli, *Int. J. Chem. Kinet.* 46 (9) (2014) 512–542.
[115] K. Banke, S.A. Kaiser, *Proceedings of the Combustion Institute* 102 (2023) 322.
[116] B. Atakan, *Int. J. Thermo* 14 (4) (2011).
[117] J. Herzler, M. Fikri, C. Schulz, *Combustion and Flame* 216 (2020) 293–299.
[118] D. Kaczmarek, S. Shaqiri, B. Atakan, T. Kasper, *Proceedings of the Combustion Institute* 38 (1) (2021) 233–241.
[119] L. Cai, H. Pitsch, *Combustion and Flame* 162 (5) (2015) 1623–1637.
[120] G. Bagheri, E. Ranzi, M. Pelucchi, A. Parente, A. Frassoldati, T. Faravelli, *Combustion and Flame* 212 (2020) 142–155.
[121] B. Koroglu, O.M. Pryor, J. Lopez, L. Nash, S.S. Vasu, *Combustion and Flame* 164 (2) (2016) 152–163.
[122] O. Mathieu, S.P. Cooper, S. Alturaifi, C.R. Mulvihill, T.M. Atherley, E.L. Petersen, *Energy Fuels* 34 (6) (2020) 7533–7544.
[123] O. Mathieu, C.R. Mulvihill, E.L. Petersen, *Fuel* 236 (12) (2019) 1164–1180.
[124] R.M. Spearrin, C.S. Goldenstein, J.B. Jeffries, R.K. Hanson, *Applied optics* 53 (9) (2014) 1938–1946.
[125] CHEMKIN-PRO 21.2, Reaction Design: San Diego, 2017.
[126] G.P. Smith, Y. Tao, and H. Wang, Foundational Fuel Chemistry Model Version 1.0 (FFCM-1), http://nanoenergy.stanford.edu/ffcm1, 2016.
[127] Y. Wu, S. Panigrahy, A.B. Sahu, C. Bariki, J. Beeckmann, J. Liang, A.A.E. Mohamed, S. Dong, C. Tang, H. Pitsch, Z. Huang, H.J. Curran, *Combustion and Flame* 226 (2021) 229–242.
[128] A.V. Joshi, H. Wang, *Int. J. Chem. Kinet.* 38 (1) (2006) 57–73.
[129] D.L. Baulch, C.T. Bowman, C.J. Cobos, R.A. Cox, T. Just, J.A. Kerr, M.J. Pilling, D. Stocker, J. Troe, W. Tsang, R.W. Walker, J. Warnatz, *Journal of Physical and Chemical Reference Data* 34 (3) (2005) 757–1397.
[130] S. Kolb, T. Plankenbühler, K. Hofmann, J. Bergerson, J. Karl, *Renewable and Sustainable Energy Reviews* 146 (2021) 111147.
[131] L. Craggs, P. Gilbert, in: *Greenhouse Gases Balances of Bioenergy Systems*, vol. 48, Elsevier, 2018, pp. 1–10.
[132] K. de Kleijne, S.V. Hanssen, L. van Dinteren, M.A.J. Huijbregts, R. van Zelm, H. de Coninck, *One Earth* 5 (2) (2022) 168–185.
[133] B. Wanten, S. Maerivoet, C. Vantomme, J. Slaets, G. Trenchev, A. Bogaerts, *Journal of CO2 Utilization* 56 (6) (2022) 101869.
[134] Y. Uytdenhouwen, K.M. Bal, E.C. Neyts, V. Meynen, P. Cool, A. Bogaerts, *Chemical Engineering Journal* 405 (2021) 126630.

[135] Y. Vadikkeettil, Y. Subramaniam, R. Murugan, P.V. Ananthapadmanabhan, J. Mostaghimi, L. Pershin, C. Batiot-Dupeyrat, Y. Kobayashi, *Renewable and Sustainable Energy Reviews* 161 (5) (2022) 112343.

[136] C. Shi, S. Wang, X. Ge, S. Deng, B. Chen, J. Shen, *Journal of CO2 Utilization* 46 (2) (2021) 101462.

[137] Z. Bao, F. Yu, in: vol. 3, Elsevier, 2018, pp. 43–76.

[138] A. Abdulrasheed, A.A. Jalil, Y. Gambo, M. Ibrahim, H.U. Hambali, M.Y. Shahul Hamid, *Renewable and Sustainable Energy Reviews* 108 (9) (2019) 175–193.

[139] I.V. Yentekakis, P. Panagiotopoulou, G. Artemakis, *Applied Catalysis B: Environmental* 296 (3) (2021) 120210.

[140] A.I. Tsiotsias, N.D. Charisiou, V. Sebastian, S. Gaber, S.J. Hinder, M.A. Baker, K. Polychronopoulou, M.A. Goula, *International Journal of Hydrogen Energy* 47 (8) (2022) 5337–5353.

[141] M. Ahadzadeh, S.M. Alavi, M. Rezaei, E. Akbari, *Molecular Catalysis* 524 (38) (2022) 112325.

[142] L. RABERG, M. JENSEN, U. OLSBYE, C. DANIEL, S. HAAG, C. MIRODATOS, A. SJASTAD, *Journal of Catalysis* 249 (2) (2007) 250–260.

[143] X. Li, Z. Yang, L. Zhang, Z. He, R. Fang, Z. Wang, Y. Yan, J. Ran, *Energy* 234 (51) (2021) 121261.

[144] P. Cao, S. Adegbite, H. Zhao, E. Lester, T. Wu, *Applied Energy* 227 (35) (2018) 190–197.

[145] A. Ashok, M.A. Katebah, P. Linke, D. Kumar, D. Arora, K. Fischer, T. Jacobs, M.'m. Al-Rawashdeh, *Reviews in Chemical Engineering* 0 (0) (2021).

[146] H. Gossler, O. Deutschmann, *International Journal of Hydrogen Energy* 40 (34) (2015) 11046–11058.

[147] O. Mathieu, P. Diévart, M.A. Turner, D.J. Mohr, C.M. Grégoire, S.A. Alturaifi, L. Catoire, E.L. Petersen, *Proceedings of the Combustion Institute* 73 (2022) 95.

[148] C.R. Mulvihill, C.L. Keesee, T. Sikes, R.S. Teixeira, O. Mathieu, E.L. Petersen, *Proceedings of the Combustion Institute* 37 (1) (2019) 735–742.

[149] U. Burke, K.P. Somers, P. O'Toole, C.M. Zinner, N. Marquet, G. Bourque, E.L. Petersen, W.K. Metcalfe, Z. Serinyel, H.J. Curran, *Combustion and Flame* 162 (2) (2015) 315–330.

[150] Hai Wang, Xiaoqing You, Ameya V. Joshi, Scott G. Davis, Alexander Laskin, Fokion Egolfopoulos & Chung K. Law. USC Mech Version II. High-Temperature Combustion Reaction Model of H2/CO/C1-C4 Compounds. (2007). http://ignis.usc.edu/USC_Mech_II.htm.

[151] W. Tsang, R.F. Hampson, *Journal of Physical and Chemical Reference Data* 15 (3) (1986) 1087–1279.

[152] D. Kovacs, J.E. Jackson, *J. Phys. Chem. A* 105 (32) (2001) 7579–7587.
[153] F. Hayes, W.D. Lawrance, W.S. Staker, K.D. King, *J. Phys. Chem.* 100 (27) (1996) 11314–11318.
[154] M. Koch, F. Temps, R. Wagener, H.G. Wagner, *Berichte der Bunsengesellschaft für physikalische Chemie* 94 (6) (1990) 645–650.
[155] [41] G. P. Smith, D. M. Golden, M. Frenklach, N. W. Moriarty, B. Eiteneer, M. Goldenberg, C. T. Bowman, R. K. Hanson, S. Song, W. C. Gardiner, Jr., V. V. Lissianski, and Zhiwei Qin http://www.me.berkeley.edu/gri_mech/.
[156] J.A. Miller, C.F. Melius, *Combustion and Flame* 91 (1) (1992) 21–39.
[157] E.L. Petersen, D.M. Kalitan, S. Simmons, G. Bourque, H.J. Curran, J.M. Simmie, *Proceedings of the Combustion Institute* 31 (1) (2007) 447–454.
[158] N.M. Marinov, W.J. Pitz, C.K. Westbrook, A.M. Vincitore, M.J. Castaldi, S.M. Senkan, C.F. Melius, *Combustion and Flame* 114 (1-2) (1998) 192–213.
[159] [46] Chemical-Kinetic Mechanisms for Combustion Applications, San Diego Mechanism web page, Mechanical and Aerospace Engineering (Combustion Research), University of California at San Diego (http://combustion.ucsd.edu).
[160] A. Jacobs, M. Wahl, R. Weller, J. Wolfrum, *Chemical Physics Letters* 158 (1-2) (1989) 161–166.
[161] D.G. Goodwin, H.K. Moffat, R.L. Speth, Cantera: An Object-Oriented Software Toolkit For Chemical Kinetics, https://cantera.org/science/reactors.html, Thermodynamics, And Transport Processes. Version 2.3.0, Zenodo, 2017.
[162] D.M. Anderson, T.M. Yun, P.A. Kottke, A.G. Fedorov, *Ind. Eng. Chem. Res.* 56 (7) (2017) 1758–1771.

DOI: 10.17185/duepublico/78622
URN: urn:nbn:de:hbz:465-20230705-160721-1